

Strategies to Optimizing Dye-Sensitized Solar Cells: Organic Sensitzers, Tandem Device Structures, and Numerical Device Modeling

THÈSE N° 4805 (2010)

PRÉSENTÉE LE 28 SEPTEMBRE 2010
À LA FACULTÉ SCIENCES DE BASE
LABORATOIRE DE PHOTONIQUE ET INTERFACES
PROGRAMME DOCTORAL EN CHIMIE ET GÉNIE CHIMIQUE

ÉCOLE POLYTECHNIQUE FÉDÉRALE DE LAUSANNE

POUR L'OBTENTION DU GRADE DE DOCTEUR ÈS SCIENCES

PAR

Sophie WENGER

acceptée sur proposition du jury:

Prof. J.-E. Moser, président du jury
Prof. M. Grätzel, directeur de thèse
 Prof. C. Ballif, rapporteur
 Prof. A. Hagfeldt, rapporteur
 Dr F. Nüesch, rapporteur



ÉCOLE POLYTECHNIQUE
FÉDÉRALE DE LAUSANNE

Suisse
2010

Abstract

Dye-sensitized solar cells (DSCs) constitute a novel class of hybrid organic-inorganic solar cells. At the heart of the device is a mesoporous film of titanium dioxide (TiO_2) nanoparticles, which are coated with a monolayer of dye sensitive to the visible region of the solar spectrum. The role of the dye is similar to the role of chlorophyll in plants; it harvests solar light and transfers the energy via electron transfer to a suitable material (here TiO_2) to produce electricity — as opposed to chemical energy in plants. DSCs are fabricated of abundant and cheap materials using inexpensive processes (e.g. screen-printing) and are likely to be a significant contributor to the future commercial photovoltaic technology portfolio.

The work conducted during this thesis aimed at optimizing the DSC using three different strategies: The use of versatile organic sensitizers for stable and efficient DSCs, the study of tandem device architectures in combination with other solar cells to harvest a larger fraction of the solar spectrum, and the development of a validated optoelectric model of the DSC.

Organic donor- π -acceptor dyes are an interesting alternative to the standard metal-organic complexes used in DSCs. Efficient photovoltaic conversion and stable performance could be demonstrated with three classes of donor systems, namely diphenylamine, difluorenylaminophenyl, and π -extended tetrathiafulvalene. The highest conversion efficiencies were obtained with a difluorenylaminophenyl donor system ($\eta = 8.3\%$ with a volatile electrolyte and $\eta = 7.6\%$ with a solvent-free ionic liquid, which was a new record for organic dyes at the time of publication). Surprisingly, efficient regeneration of the oxidized dye by the I^-/I_3^- redox mediator was found with the π -extended tetrathiafulvalene system, even though the thermodynamic driving force was as low as 150 mV. So far driving forces of 300–500 mV had been regarded as necessary for efficient regeneration of the dye cation. Also, important structure-property relationships pertaining to the recombination of electrons with the electrolyte and to the stability of the device could be identified (i.e. effect of linear vs. branched structure, linker length, and moieties used).

The power conversion efficiency of solar cells can be extended beyond the limit for a single cell ($\sim 30\%$) by using multiple cells with different optical gaps in

a tandem device. DSCs and chalcopyrite Cu(In,Ga)Se₂ (CIGS) solar cells have complementary optical gaps and are thus suitable systems for integration in a tandem device. It was shown that a monolithic DSC/CIGS tandem device has the potential for increased efficiency over a mechanically stacked device due to increased light transmission to the bottom cell, and a monolithic DSC/CIGS device with an initial efficiency of $\eta = 12.2\%$ was demonstrated. The degradation of the devices — induced by the corrosion of the CIGS cell in contact with the I⁻/I₃⁻ redox mediator — could be retarded with a protective thin conformal ZnO/TiO₂ oxide layer coated on the CIGS cell by atomic layer deposition.

Finally, an experimentally validated optical and electrical model of the DSC has been developed to assist the optimization process, which is predominantly conducted by empirical means in the DSC research community. The optical model allows to accurately calculate the *internal* quantum efficiency of devices, i.e. the ratio of extracted electrons to absorbed photons by the dye, a crucial and so far difficult to determine characteristic. Intrinsic parameters — like injection efficiency, electron diffusion length, or distribution of trap states in the TiO₂ — can be extracted from experimental steady-state and time-dependent data with the electric model. The model allows to make a comprehensive and quantitative loss analysis of the different optical and electric loss channels in the DSC. The model has been implemented with a graphical user interface for straightforward usage.

All three optimization strategies — organic dyes, tandem architecture, and device modeling — developed during this thesis make a valuable contribution to the development and commercialization of inexpensive and high efficiency DSCs. They enable a comprehensive view of the system and pave the way for a systematic analysis and reduction of losses, which has been the ultimate route to success for several established photovoltaic technologies.

Keywords: Photovoltaics, dye-sensitized solar cell, organic sensitizer, donor-acceptor system, tandem solar cell, multijunction, Cu(In,Ga)Se₂, CIGS, optical and electric model, loss analysis, electron transport and recombination, nanostructure

Zusammenfassung

Farbstoffsolarzellen stellen eine neue Klasse von hybriden organischen/anorganischen Solarzellen dar. Das Kernelement der Zelle ist eine poröse Schicht aus Titanidioxid (TiO_2) Nanopartikeln, die mit einem Farbstoff beschichtet ist, der Licht im sichtbaren Bereich des Sonnenspektrums absorbiert. Der Farbstoff erfüllt eine ähnliche Funktion wie der natürliche Farbstoff Chlorophyll in Pflanzen: Er absorbiert das Sonnenlicht und gibt die aufgenommene Energie via Elektronen-Transfer weiter an ein geeignetes Material (hier TiO_2). In der Farbstoffsolarzelle wird daraus Elektrizität erzeugt, wohingegen in einer Pflanze mit einem ähnlichen Prozess chemische Energie erzeugt wird. Farbstoffsolarzellen bestehen aus günstigen und ausreichend verfügbaren Materialien und werden mit energiearmen Verfahren hergestellt (z.B. Siebdruck). Aus diesen Gründen ist die Farbstoffsolarzelle ein wichtiger Hoffnungsträger für die zukünftige Produktion von kostengünstigem Solarstrom.

Im Rahmen dieser Dissertation wurden drei Strategien zur Optimierung von Farbstoffsolarzellen im Detail untersucht: Die Anwendung von vielfältigen organischen Farbstoffen für stabile und effiziente Zellen, die Anordnung in "Tandem-Zellen", so dass ein gröserer Anteil des Sonnenlichts absorbiert wird, und die Entwicklung eines validierten optoelektrischen Models der Farbstoffsolarzelle.

Organische Donator- π -Akzeptor Farbstoffe sind eine interessante Alternative zu den überwiegend verwendeten metall-organischen Komplexen. Es wurden drei Donator-Familien untersucht (Diphenylamin, Difluorenylaminophenyl und π -erweitertes Tetrathiafulvalen), mit denen effiziente photovoltaische Umwandlung und stabile Leistungen in Farbstoffsolarzellen nachgewiesen werden konnte. Der höchste Wirkungsgrad wurde mit einem Difluorenylaminophenyl Donator-System erzielt ($\eta = 8.3\%$ mit einem volatilen Elektrolyten und $\eta = 7.6\%$ mit einer lösungsmittelfreien ionischen Flüssigkeit, was einen neuen Rekord für organische Farbstoffe zum Publikationszeitpunkt darstellte). Mit dem π -erweiterten Tetrathiafulvalen konnte erstaunlicherweise die effiziente Regeneration von oxidiertem Farbstoff durch den I^-/I_3^- Redox-Mediator beobachtet werden, obwohl die thermodynamische Triebkraft nur 150 mV betrug. Bis anhin wurde eine Triebkraft von 300–500 mV für eine effiziente Regeneration des Farbstoffs vorausgesetzt. Des weiteren konnten

wichtige Beziehungen zwischen der molekularen Struktur des Farbstoffs und der Rekombination von Elektronen mit dem Elektrolyten sowie der Langzeitstabilität identifiziert werden (Auswirkung von linearer vs. verzweigter Struktur, Länge des Donator-Akzeptor Bindegliedes und diverser molekularer Bausteine).

Der Wirkungsgrad von Solarzellen (theoretisches Maximum für eine einzelne Zelle $\eta \sim 30\%$) kann erhöht werden, wenn mehrere Zellen mit verschiedenen optischen Bandlücken übereinander in einer Tandem-Konfiguration angeordnet sind. Farbstoffsolarzellen und Chalkopyrit Cu(In,Ga)Se₂ (CIGS) Solarzellen haben komplementäre Absorptionscharakteristiken und sind geeignete Kandidaten für den Zusammenschluss in einer Tandemzelle. Es wurde eine monolithische Farbstoff/CIGS-Tandemzelle mit einem anfänglichen Wirkungsgrad von $\eta = 12.2\%$ hergestellt und gezeigt, dass dieser Aufbau optische Vorteile gegenüber der Aufeinanderschichtung von zwei Einzelzellen hat. Die Stabilitätsprobleme — eine Folge der Korrosion der CIGS Zelle durch den Elektrolyten — konnten mit einer dünnen ZnO/TiO₂ Schicht, die mittels Atomlagenabscheidung auf die CIGS Zelle aufgetragen wurde, reduziert werden.

Zur Unterstützung des empirischen Optimisierungsprozesses wurde ein validiertes optisches und elektrisches Model der Farbstoffsolarzelle entwickelt. Mit dem optischen Model kann die *interne* Quanteneffizienz, d.h. das Verhältnis von entnommenen Elektronen zu den vom Farbstoff absorbierten Photonen, genau beziffert werden, was bisher schwierig zu bestimmen war. Intrinsische Parameter — wie die Injektionseffizienz, die Elektronen Diffusionslänge oder die Verteilung von Elektronenfallen im TiO₂ — können mit dem elektrischen Model aus stationären oder zeitabhängigen Messungen extrahiert werden. Mit dem Model können optische und elektrische Modelle nun ganzheitlich quantifiziert werden. Das Model wurde mit einer graphischen Benutzeroberfläche ausgestattet.

Alle drei Optimierungsstrategien — organische Farbstoffe, Tandemaufbau und Zellmodellierung — die während dieser Dissertation entwickelt wurden, liefern wertvolle Beiträge für die Weiterentwicklung und Kommerzialisierung von kostengünstigen und effizienten Farbstoffsolarzellen. Sie erlauben eine ganzheitliche Sicht des Systems und ebnen den Weg für eine systematische Analyse und Reduktion der Verluste — der Königsweg für viele etablierte Solarzellen-Technologien.

Schlüsselwörter: Photovoltaik, Farbstoffsolarzelle, organische Farbstoffe, Donator-Akzeptor System, Tandem Solarzelle, Cu(In,Ga)Se₂, CIGS, optisches und elektrisches Model, Velustanalyse, Elektronenrekombination und -transport

Contents

1	Introduction	3
1.1	Motivation	3
1.2	Basics of photovoltaic energy conversion	4
1.2.1	The solar spectrum	5
1.2.2	Theoretical maximum conversion efficiency	6
1.2.3	Basic structure of a solar cell	7
1.2.4	Overview of photovoltaic technologies and market	10
1.3	The dye-sensitized solar cell	15
1.3.1	Basic principle and historical background	15
1.3.2	Device structure	16
1.3.3	Electron generation, transport, and recombination	17
1.4	Objectives and contributions of this work	19
	Bibliography	21
2	Experimental methods	25
2.1	Device fabrication	25
2.1.1	Materials	25
2.1.2	Device assembly	27
2.2	Steady-state photovoltaic characterization	28
2.2.1	Spectral response and quantum efficiency	28
2.2.2	Current-voltage characteristics	30
2.3	Time-resolved transient characterization	33
2.3.1	Laser transient absorbance measurements	33
2.3.2	Transient photovoltage and photocurrent decay measurements	34
2.4	Optical characterization	39
2.4.1	UV-vis-NIR absorption	39
2.4.2	Spectroscopic ellipsometry	40
2.4.3	Fourier transformed infrared spectroscopy	41
	Bibliography	41

3 Organic sensitizers for stable and efficient dye-sensitized solar cells	43
3.1 Introduction	43
3.2 Experimental	46
3.3 Diphenylamine donor systems	48
3.3.1 Results and discussion	49
3.4 Difluorenylaminophenyl donor systems	55
3.4.1 Results and discussion	56
3.5 π -Extended tetrathiafulvalene donor systems	61
3.5.1 Results and discussion	62
3.6 Conclusions	70
Bibliography	72
4 Monolithic dye-sensitized $TiO_2/Cu(In,Ga)Se_2$ tandem solar cells	77
4.1 Introduction	77
4.2 Tandem device structure	80
4.3 Experimental	83
4.4 Results	84
4.4.1 Photovoltaic performance and stability	84
4.4.2 Optical loss analysis	88
4.5 Conclusions	93
Bibliography	94
5 Optical and electrical modeling of dye-sensitized solar cells	99
5.1 Introduction	99
5.2 Theory	102
5.2.1 Optical model	102
5.2.2 Electrical model	105
5.2.2.1 Linear recombination	107
5.2.2.2 Non-linear recombination	110
5.2.2.3 Trapping and detrapping	110
5.2.2.4 Time-dependent case	112
5.2.2.5 Ionic transport in the electrolyte	114
5.2.2.6 Resistances and overpotential at the counter electrode .	115
5.3 Experimental	116
5.4 Results and discussion	117
5.4.1 Optical simulations	117
5.4.2 Steady-state electrical simulations	125

5.4.3	Time-dependent electrical simulations	129
5.4.4	Loss analysis	130
5.4.5	Graphical user interface	133
5.4.5.1	Simulation example	135
5.5	Conclusions	140
	Bibliography	141
6	Final conclusions and outlook	147
A	Optical constants of materials in CIGS solar cell	151
B	Modeling of dye-sensitized solar cells	153
B.1	Extracting the complex index of refraction of a thick film	153
B.2	Four-flux analysis of sensitized mesoporous TiO ₂ films between microscope glasses	154
B.3	General solution of the linear continuity equation for conduction band electrons	157
	Bibliography	159
	Acknowledgements	163
	Curriculum vitae and list of publications	165

Chapter 1

Introduction

“Sun spreads through the treetops like an epidemic.”

— Dave Bonta, from the morningporch.com blog

1.1 Motivation

Solar radiation is the single most abundant energy source of our planet. For many millennia, humanity relied solely on renewable forms of solar energy — making use of direct forms like lighting or heat, and indirect forms like biomass or wind. With the explosion of the world population at the beginning of the 20th century and its growing energy demand, humans started to tap fossil non-renewable forms of ancient biomass like oil, gas and coal extensively [1]. Fossil energy sources possess a very high energy density and can be stored and transported easily — seemingly a blessing for humanity's energy needs.

We know now that our dependence on the burning of fossil fuels actually is a curse, which causes geopolitical tensions, environmental damage, and tragically puts our climate — our sustenance — at stake [2]. We clearly must move toward a more sustainable energy economy.

Today, global primary energy is consumed at a rate of about 15 TW [1], whereas our planet receives about 174×10^3 TW of solar radiation. Even if only a fraction of this energy can be harvested, the solar energy source is enormous and dwarfs all known non-renewable sources.

Energy from renewable sources — i.e. biomass, hydropower, wind, solar, and geothermal — currently accounts for about 13 % of global energy consumption. The largest share comes from the burning of traditional biomass. If we only consider global electricity

consumption, close to 20 % is covered by renewables, mainly hydropower. Though the installed renewable energy capacities are constantly growing, their shares in global energy and electricity consumption have remained constant for the past two decades [3, 4].

Progressive energy policies are being implemented in many countries to accelerate the deployment of renewables. In many regions — notably in certain European countries like Germany — these policies have induced a “green economy” boom, in particular in the wind and solar electricity (photovoltaics) sectors. Wind clearly outperforms photovoltaics in terms of installed capacity. However, photovoltaics is the fastest growing power generation technology. The sector has been growing with an annual rate of about 40 % for the past two decades [5].

The photovoltaic sector owes its stunning growth rates to a combination of decreasing prices, due to economies of scale, and the development of new, less expensive, thin-film technologies. In countries with high solar irradiation, these thin-film technologies now produce electricity at a similar price to end-user grid electricity. However, for a truly significant impact of photovoltaics in our future electricity-mix, we need efficient and low-cost solar cells fabricated of abundant non-toxic materials with simple manufacturing processes.

The dye-sensitized solar cell, a technology invented at the Ecole Polytechnique Fédérale de Lausanne in 1991, fulfills these requirements and is likely to be a significant contributor to the future commercial photovoltaic technology portfolio. This thesis intends to support the development of the dye-sensitized solar cell by assisting the academic optimization process on the materials, device architecture, and numerical modeling level.

We are bathed in sunshine, and we can profit from it immensely. Back in 1931, Thomas Edison told his friends Henry Ford and Harvey Firestone: “I’d put my money on the sun and solar energy. What a source of power! I hope we don’t have to wait until oil and coal run out before we tackle that.”

1.2 Basics of photovoltaic energy conversion

Solar radiation can be transformed into various other energy forms like heat, chemical energy (e.g. via photosynthesis), or electricity. Here we will focus on the latter transformation, which is known as photovoltaic (PV) energy conversion. A photovoltaic device, or solar cell, contains two terminals, a cathode and an anode. It builds up a voltage across its two terminals when irradiated with light (photons).

The photovoltaic effect was discovered in 1839 by Edmond Bequerel, who was experimenting with illuminated metal electrodes in an electrolyte [6]. Almost half a century

later, in 1883, the first solar cell made of a selenium/gold junction with an efficiency of about 1 % was reported by Charles Fritts. The photovoltaic effect could finally be explained in 1905 with the pioneering theoretical work of Albert Einstein on the photoelectric effect (for which he later received the Nobel prize) [7]. He suggested that electrons were emitted from a solid due the absorption of “light quanta” — now called photons.

Today, the physics of photovoltaic conversion in classical semiconductor devices, namely in crystalline or polycrystalline silicon junctions, is fairly well understood. This is briefly outlined in this Section. Wafer-based silicon solar cells currently dominate the commercial PV market. However, less expensive semiconductor thin-film technologies (e.g. thin-film silicon, CdTe, or Cu(In,Ga)Se₂) are seizing growing market shares. Emerging “hybrid” technologies based on organic and inorganic materials, like the dye-sensitized solar cell, introduce a new, more versatile, approach to photovoltaic energy conversion.

1.2.1 The solar spectrum

The irradiation of the sun can be well approximated by a black body at a temperature of 5800 K emitting according to Planck’s distribution [8]. The tabulated solar irradiance outside the earths atmosphere (AM 0), the black body spectrum, and the standard solar reference spectrum (AM 1.5G) are compared in Figure 1.1. The total incident irradiance is given by the integral of the curves and is

$$I_{AM0} = 1366.1 \text{ W m}^{-2} \quad \text{and} \quad I_{AM1.5G} = 1000.4 \text{ W m}^{-2} \quad (1.1)$$

for the extraterrestrial spectrum and for the reference AM 1.5G spectrum, respectively.

The spectrum at the earth’s surface is attenuated by absorption, reflection, and scattering. Light is absorbed in the visible and UV region by oxygen (O₂), ozone (O₃), nitrous oxide (N₂O), and methane (CH₄), in the mid-infrared region by water vapor (H₂O), and in the far infrared region by carbon dioxide (CO₂).

Absorption increases with the path length of the light through the atmosphere. For a thickness l_0 of the atmosphere, the path length l through the atmosphere for radiation from the sun incident at an angle α relative to the normal to the earth’s surface is $l = l_0 / \cos \alpha$. The ratio l/l_0 is called the *air-mass* (AM) coefficient. The spectrum outside the atmosphere is designated by AM 0, and the spectrum on the surface of the earth for normal incidence by AM 1. The standard reference spectrum in photovoltaics is designated by AM 1.5G, which corresponds to the total global (hemispherical) irradiance

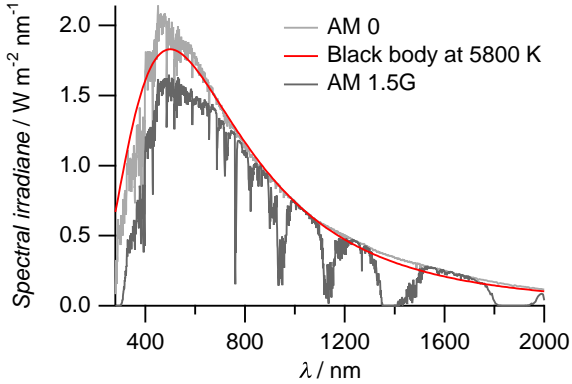


Figure 1.1: Spectra of a black body absorber at $T = 5800$ K, the extraterrestrial AM 0 radiation, and the AM 1.5G standard solar reference radiation. Solar spectra taken from [9].

under specified atmospheric conditions at an angle of incidence of 48° [9]. The AM 1.5G spectrum is defined and modeled by the American Society for Testing and Materials (ASTM) [10].

1.2.2 Theoretical maximum conversion efficiency

It is instructive to have a feeling for the maximum achievable solar energy conversion efficiency in an ideal thermodynamic converter (which is of course smaller than unity) and in a photovoltaic cell, in order to put the experimentally achieved values in perspective.

We first discuss the maximum solar energy conversion efficiency based on the comprehensive discussion in the textbook of Würfel [11]. We consider the arrangement shown in Figure 1.2 to convert solar radiation to work. The radiation is concentrated on a black body absorber with cross-sectional area A_A and temperature T_A within a totally reflecting sphere. Heat is extracted from the absorber with an ideal heat engine, i.e. a Carnot engine, to obtain the greatest amount of work possible. The heat engine is in contact with the earth at temperature T_0 . The absorber receives an energy current I_{abs} from the sun and emits an energy current I_{em} according to the Stefan-Boltzmann law:

$$I_{abs} = \frac{\sigma T_{sun}^4}{\pi} \Omega_L A_A \quad \text{and} \quad I_{em} = \frac{\sigma T_A^4}{\pi} \Omega_L A_A. \quad (1.2)$$

Here, σ is the Stefan-Boltzmann constant, T_{sun} is the temperature of the sun, and Ω_L is the solid angle between the lens and the absorber. The same solid angle is used for incident and emitted radiation, i.e. the case of maximum concentration is considered. To obtain a useful net absorbed energy current $I_{use} = I_{abs} - I_{em}$, the temperature of the absorber T_A must be lower than the temperature of the sun T_{sun} . The conversion

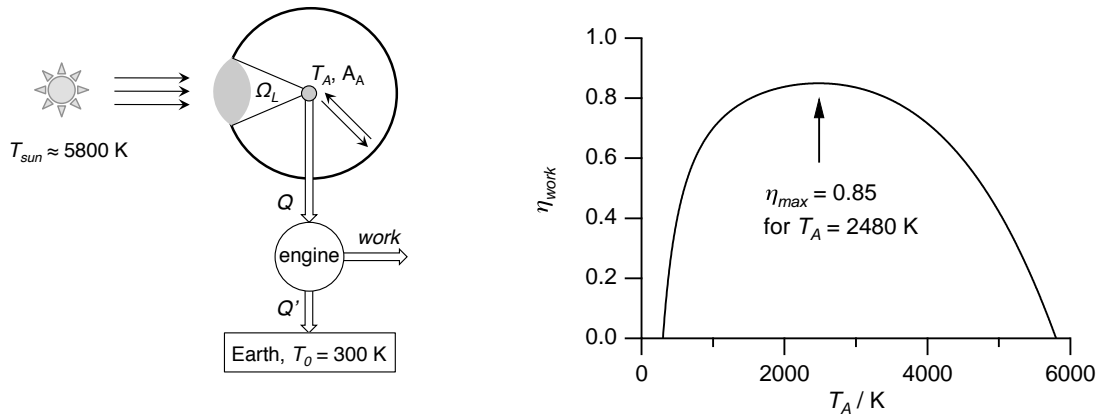


Figure 1.2: Left: Schematic of an ideal solar energy conversion arrangement. The solar radiation is concentrated on an absorber with cross-sectional area A_A and temperature T_A surrounded by a totally reflecting sphere. Heat from the absorber runs a reversible heat (Carnot) engine in contact with the temperature of the earth and produces work. Right: Efficiency of conversion of solar radiation to work with the arrangement to the left.

efficiency for obtaining useful energy is

$$\eta_{\text{use}} = \frac{I_{\text{use}}}{I_{\text{abs}}} = 1 - \frac{T_A^4}{T_{\text{sun}}^4}. \quad (1.3)$$

The well-known Carnot efficiency for a heat engine operating between two heat sinks T_A and T_0 is

$$\eta_{\text{Carnot}} = \frac{I_{\text{work}}}{I_{\text{use}}} = 1 - \frac{T_A}{T_0}. \quad (1.4)$$

The overall efficiency for conversion of solar energy to work by a black-body absorber combined with a Carnot engine then is

$$\eta_{\text{work}} = \frac{I_{\text{work}}}{I_{\text{abs}}} = \eta_{\text{use}} \eta_{\text{Carnot}} = \left(1 - \frac{T_A^4}{T_{\text{sun}}^4}\right) \left(1 - \frac{T_A}{T_0}\right). \quad (1.5)$$

The graph in Figure 1.2 displays η_{work} as a function of T_A for $T_{\text{sun}} = 5800 \text{ K}$ and $T_0 = 300 \text{ K}$. The theoretical maximum efficiency of 85 % is obtained with an absorber at temperature $T_A = 2480 \text{ K}$.

1.2.3 Basic structure of a solar cell

The key element of a solar cell is an absorber with an intrinsic electronic band gap, which absorbs photons with an energy equal or higher than this gap to produce an

electron-hole pair (also known as exciton). This weakly bound exciton can be separated with a favorable energetic alignment of materials, such that the electron moves to the anode and the hole to the cathode. With the accumulation of charges at the contacts, a photovoltage builds up. When the contacts are connected via an external circuit, the cell can produce work at an external load.

Most solar cells are based on semiconductor *p-n* junctions, making this the most studied system. This system will be used to discuss the maximum conversion efficiency in a photovoltaic device.

Properties of a *p-n* junction. Conventional semiconductor solar cells are based on *p-n* junctions. In a *p-n* junction, two semiconductors with different majority charge carriers and doping concentrations — a *n*-doped and a *p*-doped material — are in close contact. Due to interdiffusion and recombination of free holes and electrons at the contact, a *depletion region* or *space charge layer* forms. In this region, donor and acceptor ions create an electric field. The drift force caused by the electric field counteracts the diffusion force such that no net current flows at equilibrium conditions (Figure 1.3). The physics of the *p-n* junction are further described in-depth in classical textbooks, e.g. [12].

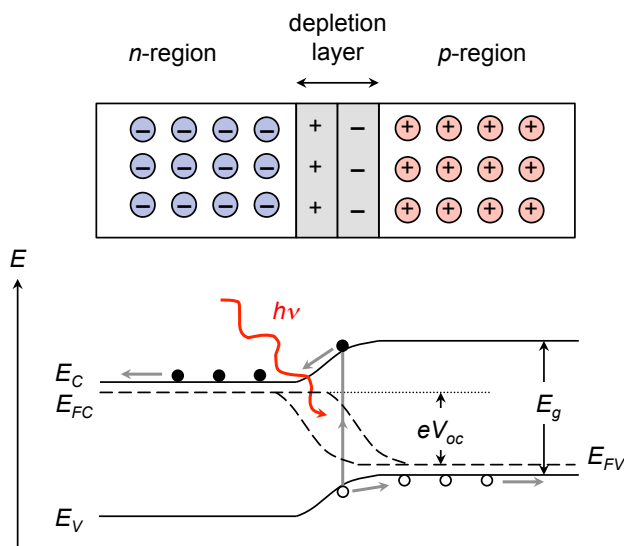


Figure 1.3: Top: Schematic of a *p-n* junction in equilibrium. Bottom: Energy band diagram of a *p-n* junction under illumination. Photons with an energy larger than the bandgap, $h\nu \geq E_g$, create an electron-hole pair, which is separated by the difference in electrochemical potentials in the *n*- and *p*-type regions. The measured photovoltage V_{oc} at the contacts is given by the difference in quasi-Fermi energy of the electrons in the conduction band (E_{FC}) and in the valence band (E_{FV}).

Under illumination an electron-hole pair is formed if the photon energy equals or exceeds the bandgap (E_g). The electron-hole pairs are separated by the differences in electrochemical potential in the n - and p -type regions, which result from the different carrier concentrations and conductivities [11]. Electrons and holes that are not extracted at the contacts eventually recombine with emission of photons or phonons (heat). The difference in potential that is measured at the two contacts, the photovoltage at open-circuit V_{oc} , is given by

$$e V_{oc} = E_{FC} - E_{FV}, \quad (1.6)$$

where e is the elementary charge, E_{FC} is the quasi-Fermi level for the electron distribution in the conduction band, and E_{FV} is the quasi-Fermi level for the electron distribution in the valence band. The energy band diagram of a p - n junction under illumination is shown in Figure 1.3.

Maximum photovoltaic energy conversion efficiency in a p - n junction. The maximum power conversion efficiency obtainable with a classical photovoltaic device, i.e. a p - n junction, was first calculated by Shockley and Queisser in 1961 [13] and is known as the famous *Shockley-Queisser limit* or *detailed balance limit*. The following assumptions are made for a semiconductor with band gap E_g :

- Every incident photon with an energy larger than the bandgap, $h\nu \geq E_g$, produces an electron-hole pair.
- The only recombination mechanism of electron-hole pairs is radiative. The maximum photocurrent is determined by the difference between the absorbed radiation and the emitted radiation (the solar cell is considered a black-body absorber).
- The difference in quasi-Fermi levels of the charge carriers at the point of generation is the same as at the external contacts (no series resistance in the device).

With these conditions one finds an expression for the maximum conversion efficiency as a function of the bandgap, $\eta_{max}(E_g)$.

The Shockley-Queisser limit for a single p - n junction irradiated by a black body at 6000 K is about 30 % for a band gap of 1.1 eV [13]. A lot of solar energy is thus lost due to insufficient absorption and thermalization. For AM 1.5G illumination, the ideal band gap lies between 1.1–1.4 eV, (Figure 1.4) [14]. Silicon (1.12 eV) and gallium arsenide (1.42 eV) are close to ideal photovoltaic materials with which the highest reported efficiencies for single-junctions, 25.0 % (Si) and 26.4 % (GaAs), have been achieved [15].

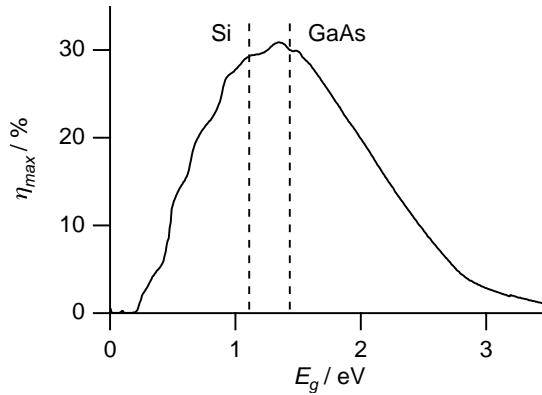


Figure 1.4: Calculated maximum conversion efficiency for AM 1.5G illumination of a *p-n* junction as a function of its band gap E_g . The band gaps of ideal materials, crystalline silicon and gallium arsenide, are indicated (adapted from [14]).

The losses in real devices are mainly due to reflection, non-radiative recombination of electron-hole pairs, and ohmic losses.

The efficiency can be extended beyond the single-junction limit by stacking different solar cells with increasing band gap on top of each other. High energy photons are absorbed by the top cell, and transmitted lower energy photons are successively absorbed by the bottom cells. Such devices are called *multijunction-* or *tandem solar cells*. The maximum efficiency increases to about 45 % for a double junction, 51 % for a triple junction, and approaches the thermodynamic limit of 85 % for an infinite number of junctions [16, 17].

1.2.4 Overview of photovoltaic technologies and market

Solar energy can be converted into electricity by a variety of technologies that can be divided into four classes: Concentrator systems, wafer-based crystalline silicon, thin-film technologies, and emerging technologies. The progress of these technologies with time in terms of best research cell efficiency can be traced in Figure 1.5. The latest efficiency records are also tracked in the regularly updated tables by M. Green et. al. [15].

Concentrator systems use different cells grown on top of each other (multijunction) to absorb a larger fraction of the solar spectrum than a single solar cell. The layers are generally based on epitaxially grown III–V semiconductors. To date, the record solar conversion efficiency of 41.6 % is held by a GaInP/GaInAs/Ge triple-junction device (measured at 364-fold concentration) [18].

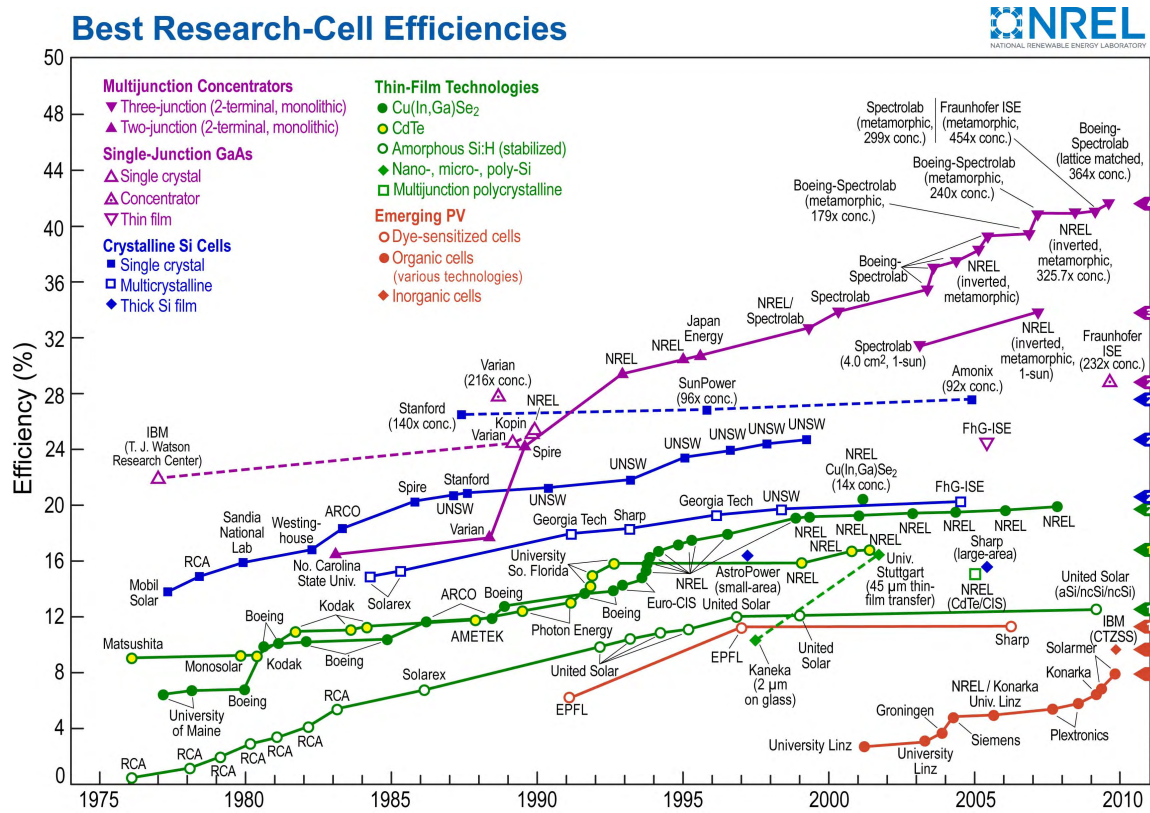


Figure 1.5: Current best photovoltaic research-cell efficiencies (figure by L. Kazmerski, National Renewable Energy Laboratory (NREL) [20]).

Wafer-based crystalline and multicrystalline silicon (c-Si and mc-Si) is the dominating technology in the commercial market. Record c-Si cells achieve up to 25.0 % conversion efficiency, which is very close to the single-junction limit. Since crystalline silicon has an indirect band gap transition and thus a low absorption coefficient, the junction consists of a relatively thick ($\sim 300 \mu\text{m}$) layer of *p*-doped silicon and a thinner $\sim 1 \mu\text{m}$ thick layer of *n*-doped silicon. c-Si cells are cut from crystalline ingots made using the Czochralski crystal growth technique. Both the crystal growth and the sawing are costly processes. mc-Si cells are produced from less expensive cast ingots, i.e. large blocks of molten silicon carefully cooled and solidified. However, their record efficiency is lower (20.4 %) because of increased charge recombination at various structural defects (e.g. grain boundaries, dislocations, or point defects). One disadvantage related to both technologies is the substantial loss of material during the sawing process [19].

Thin-film technologies include solar cells made of polycrystalline compounds like Cu(In,Ga)Se₂ (CIGS), CdTe, and lately Cu₂ZnSn(S,Se)₄ (CZTS), or thin-film silicon solar cells (amorphous silicon (a-Si) and microcrystalline silicon (μ c-Si)). The compound materials (CIGS, CdTe, CZTS) have direct band gap transitions, which allows for thinner

absorber layers $\leq 1 \mu\text{m}$. Optimized CIGS cells have an ideal band gap of $\sim 1.1 \text{ eV}$ and reach similar record efficiencies as mc-Si (19.4 %). The band gap of CdTe (1.5 eV) is larger, and lower record efficiencies of 16.7 % have been reported. CIGS and CdTe cells all commonly fabricated by (co)evaporating the absorber elements in a vacuum chamber [21]. The toxicity or rarity of certain elements (Cd, In, Te) is a true concern for large scale production. Compounds consisting of earth-abundant materials that can be deposited by liquid processes, as recently demonstrated with CZTS ($\eta \sim 10 \%$) [22], are much more promising candidates.

Thin-film silicon is deposited by plasma-enhanced chemical vapor deposition (PECVD) from a silane (SiH_4) gas precursor [19]. Both microcrystalline and amorphous silicon contain mid-gap defects that are associated with dangling bonds, which must be hydrogenated to reduce recombination at these centers ($\mu\text{c-Si:H}$, a-Si:H). The absorption coefficient of a-Si:H is higher than $\mu\text{c-Si:H}$ for photon energies $> 1.75 \text{ eV}$ due to its structural disorder [23]. This allows for integration of the two materials in a so-called *micromorph* tandem solar cell. Current (stabilized) record efficiencies for individual a-Si and $\mu\text{c-Si}$ cells lie at 10.1 %, and micromorph devices reach 11.7–12.5 % (thin submodule and laboratory cell, respectively).

Emerging technologies bear the promise of truly inexpensive production with reasonable module power conversion efficiencies [24]. Synthesized dyes or organic semiconductors are used as absorbers in devices that are frequently assembled by cost- and time-efficient techniques. For many devices, nanostructuring of the materials is key to achieving good efficiencies. Dye-sensitized solar cells, which constitute the research topic of this thesis, are assembled with non-vacuum processes (generally screen-printing) and achieve record efficiencies of over 11 % [25, 26]. Organic “plastic” solar cells generally consist of a nanostructured blend of donor and acceptor polymers or small molecules deposited from solution or by evaporation. Remarkable improvements have been achieved in the past decade with current cells reaching close to 8 % efficiency [27].

Market development. Electricity from photovoltaic systems still constitutes a tiny share of the global electric power production. Of a total worldwide electric power capacity in 2008 of about 4700 GW, only 13 GW were provided by solar photovoltaics [3]. The cumulative PV power installed in the last two decades in a large selection of countries is shown in Figure 1.7. PV is the fastest growing power generation technology with annual growth rates in the range of 40–70 % [5]. This stunning development is due to a combination of continuously decreasing prices — resulting from the economies of scale and market penetration of less expensive thin-film technologies — and the implementation

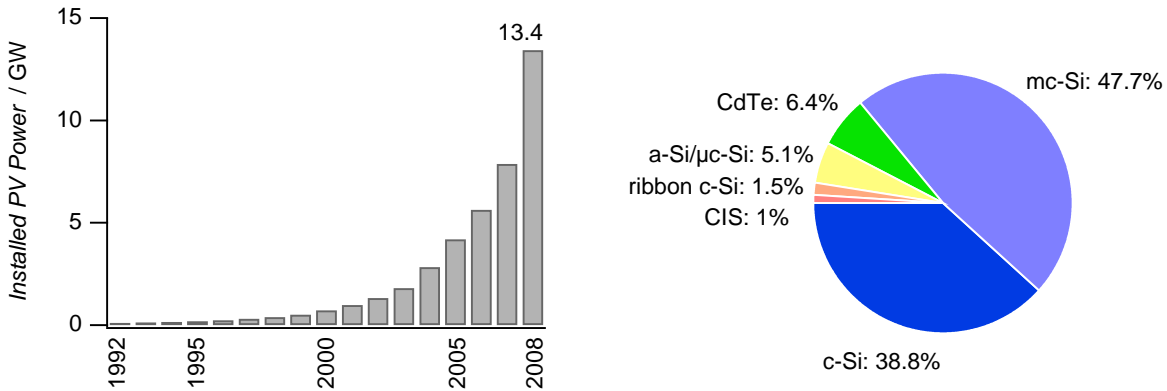


Figure 1.6: Right: Cumulative installed PV capacity (off- and on-grid connected) in countries reporting to the International Energy Agency - Photovoltaic Power Systems Programme (adapted from [5]). Left: PV technology shares in 2008 (adapted from [28]).

of progressive renewable energy policies in many countries [3]. The current commercial PV market is dominated by c-Si and mc-Si technology with a market share of almost 90 %. Thin-film technologies like CdTe, a-Si/μc-Si, ribbon c-Si, and CI(G)S account for the other 10 % (Figure 1.7). The share of thin-film technologies, however, is constantly growing [5].

The prices for PV modules and complete systems (including inverters, mounting systems, cables and installation) have been tumbling in 2009 because of the worldwide financial crisis and overcapacities. Entire PV systems can be purchased at about 3.5 €/W_p¹ and individual (thin-film) modules at less than 1 €/W_p [29]. The costs for solar electricity are thus rapidly approaching end-user grid electricity costs or have already reached the so-called *grid-parity* in regions with strong solar irradiation (e.g. in Spain). As a rule of thumb, grid-parity is achieved in western countries at PV system costs of about 1–2 €/W_p.

Market and technology outlook. Solar electricity production is expected to grow at a similar pace in many outlook scenarios. The latest statistics for 2009 show an increase of total global installed capacity of 45 % to 22.9 GW. The share of thin-film technologies amounts to 22 %, the largest contributor being CdTe (~ 15 % of total installed PV capacity). In the next few years, the total capacity is expected to grow between 10 and 25 GW *annually* depending on the policy measures [30]. According to the outlook of the International Energy Agency, the total capacity will grow 250-fold by 2030 [31].

¹W_p stands for “Watt-peak”, the maximum power of a module under standard testing conditions.

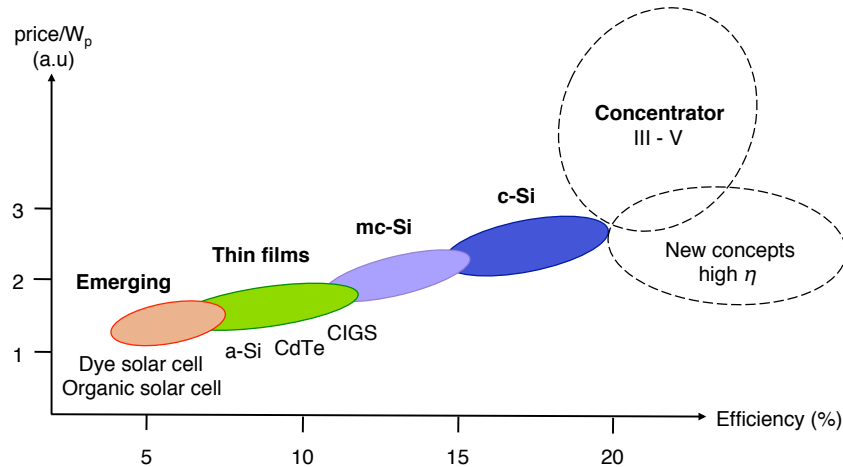


Figure 1.7: Relation between module efficiency and cost per W_p (Watt peak, i.e. maximum power at full irradiation) for different PV technologies (adapted from [32]).

Emerging technologies — like dye-sensitized and organic solar cells — are expected to have a growing share in the next ten to twenty years. Though these technologies have lower module efficiencies, their cost per Watt is estimated to be three to four times lower than for conventional c-Si systems [32]. Both dye-sensitized and organic solar cells are being developed industrially in pilot plants and are close to commercialization (e.g. by the companies Dyesol, G24i, Konarka and Heliatek). In the future, it is likely that all PV technologies will coexist, since the various market segments — such as on- and off-grid, rural electrification, small consumer applications — have specific surface area, cost, or efficiency requirements, which are unlikely met by one single technology (Figure 1.7).

New “exotic” concepts with potentially very high efficiencies beyond the single junction limit at low cost, often referred to as third-generation photovoltaics², might attend to our electricity needs in the long run. Concepts include multiple exciton generation, hot carrier cells, multiband cells, quantum wells, and quantum dots [33]. Though these concepts are all pursued on a fundamental research level, they are an integral part of strategic PV research agendas [34].

²Wafer-based silicon is regarded as first-generation technology and thin film and emerging PV as second-generation technology.

1.3 The dye-sensitized solar cell

1.3.1 Basic principle and historical background

The dye-sensitized solar cell (DSC) is a nanostructured photoelectrochemical device. Light is absorbed by a dye attached to the surface of a mesoporous large band gap semiconductor. Solar energy is transformed into electricity via the photoinduced injection of an electron from the excited dye into the conduction band of the semiconductor. The electrons move through the semiconductor to a current collector and external circuit. A redox mediator in the pores ensures that oxidized dye species are continuously regenerated and that the process is cyclic [35].

Dye-sensitization of large band gap semiconductors can be traced back to the late 19th century. In 1873 Vogel discovered that the spectral sensitivity of photographic silver halide emulsions, which back then had been sensitive to the blue and UV region only, could be extended to the green region by the addition of a dye [36]. A few years later Moser reported enhanced photoelectrochemical response in a dye-sensitized photoelectrode [37]. A clear link between the two phenomena — photography and photoelectrochemistry — could be made in 1964 by Namba and Hishiki, who demonstrated both processes with the same dyes [38]. In the sixties and seventies it could be established, that the sensitization process involved charge transfer from the dye to the semiconductor rather than energy transfer [39, 40]. At the time, measured photocurrents were quite low since the light was absorbed by a monolayer of dye attached to a single crystal. Tsubomura et. al. used porous ZnO to enhance the overall sensitized surface area and obtained a conversion efficiency of 1.5 % for monochromatic irradiance at 563 nm [41]. The interest in photovoltaic energy conversion by dye-sensitization finally exploded in 1991 with the seminal publication of O'Regan and Grätzel reporting a device made of sensitized mesoporous TiO₂ with a conversion efficiency of 7.1 % [42].

DSCs now achieve certified conversion efficiencies of over 11 % with laboratory-scale devices [25] and 8.5 % with small submodules [43]. The workhorse dyes are functional ruthenium(II)-polypyridyl complexes. However, the scarcity of ruthenium and the intricate synthesis of the metal complex might hinder large-scale production. Metal-free organic dyes are more easily synthesized and are catching up; devices with stable organic dyes reach up to 9.8 % efficiencies [44].

The DSC is recognized as a highly promising technology for inexpensive solar electricity production far beyond the research community. The DSC and its inventor, Prof. Grätzel, have received prestigious awards, including the Balzan Prize in 2009 and the 2010 Millennium Technology Prize, the largest technology prize in the world. Several

companies have accepted the challenge to bring DSC technology “from the lab to the fab” (Dyesol, G24i, Sony, Sharp, and Toyota, among others).

The facile assembly — functional cells sensitized with berry juice can be assembled by children within fifteen minutes — the large choice of colors, the option of transparency and mechanical flexibility, and the parallels to natural photosynthesis all contribute to the widespread fascination for DSCs.

1.3.2 Device structure

A schematic of a typical device is shown in Figure 1.8. The mesoporous semiconductor layer is the key element of the device. Commonly, a colloidal TiO_2 paste is deposited on a glass substrate coated with a thin transparent conducting oxide (TCO, generally fluorine doped tin oxide). The interconnected TiO_2 particles have typical sizes of 20–30 nm and are nanocrystalline. The films are about 10 μm thick with a porosity of $\sim 60\%$. The internal surface area of such a film is over a thousand times larger than the projected surface area. The sensitizing dye attached to this huge surface area can absorb virtually all incident light in the wavelength range of peak dye absorption. The pores of the TiO_2 film are permeated by a redox mediator, commonly by the iodide/tri-iodide redox couple in an organic solvent. The electrode with the mesoporous film (the photoanode) is sandwiched together with a second conducting glass substrate and a suitable sealant (e.g. hot-melt gasket). The second electrode is coated with catalytically active platinum particles for efficient reduction of oxidized redox species.

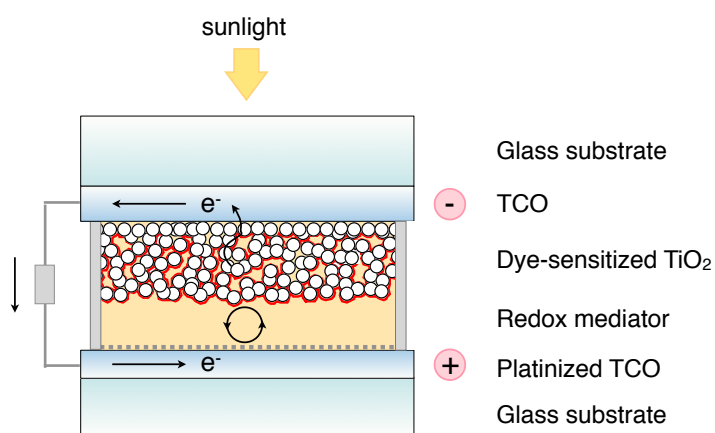


Figure 1.8: Device structure of the nanostructured electrochemical dye-sensitized solar cell.

1.3.3 Electron generation, transport, and recombination

Efficient photovoltaic conversion in dye-sensitized solar cells occurs because of a carefully balanced interplay of different kinetic processes. These are illustrated in the energy diagram in Figure 1.9.

In the dark, the Fermi level of electrons in the TiO_2 is equilibrated with the redox energy level of the electrolyte ($E_{F0} = E_{redox}$). When a photon is absorbed by the sensitizer (S), the excited molecule (S^*) injects an electron into the conduction band (E_C) of the semiconductor on a femto- to picosecond timescale (reaction (1.7)) before the dye can relax back to its ground state (reaction (1.11)). The oxidized dye (S^+) is regenerated by iodide in the electrolyte within a few microseconds (reaction (1.8)), which generally occurs more rapidly than reduction by photoinjected electrons in the TiO_2 (reaction (1.12)). The tri-iodide formed upon the dye regeneration is reduced at the platinized counterelectrode (reaction (1.10)). The additional charge in the TiO_2 under illumination defines a quasi-Fermi level E_{Fn} . Electrons in the TiO_2 are affected by two competing processes: Recombination with tri-iodide in the electrolyte (reaction (1.13)) and diffusion through the mesoporous TiO_2 to the front electrode. The effective time-constants for these processes strongly depend on trapping and detrapping events as discussed later. Recombination occurs in the millisecond to second range, and diffusion ideally occurs on a timescale one to two orders of magnitude smaller such that a large

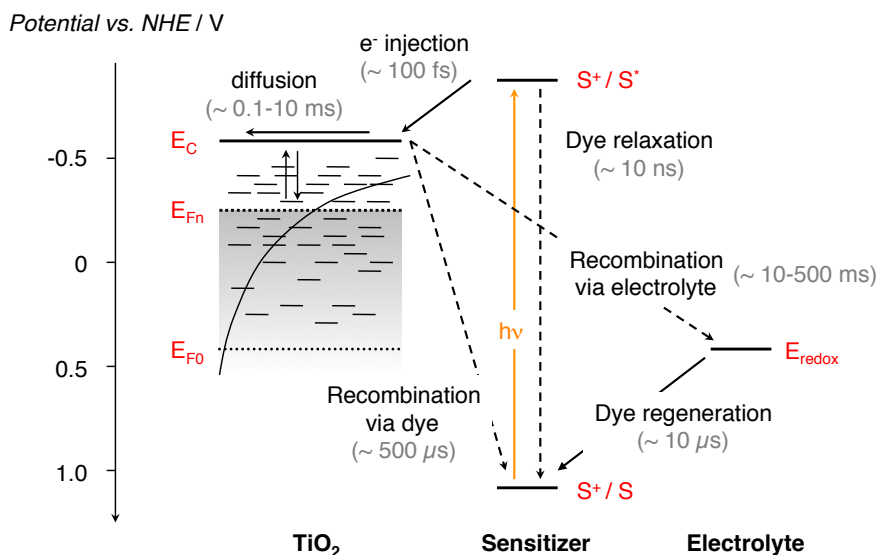
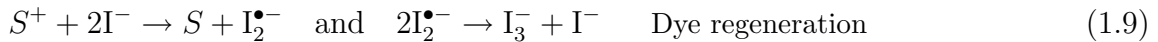


Figure 1.9: Energy diagram of the DSC showing different kinetic processes occurring in the cell and their timescales.

fraction of electrons is extracted at the front electrode.



In an ideal device, every absorbed photon is extracted as an electron at the anode. State-of-the-art laboratory devices reach absorbed photon-to-current conversion efficiencies close to 100 % in the region of maximum dye absorption. The losses in average cells can be due to dye relaxation (i.e no electron is injected), dye regeneration by the injected electron, or recombination of electrons in the TiO_2 with tri-iodide (reactions (1.11)–(1.13)). The first two processes are negligible for standard ruthenium bipyridine dyes [45]. However, injection, dye regeneration, and charge recombination with I_3^- depend on coadsorbants attached to the surface, which can shift the TiO_2 conduction band level, and on certain dye moieties that affect the iodine/tri-iodide concentration close to the TiO_2 surface (e.g. thiophene units) [46–49].

The difference in electrochemical potentials (or Fermi energies) of the electrons at the opposite contacts, i.e. E_{Fn} and E_{redox} , defines the photovoltage generated by the cell. The quasi-Fermi level E_{Fn} of electrons in the TiO_2 depends on the charge generation rate in the TiO_2 , the transport rate, and the recombination rate. The quasi-Fermi level and the charge density in the film can be described mathematically with a continuity equation. Electron transport is described as a diffusive process driven by the concentration gradients. Drift terms due to an electric field in the mesoporous TiO_2 can be neglected due to the effective screening of charges by the cations in the electrolyte in the pores [50].

A particular feature of electron transport in the mesoporous TiO_2 are multiple trapping and detrapping events, which have been observed with several time-dependent techniques. The measured response of the photocurrent and -voltage with varying charge density in the film (controlled by the incident irradiation or an applied electrical bias) suggests there is a high density of exponentially distributed trap states in the band gap. In fact, even though transport and charge recombination occurs predominantly via the

conduction band, the largest fraction of charge is actually trapped in intraband states. However, trapping and detrapping events seem to occur at time scales much faster than transport and recombination, such that trapping effects are irrelevant in steady-state measurements ([51] and references therein).

The mathematical description of charge generation, transport, and recombination in the DSC will be discussed in detail in Chapter 5 on the modeling of DSCs.

1.4 Objectives and contributions of this work

This thesis makes a contribution to the optimization and better understanding of DSCs. Since the seminal presentation of the DSC concept in 1991 [42], this technology has experienced a rapid development from the laboratory-scale device to industrial-scale pilot production. Still, there is a lot of room for optimization. Important optimization cycles — materials, device architecture, and modeling — are shown in Figure 1.10.

A lot of the work in the DSC research community focuses on materials; many new ruthenium-based or organic dyes are constantly being developed, the nanostructure of the TiO_2 is modified (e.g. using nanotubes, wires, or template-based structures) and other materials and core-shell structures are tested. An emphasis is also placed on solvent-free or solid state electrolytes, and some work is done on alternative electrodes and catalysts.

The optimization of the DSC device architecture constitutes a smaller research field. Some work is done on transparent bifacial cells, flexible plastic or steel substrates (predominantly in industrial R&D), and the extension of the spectral sensitivity to the infrared region with tandem approaches.

The modeling of DSC devices also constitutes a small field, even though mathematical modeling on the molecular and device scale is a valuable tool to interpret measurements, understand the chemistry and physics in the device, and assist the optimization process time-efficiently on the computer. Often, individual processes are modeled, like the molecular properties of dyes or the charge transport processes in specific nanostructures.

Ideally, these three fields are interlinked, and the obtained findings boost the overall DSC optimization process in an iterative manner.

The thesis started with the assignment to investigate the potential of enhanced power conversion efficiency in DSC/ $\text{Cu}(\text{In},\text{Ga})\text{Se}_2$ tandem solar cells. Along the way, several organic dyes of collaborating synthesis groups were tested. Later on, funding for the development of a comprehensive, experimentally validated, optical and electrical DSC

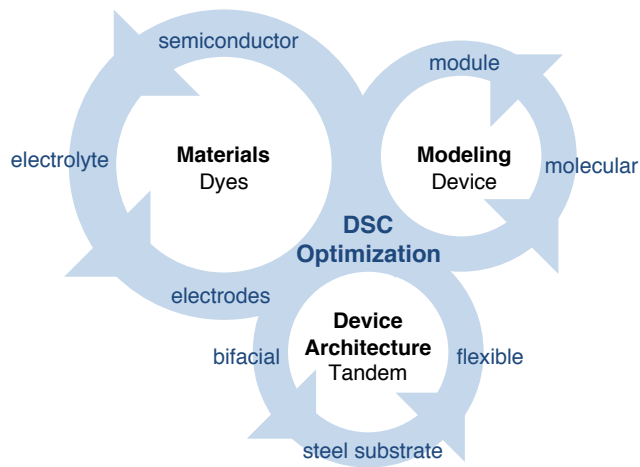


Figure 1.10: Optimization cycles essential to the development of the dye-sensitized solar cell (DSC). In this thesis, new organic sensitizers for stable, efficient, and inexpensive DSCs, advanced tandem structures for enhanced light harvesting in the infrared region, and optical and electrical device modeling for an in-depth understanding of the DSC were investigated in detail.

model could be acquired. Finally, the research conducted during this thesis could make valuable contributions to all three DSC optimization fields, namely:

Organic sensitizers — (Chapter 3) Of the several tested stable organic sensitizers, one achieved a new conversion efficiency record of 7.6 % in a solvent-free DSC. With a novel class of organic sensitizers (π -extended tetrathiafulvalenes) we could demonstrate efficient photovoltaic conversion in a system that had a very low thermodynamic driving force for dye regeneration. We also found correlations between the dye structures and the recombination dynamics of electrons with I_3^- in the electrolyte.

DSC/Cu(In,Ga)Se₂ tandem cell — (Chapter 4) A prototype monolithic DSC/CIGS tandem structure was developed with a promising initial efficiency of 12.2 % and a photovoltage of 1.22 V. First optical calculations with experimentally extracted optical constants show that the amount of light absorbed in each photoactive layer is well balanced — a crucial condition for current-matching in series-connected tandem cells — and that there is ample room for optical optimization of the stack to achieve efficiencies of up to 16 %.

DSC device modeling — (Chapter 5) We set up an experimentally validated coupled optical and electrical model of the DSC. With this model, the optics of the device and the light absorbed by the dye can be calculated accurately. Light absorption is coupled to charge generation with the electrical model, which allows to calculate

various steady-state and time-dependent electrical properties of the device. This model was implemented with a graphical user interface, such that it can be used easily by researchers in the future.

Much of the presented work was published in peer-reviewed publications or conference proceedings. A full list of publications is given on page 166.

Bibliography

- [1] *BP Statistical Review of World Energy June 2010*. BP, London **2010**.
- [2] S. Solomon, D. Qin, M. Manning, Z. Chen, M. Marquis, K. B. Averyt, M. Tignor, and H. L. Miller, editors. *IPCC, 2007: Climate Change 2007: The Physical Science Basis. Contribution of Working Group I to the Fourth Assessment Report of the Intergovernmental Panel on Climate Change*. Cambridge University Press, Cambridge, United Kingdom and New York, NY, USA **2007**.
- [3] *Renewables Global Status Report: Update 2009*. Renewable Energy Policy Network for the 21st Century, Paris **2009**.
- [4] *Erneuerbare Energie in Zahlen: Nationale und internationale Entwicklung*. Bundesministerium für Umwelt, Naturschutz und Reaktorsicherheit, Berlin **2009**.
- [5] *Trends in Photovoltaic Applications: Survey report of selected IEA countries between 1992 and 2008*. International Energy Agency - Photovoltaic Power Systems Programme **2009**.
- [6] E. Bequerel. Recherche sur les effets de la radiation chimique de la lumière solaire, au moyen des courants électriques. *Comptes rendus hebdomadaires des séances de l'Académie des Sciences* **1839**, 9, 145–149.
- [7] A. Einstein. Über einen die Erzeugung und Verwandlung des Lichts betreffenden heuristischen Gesichtspunkt. *Annalen der Physik* **1905**, 17, 132–148.
- [8] M. Planck. Ueber das Gesetz der Energieverteilung im Normalspectrum. *Annalen der Physik* **1901**, 4, 553–563.
- [9] <http://rredc.nrel.gov/solar/spectra/>.
- [10] ASTM G173 - 03e1, Standard Tables for Reference Solar Spectral Irradiances: Direct Normal and Hemispherical on 37° Tilted Surface.
- [11] P. Würfel. *Physics of Solar Cells: From Basic Principles to Advanced Concepts*. WILEY-VCH Verlag GmbH & Co. KGaA, Weinheim, 2nd edition **2009**.
- [12] S. M. Sze. *Semiconductor devices, physics and technology*. John Wiley & Sons, New York, 2nd edition **2002**.

- [13] W. Shockley and H. J. Queisser. Detailed balance limit of efficiency of *p-n* junction solar cells. *Journal of Applied Physics* **1961**, *32*, 510–519.
- [14] C. H. Henry. Limiting efficiencies of ideal single and multiple energy gap terrestrial solar cells. *Journal of Applied Physics* **1980**, *51*, 4494–4500.
- [15] M. A. Green, K. Emery, Y. Hishikawa, and W. Warta. Solar cell efficiency tables (version 36). *Progress in Photovoltaics: Research and Applications* **2010**, *18*, 346–352.
- [16] A. Martí and G. L. Araújo. Limiting efficiencies for photovoltaic energy conversion in multigap systems. *Solar Energy Materials and Solar Cells* **1996**, *43*, 203–222.
- [17] A. S. Brown and M. A. Green. Detailed balance limit for the series constrained two terminal tandem solar cell. *Physica E: Low-dimensional Systems and Nanostructures* **2002**, *14*, 96–100.
- [18] R. R. King, A. Boca, W. Hong, X.-Q. Liu, D. Bhusari, D. Larrabee, K. Edmondson, D. Law, C. Fetzer, S. Mesropian, and N. Karam. Band-gap-engineered architectures for high-efficiency multijunction concentrator solar cells. *Proceedings of the 24th European Photovoltaic Solar Energy Conference, Hamburg* **2009**, 55 – 61.
- [19] A. Goetzberger, C. Hebling, and H. W. Schock. Photovoltaic materials, history, status and outlook. *Materials Science and Engineering R: Reports* **2003**, *40*, 1–46.
- [20] Available from http://en.wikipedia.org/wiki/Solar_cell.
- [21] A. Romeo, A. Terheggen, D. Abou-Ras, D. L. Batzner, F. J. Haug, M. Kalin, D. Rudmann, and A. N. Tiwari. Development of thin-film Cu(In,Ga)Se₂ and CdTe solar cells. *Progress in Photovoltaics* **2004**, *12*, 93–111.
- [22] T. K. Todorov, K. B. Reuter, and D. B. Mitzi. High-efficiency solar cell with earth-abundant liquid-processed absorber. *Advanced Materials* **2010**, *22*, E156–E159.
- [23] A. V. Shah, H. Schade, M. Vanecek, J. Meier, E. Vallat-Sauvain, N. Wyrsch, U. Kroll, C. Droz, and J. Bailat. Thin-film silicon solar cell technology. *Progress in Photovoltaics: Research and Applications* **2004**, *12*, 113–142.
- [24] N. S. Lewis. Toward cost-effective solar energy use. *Science* **2007**, *315*, 798–801.
- [25] Y. Chiba, A. Islam, Y. Watanabe, R. Komiya, N. Koide, and L. Han. Dye-sensitized solar cells with conversion efficiency of 11.1%. *Japanese Journal of Applied Physics* **2006**, *45*, L638–L640.
- [26] M. K. Nazeeruddin, F. De Angelis, S. Fantacci, A. Selloni, G. Viscardi, P. Liska, S. Ito, B. Takeru, and M. Grätzel. Combined Experimental and DFT-TDDFT Computational Study of Photoelectrochemical Cell Ruthenium Sensitizers. *Journal of the American Chemical Society* **2005**, *127*, 16835–16847.
- [27] H.-Y. Chen, J. Hou, S. Zhang, Y. Liang, G. Yang, Y. Yang, L. Yu, Y. Wu, and G. Li. Polymer solar cells with enhanced open-circuit voltage and efficiency. *Nature Photonics* **2009**, *3*, 649–653.

- [28] *Photovoltaic Fact Sheet: The Status of the PV Industry*. PhotoVoltaic Technology Platform **2010**. <http://www.eupvplatform.org>.
- [29] Up to date PV module and system prices available at <http://www.solarbuzz.com>.
- [30] *Global Market Outlook for Photovoltaics until 2014*. European Photovoltaic Industry Association, Brussels **2010**. <http://www.epia.org>.
- [31] *World Energy Outlook 2008*. International Energy Agency, Paris, France **2008**.
- [32] W. Hoffmann. PV solar electricity industry: Market growth and perspective. *Solar Energy Materials and Solar Cells* **2006**, *90*, 3285–3311.
- [33] M. A. Green. Third generation photovoltaics: Ultra-high conversion efficiency at low cost. *Progress in Photovoltaics: Research and Applications* **2001**, *9*, 123–135.
- [34] *A Strategic Research Agenda for Photovoltaic Solar Energy Technology*. European Photovoltaic Technology Platform **2007**. <http://www.eupvplatform.org>.
- [35] M. Grätzel. Photoelectrochemical cells. *Nature* **2001**, *414*, 338–344.
- [36] W. West. First hundred years of spectral sensitization. *Photographic Science and Engineering* **1974**, *18*, 35–48.
- [37] J. Moser. Notiz über Verstärkung photoelektrischer Ströme durch optische Sensibilisierung. *Monatshefte für Chemie* **1887**, *8*, 373.
- [38] S. Namba and Y. Hishiki. Color sensitization of zinc oxide with cyanine dyes. *The Journal of Physical Chemistry* **1965**, *69*, 774–779.
- [39] H. Gerischer and H. Tributsch. Electrochemistry of ZnO Monocrystal Spectral Sensitivity. *Berichte der Bunsen-Gesellschaft für Physikalische Chemie* **1968**, *72*, 437.
- [40] K. Hauffe, H. J. Danzmann, H. Pusch, J. Range, and H. Volz. New Experiments on the Sensitization of Zinc Oxide by Means of the Electrochemical Cell Technique. *Journal of the Electrochemical Society* **1970**, *117*, 993–999.
- [41] H. Tsubomura, M. Matsumura, Y. Nomura, and T. Amamiya. Dye sensitised zinc oxide: aqueous electrolyte: platinum photocell. *Nature* **1976**, *261*, 402–403.
- [42] B. O'Regan and M. Grätzel. A low-cost, high-efficiency solar cell based on dye-sensitized colloidal TiO₂ films. *Nature* **1991**, *353*, 737–740.
- [43] M. A. Green, K. Emery, Y. Hishikawa, and W. Warta. Solar cell efficiency tables (version 35). *Progress in Photovoltaics: Research and Applications* **2010**, *18*, 144–150.
- [44] G. Zhang, H. Bala, Y. Cheng, D. Shi, X. Lv, Q. Yu, and P. Wang. High efficiency and stable dye-sensitized solar cells with an organic chromophore featuring a binary π-conjugated spacer. *Chemical Communications* **2009**, 2198–2200.

- [45] Y. Tachibana, J. E. Moser, M. Grätzel, D. R. Klug, and J. R. Durrant. Subpicosecond interfacial charge separation in dye-sensitized nanocrystalline titanium dioxide films. *Journal of Physical Chemistry* **1996**, *100*, 20056–20062.
- [46] S. A. Haque, Y. Tachibana, R. L. Willis, J. E. Moser, M. Grätzel, D. R. Klug, and J. R. Durrant. Parameters influencing charge recombination kinetics in dye-sensitized nanocrystalline titanium dioxide films. *The Journal of Physical Chemistry B* **1999**, *104*, 538–547.
- [47] Y. Tachibana, S. A. Haque, I. P. Mercer, J. E. Moser, D. R. Klug, and J. R. Durrant. Modulation of the rate of electron injection in dye-sensitized nanocrystalline TiO₂ films by externally applied bias. *The Journal of Physical Chemistry B* **2001**, *105*, 7424–7431.
- [48] P. Wang, S. M. Zakeeruddin, J.-E. Moser, and M. Grätzel. A new ionic liquid electrolyte enhances the conversion efficiency of dye-sensitized solar cells. *The Journal of Physical Chemistry B* **2003**, *107*, 13280–13285.
- [49] T. Marinado, K. Nonomura, J. Nissfolk, M. K. Karlsson, D. P. Hagberg, L. Sun, S. Mori, and A. Hagfeldt. How the nature of triphenylamine-polyene dyes in dye-sensitized solar cells affects the open-circuit voltage and electron lifetimes. *Langmuir* **2010**, *26*, 2592–2598.
- [50] L. M. Peter. Characterization and modeling of dye-sensitized solar cells. *Journal of Physical Chemistry C* **2007**, *111*, 6601–6612.
- [51] L. Peter. Transport, trapping and interfacial transfer of electrons in dye-sensitized nanocrystalline solar cells. *Journal of Electroanalytical Chemistry* **2007**, *599*, 233–240.

Chapter 2

Experimental methods

2.1 Device fabrication

The DSC test devices were fabricated and assembled according to well established procedures unless indicated otherwise. A comprehensive review of the DSC fabrication process was given by Ito et. al. [1].

2.1.1 Materials

Colloidal TiO₂ paste. Colloidal TiO₂ pastes for the fabrication of the mesoporous TiO₂ layer were prepared according to standard procedures, which are described in detail elsewhere [1–3]. For the “transparent” layer, 20 nm sized anatase TiO₂ particles were used. In brief, titanium iso-propoxide and acetic acid were hydrolyzed with water and peptized with nitric acid. The colloidal particles were then grown hydrothermally. The as-grown particles were redispersed by sonication and concentrated with a rotary-evaporator. Ethyl cellulose and terpineol was then added to the centrifuged and washed material to obtain a homogeneous paste. For the light scattering layer consisting of 400 nm sized anatase TiO₂ particles, a paste prepared by CCIC, Japan, was used.

Fabrication of mesoporous TiO₂ photoanode. The working electrode, a glass substrate coated with fluorine-doped tin oxide (FTO, 10 Ω/□ sheet resistance, Nippon Sheet Glass, Japan), was cleaned with detergent in an ultrasonic bath and rinsed with water and ethanol. The FTO plate was immersed into a 40 mM aqueous TiCl₄ solution at 70 °C for 30 min to produce a thin compact layer of TiO₂ on the FTO surface to prevent charge recombination via the FTO to the electrolyte in the assembled device. The colloidal TiO₂ paste of 20 nm sized particles was then screen-printed onto the FTO in consecutive steps with intermediate drying at 125 °C to obtain the desired film thick-

ness (generally between 5–10 μm). In many cases, two additional layers of 400 nm sized particles were screen-printed on the transparent layer to obtain a 4–5 μm thick scattering layer. The electrodes were gradually heated to 500 °C and sintered for 15 min. The final TiO₂ “double layer” was treated again with a TiCl₄ solution and sintered at 500 °C for 30 min. After cooling to about 80 °C, the electrode was immersed into a dye solution for sensitization. The TiO₂ films typically had a circular ($\sim 0.28 \text{ cm}^2$) or square ($0.4 \times 0.4 \text{ cm}^2$) geometry.

Sensitizers. The organic donor- π -acceptor sensitizers studied in this thesis — namely diphenylamine (**LIN**, **BRA**), difluorenlyaminophenyl (**C203**, **C204**, **C205**), and π -extended tetrathiafulvalene (**PAB-1**, **PAB-2**, **PAB-3**) donor systems — are described in detail in Chapter 3.

For the tandem architecture (Chapter 4) and device modeling studies (Chapter 5), two well known ruthenium(II)-bipyridine complexes were used: An amphiphilic dye coded **Z907** with long hydrophobic hydrocarbon chains [4], and a dye coded **C101** with extended π -conjugation in the linker [5] (Figure 2.1). **Z907** has an extinction coefficient of $\epsilon = 12.2 \times 10^3 \text{ M}^{-1} \text{ cm}^{-1}$ at $\lambda = 524 \text{ nm}$ and shows excellent long-term stability after 1000 h of heating at 80 °C [6]. **C101** yields high efficiencies of up to 11.0 % with a volatile electrolyte, due to a higher extinction coefficient ($\epsilon = 17.5 \times 10^3 \text{ M}^{-1} \text{ cm}^{-1}$ at $\lambda = 547 \text{ nm}$) and shows excellent stability after 1000 h of light soaking at 60 °C. The synthesis of these dyes is described in detail in their respective publications.

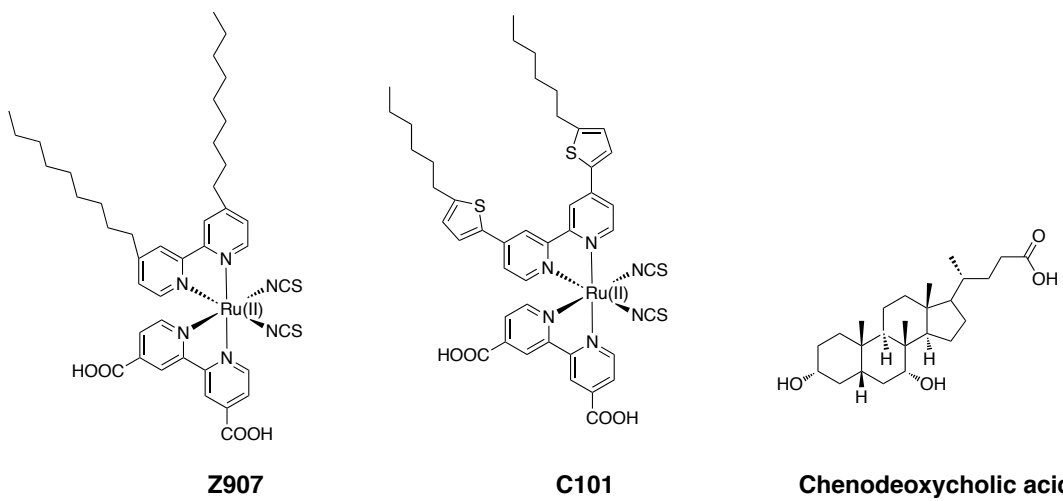


Figure 2.1: Molecular structures of the ruthenium(II)-bipyridine complexes used for parts of this thesis. Chenodeoxycholic acid (cheno) was added as co-adsorbant in some dye solutions.

The sensitizers were dissolved in a suitable solvent (~ 0.3 mM). Chenodeoxycholic acid (cheno) was added as co-adsorbant to break aggregation if necessary (namely in combination with organic dyes and with **C101**). The precise dye solution composition is mentioned in the respective Section.

Electrolyte. Two types of state-of-the-art electrolytes were used: A volatile acetonitrile-based electrolyte (coded Z960) and a ternary ionic liquid (coded Z952) [7]. The composition of the electrolytes was:

Z960 — 1.0 M 1,3-dimethylimidazolium iodide, 0.03 M iodide, 0.1 M guanidinium thiocyanate, 0.5 M tert-butylpyridine, 0.05 M lithium iodide in a mixture of acetonitrile and valeronitrile (volume ratio 85/15), and

Z952 — 1,3-dimethylimidazoliumiodide/1-ethyl-3- methylimidazoliumiodide/1-ethyl-3-methylimidazolium tetracyanoborate/iodine/N-butylbenzimidazole/guanidinium thiocyanate (molar ratio 12/12/16/1.67/3.33/0.67).

2.1.2 Device assembly

The sensitized TiO_2 film was rinsed with the solvent used for the dye solution and assembled with a platinum covered FTO electrode (Pilkington, TEC 15, $15 \Omega/\square$) containing a hole in a sandwich-type configuration (Figure 2.2). The counterelectrode was thermally platinized with a drop of H_2PtCl_6 in ethanol at 400°C for 15 min. The two electrodes were sealed with a 25 μm thick polymer spacer (Surlyn, DuPont). The hole of the coun-

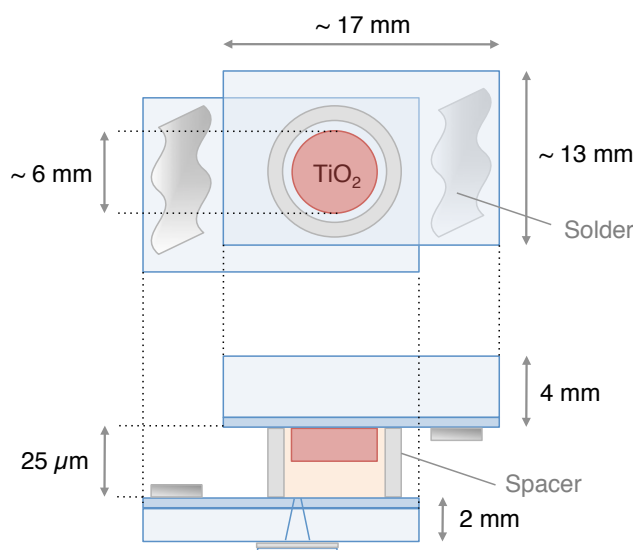


Figure 2.2: Cartoon of the sandwich-type DSC assembly for laboratory test cells.

terelectrode was sealed with a Surlyn sheet. The void between the electrodes was then filled with an iodide/tri-iodide based electrolyte via vacuum backfilling through a hole pierced through the Surlyn sheet. The hole was then sealed with a Surlyn disc and a thin glass to avoid leakage of the electrolyte. A solder (Cerasolza, Asahi Glass) was applied on each side of the FTO electrodes to ensure a good electrical contact with measurement cables. In some cases, the photoanode was covered with a UV-cutoff/antireflecting polymer (ARCTOP, Asahi Glass).

2.2 Steady-state photovoltaic characterization

The basic characteristics of a solar cell — i.e. the quantum efficiency and current-voltage curve — are measured under steady-state conditions. This means that the charge density in a small volume element of the TiO_2 film does not change with time. The rate of charges generated by the irradiation is thus balanced by the rate of charge recombining with tri-iodide in the electrolyte and by the rate of charge being transported out or into the volume element.

2.2.1 Spectral response and quantum efficiency

A crucial characteristic of a solar cell is its *spectral response* to various incident wavelengths. The spectral response ($SR(\lambda)$) is defined as the ratio of the current generated by the solar cell to the power incident on the solar cell and is given in units of A W^{-1} . More commonly, the *external quantum efficiency* is used to describe solar cells. The external quantum efficiency gives the number of electrons output by the solar cell compared to the number of photons incident on the device and is dimensionless. The external quantum efficiency ($EQE(\lambda)$) is calculated from the spectral response using

$$EQE(\lambda) = SR(\lambda) \frac{hc}{e\lambda}, \quad (2.1)$$

where h is Plank's constant, c is the speed of light, and e is the elementary charge. In the DSC community, the external quantum efficiency is also called the *incident photon-to-current conversion efficiency* (IPCE).

The expected short-circuit current density (J_{sc}) of the test device for any given incident photon flux $\phi(\lambda)$ (in units of $\text{m}^{-2} \text{nm}^{-1} \text{s}^{-1}$) is

$$J_{sc} = \int e EQE(\lambda) \phi(\lambda) d\lambda. \quad (2.2)$$

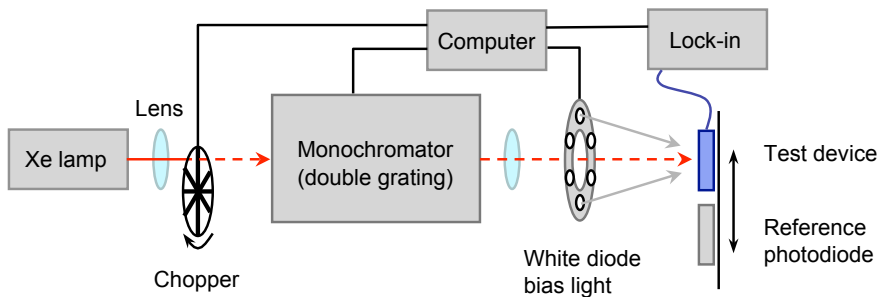


Figure 2.3: Schematic of the setup for external quantum efficiency measurements. Chopped light from a xenon source is sent through a monochromator and focused on the test device. The modulated AC photocurrent in the test device is detected by a lock-in amplifier. A calibrated reference photodiode measures the intensity of the incident beam. Additional stable DC white bias light can be applied to ensure the test device is operating in a linear response region.

Setup. In our laboratory we used a home-built setup to measure the *EQE* of test devices (Figure 2.3). Broadband light from a 300 W xenon arc lamp (ILC Technology) is modulated with a computer-controlled chopper at 1–4 Hz and focused through a Gemini-180 double monochromator (Jobin Yvon Ltd., UK). The photon flux of monochromatic light incident on the devices is measured using a calibrated silicon photodiode (independent calibrations performed at Fraunhofer ISE, Freiburg, Germany, and NREL, Colorado, USA) with a spectral response modified with a filter (KG5 Schott) to approximately match the absorption profile of the dyes. The intensity of the monochromatic beam was about 0.1 mW cm^{-2} ($\sim 0.1\% \text{ sun}$). The IPCE of a typical reference cell is shown in Figure 2.4. The modulated AC photocurrent of the test device is measured under short-circuit conditions with a lock-in amplifier (SR 830, Stanford Research Systems). To ensure the device is operating in a linear response regime, additional DC

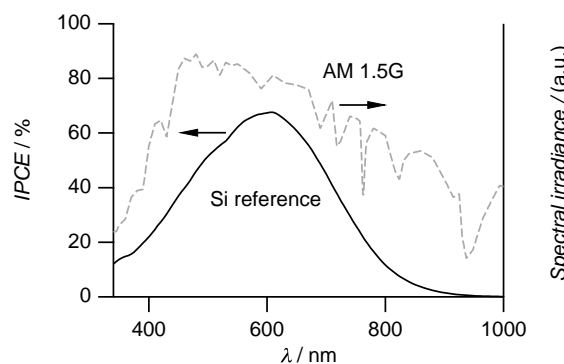


Figure 2.4: Incident photon-to-current conversion efficiency (IPCE) of the calibrated silicon reference photodiode.

white bias light from light emitting diodes with an intensity of 1–100 mW cm⁻² (1–10 % full sunlight) can be applied to generate a constant photocurrent in the cell.

2.2.2 Current-voltage characteristics

The power conversion efficiency of a solar cell is determined from the current versus applied voltage (*I-V*) characteristics under illumination. The *I-V* curve and device efficiency are reported with respect to a standard reference spectral irradiance distribution, the *air mass 1.5 global* (AM 1.5G) spectrum (see Section 1.2.1).

The *I-V* characteristics of a solar cell are well described by an equivalent electric circuit (Figure 2.5) [8]. Under illumination, a constant photocurrent (I_{ph}) is generated. If a forward voltage bias is applied, a dark diode current (I_{dark}) flows in the opposite direction. A shunt resistance (R_{shunt}) may arise from charge recombination in the photoactive layer and induce a shunting current (I_{shunt}). The series resistance (R_{series}) includes the contact resistance at interfaces, the bulk resistance, and the sheet resistance of the transparent electrodes. The total measured current then is

$$I = I_{ph} - I_{dark} - I_{shunt} = I_{ph} - I_s \left(e^{\frac{eV}{mkT}} - 1 \right) - \frac{V + IR_{series}}{R_{shunt}}, \quad (2.3)$$

where I_s is the diode saturation current, V is the applied bias voltage, m is an ideality factor ($m = 1$ for an ideal cell), k is the Boltzmann constant, and T is the device temperature. If we neglect the shunt and series resistance ($R_{shunt} \rightarrow \infty$, $R_{series} \rightarrow 0$), we find simple expressions for the short-circuit current (I_{sc}) and the open-circuit voltage (V_{oc}) of the device:

$$I_{sc} = I_{ph} \quad \text{for } V = 0, \quad \text{and} \quad (2.4)$$

$$V_{oc} = \frac{mkT}{e} \ln \left(\frac{I_{ph}}{I_s} + 1 \right) \quad \text{for } I = 0. \quad (2.5)$$

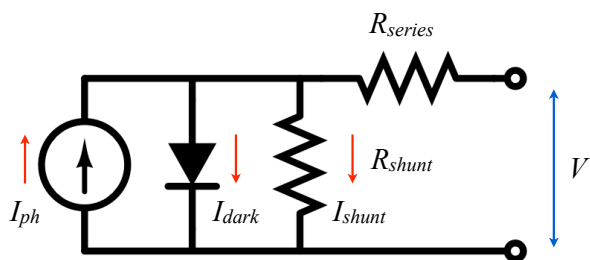


Figure 2.5: Equivalent circuit of a solar cell.

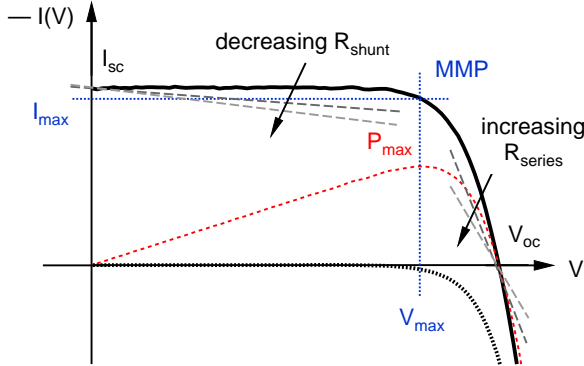


Figure 2.6: I-V curve of a typical solar cell under illumination (bold dark curve) and in the dark (dotted dark curve). Further indicated are the power curve (red), the maximum power point (MMP, blue) conditions, and the effect of the series and shunt resistance (R_{series} and R_{shunt}).

The maximum-power operating point defines the condition at which the power output $P_{max} = I_{max} V_{max}$ of the device is maximal. The so-called fill factor (FF) is often used to characterize the maximum power point,

$$FF = \frac{I_{max} V_{max}}{I_{sc} V_{oc}}. \quad (2.6)$$

The *solar to electric power conversion efficiency* (η), the key parameter of the device, is given by the ratio of the maximum extractable power to the incident solar power (P_s),

$$\eta = \frac{P_{max}}{P_s} = \frac{I_{max} V_{max}}{P_s} = \frac{FF I_{sc} V_{oc}}{P_s}. \quad (2.7)$$

A typical I-V curve of a solar cell is shown in Figure 2.6. By convention, the applied bias voltage is positive, and the measured solar cell current is negative. In real solar cells a high series resistance and a small shunt resistance reduce the fill factor as shown in the Figure.

Setup. In our laboratory we used a home-built setup to measure the I - V curves of test devices (Figure 2.7). Cells were illuminated with light from a 450 W xenon lamp (LOT Oriel) matched to AM 1.5G sunlight irradiation with filters in the range of 350–750 nm (Schott K113 Tempax Sunlight Filter, Präzisions Glas & Optik GmbH, Germany). Alternatively, cells could be illuminated with a 1000 W xenon lamp (LOT Oriel), which had a spectral output closer to AM 1.5G above 750 nm. The irradiation spectra are compared

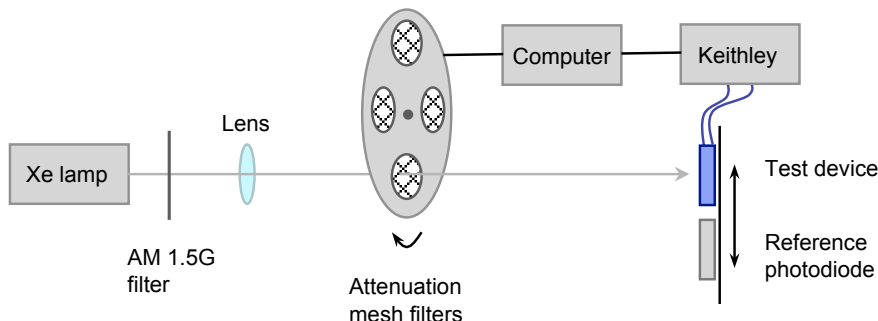


Figure 2.7: Schematic of the setup for photocurrent-voltage measurements. Broadband light from a xenon source is filtered to simulate AM 1.5G solar illumination. The beam intensity is attenuated with various wavelength-neutral mesh filters. A Keithley 2400 SourceMeter applies a bias voltage to the test device and simultaneously measures its photocurrent. A calibrated reference photodiode measures the intensity of the incident beam.

to the standard AM 1.5G spectrum in Figure 2.8. The beam intensity was measured with a calibrated silicon photodiode similar to the one described in Section 2.2.1. The current and voltage were measured and controlled with a Keithley 2400 source meter. The incident light intensity was varied with wavelength-neutral wire mesh attenuators. The effective area of the devices was defined with a metal mask. No mismatch correction [9] was applied to the measured data.

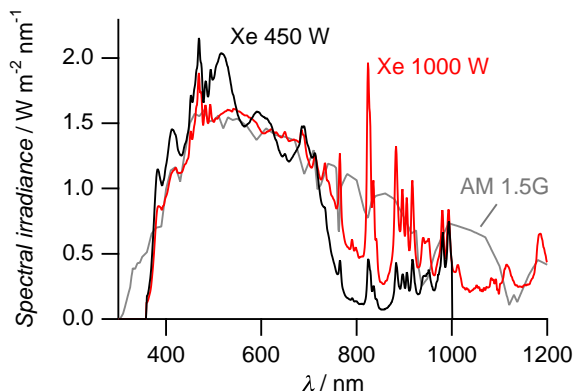


Figure 2.8: Spectral irradiance from the 450 W and 1000 W xenon light source matched to AM 1.5G with filters. The integral of the product with the IPCE of the silicon reference (Figure 2.4) yields 12.48 mA cm⁻² for all three spectra.

2.3 Time-resolved transient characterization

In the dye-sensitized solar cell, various kinetic processes — such as charge injection, sensitizer regeneration, electron recombination, and transport — take place at different time-scales (see Section 1.3.3). Suitable time-resolved characterization techniques can probe these individual time-dependent processes.

2.3.1 Laser transient absorbance measurements

The kinetics of excited dye states can be studied with time-resolved optical spectroscopy using a pump-probe technique. The sensitizer (S) is pumped into a transient excited state (S^*) with short probe pulses of light in the femto- to nanosecond range using a specific excitation wavelength. This excited state can be probed with a second monochromatic pulse after an adjustable time delay to measure the transmission (or absorption) of the excited state. By monitoring the probe signal as a function of the time delay, one obtains information on the decay of the excited state.

The ultrafast injection of electrons from the excited dye state is most conveniently probed with femtosecond laser spectroscopy [10].

Recombination of the excited dye state with an injected electron or with iodide occurs on a longer time-scale and is studied with nanosecond transient absorbance [11]. Within the framework of this thesis, we studied the dye recombination kinetics of the novel organic sensitizers **PAB-1**, **PAB-2**, and **PAB-3** (π -extended tetrathiafulvalene donors, see Section 3.5). The samples were excited by pulses produced by a broad-band optical parametric oscillator (OPO GWU-355) pumped with a Continuum Powerlite 7030 frequency-tripled (i.e. 355 nm) Q-switched Nd:YAG running at 30 Hz. The output excitation wavelength was tuned at $\lambda = 505$ nm with a pulse width of 7 ns (FWHM). The pulse energy was attenuated with neutral density grey filters down to $30 \mu\text{J cm}^{-2}$, a fluence under which the samples exhibit, on average, less than one injected electron per nanoparticle. The probe light was produced by a xenon arc lamp. This light was filtered through a monochromator and diverse filters, focused onto the sample, and then collected in a second monochromator. It was then detected by a fast photomultiplier tube biased with 750 V. Averaging over 1000 to 2000 laser shots was necessary to obtain satisfactory signal to noise ratios. Combination of several transients recorded at different wavelengths allowed the reconstruction of the transient spectrum.

2.3.2 Transient photovoltage and photocurrent decay measurements

The transport of electrons in the TiO_2 conduction band and their recombination with tri-iodide in the electrolyte occur in the millisecond to second time range. Several different time-dependent techniques that probe these processes — such as small-perturbation voltage and current decay, intensity modulated voltage and current spectroscopy, and electrochemical impedance spectroscopy — show that the characteristic time constants vary exponentially with illumination or electrical bias. This is attributed to a high density of exponentially distributed trap states in the TiO_2 band gap, whose origin to date is still not well defined ([12, 13] and references therein).

Figure 2.9 shows the effect of the exponential distribution of trap states on kinetic processes at different biases. The bias can be a light or electrical bias and fixes a steady state, and steady charge concentration, in the device.

High bias — A lot of charge is injected into the TiO_2 , and the quasi-Fermi level E_{Fn} lies close to the TiO_2 conduction band. All trap states below E_{Fn} are filled. Electrons in the conduction band fall into shallow trap states and undergo rapid trapping and detrapping events before they recombine with I_3^- or are extracted at the front electrode. Under high bias, the measured recombination and transport rates are high.

Low bias — Only little charge is injected into the TiO_2 , and the quasi-Fermi level E_{Fn} lies close to the redox energy level. Electrons in the conduction band fall into deeper trap states, and detrapping is less rapid. Under low bias, the measured recombination and transport rates are thus lower.

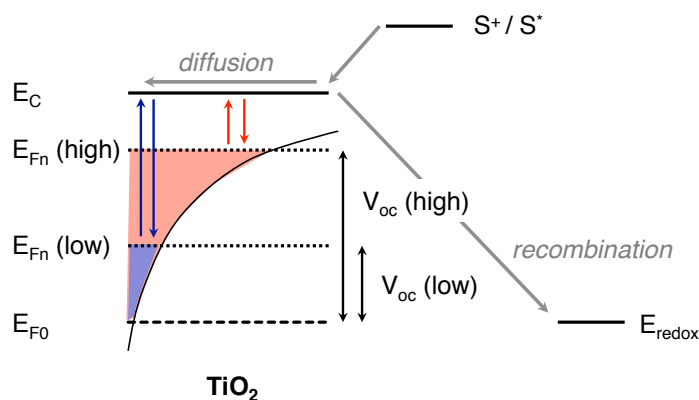


Figure 2.9: Cartoon showing the occupation of the exponentially distributed trap states in the TiO_2 particles under high light bias (red) and under low light bias (blue).

In this work, we used, in particular, small perturbation photovoltage decays to study the recombination rates of electrons in the TiO_2 with I_3^- at different bias light intensities and hence different charge densities in the film.

Total current decay or charge extraction. A quite straightforward method to measure charge density in the TiO_2 film of an illuminated device, and hence probe the density of trap states, was proposed by Duffy et. al. [14]. The device is set to open-circuit and illuminated with constant white light to produce a steady-state photovoltage (V_{oc}). The illumination source is then shut off. The photovoltage starts to decay due to recombination of free electrons with tri-iodide. After a variable time delay, the cell is short-circuited. The integral of the measured current spike corresponds closely to the remaining charge stored in the film. However, a small fraction of the charge will recombine with tri-iodide during the extraction process. This procedure is repeated with various time delays to obtain the extracted charge as a function of photovoltage. Figure 2.10a shows a typical voltage decay curve $V_{oc}(t)$ and the extracted charge per active surface area ΔQ (in units of C cm^{-2}) for different time delays. The total charge density in the TiO_2 film is then given by

$$n_e = \frac{\Delta Q}{e d (1 - p)}, \quad (2.8)$$

where d is the TiO_2 film thickness, and p is the porosity of the film. n_e is plotted as a function of V_{oc} in Figure 2.10b. Clearly, at least for low photovoltages, the extracted

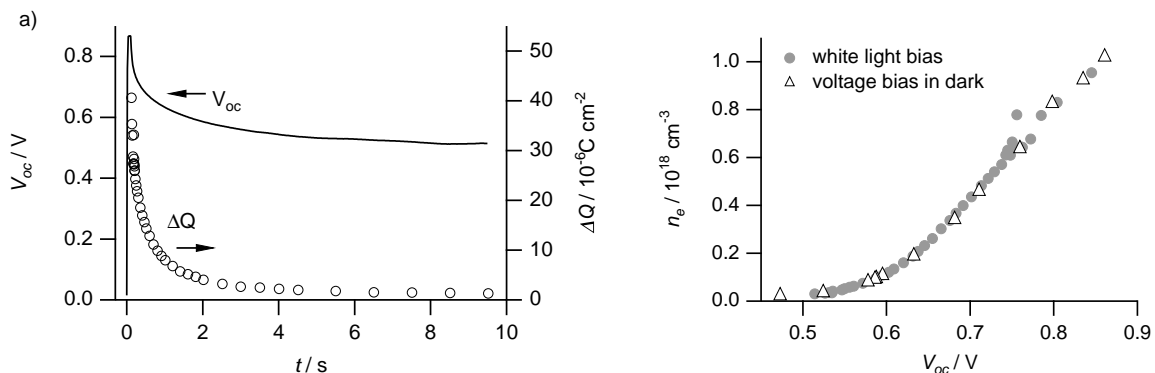


Figure 2.10: a) Open-circuit voltage decay in the dark after illumination at 1.5 sun. The extracted charge ΔQ is calculated from the integral of the current spike after short-circuiting the cell. The total voltage decay was repeated several times to obtain the extracted charge as a function of time and V_{oc} . b) Comparison of calculated charge density in the film as function of voltage using the extracted charge ΔQ after illumination (grey filled dots) or after electrical bias in the dark (empty triangles).

charge follows an exponential function, which is a strong indication for an exponential distribution of trap states in the TiO₂ band gap.

Alternatively, the device can be biased in the dark with a positive electrical potential to fill the TiO₂ film with charge. After reaching a steady-state, the cell is short-circuited to obtain the stored charge in the film. Charge density values obtained with “dark charge extraction” are shown in Figure 2.10b for comparison. The agree well with values obtained with the “charge extraction after illumination”. This is expected, since both methods compare the stored charge at open-circuit in the film at a certain photovoltage, i.e. a certain flat quasi-Fermi level in the film. In one case the photovoltage is established with illumination (photogeneration), and in the other case with a voltage bias.

Small perturbation open-circuit voltage decay. To analyze electron lifetimes (or electron recombination rates), it is convenient to perturb the photovoltage at open-circuit only slightly around a steady state. Duffy et. al. have suggested to superimpose a small amplitude laser excitation on a steady background illumination [15]. If the perturbation is sufficiently small, the photovoltage decay is a linear function of the total electron density, and the transient response can be fitted with a constant value of the electron lifetime τ_e .

A typical voltage transient at 1.0 sun white bias light with a superimposed 50 ms red light pulse is plotted in Figure 2.11a. The perturbation ($\Delta V = 3.8$ mV) is very small compared to the steady-state photovoltage ($V_{oc}^{ss} = 790.5$ mV). To extract the electron

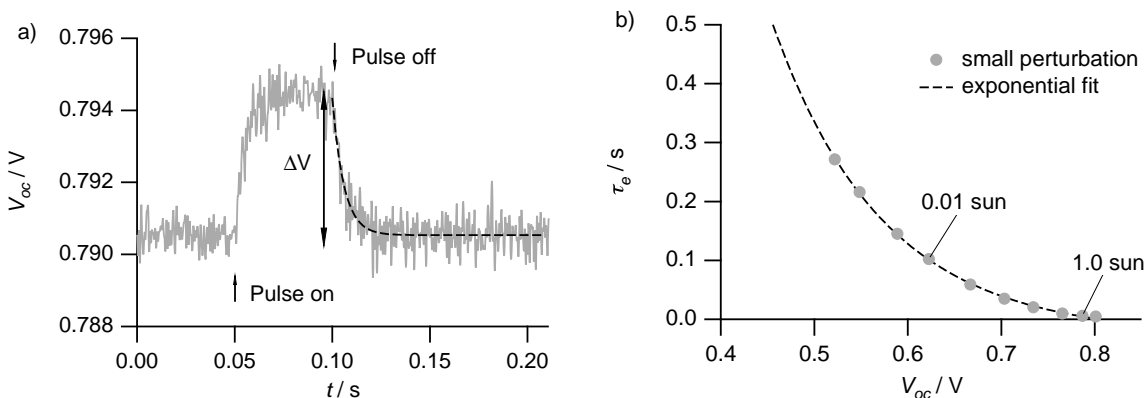


Figure 2.11: a) Typical small perturbation photovoltage decay transient of a device under steady white illumination (1 sun light intensity) after a small red light pulse. The exponential fit (dashed black line) yields a lifetime of $\tau_e = 5.9$ ms. b) Electron lifetime derived from small perturbation transients at various white bias light intensities and corresponding V_{oc} (grey dots). Lifetimes increase exponentially with lower charge density in the film.

lifetime τ_e , the voltage decay is fit to a simple exponential of the form

$$V(t) = V_0 + a e^{-t/\tau_e}, \quad (2.9)$$

where V_0 and a are fitting coefficients. This procedure can be repeated for different white light bias intensities and corresponding V_{oc} to obtain τ_e as a function of V_{oc} (Figure 2.11b). τ_e increases with decreasing V_{oc} and charge density, which reflects the trap-mediated recombination process.

Small perturbation short-circuit current decay. In analogy to the small perturbation open-circuit voltage transient, one can measure the decay of a perturbed short-circuit current. A typical current transient at 1.0 sun white bias light with a superimposed 50 ms red light pulse is plotted in Figure 2.12. The same pulse intensity as for the voltage decay in Figure 2.11a was used. The current decay can be fit to a simple exponential of the form

$$J(t) = J_0 + b e^{-t/\tau_c}, \quad (2.10)$$

where J_0 and b are fitting coefficients. The lifetime τ_c depends on both the transport and the recombination rate of free electrons at the quasi-Fermi level fixed by the white light bias,

$$\tau_c^{-1} = k_c = k_{trans} + k_{rec}. \quad (2.11)$$

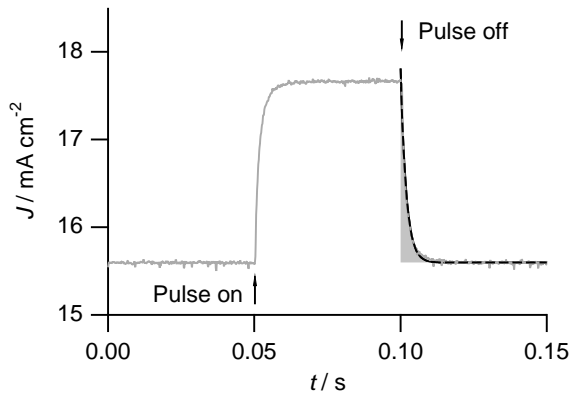


Figure 2.12: Typical transient short-circuit current decay at 1 sun white bias light after small red perturbation pulse. The monoexponential fit (dashed black line) yields a lifetime of $\tau_c = 1.92$ ms. The grey shaded area represents the additional charge ΔQ injected by the pulse.

In principle, the recombination rate k_{rec} can be derived from the voltage decay transient via $k_{rec} = \tau_e^{-1}$. However, the voltage decay is measured under open-circuit conditions. For the same incident light intensity, the charge in the TiO_2 under open-circuit conditions is several orders of magnitude higher than under short-circuit conditions. The difference in quasi-Fermi energies is in the order of 0.5 eV. This can be calculated by solving the continuity equation for electrons [16], and it can be determined experimentally with a titanium electrode evaporated on the mesoporous TiO_2 [17]. The two measurements — voltage and current decay measured at equal bias light intensity — can thus not be directly related.

Because of these experimental issues, we refrain from determining values for the transport rate from small-perturbation voltage and current decays. Instead, we will use current decay measurements to extract information on the trap state distribution using the DSC model discussed in Chapter 5.

Setup. Transient decays were measured with a home-built setup as shown in Figure 2.13. Cells were illuminated with a white light steady-state bias at different intensities and a superimposed small red light perturbation pulse from light-emitting diodes (LEDs). The voltage dynamics were recorded at open-circuit on a PC-interfaced Keithley 2602 source meter with a 40 μs response time. The perturbation light source was set to a suitably low level for the voltage decay kinetics to be monoexponential (~ 0.05 s square pulse width, 100 ns rise and fall time). The current dynamics were recorded at short-circuit. The spectral irradiance of the white bias light and the red perturbation light are shown in Figure 2.14.

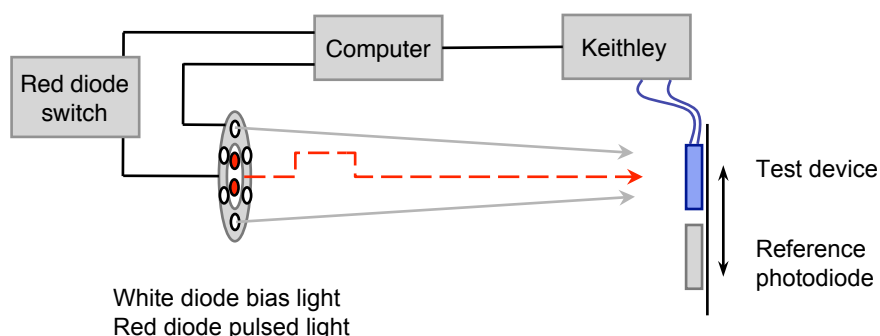


Figure 2.13: Schematic of the setup for time-resolved transient photocurrent or photovoltage measurements. A steady-state is established in the device with illumination from white LED lights, and the system is perturbed with a red LED light pulse controlled with a solid-state switch. A calibrated reference photodiode measures the intensity of the incident white light.

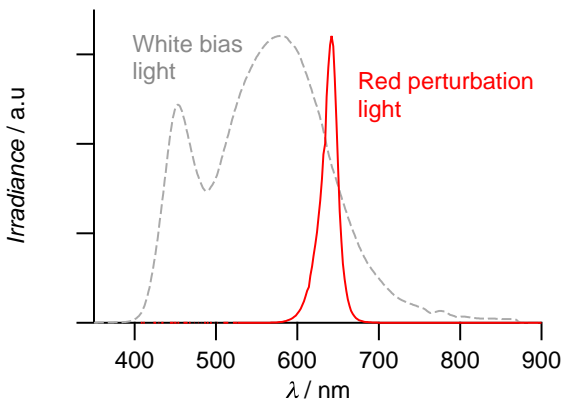


Figure 2.14: Spectra of the white LED bias light, which establishes a steady charge density in the TiO₂ film, and the red LED perturbation light.

2.4 Optical characterization

2.4.1 UV-vis-NIR absorption

UV-visible absorption spectra of solutions were measured in a 1 cm path length quartz cell on a Cary 5 spectrophotometer. The absorbance of sensitized TiO₂ films was measured by attaching the samples with double-sided tape to a sample holder with an aperture of $\sim 0.2 \text{ cm}^2$. The beam was then incident from the glass side. The “dye loading”, i.e. the concentration of dye in the mesoporous TiO₂ film, was calculated from the absorbance of the sensitized film (A), from which the absorbance of the blank TiO₂ film had been subtracted, using Lambert-Beer’s law,

$$A = \epsilon c d, \quad (2.12)$$

where ϵ is the extinction coefficient of the dye in solution, c is the dye concentration in the TiO₂ film, and d is the film thickness. In some cases the dye was desorbed from the sensitized film with a suitable base, and the concentration was determined from the solution using Lambert-Beer’s law.

The total and diffuse transmittance of samples was measured with an integrating sphere attached to the spectrophotometer. The integrating sphere is coated with a highly reflecting material and possesses an entrance and an exit port along the axis of the incident beam (entrance port: $19 \times 17 \text{ mm}^2$; exit port: circular with a diameter of 16 mm). To measure the total transmittance (T_{tot}) of a sample, it was placed in front of the entrance port, and the exit port was sealed with a highly reflecting plug such that both the collinear and diffuse transmittance ($T_{tot} = T_{collinear} + T_{diff}$) could

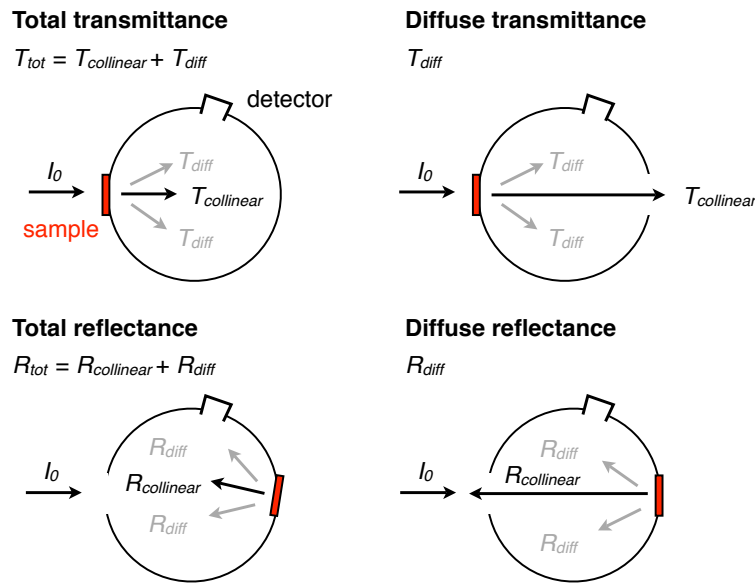


Figure 2.15: Configurations of the sample and entrance and exit ports in an integrating sphere to determine the total and diffuse transmittance and reflectance of a sample.

be detected. To measure the diffuse transmittance only, the exit port was opened. The total reflectance ($R_{tot} = R_{collinear} + R_{diff}$) was measured by placing the sample behind the exit port with a small tilt. The diffuse transmittance was measured by placing the sample behind the exit port normal to the incident beam (Figure 2.15).

2.4.2 Spectroscopic ellipsometry

Spectroscopic ellipsometry was used to assist the determination of the complex refractive indices of individual layers of the DSC (see Chapter 5). This technique makes use of the fact that linearly polarized light is reflected from a sample as elliptically polarized light. The ellipsometer measures the ratio of the amplitude reflection coefficients for p- and s-polarizations, which is a function of the sample's film thickness and complex refractive index. In principle, the thickness can be determined with ångström resolution since the technique exploits phase information and the polarization state. This requires well-defined layers that are optically homogeneous and isotropic. Ellipsometry is an indirect characterization technique; the complex refractive indices are obtained by fitting the results of an optical (multi)layer model to the data.

Samples were characterized with a Sopra GES 5E spectroscopic ellipsometer in the wavelength range $\lambda = 350\text{--}1600\text{ nm}$. The complex refractive indices were extracted by fitting the data with the *WINELLI 2* software package from Sopra.

2.4.3 Fourier transformed infrared spectroscopy

Attenuated total reflection Fourier transformed infrared spectroscopy (ATR-FTIR) was used to analyze the surface chemistry of the TiO₂ films sensitized with π -extended tetrathiafulvalene dyes (Section 3.5). The spectra were measured with an FTS 7000 FTIR spectrometer (Digilab, USA). The data were taken with a Golden Gate diamond anvil ATR accessory. Spectra were derived from 64 scans at a resolution of 2 cm⁻¹. The samples were measured under the same mechanical force pushing the samples in contact with the diamond window. No ATR correction has been applied to the data. It has to be noted that this ATR technique probes at most 1 μm of sample depth and that this depends on the sample refractive index, the porosity, etc. Some of the spectra show artifacts due to attenuation of the light by the diamond window in the 2000 to 2350 cm⁻¹ region. Dye-coated films were rinsed with acetonitrile and dried prior to measuring the spectra. The obtained data was further processed with a home-built software to subtract the absorption of the TiO₂, surface water and carbon dioxide for purpose of clarity.

Bibliography

- [1] S. Ito, T. N. Murakami, P. Comte, P. Liska, C. Grätzel, M. K. Naziruddin, and M. Grätzel. Fabrication of thin film dye sensitized solar cells with solar to electric power conversion efficiency over 10%. *Thin Solid Films* **2008**, *516*, 4613–4619.
- [2] C. J. Barbé, F. Arendse, P. Comte, M. Jirousek, F. Lenzmann, V. Shklover, and M. Grätzel. Nanocrystalline titanium oxide electrodes for photovoltaic applications. *Journal of the American Ceramic Society* **1997**, *80*, 3157–3171.
- [3] P. Wang, S. M. Zakeeruddin, P. Comte, R. Charvet, R. Humphry-Baker, and M. Grätzel. Enhance the performance of dye-sensitized solar cells by co-grafting amphiphilic sensitizer and hexadecylmalonic acid on tio₂ nanocrystals. *The Journal of Physical Chemistry B* **2003**, *107*, 14336–14341.
- [4] S. M. Zakeeruddin, M. K. Naziruddin, R. Humphry-Baker, P. Péchy, P. Quagliotto, C. Barolo, G. Viscardi, and M. Grätzel. Design, synthesis, and application of amphiphilic ruthenium polypyridyl photosensitizers in solar cells based on nanocrystalline tio₂ films. *Langmuir* **2002**, *18*, 952–954.
- [5] F. Gao, Y. Wang, D. Shi, J. Zhang, M. K. Wang, X. Y. Jing, R. Humphry-Baker, P. Wang, S. M. Zakeeruddin, and M. Grätzel. Enhance the optical absorptivity of nanocrystalline TiO₂ film with high molar extinction coefficient ruthenium sensitizers for high performance dye-sensitized solar cells. *Journal of the American Chemical Society* **2008**, *130*, 10720–10728.
- [6] P. Wang, S. M. Zakeeruddin, J. E. Moser, M. K. Naziruddin, T. Sekiguchi, and M. Grätzel. A stable quasi-solid-state dye-sensitized solar cell with an amphiphilic ruthenium sensitizer and polymer gel electrolyte. *Nature Materials* **2003**, *2*, 402–407.

- [7] Y. Bai, Y. Cao, J. Zhang, M. Wang, R. Li, P. Wang, S. M. Zakeeruddin, and M. Grätzel. High-performance dye-sensitized solar cells based on solvent-free electrolytes produced from eutectic melts. *Nature Materials* **2008**, *7*, 626–630.
- [8] S. M. Sze. *Semiconductor devices, physics and technology*. John Wiley & Sons, New York, 2nd edition **2002**.
- [9] C. H. Seaman. Calibration of solar cells by the reference cell method - The spectral mismatch problem. *Solar Energy* **1982**, *29*, 291–298.
- [10] Y. Tachibana, J. E. Moser, M. Grätzel, D. R. Klug, and J. R. Durrant. Subpicosecond interfacial charge separation in dye-sensitized nanocrystalline titanium dioxide films. *Journal of Physical Chemistry* **1996**, *100*, 20056–20062.
- [11] S. A. Haque, Y. Tachibana, R. L. Willis, J. E. Moser, M. Grätzel, D. R. Klug, and J. R. Durrant. Parameters influencing charge recombination kinetics in dye-sensitized nanocrystalline titanium dioxide films. *The Journal of Physical Chemistry B* **1999**, *104*, 538–547.
- [12] L. Peter. Transport, trapping and interfacial transfer of electrons in dye-sensitized nanocrystalline solar cells. *Journal of Electroanalytical Chemistry* **2007**, *599*, 233–240.
- [13] J. Bisquert and V. S. Vikhrenko. Interpretation of the time constants measured by kinetic techniques in nanostructured semiconductor electrodes and dye-sensitized solar cells. *Journal of Physical Chemistry B* **2004**, *108*, 2313–2322.
- [14] N. W. Duffy, L. M. Peter, R. M. G. Rajapakse, and K. G. U. Wijayantha. A novel charge extraction method for the study of electron transport and interfacial transfer in dye sensitised nanocrystalline solar cells. *Electrochemistry Communications* **2000**, *2*, 658–662.
- [15] N. W. Duffy, L. M. Peter, and K. G. U. Wijayantha. Characterisation of electron transport and back reaction in dye-sensitised nanocrystalline solar cells by small amplitude laser pulse excitation. *Electrochemistry Communications* **2000**, *2*, 262–266.
- [16] L. M. Peter. Characterization and modeling of dye-sensitized solar cells. *Journal of Physical Chemistry C* **2007**, *111*, 6601–6612.
- [17] K. Lobato, L. M. Peter, and U. Würfel. Direct measurement of the internal electron quasi-Fermi level in dye sensitized solar cells using a titanium secondary electrode. *Journal of Physical Chemistry B* **2006**, *110*, 16201–16204.

Chapter 3

Organic sensitizers for stable and efficient dye-sensitized solar cells

3.1 Introduction

Dye-sensitized solar cells (DSCs) have reached efficiencies of over 11 % in the laboratory with ruthenium(II)-polypyridyl complexes [1–5]. However, the scarcity of ruthenium metal combined with intricate synthesis and purification steps might retard future large-scale power production by DSCs. Metal-free organic sensitizers can be synthesized rather inexpensively, and their absorption properties can be easily tuned by suitable molecular design. High extinction coefficients and expansion of the absorption into the near-IR region can be achieved with the well-known structure-property relationships of color chemistry [6].

Reports of new organic sensitizer structures and their performance in DSCs have been mushrooming in the past years, as shown in a recent extensive review [7]. Organic sensitizers for DSCs generally consist of an electron donor connected to a cyanoacrylic acid acceptor with a π -conjugated spacer (donor- π -acceptor system, Figure 3.1). Promising donors come from the family of electron-rich *aryl amines*: di- and triphenylamine, aminocoumarine, and indoline. The π -conjugated bridge frequently contains *thiophene* units, such as oligothiophenes or dithienophenes, which have excellent transport properties [8]. In most cases, *cyanoacrylic acid* is used as acceptor, though rhodanine-3-acetic acid has also given good results. Record conversion efficiencies of up to 9.8 % and stable performance were obtained with a dihexyloxy-substituted triphenylamine donor and binary thiophene-based conjugated spacer [9]. Very good (9.5 %) but unstable efficiencies due to dye desorption were achieved with an indoline donor and rhodanine acceptor system [10].

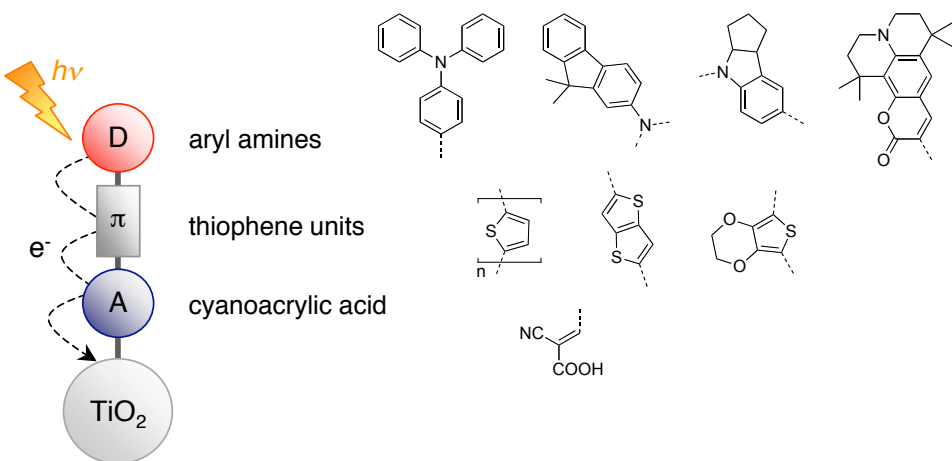


Figure 3.1: Design principle of an organic donor- π -bridge-acceptor (D- π -A) sensitizer for TiO_2 photoanodes. Most promising donor moieties include triphenylamine, (di)fluorenlylamine, indoline, and coumarine (from left to right). The bridge typically contains oligothiophenes, dithienothiophene, or ethylenedioxythiophene. Cyanoacrylic acid usually serves as acceptor and anchoring group to the TiO_2 particle.

The performance of organic dyes in DSCs can still be further enhanced. The photocurrent could be increased with a stronger optical response of the dyes in the near-infrared (IR) region, and the photovoltage could be increased by blocking interfacial recombination between injected electrons in the mesoporous TiO_2 and the redox couple, which is substantial for some organic dyes.

Organic dyes with a narrow spectral response have interesting applications as well. From a commercial point of view, DSCs with a variety of colors allow for aesthetically appealing small-scale PV products or building-integrated PV panels. A combination of dyes with small absorption windows can also be used in “cocktail” DSC systems, where the TiO_2 is co-sensitized by several dyes to achieve a panchromatic response [11–13]. Different dyes can also be exploited by making use of Förster energy transfer (FRET); low energy photons are absorbed by a dye attached to the TiO_2 (sensitizing dye), and high energy photons are absorbed by a dye dissolved in the redox mediator (energy relay dye), which transfers the absorbed energy via FRET to the sensitizing dye [14, 15].

For good power conversion efficiencies in a conventional DSC, the organic dye must fulfill the following conditions:

- The absorption range of the dye adsorbed to the TiO_2 should cover the visible and the near-IR range, and its molar extinction coefficient should be high, such that thin films can be used.

- For efficient injection of photoexcited electrons into the TiO₂, the lowest unoccupied molecular orbital (LUMO) should be localized near the anchoring group and should lie higher than the conduction band edge of the semiconductor.
- For efficient regeneration of the oxidized dye, the highest occupied molecular orbital (HOMO) should lie below the energy level of the redox mediator. Additionally, the HOMO should be localized on the donor group to reduce recombination of photoinjected electrons with the dye cation or with oxidized redox species (tri-iodide ions).
- Preferably, the periphery of the dye should be hydrophobic to minimize the direct contact between water in the electrolyte and the TiO₂ surface, which could desorb the dye.
- Finally, the dye should not form aggregates. The formation of dimers, *H*-, or *J*-aggregates changes the optoelectronic properties of the dye [16, 17]. Also, large aggregates may inject electrons less efficiently into the semiconductor, as observed for aggregated ruthenium-complex systems [18].

In this chapter, we discuss the photovoltaic performance of three classes of organic dyes synthesized by various international collaborators. The investigated systems have a diphenylamine, difluorenylaminophenyl, or a novel π -extended tetrathiafulvalene donor, a cyanoacrylic acid acceptor, and thiophene-based bridging moieties. The molecular structures of the dyes are shown in Figure 3.2.

The diphenylamine donor systems (dyes **LIN** and **BRA** [19], Section 3.3) were tested in collaboration with the group of Prof. P. Bäuerle at the Institute of Organic Chemistry II and Advanced Materials at the University of Ulm, Germany. The difluorenylaminophenyl donor systems (dyes **C203** [20], **C204**, and **C205** [21], Section 3.4) were tested in collaboration with the group of Prof. P. Wang at the State Key Laboratory of Polymer Physics and Chemistry, Changchun Institute of Applied Chemistry, Chinese Academy of Sciences, China. The π -extended tetrathiafulvalene donor systems (dyes **PAB-1**, **PAB-2**, and **PAB-3** [22], Section 3.5) were tested in collaboration with the group of Prof. N. Martín at the Departamento de Química Orgánica, Universidad de Complutense, Madrid. The dyes were designed and synthesized by the respective collaborators. Test devices were assembled and characterized at the EPFL by the author and colleagues.

3.2 Experimental

Device fabrication. The dyes were tested in photovoltaic devices that were fabricated as described in Section 2.1. The devices contained standard mesoporous TiO₂ films, either in a single layer configuration with “transparent” 20 nm sized particles, or in a double layer configuration with an additional layer of scattering 400 nm sized particles. The circular TiO₂ surface area was about 0.28 cm². The precise layer thickness used is mentioned in the respective Section. Films were immersed for 5 h in a solution of 0.3 mM dye and up to 10 mM chenodeoxycholic acid (cheno) as co-adsorbant in a suitable solvent (mentioned in Section). All devices were tested with a volatile acetonitrile-based electrolyte (coded Z960) and ternary ionic liquid (coded Z952). The composition of the electrolytes is given on page 27. The photoanodes were covered with a UV-cutoff/antireflecting polymer.

Photovoltaic characterization and stability tests. The current-voltage characteristics of the cells were measured under the irradiance of a 450 W xenon light source matched to AM 1.5G with filters (see Section 2.2.2). The external quantum efficiency, or incident photon-to-current conversion efficiency (IPCE), was measured as described in Section 2.2.1. The effective area of the devices was defined with a metal mask with an aperture of 0.159 cm². For stability tests, devices were irradiated at open-circuit under a Suntest CPS plus lamp (ATLAS GmBH, 100 mW cm⁻²) in ambient air at 60 °C.

Transient photovoltage measurements. Transient small perturbation photovoltage decays at open-circuit conditions were measured with different white light steady-state biases and a superimposed red light perturbation pulse (0.05 s square pulse width, 100 ns rise and fall time), incident on the photoanode side of the test device as described in Section 2.3.2. By varying the white light bias intensity, the recombination rate constant could be estimated for different photovoltages, i.e. different charge densities in the TiO₂ film.

Nanosecond laser transient absorbance measurements. Nanosecond transient absorbance measurements were performed on the **PAB-3** system to study the dye cation regeneration dynamics in more detail. 4.8 μm thick transparent nanocrystalline anatase TiO₂ films (16 nm particle diameter, porosity = 0.625) were coated with dye **PAB-3** for ~ 12 h. This measurement is described in Section 2.3.1.

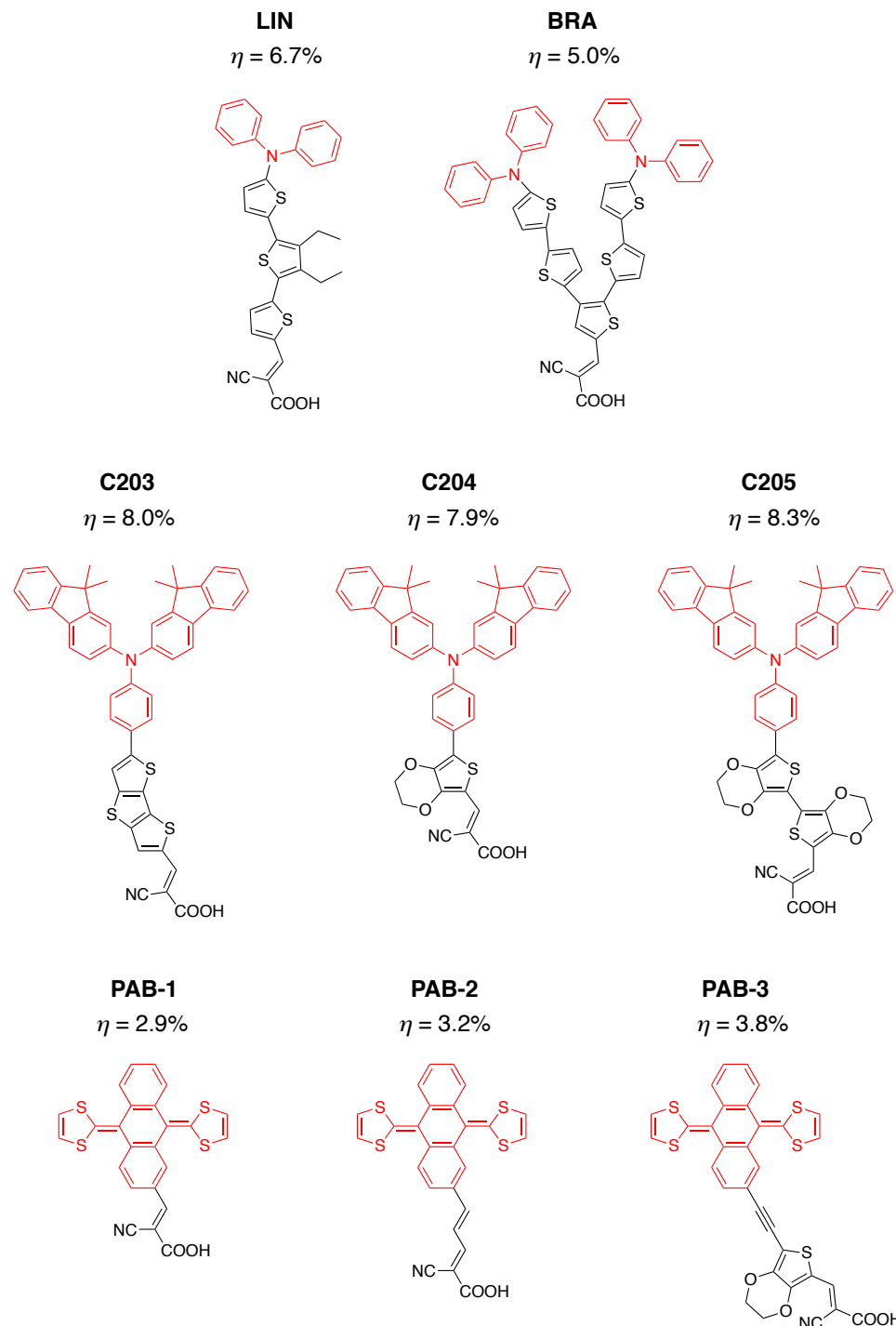


Figure 3.2: Molecular structures of the studied dyes. The donor moiety (red) consists of a diphenylamine (**LIN**, **BRA**), difluorenlylaminophenyl (**C203**, **C204**, **C205**), or π -extended tetrathiafulvalene (**PAB-1**, **PAB-2**, **PAB-3**) unit. The π -extended bridge is thiophene-based in most cases and connects to the cyanoacrylic acid group acceptor. Best power conversion efficiencies for test devices using a volatile electrolyte are indicated.

3.3 Diphenylamine donor systems

Organic sensitizers with a triarylamine donor unit constitute a very promising class of light harvesters for DSCs [23]. Quite frequently, triphenylamine moieties are used. The nitrogen core is oxidized very easily, and positive charges can be transported via the radical cations, which makes triphenyl-based materials also interesting for organic light emitting diodes, organic field-effect transistors, or xerography applications [24]. The nonplanar propeller-like configuration of the triphenylamine moiety also hinders molecular aggregation in DSCs.

Here we studied the photovoltaic behavior of two sensitizers with diphenylthienylamine donor moieties and a linear (**LIN**) or branched (**BRA**) oligothiophene bridging unit (Figure 3.2) [19]. These sensitizers can be considered as analogues of similar systems with triphenylamine donors reported by Justin Thomas et. al. (~ 6 % efficiency with volatile electrolyte for a linear and branched structure) [25]. Yum et. al. reported on a linear system with methoxy groups and hydrophobic ligands (coded **D21L6**) showing 7.2 % with volatile electrolyte and high stability with an ionic liquid [26]. An enhanced red response and long-term stability had been previously observed with methoxy-substituted triphenylamine systems [27]. The structures of the analogues are shown in Figure 3.3.

Experimental. The synthesis of the dyes **LIN** and **BRA** is described in detail in the publication [19]. Dyes were tested in photovoltaic devices using a double layer TiO₂ film with a 8 μm thick transparent layer of 20 nm sized particles and a scattering 5 μm thick

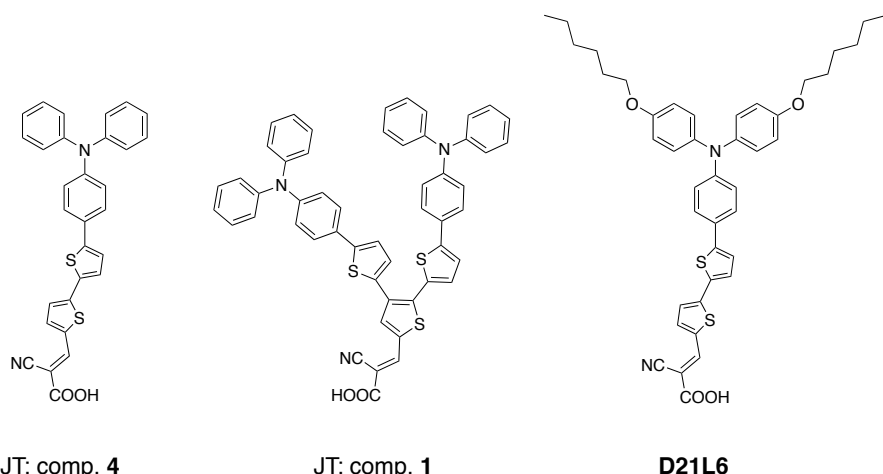


Figure 3.3: Molecular structures of triphenylamine donor systems that are comparable to the dyes studied in this Section. JT (Justin Thomas) compounds **1** and **4** taken from [25], **D21L6** taken from [26].

layer of 400 nm sized particles (8+5 film). Films were immersed for 5 h in a solution of 0.3 mM dye and 10 mM chenodeoxycholic acid as co-adsorbant in dichloromethane.

3.3.1 Results and discussion

Electronic absorption and redox behavior. The absorption spectrum of the dyes **LIN** and **BRA** in dichloromethane is shown in Figure 3.4a. The linear dye had an absorption maximum in the visible region at 450 nm with an extinction coefficient of $\epsilon = 19.6 \times 10^3 \text{ M}^{-1} \text{ cm}^{-1}$. The branched dye had a shoulder in the visible at 503 nm ($\epsilon = 16.0 \times 10^3 \text{ M}^{-1} \text{ cm}^{-1}$) and a maximum in the UV at 390 nm ($\epsilon = 31.2 \times 10^3 \text{ M}^{-1} \text{ cm}^{-1}$). The low energy absorption bands were attributed to $\pi - \pi^*$ charge-transfer (CT) transitions. The shape of the absorption spectra is similar to the spectra of the triphenylamine analogues [25]. We observed an about 20 nm blue-shift of the CT band of **LIN** with increasing solvent polarity, which can be attributed to a partial deprotonation of the carboxylic acid. The UV-band of **BRA** remained unchanged with increasing solvent polarity, but the magnitude of the shoulder at 503 nm decreased [19].

The absorbance spectra of the dyes adsorbed to a 5 μm thin mesoporous TiO_2 film is plotted in Figure 3.4a for comparison. Absorption of the blank TiO_2 film was subtracted from the curves. The magnitude of the blue-shift of the absorption maxima of the adsorbed dyes (28 nm for **LIN** and 10 nm for the UV-band of **BRA**) is similar to the

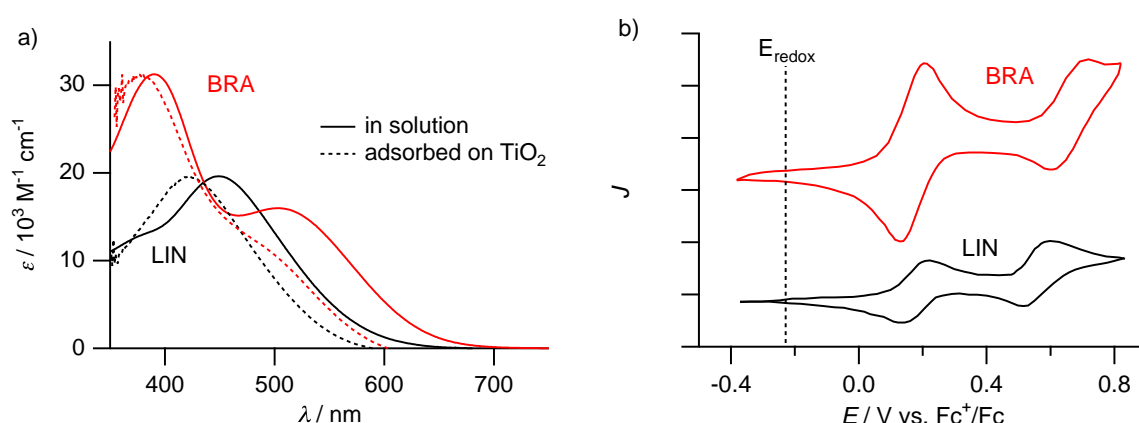


Figure 3.4: a) Molar extinction coefficient (ϵ) of the dye **LIN** and **BRA** in dichloromethane (solid lines). The normalized absorbance spectra of the dye adsorbed to a 5 μm thin mesoporous TiO_2 film (dashed lines) in air are blue-shifted compared to the spectra in solution. Absorption of the blank TiO_2 film was subtracted from the measurements. b) Cyclic voltammograms of **LIN** and **BRA** in dichloromethane and 0.1 M of tetrabutylammonium hexafluorophosphate as supporting electrolyte. The approximate potential level of the redox mediator is indicated with a dashed line.

shifts observed in polar solvents. The shifts can thus be attributed to the deprotonation of the carboxylate groups. A blue-shift in the spectral response has also been observed for other organic dyes adsorbed to the surface of TiO₂ [21, 25, 28].

From the absorbance maxima, we estimated the dye concentration on the film to be 0.23 M for the linear dye and 0.11 M for the branched dye. These clear differences in dye loading are likely due to the structure of the molecules, as the bulky structure of the branched dye probably hinders compact packing on the TiO₂ surface.

Semiempirical quantum chemical calculations using the Austin Model 1 method under restricted Hartree Fock conditions were performed to analyze the electron distribution of the frontier orbitals of the dyes. As can be seen in Figure 3.5, the highest occupied molecular orbital (HOMO) of both molecules is mainly located on the oligothiophene and diphenylamine moieties, whereas the lowest unoccupied molecular orbital (LUMO) is primarily located on the cyanoacrylic acid acceptor and the neighboring thiophene ring. The pronounced electron density relocation between the HOMO and LUMO supports the presence of intramolecular CT transitions in the visible spectrum. Furthermore, the electron distribution shows favorable directionality for injection of photoexcited electrons from the donor group to the TiO₂ film via the anchoring group.

The oxidation potential of the dyes was measured by cyclic voltammetry in dichloromethane and referenced against the ferrocinium/ferrocene (Fc⁺/Fc) couple (Fig-

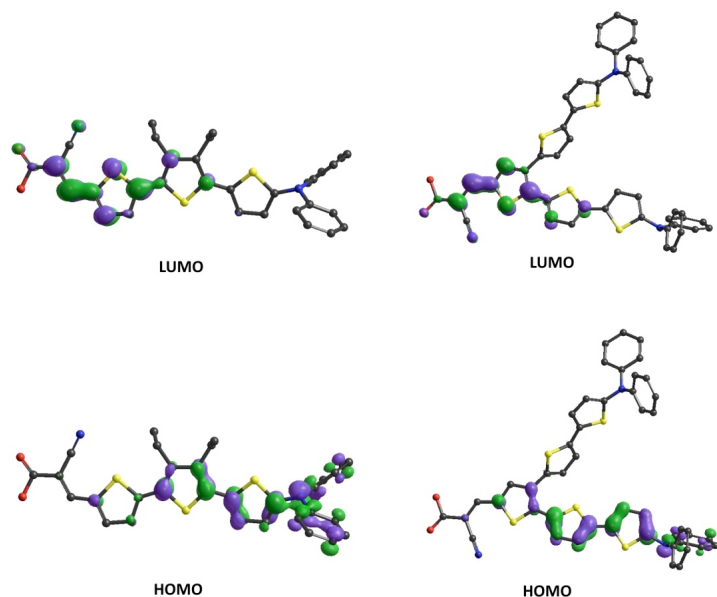


Figure 3.5: Calculated highest occupied molecular orbitals (HOMO) and lowest unoccupied molecular orbitals (LUMO) of the linear and branched dye showing favorable directionality for photoinduced injection of electrons into the TiO₂ via the anchoring group.

ure 3.4b). The first oxidation potential (E_{ox1}) for both compounds, indicating the HOMO level, was found at 0.18 V vs. Fc^+/Fc and is assigned to the oxidation of the diphenylthienylamine moiety [29]. The second oxidation potential (E_{ox2}) at 0.56 V for dye **LIN** and 0.65 V for dye **BRA** is assigned to the oxidation of the oligothiophene units. The HOMO level is about 390 mV more positive than the redox potential of I^-/I_3^- (-0.21 V vs. Fc^+/Fc in ionic liquid [30]), ensuring sufficient driving force for regeneration of dye cations. The LUMO levels were estimated from the absorption onset values ($E_g^{opt} = 2.14 \text{ eV}$ and 1.94 eV , respectively) to lie at -1.96 V vs. Fc^+/Fc for dye **LIN** and -1.76 V for dye **BRA**, which is suitably more negative than the conduction band edge of TiO_2 .

Photovoltaic performance and stability. The incident photon-to-current conversion efficiency (IPCE) of devices with the linear or branched dye and an acetonitrile-based electrolyte (Z960) are shown in Figure 3.6a. The IPCE of the linear dye exceeded 80 % in the spectral region of 500–550 nm. In contrast, the IPCE of the branched dye had a lower maximum of 67 % at 510 nm. We can make a crude estimate of the fraction of absorbed light by the dye in the TiO_2 film using

$$A_{dye} \approx (1 - R_{tot}) (1 - 10^{-\epsilon c d}), \quad (3.1)$$

where R_{tot} is the total reflectance of the device when illuminated from the TiO_2 side, ϵ is the extinction coefficient of the dye in solution, c is the dye concentration in the TiO_2 film, and d is the film thickness. For $R_{tot} \approx 0.1$ (see also Chapter 5 on the optical characterization of DSCs), we find a dye absorptance at 510 nm of about 89 % in the

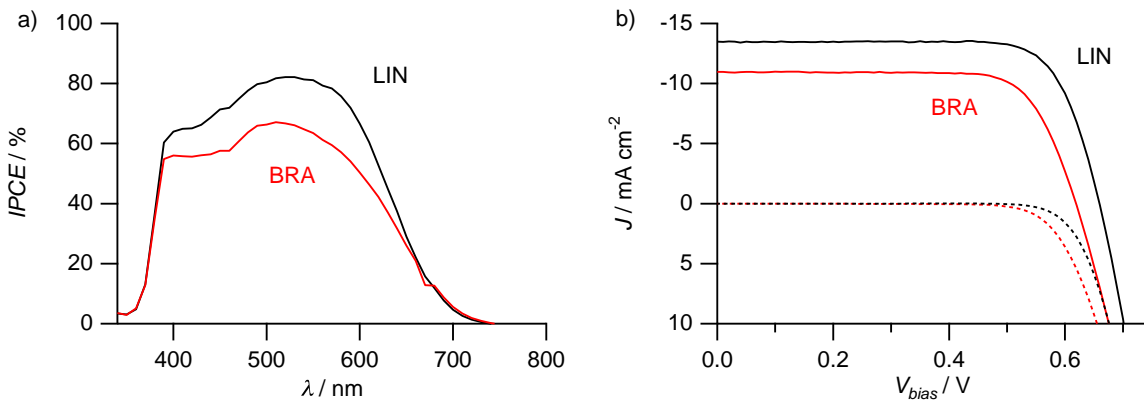


Figure 3.6: IPCE (a) and photocurrent-voltage curves (b) under simulated full sunlight (AM 1.5G, 100 mW cm^{-2}) and in the dark of devices with a 8+5 TiO_2 film, dye **LIN** or **BRA**, and an acetonitrile-based electrolyte (Z960).

Table 3.1: Photovoltaic parameters of devices with an 8+5 TiO₂ film sensitized with the dye **LIN** or **BRA**. The redox mediator was a volatile electrolyte (Z960) or an ionic liquid (Z952). Parameters with ionic liquid are stabilized values after 24 h of light-soaking. Devices were measured under simulated AM 1.5G illumination (100 mW cm⁻²).

Dye	Redox	V_{oc} / mV	J_{sc} / mA cm ⁻²	FF	η / %
LIN	volatile	659	-13.5	0.76	6.7
	ionic liquid	659	-11.9	0.75	5.9
BRA	volatile	619	-11.0	0.74	5.0
	ionic liquid	570	-6.1	0.75	2.6

device with dye **LIN** and 87 % in the device with dye **BRA**. The estimated absorbed photon-to-current conversion efficiency (APCE, or internal quantum efficiency), which is the ratio of the IPCE to the fraction of absorbed light by the dye A_{dye} , is 90 % for the device with **LIN** and 77 % for the device with **BRA**. An APCE smaller than unity can be due to a combination of insufficient injection from the excited dye state and recombination of photoinjected electrons in the TiO₂ with dye cations or tri-iodide ions in the electrolyte. Here, the low APCE obtained with the **BRA** system is most likely due to a high recombination rate of electrons in the TiO₂ with I₃⁻ via the large fraction of uncovered TiO₂ surface area. This hypothesis was supported with photovoltage decay experiments (see page 53).

The photovoltaic parameters, i.e. the conversion efficiency (η), short-circuit current density (J_{sc}), the open-circuit photovoltage (V_{oc}), and the fill factor (FF) under simulated full sunlight (AM 1.5G, 100 mW cm⁻²) of devices employing a volatile electrolyte or ionic liquid are summarized in Table 3.1. The photocurrent-voltage curves of devices with volatile electrolyte are shown in Figure 3.6. With the volatile electrolyte we measured a conversion efficiency of 6.7 % for the linear dye and 5.0 % for the branched dye. The lower J_{sc} of the device with the branched dye is consistent with the lower IPCE, and the 40 mV lower V_{oc} can be explained with increased charge recombination via the larger fraction of uncovered TiO₂. With the ionic liquid electrolyte we obtained stabilized values after 24 h of light soaking of 5.9 % with the linear dye and 2.6 % with the branched dye. The markedly lower J_{sc} of the device with dye **BRA** and ionic liquid is likely due to the larger recombination current, which is induced by the high concentration of I₃⁻ in the ionic liquid compared to the volatile electrolyte (about 0.24 M vs. 0.03 M [31]).

The stability of devices with ionic liquid was tested for over 1000 h at full sunlight and 60 °C. The evolution of the photovoltaic parameters is shown in Figure 3.7. The

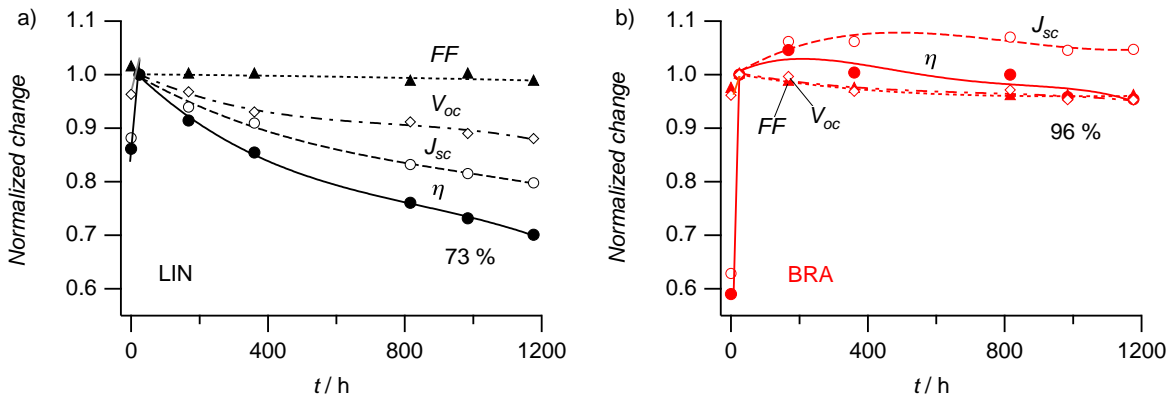


Figure 3.7: Temporal evolution of photovoltaic parameters of a device with dye **LIN** (a) or **BRA** (b) using an ionic liquid (Z952) during a 1000 h accelerated stability test (full sunlight, 60 °C). Parameters are normalized to stabilized values after 24 h of light soaking. Lines are guides to the eye.

parameters were normalized to stabilized values after 24 h of light soaking, which allowed for optimal reorganization of the dye molecules on the TiO₂ surface. The device with the dye **LIN** showed a rapid degradation of performance, retaining only 73 % of its initial efficiency after 1000 h. We attribute this degradation to a desorption of dye molecules, which causes a J_{sc} and associated V_{oc} loss. In contrast, the device with the dye **BRA** showed excellent stability, retaining 96 % of its initial efficiency after 1000 h. The higher stability of the branched dye can be ascribed to the bulky structure; it probably shields the TiO₂ surface against water molecules, which could desorb the dye. Also, the solubility of the branched system might be inferior to the linear system in the electrolyte.

Charge recombination. We measured the small-perturbation photovoltage decay transients at open-circuit conditions of devices with the volatile electrolyte. The recombination rates between electrons in the TiO₂ and I₃⁻ ions in the electrolyte were studied at various white light bias intensities and charge densities. The recombination rates (k_e) are plotted in Figure 3.8 versus the open-circuit potential (V_{oc}) in the device induced by the white light bias. Since the V_{oc} in the device is given by the difference between the redox level of the electrolyte and the quasi-Fermi level in the TiO₂, which is determined by the concentration of free charge carriers, this plot allows us to compare the recombination rate at equal charge density in the TiO₂ film. The recombination rate is known to increase exponentially with increasing bias light due to the filling of intraband trap states in the TiO₂, which allows for a faster detrapping of electrons to the conduction band and subsequent recombination with I₃⁻ [32]. We measured an about fourfold

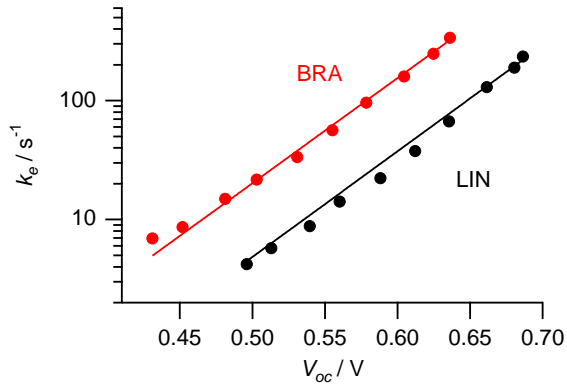


Figure 3.8: Comparison of the interfacial recombination rate (k_e) of electrons in the TiO_2 with I_3^- in the electrolyte as a function of bias light induced photovoltage. Devices contain a 8+5 TiO_2 film, dye **LIN** or **BRA**, and a volatile electrolyte (Z960). Recombination is increased about fourfold with **BRA**, since the TiO_2 surface is less densely covered by the branched dye. Lines are exponential fits to data.

increased recombination rate for the device with the dye **BRA** compared to the device with dye **LIN**, which we attribute to recombination via the larger fraction of uncovered TiO_2 surface.

Preliminary conclusions. The studied diphenylthienylamine donor systems are similar to their triphenylamine analogues [25] in terms of photovoltaic performance. The moderate photovoltage obtained with both dyes **LIN** and **BRA** might be related to the length of the oligothiophene bridge. Other studies on the effect of thiophene-based linker length in organic D- π -A systems have shown a decrease in V_{oc} with increasing linker length, which might be due to an interaction between the thiophene units and I_3^- or I_2 [33, 34]. We have observed two interesting effects related to the branched structure of **BRA**:

1. The large bulky structure limits the dye loading on the TiO_2 surface to about half the loading obtainable with the linear system. Still, similar fractions of light are absorbed by the two dyes in the TiO_2 film (87–89 %). The number of absorbed photons extracted as electrons, however, is manifestly lower in the device with the branched system, which is due to increased recombination of photojected electrons with I_3^- at the larger fraction of uncovered TiO_2 surface.
2. Accelerated aging studies of devices with ionic liquid show excellent photochemical and thermal stability for the branched dye. Devices using the linear dye degraded rapidly; namely the photocurrent declined — and the photovoltage accordingly. This is likely due to desorption of the linear dye. The branched dye seems to

hinder desorption by blocking the TiO₂ surface against bond-breaking species, such as water.

Diphenylthienylamine donors seem to be moderately appropriate for high efficiency organic dyes because of the thiophene unit. Probably, substituted triphenylamine analogues with a linear structure bear more promise, as demonstrated with a stable dihexyloxy-substituted triphenylamine donor with a bithiophene bridge [26].

3.4 Difluorenylaminophenyl donor systems

Difluorenylaminophenyl donor systems for application in DSCs were first introduced by Kim et. al. in 2006 [35]. The dyes coded **JK-1** and **JK-2**, which feature one or two thiophene bridging units and a cyanoacrylic acid acceptor (Figure 3.9), showed promising efficiencies of 7.2 % and 8.0 %, respectively, in devices with a volatile electrolyte. Accelerated aging under illumination at 60 °C of a device with dye **JK-2** and ionic liquid showed a drop in efficiency of 20 % after 1000 h, which was mainly due to a drop in photovoltage. The same group later reported on two similar systems (coded **JK-45** and **JK-46**, Figure 3.9) possessing three thiophene bridging units with aliphatic chains [36]. Devices with ionic liquid showed excellent long-term stability with these dyes, which was attributed to the hydrophobic hexyl chains preventing water-induced desorption. Wang and co-workers presented a system with a thienothiophene bridge (coded **C201**, Figure 3.9) showing excellent stability in a device with ionic liquid; 93 % of the initial

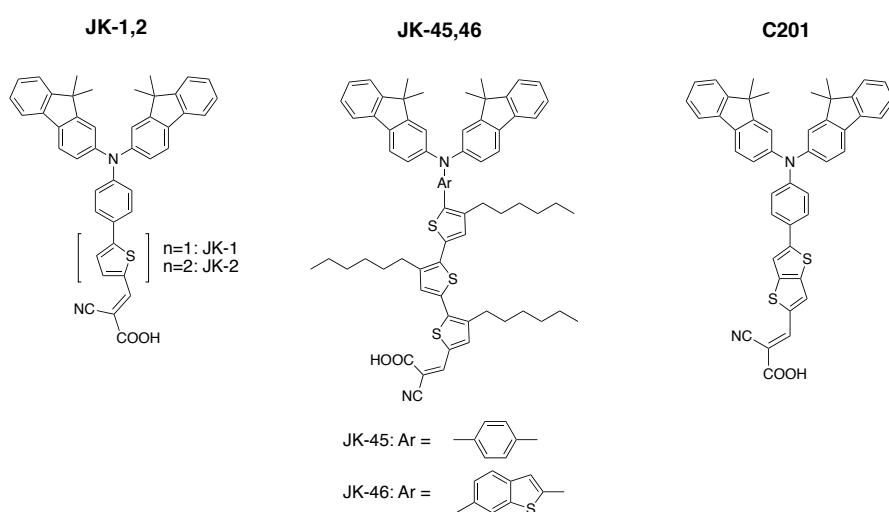


Figure 3.9: Molecular structures of difluorenylaminophenyl donor systems that are comparable to the dyes studied in this Section.

efficiency were retained after 1000 h [37]. Both devices using **JK-46** or **C201** with ionic liquid showed impressive initial efficiencies of 7.0 %.

Here, we studied the photovoltaic performance of three dye systems with difluorophenylaminophenyl donors, a fused dithienothiophene bridge (**C203**) [20] or an ethylene-dioxythiophene (EDOT) bridge (dyes **C204** and **C205**) [21]. The molecular structures are shown in Figure 3.2.

Experimental. The synthesis of the dyes **C203**, **C204**, and **C205** is described in detail in the publications [20, 21]. Dyes were tested in photovoltaic devices using a double layer TiO₂ film with a 7 µm thick transparent layer of 20 nm sized particles and a scattering 5 µm thick layer of 400 nm sized particles (7+5 film). Films were immersed for 5 h in a solution of 0.3 mM dye and 10 mM (for **C203** and **C205**) or 2 mM (for **C204**) chenodeoxycholic acid. **C203** was dissolved in dichloromethane, and **C204** and **C205** were dissolved in a mixture of acetonitrile and *tert*-butyl alcohol (volume ratio 1/1).

3.4.1 Results and discussion

Electronic absorption and redox behavior. The absorption and emission spectra were measured in chloroform (Figure 3.10a). **C203** had an absorption maximum in the visible region at 525 nm with $\epsilon = 44.8 \times 10^3 \text{ M}^{-1} \text{ cm}^{-1}$, **C204** at 525 nm with $\epsilon = 33.5 \times 10^3 \text{ M}^{-1} \text{ cm}^{-1}$, and **C205** at 544 nm with $\epsilon = 38.5 \times 10^3 \text{ M}^{-1} \text{ cm}^{-1}$. The absorption of these low-energy bands mainly stemmed from $\pi - \pi^*$ charge-transfer transitions. The absorbance spectra of the dyes in air adsorbed to a 5 µm thin mesoporous TiO₂ film are plotted as dotted lines in Figure 3.10a. The absorbance of the blank TiO₂ film was subtracted from the measurement. The absorbance maximum was blue-shifted for all three dyes (**C203** 454 nm, **C204** 463 nm, **C205** 499 nm), which can be attributed to the coupling of the dye with the semiconductor. The emission peak was centered at 718 nm for **C203**, 688 nm for **C204**, and 697 nm for **C205**. The excitation transition energy (E_{0-0}) was estimated from the crossing point of the absorbance and emission spectra to be 2.04 eV, 2.08 eV, and 2.00 eV, respectively. Clearly, the high degree of π -conjugation in the fused dithienothiophene unit (**C203**) causes a stronger absorption than in **C204** with one EDOT unit. Extension of the conjugation length from one to two EDOT units, however, strongly red-shifts the response when adsorbed to the TiO₂ film by 45 nm.

The redox potentials of the sensitizers were measured by square-wave voltammetry with a Pt ultramicroelectrode in dimethylformamide (DMF) solution and 0.1 M tetra-*n*-butylammonium hexafluorophosphate as supporting electrolyte in a nitrogen-filled glovebox (Figure 3.10b). The measured LUMO of **C203** (-0.76 V vs. NHE), **C204** and **C205**

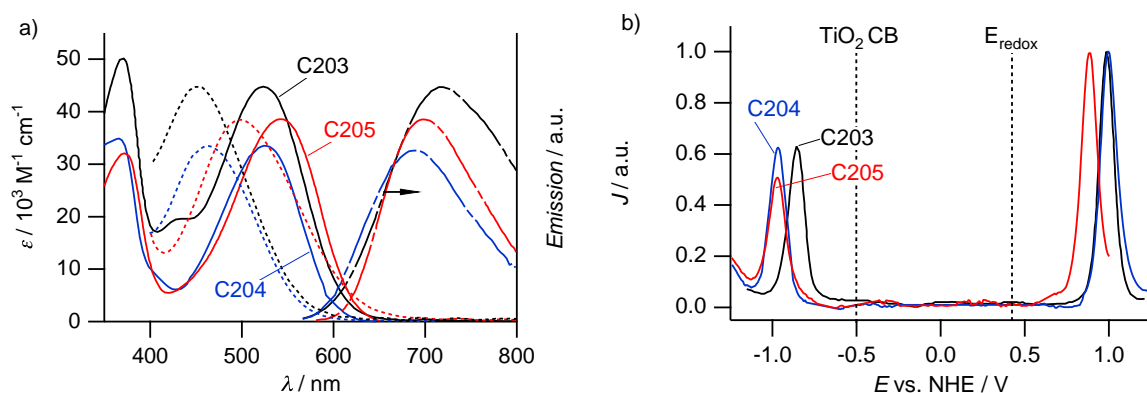


Figure 3.10: a) Molar extinction coefficient (ϵ) of the dyes **C203**, **C204**, and **C205** in chloroform (solid lines). The absorbance spectra of the dye adsorbed to a $5 \mu\text{m}$ thin mesoporous TiO_2 film (dashed lines) in air are blue-shifted compared to the spectra in solution. The absorbance of the blank TiO_2 film was subtracted from the measurement. The maxima of the absorbance spectra on the film and of the emission spectra (solid lines, right scale) are normalized to the respective peak values in solution. b) Square-wave voltammograms of **C203**, **C204**, and **C205** in DMF using a Pt ultramicroelectrode. 0.1 M tetra-*n*-butylammonium hexafluorophosphate was used as supporting electrolyte. The approximate potential level of the TiO_2 conduction band and the redox mediator is indicated with dashed lines.

(-0.87 V) is more negative than the conduction band edge of TiO_2 ($\sim -0.5 \text{ V}$), ensuring ample thermodynamic driving force for photoinduced electron injection from the excited dye state into the conduction band. The HOMO, given by the oxidation potential, was located at 0.99 V vs. NHE for **C203**, 1.00 V for **C204**, and 0.89 V for **C205**. These potential values are all more positive than the redox potential of the iodide/triiodide couple ($\sim 0.4 \text{ V}$ vs. NHE), providing sufficient driving force for the reduction of dye cations by the redox mediator after charge injection. Notably, the second EDOT unit in **C205** raises the HOMO by 110 mV , whereas the LUMO remains unchanged.

The electronic distribution of frontier orbitals was assessed with the ZINOD/S method in the Gaussian 03W program suite. The low energy absorption mainly stems from HOMO to LUMO and HOMO-1 to LUMO transitions. The HOMO of all dyes is located primarily on the substituted triphenylamine moiety, and the LUMO is delocalized over the thienothiophene or EDOT units and the cyanoacrylic acid group (see the Supporting Information of [20] and [21]).

Photovoltaic performance and stability. The incident photon-to-current conversion efficiency (IPCE) of a device with dye **C203**, **C204**, or **C205** and an acetonitrile-based electrolyte is shown in Figure 3.11a. For **C203**, the IPCE exceeded 80 % in the spectral region of 410–590 nm and reached a maximum of 93 % at 530 nm. For **C204** and **C205**,

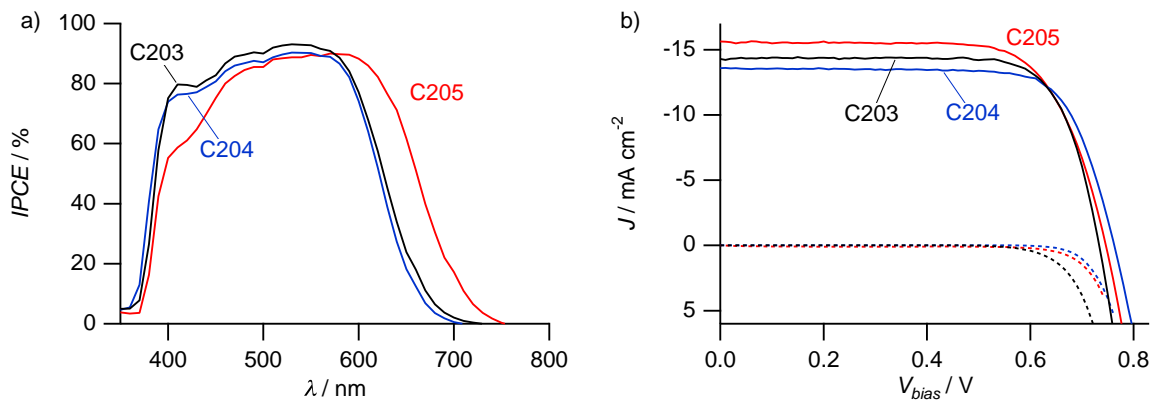


Figure 3.11: IPCE (a) and photocurrent-voltage curves (b) under simulated full sunlight (AM 1.5G, 100 mW cm⁻²) and in the dark of devices with a 7+5 TiO₂ film, dye **C203**, **C204**, or **C205**, and an acetonitrile-based electrolyte (Z960).

the IPCE showed a broad plateau in the visible, reaching up to 90 %. The response of the device with **C205** was red-shifted in the near-infrared region by about 40 nm in accordance with the absorbance measurements on TiO₂ in Figure 3.10a. Considering the total reflection losses of the device, the estimated APCE is close to unity in all three cases.

Under full sunlight illumination, conversion efficiencies of up to 8.0 % (**C203**), 7.9 % (**C204**), 8.3 % (**C204**) were obtained with a volatile electrolyte (Figure 3.11b and Table 3.2). The high efficiency with **C205** is largely due to the enhanced near-IR response and the higher photocurrent. With ionic liquid, values of 7.0–7.6 % were achieved. At the time of publication, the efficiency of 7.6 % with dye **C205** set a new record for solvent-free DSCs using organic sensitizers. The similar photocurrents measured with volatile electrolyte and ionic liquid for **C203** and **C204** are encouraging; if we assume a similar dye loading and charge injection for both devices, this finding indicates that the charge recombination rate at short-circuit is not strongly affected by the higher I₃⁻ concentration in the ionic liquid.

Devices with ionic liquid and **C203**, **C204**, or **C205** dye showed excellent stability under accelerated aging tests under full sunlight at 60 °C. After 1000 h, the devices retained 90–92 % of their initial efficiency (Figure 3.12). In all three cases, the photocurrent remained quasi constant. The drop in efficiency was mainly due to a photovoltage loss of ∼ 50 mV. The stable photocurrent proves the photochemical long-term stability of the dyes. The loss in photovoltage might be due to desorption of certain coadsorbants, like cheno, which results in more exposed TiO₂ surface for interfacial charge recombination.

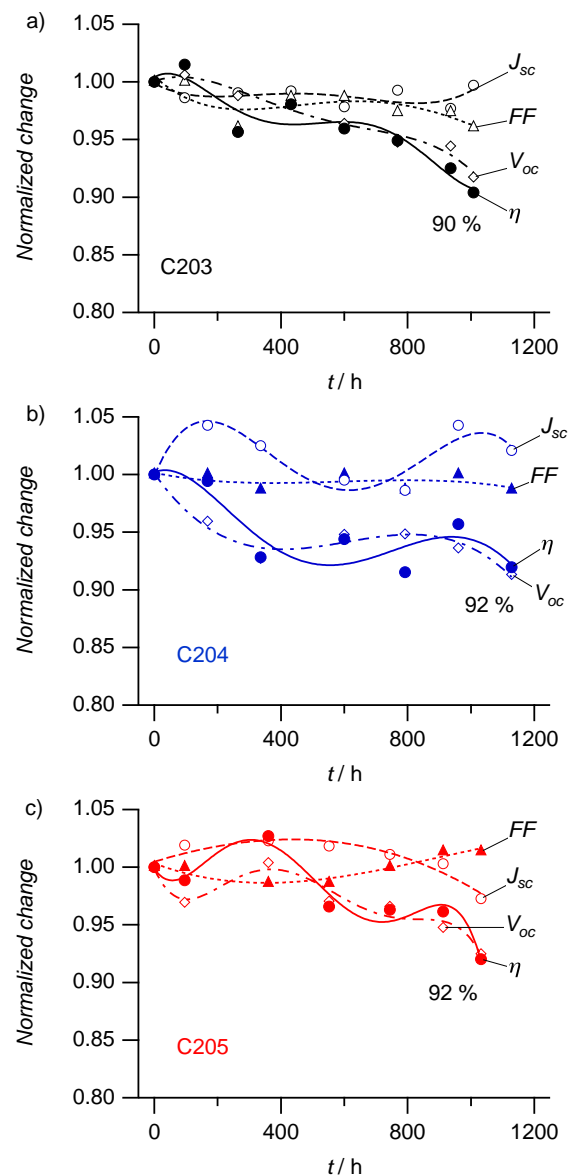


Figure 3.12: Temporal evolution of photovoltaic parameters of a device with dye **C203** (a), **C204** (b) or **C205** (b) and ionic liquid (Z952) during a 1000 h accelerated stability test (full sunlight, 60 °C).

Table 3.2: Photovoltaic parameters of devices with a 7+5 TiO₂ film sensitized with the dye **C203**, **C204**, or **C205**. The redox mediator was a volatile electrolyte (Z960) or an ionic liquid (Z952). Devices were measured under simulated AM 1.5G illumination (100 mW cm⁻²).

Dye	Redox	V_{oc} / mV	J_{sc} / mA cm ⁻²	FF	η / %
C203	volatile	734	-14.3	0.76	8.0
	ionic liquid	676	-14.1	0.74	7.0
C204	volatile	762	-13.8	0.75	7.9
	ionic liquid	708	-13.6	0.76	7.3
C205	volatile	746	-15.7	0.71	8.3
	ionic liquid	696	-14.8	0.73	7.6

Charge recombination. We measured the small-perturbation photovoltage decay transients under open-circuit conditions of devices with the volatile electrolyte. The recombination rates between electrons in the TiO₂ and I₃⁻ ions in the electrolyte were studied at various white light bias intensities and charge densities. The recombination rates (k_e) are plotted in Figure 3.13 versus the open-circuit potential (V_{oc}) in the device induced by the white light bias. The recombination rate increases exponentially with increasing V_{oc} , i.e. charge density in the TiO₂ film, as expected [32]. k_e is highest for the device with **C203**, and about 2.3 times lower for the device with **C205**. We note that k_e of the device with **C205** is similar to measured rates at comparable V_{oc} for “champion cells”

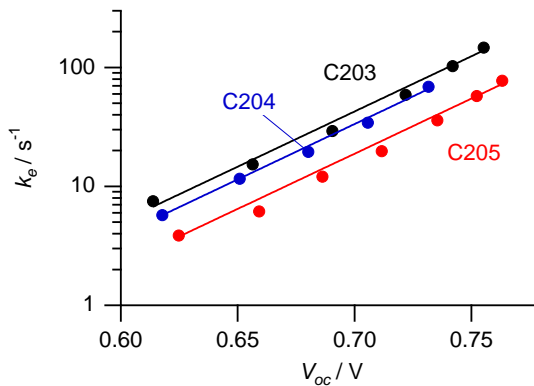


Figure 3.13: Comparison of the interfacial recombination rate (k_e) of electrons in the TiO₂ with I₃⁻ in the electrolyte, as a function of bias light induced photovoltage V_{oc} . Devices contain a 7+5 TiO₂ film, dye **C203**, **C204**, or **C205**, and a volatile electrolyte (Z960). Recombination is highest for the dye with the fused dithienothiophene unit (**C203**) and decreases to about half the rate for the dye with two EDOT units (**C205**).

with ruthenium complex dyes [1]. The higher recombination rate with **C203** might be due to an interaction of the fused thiophene unit with I_3^- or I_2 [33], which could enhance the local concentration of I_3^- ions close to the TiO_2 interface. This interaction seems to be less pronounced with the EDOT units. In addition, the longer chain length of the biEDOT unit (**C205**) seems to additionally block the TiO_2 surface from I_3^- ions. We also note, that k_e of **C203** at similar V_{oc} is about seven times lower than k_e of the linear diphenylamine dye **LIN** possessing three thiophene units (see Section 3.3). This suggests that the bulky difluorenylaminophenyl donor blocks I_3^- ions from the TiO_2 surface more successfully than the diphenylamine donor.

Preliminary conclusions. The studied difluorenylaminophenyl donor systems showed promising photovoltaic performance. In particular, at the time of publication, a new efficiency record of 7.6 % for solvent-free DSCs with organic sensitizers could be set with the system comprising two bridging EDOT units (**C205**). This can be mainly attributed to the enhanced near-IR response of the dye. All three dye systems showed excellent stability in devices with ionic liquid during long-term aging; the dyes were completely stable and did neither desorb nor degrade. Only the photovoltage dropped slightly, which might be due to a desorption of coadsorbants. The bulky difluorenylaminophenyl donor systems seem to shield the TiO_2 surface more effectively against charge recombination with I_3^- ions than diphenylamine donor systems. Furthermore, the replacement of the fused dithienothiophene unit in **C203** with an EDOT (**C204**) or biEDOT unit (**C205**) successively reduces the charge recombination rate, which further supports the observation that thiophene-based bridging units promote interfacial charge recombination.

3.5 π -Extended tetrathiafulvalene donor systems

Tetrathiafulvalenes with extended π -conjugation (exTTF) are a well known class of electron donor systems [38, 39]. Several studies have investigated charge transfer events in exTTFs attached to fullerenes [40–42] and to single-walled carbon nanotubes [43]. The out-of-plane butterfly shape of the exTTF provides steric hindrance [39], preventing self-aggregation of the sensitizer, a significant parameter in the dye performance of DSCs.

A series of three new exTTF sensitizers coded **PAB-1**, **PAB-2**, and **PAB-3** (see Figure 3.2) was designed and synthesized to study their photovoltaic properties in DSCs. The sensitizers, which have in common the donor (exTTF) and acceptor/anchoring (cyanoacrylic acid) group, are differentiated by the extent of π -conjugation in the spacer.

In **PAB-3**, an electron rich 3,4-ethylenedioxythiophene (EDOT) unit is used to considerably enhance its molar extinction coefficient. EDOT spacers have been successful to red shift the spectral response and enhance the molar extinction coefficient of substituted triarylamine donor sensitizers (see **C204**, **C205**, Section 3.4) [9, 21].

Experimental. The synthesis of the dyes **PAB-1**, **PAB-2**, and **PAB-3** is described in detail in the publication [22]. Dyes were tested in photovoltaic devices using a single layer TiO₂ film with a 5 μm thick transparent layer of 20 nm sized particles. Films were immersed for 5 h in a solution of 0.3 mM dye and 10 mM chenodeoxycholic acid in a mixture of ethanol and dimethyl sulfoxide (volume ratio 9/1).

3.5.1 Results and discussion

Electronic absorption and redox behavior. The absorption spectra in Figure 3.14a in dimethylsulfoxide had a maximum in the visible region for **PAB-1** at 399 nm ($\epsilon = 14.1 \times 10^3 \text{ M}^{-1} \text{ cm}^{-1}$), for **PAB-2** at 411 nm ($\epsilon = 25.1 \times 10^3 \text{ M}^{-1} \text{ cm}^{-1}$), and for **PAB-3** at 411 nm ($\epsilon = 36.0 \times 10^3 \text{ M}^{-1} \text{ cm}^{-1}$). The maxima were attributed to $\pi - \pi^*$ charge-transfer transitions. The gradual increase in ϵ and the slightly red-shifted absorbance peaks are due to the extended π -conjugation in the spacer. For comparison, the absorbance spectra of the dyes adsorbed to a 5 μm thin mesoporous TiO₂ film is plotted. The absorbance of the blank TiO₂ film was subtracted from the measurement. The absorbance maxima were normalized to the respective peak values in solution. In sensitized films we observed a small red-shift of the peak for **PAB-1** (414 nm) and **PAB-2** (416 nm) and a blue-shift for **PAB-3** (404 nm), which is attributed to the coupling of the carboxylate moiety with the semiconductor. Notably, blue-shifts have been previously observed with organic sensitizers containing an EDOT spacer [21]. The concentration of dye molecules adsorbed on the TiO₂ film was estimated by desorbing sensitized films with tetrabutylammonium hydroxide in N,N-dimethylformamide solution. A similar dye loading was obtained for **PAB-1** and **PAB-2** ($c = 0.13 \text{ M}$), and a slightly better packing behavior on the TiO₂ surface was seen for **PAB-3** ($c = 0.16 \text{ M}$).

The electrochemical oxidation of the exTTF chromophore was previously reported as an overall two-electron process [44–46] occurring with potential inversion, i.e. the second electron is removed more easily than the first. The extent of potential inversion is estimated to be about 0.16 V from simulations of cyclic voltammograms [47]. Formation of the short-lived radical cation and its disproportionation into the stable dication has been studied with radiolytic oxidation [48] and flash photolysis techniques [48, 49]. The electrochemical properties of the sensitizers were assessed with differential pulse voltamme-

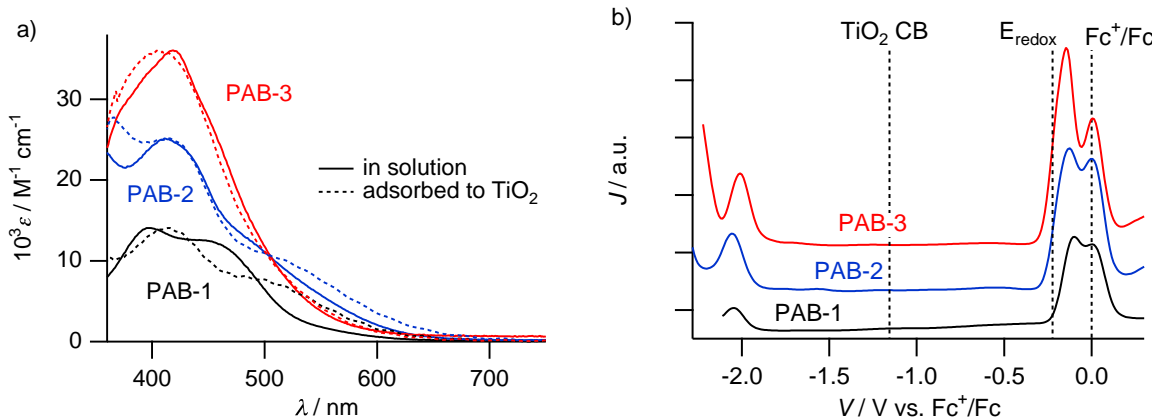


Figure 3.14: a) Molar extinction coefficient (ϵ) of **PAB-1**, **PAB-2**, and **PAB-3** dye in dimethylsulfoxide (solid lines). The absorbance spectra of the dye adsorbed to a $5 \mu\text{m}$ thin mesoporous TiO_2 film (dashed lines) in air are normalized to the respective peak values. The absorbance of the blank TiO_2 film was subtracted from the measurement. b) Differential pulse voltammograms of **PAB-1**, **PAB-2**, and **PAB-3** with ferrocene in DMF using 0.1 M TBAPF₆ as a supporting electrolyte. Working electrode: glassy carbon disk, 0.07 cm^2 . The approximate potential level of the TiO_2 conduction band and the redox mediator is indicated with dashed lines.

try in dimethylformamide (DMF) solution using tetrabutylammonium hexafluorophosphate (TBAPF₆) as a supporting electrolyte and referenced to the ferrocinium/ferrocene (Fc^+/Fc) couple (Figure 3.14b). The two-electron oxidation potential (E_{ox}) of the compounds, indicating the HOMO, was -0.11 V vs. Fc^+/Fc for **PAB-1**, -0.12 V for **PAB-2**, and -0.14 V for **PAB-3**. Interestingly, E_{ox} is up to 300 mV more negative than E_{ox} of a standard Ru-complex sensitizer ($+0.16 \text{ V}$ vs. Fc^+/Fc) [50]. The one-electron oxidation potential (**PAB-1** \rightarrow **PAB-1**^{•+}) is estimated to be 80 mV more positive due to potential inversion [47]. Consequently, the driving force for regeneration of the oxidized species by the I^-/I_3^- redox mediator (-0.21 V vs. Fc^+/Fc in ionic liquid) [30] is as low as 150 mV. The reduction potential (E_{red}) of the dyes, indicating their LUMO, was considerably more negative than the TiO_2 conduction band, providing ample driving force for electron transfer (-2.05 V vs. Fc^+/Fc for **PAB-1**, -2.06 V for **PAB-2**, and -2.01 V for **PAB-3**).

Density functional theory calculations were performed with the Spartan software package using the B3LYP hybrid functional and the 6-31*G basis set to investigate the electronic properties of the sensitizers. The orbital energy levels in vacuum, minimum energy conformations, and electron density plots are shown in Figure 3.15. The well-known structure of the neutral state is saddle-shaped [46, 51]. The HOMO of **PAB-1** and **PAB-2** are at a similar energy level, whereas the HOMO of **PAB-3** is raised due to

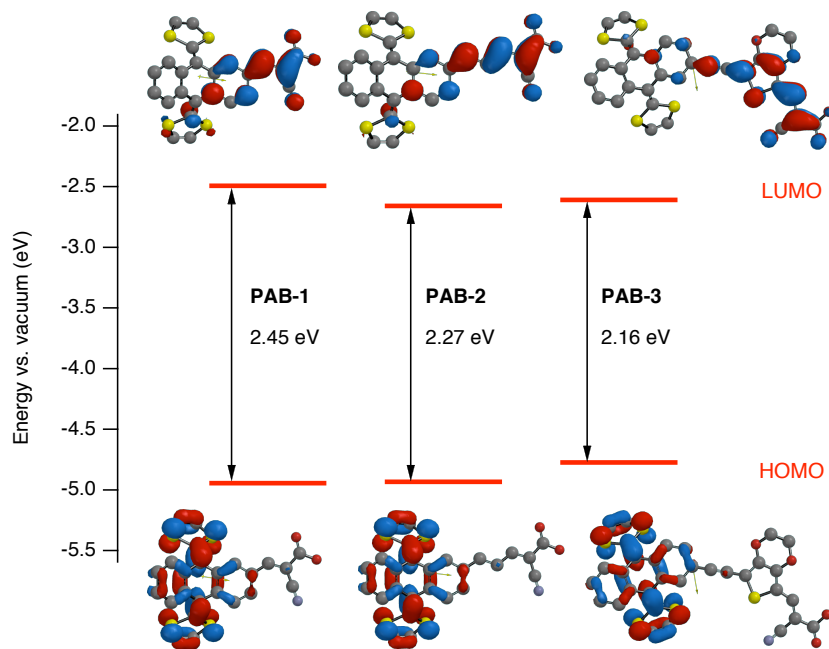


Figure 3.15: Calculated molecular orbital levels and electron density contours of the HOMO and LUMO of sensitizers **PAB-1**, **PAB-2**, and **PAB-3**. Conformations are minimum energy B3LYP/6-31*G-optimized.

the high electron density in the EDOT spacer. The LUMO of **PAB-2** and **PAB-3** are lower than the LUMO of **PAB-1** due to extended π -conjugation in the spacer. In all three cases, the HOMO is delocalized over the anthracene and dithiophene units, and the LUMO is delocalized over the cyanoacrylic acid group, facilitating electron transfer from the excited state to the TiO_2 conduction band via the carboxylate anchoring group.

The ATR-FTIR spectra of the sensitizers in powder form and anchored on a mesoporous TiO_2 film are shown in Figure 3.16. The powder spectra show a distinct band at 1700 cm^{-1} for the $\text{C}=\text{O}$ stretch in the carboxyl group. This band was not observed in the spectra of the sensitized films. Instead, the spectra clearly show bands at 1630 cm^{-1} and 1385 cm^{-1} for the asymmetric and symmetric stretching modes of the carboxylate groups, indicating that the carboxylic acid is deprotonated and involved in the adsorption of the dye on the TiO_2 surface.

Photovoltaic performance and stability. The IPCE in Figure 3.17a shows peak values of 48 % at 510 nm for **PAB-1**, 54 % at 520 nm for **PAB-2**, and 72 % at 460 nm for **PAB-3**, in accordance with the shape and magnitude of the respective extinction coefficients. We estimate the fraction of absorbed light by the dye in the TiO_2 film using equation (3.1) and accounting for reflection losses of about 10 %. At 430 nm we find a dye absorptance

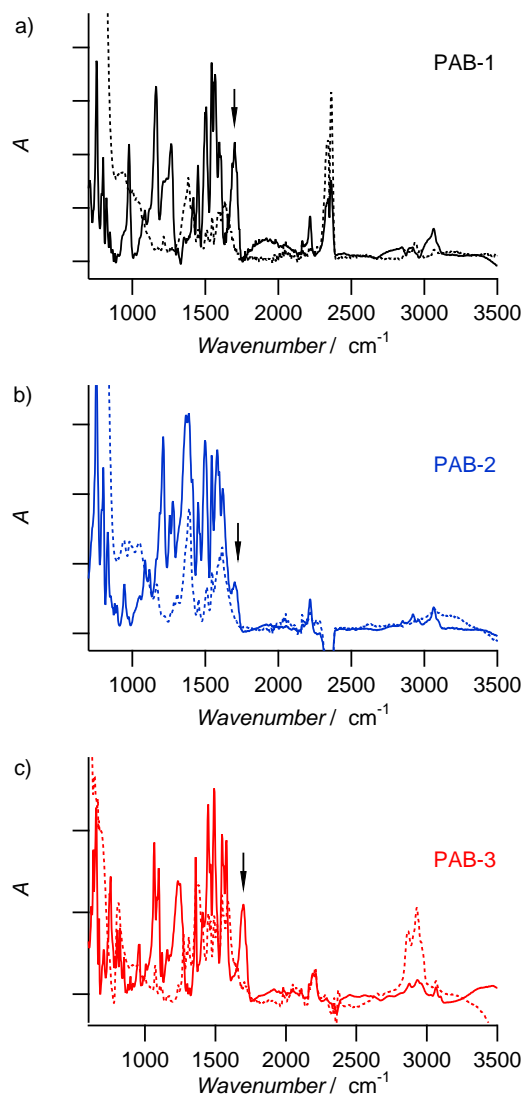


Figure 3.16: FTIR spectra of sensitizers **PAB-1** (a), **PAB-2** (b) and **PAB-3** (c) in powder form (solid lines) and attached to a sensitized mesoporous TiO_2 film (dashed lines). The spectrum of a TiO_2 reference film heated at 500 °C to remove surface-adsorbed water was subtracted for clarity of presentation. The arrow indicates the C=O stretch in the carboxyl group at 1700 cm^{-1} , which is only visible in powder form. The aromatic ring modes peak at 3065 cm^{-1} (C-H stretch), 1590–1599 cm^{-1} and 1509 cm^{-1} (ring stretches). The asymmetric and symmetric stretch vibrations of the $-\text{CH}_2-$ linker peak at 2932 cm^{-1} and 2864 cm^{-1} .

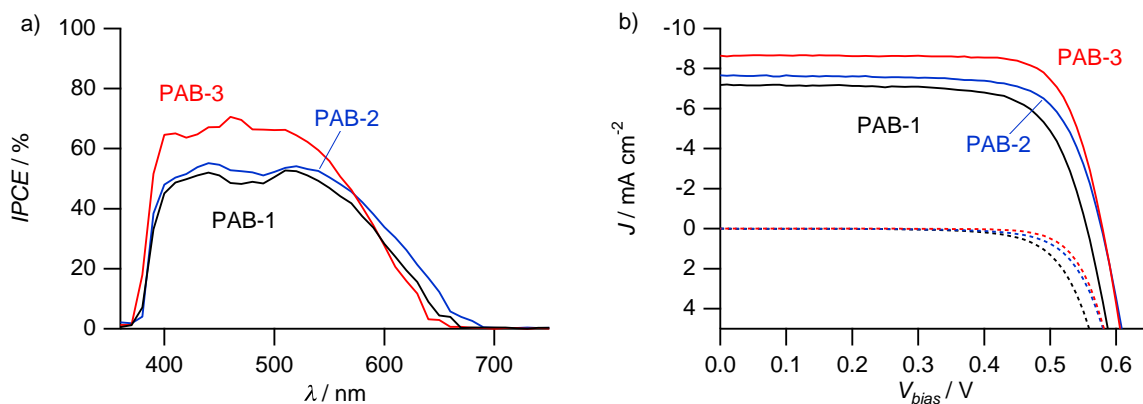


Figure 3.17: IPCE and photocurrent-voltage curves of devices with a 5 μm TiO_2 film, dye **PAB-1**, **PAB-2**, or **PAB-3**, and volatile electrolyte (Z960).

of about 76 % (**PAB-1**) to 90 % (**PAB-3**). The APCE of these devices is clearly lower than unity and estimated to be 63 % (**PAB-1**) to 80 % (**PAB-3**) in the range of maximum absorption. An APCE smaller than unity can be due to a combination of insufficient injection from the excited dye state and recombination of photojected electrons in the TiO_2 with the radical dye cations, dications, or I_3^- ions in the electrolyte. Supplementary studies, namely photovoltage decay transients and laser transient absorbance measurements, show that the losses are mainly due to recombination of electrons with I_3^- ions (see page 67 ff.).

Under full sunlight illumination, conversion efficiencies of up to 3.8 % were obtained with **PAB-3** and a volatile electrolyte (Figure 3.17b and Table 3.3). The increase in efficiency from 2.9 % (**PAB-1**) to 3.8 % (**PAB-3**) is largely due to an increase in photocurrent, in agreement with the measured IPCEs, and an associated small increase in photovoltage. Overall, the measured photovoltage of about 580 mV is relatively low.

Table 3.3: Photovoltaic parameters of devices with a 5 μm mesoporous transparent TiO_2 film sensitized with the dye **PAB-1**, **PAB-2**, or **PAB-3**. The redox mediator was a volatile electrolyte (Z960). Devices were measured under simulated AM 1.5G illumination (100 mW cm⁻²).

Dye	V_{oc} / mV	J_{sc} / mA cm ⁻²	FF	η / %
PAB-1	555	-7.2	0.72	2.9
PAB-2	578	-7.7	0.73	3.2
PAB-3	579	-8.6	0.76	3.8

With state-of-the-art DSCs one can expect a V_{oc} of over 750 mV at comparable current densities [1]. This is a further indication for substantial charge recombination losses.

Devices with the most promising **PAB-3** dye and ionic liquid showed excellent stability under accelerated aging tests under full sunlight at 60 °C. Parameters were normalized to the stabilized values after 5 days of light soaking ($\eta = 2.7\%$, $J_{sc} = -6.8 \text{ mA cm}^{-2}$, $V_{oc} = 534 \text{ mV}$, $FF = 0.74$), which allowed for optimal reorganization of the dye molecules on the TiO_2 surface. After 1000 h, the device retained 99 % of its initial efficiency (Figure 3.18a).

Charge recombination. Electron recombination rates (k_e) extracted from photovoltage transients at open-circuit conditions under white bias light are plotted against V_{oc} in Figure 3.18b. For a given V_{oc} , i.e. charge density in the TiO_2 film at open-circuit conditions, the recombination rate is lowest for a device using **PAB-3**. This is probably due to the better packing of the dye on the TiO_2 surface. Also, the EDOT unit in **PAB-3** seems to shield the TiO_2 surface more efficiently against I_3^- ions, which was also observed with the difluorenlyaminophenyl dyes **C204** and **C205** (Section 3.4). However, k_e of the device with **PAB-3** is still two orders of magnitude higher than the rate of a state-of-the-art device with a ruthenium-complex dye [1]. Increased recombination, and consequently low V_{oc} , has been observed for many classes of organic sensitizers and might be catalyzed by the formation of an iodine/dye complex [33, 52].

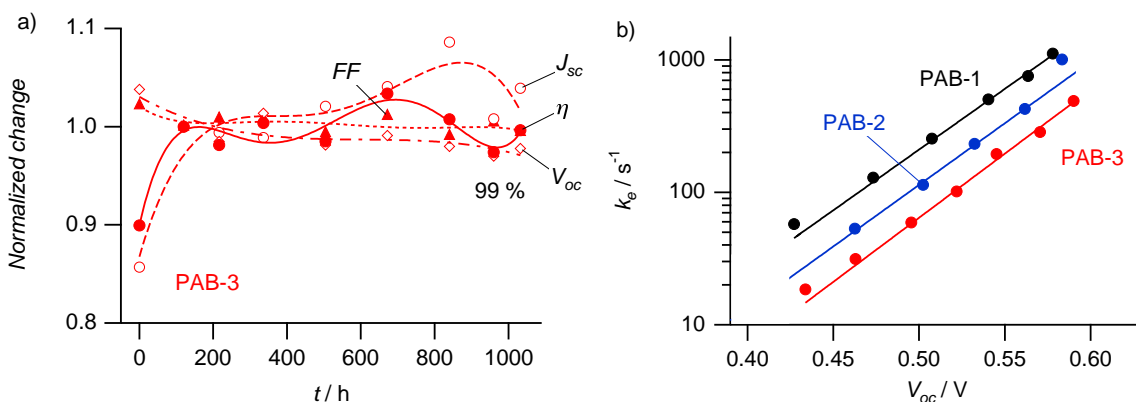
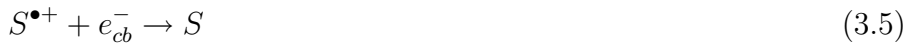
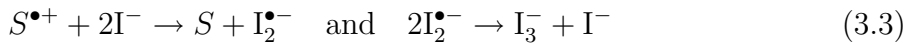


Figure 3.18: a) Temporal evolution of photovoltaic parameters of a device with dye **PAB-3** and ionic liquid (Z952) during a 1000 h accelerated stability test at full sunlight and 60 °C. Parameters are normalized to stabilized values after 5 days of light soaking. Lines are guides to the eye. b) Comparison of the interfacial recombination rate (k_e) of electrons in the TiO_2 with I_3^- in the electrolyte, as a function of bias light induced photovoltage, of a device with a 5 μm TiO_2 film, dye **PAB-1**, **PAB-2**, or **PAB-3**, and a volatile electrolyte (Z960). Lines are exponential fits to experimental data.

Nanosecond laser transient absorbance measurements. We used time-resolved spectroscopy on sensitized TiO_2 films to probe the formation of the radical cation (reaction (3.2)), its interception by iodide (reaction (3.3)), and a possible disproportionation of the radical cation into the dication (reaction (3.4)). The oxidation of the nonfunctionalized exTTF chromophore is well known; the short-lived radical cation ($\sim 500 \mu\text{s}$) shows a fingerprint at about 650 nm and rapidly disproportionates into the stable dication [48, 49].



The transient absorption spectrum of a **PAB-1** sensitized film in Figure 3.19a (no redox mediator) clearly showed the signature of the radical cation at 650 nm. The time-dependent signature at 650 nm of films sensitized with **PAB-1**, **PAB-2**, or **PAB-3** is depicted in Figure 3.19b. In the absence of a redox mediator (only acetonitrile, ACN), the decay could be fitted with a mono-exponential function with a time constant of $\tau = 2.3 \text{ ms}$ ($k_b = 435 \text{ s}^{-1}$) for **PAB-1**, $\tau = 256 \mu\text{s}$ for **PAB-2**, and $\tau = 494 \mu\text{s}$ for **PAB-3**, reflecting the lifetime of the radical dye cation when reduced only by electrons from the TiO_2 conduction band (reaction (3.5)). In the presence of a redox mediator (ACN-based redox electrolyte), the decay was accelerated by one to two orders of magnitude ($\tau = 7.4 \mu\text{s}$, $k_r = 1.35 \times 10^5 \text{ s}^{-1}$ for **PAB-1**, $\tau = 18 \mu\text{s}$ for **PAB-2**, $\tau = 25 \mu\text{s}$ for **PAB-3**) due to rapid interception of the cation by iodide (equation (3.3)). These timescales are similar to values reported for Ru-based sensitizers [53]. The dye regeneration yield by iodide, given by the $k_r/(k_b + k_r)$ ratio, exceeded 99 % for **PAB-1** and 93 % for **PAB-3**. This finding is remarkable, as it shows, that a very small driving force of about 150 mV between the redox potential of the electrolyte and the oxidation potential of the sensitizer is sufficient for efficient regeneration of the cation. The transient signature of **PAB-1** at 550 nm in ACN only (Figure 3.19c) showed an initial bleaching of the ground state after charge injection. Recovery of the dye absorption took place with a half reaction time of $\tau = 55 \mu\text{s}$. The positive signal observed $> 50 \mu\text{s}$ after the laser pulse excitation is attributed to the dication absorption. The kinetic process is thus likely to be due to the dye cation disproportionation (reaction (3.4)). In the presence of the electrolyte, this positive absorbance disappeared completely, and only a fast recovery of the ground state was observed with $\tau = 4.6 \mu\text{s}$ (the rapid component of a double-exponential fit),

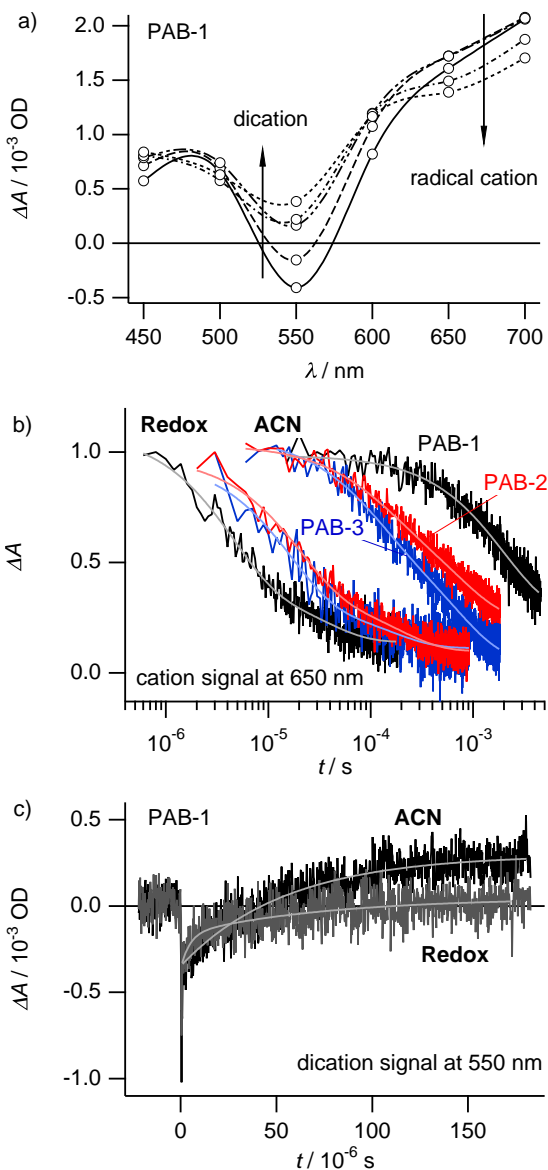


Figure 3.19: a) Temporal evolution of the transient absorption spectrum of a **PAB-1** sensitized TiO_2 film in acetonitrile (ACN), showing the decay of the radical cation signature at 650 nm and the formation of the dication signal at 550 nm (bold line 10 μs and dotted line 180 μs after excitation). b) Normalized transient absorption decay at 650 nm of the radical cation of **PAB-1** (black), **PAB-2** (blue), or **PAB-3** (red) in ACN and in the presence of an iodide/tri-iodide redox electrolyte. Continuous lines drawn on top of experimental data are single exponential fits with the following time constants: In ACN: $\tau = 2.3 \text{ ms}$ (**PAB-1**), $\tau = 256 \mu\text{s}$ (**PAB-2**), $\tau = 494 \mu\text{s}$ (**PAB-3**). In electrolyte: $\tau = 7 \mu\text{s}$ (**PAB-1**), $\tau = 18 \mu\text{s}$ (**PAB-2**), $\tau = 25 \mu\text{s}$ (**PAB-3**)). c) Transient absorption at 550 nm of the dication of **PAB-1** in ACN ($\tau = 55 \mu\text{s}$) and in electrolyte ($\tau = 5 \mu\text{s}$, rapid part of a double-exponential fit). Absorbance changes were measured using 505 nm laser excitation (7 ns FWHM pulse duration, 30 $\mu\text{J cm}^{-2}$ pulse fluence).

corresponding to the kinetics of the reduction of dye cations by iodide observed in the red spectral region. Consequently, little dication species should be formed in a working cell under full sunlight illumination.

Preliminary conclusions. We have successfully demonstrated photovoltaic energy conversion in stable π -extended tetrathiafulvalene-sensitized solar cells. Compared to standard ruthenium-complex sensitizers, these new dyes show an up to 300 mV more negative oxidation potential, which could impair efficient reduction by the redox mediator. With time-resolved spectroscopy, however, we could prove for the first time that efficient regeneration of sensitizers with as little as a 150 mV driving force between the oxidation potential of the sensitizer and the redox potential of the mediator is possible. Since large driving forces imply a loss in photovoltage, this finding provides a valuable proof-of-principle for the use and design of efficient sensitizers with a low regeneration driving force for high efficiency dye-sensitized solar cells. A drawback of this particular system, however, is the high charge recombination rate with I_3^- ions, which might be due to a strong interaction between I_3^- or I_2 and the ex-TTF donor.

3.6 Conclusions

Organic donor- π -acceptor dyes offer a very high degree of flexibility for the design of stable and efficient DSCs. We could show with three classes of donor systems — diphenylamine, difluorenylaminophenyl, and π -extended tetrathiafulvalene — how optical, electrochemical, and photovoltaic properties can be varied and optimized.

Overall, we have found the highest photovoltaic performance, both with volatile electrolyte and ionic liquid, with a dye containing a difluorenylaminophenyl donor and two EDOT bridging units (coded **C203**). This high efficiency could be attributed to an enhanced response in the near-IR and to a low recombination flux between electrons in the TiO_2 and I_3^- ions in the electrolyte, which is likely related to the TiO_2 surface shielding effect of the biEDOT unit. The bulky difluorenylaminophenyl donor seems to further assist this shielding effect.

Compared to other organic and ruthenium-based dyes, the π -extended tetrathiafulvalene dyes have a negatively shifted oxidation potential of up to 300 mV, which implies low driving forces of as little as 150 mV for regeneration of dye cations by the redox mediator. We could give a valuable proof-of-concept for efficient dye regeneration in DSCs with such a low driving force.

With some dyes, we have observed quite high recombination fluxes of electrons in the TiO₂ with I₃⁻ ions, which strongly reduced the absorbed photon-to-current conversion efficiency; the recombination rate increased with lower dye loading and exposed TiO₂ surface area, as observed with a bulky branched dye (coded **BRA**). Also, the rate increased with increasing thiophene linker length and was particularly strong with the π-extended tetrathiafulvalene dyes. Here, some interaction of I₃⁻ or I₂ with the moieties might be occurring, which enhances the local concentrations of the ions close to the TiO₂ surface and hence the recombination rate. It is encouraging to see, however, that with a suitable design the recombination rate of organic dyes can be suppressed to levels observed with high efficiency dyes, as was seen with the dye **C203**.

We could observe excellent device stability with all three donor classes. However, for the diphenylamine donor system, only the branched dye showed good stability, indicating that the linear system could not shield the TiO₂ surface sufficiently from species favoring desorption, like water. The bulky difluorenylaminophenyl donor moieties seem to be excellent shielding moieties against water and other additives. Interestingly, the π-extended tetrathiafulvalene dye is only stable with an EDOT linker.

For the future improvement of organic sensitizers, these design principles seem to be particularly useful:

- Bulky or hydrophobic donor moieties strongly reduce interfacial recombination between electrons in the TiO₂ and I₃⁻ in the electrolyte. This allows for good current collection and high photovoltages. Examples include difluorenylaminophenyl donors (**C203**) and dihexyloxy-substituted triphenylamine donors (see current organic “champion” dye [9] or [26]). These donors also inhibit desorption of the dye from the TiO₂ surface.
- Electron-rich linkers with strong π-conjugation enhance the near-IR spectral response of devices. Good candidates are EDOT units and (fused) thienothiophene, or a combination of both [9]. Other linkers that are suspected of forming intermediates with iodine or tri-iodide, like thiophene units, should be avoided.
- A careful and comprehensive optimization of the complete staining procedure — which can include the solvent, coadsorbants, dipping time, and even the rinsing procedure and the dipping temperature — can yield remarkable enhancements in efficiency [9]. It goes without saying that this step is tedious and laborious.

These principles should assist the very good progress made in the past years with organic dyes for stable and efficient DSCs.

Bibliography

- [1] F. Gao, Y. Wang, D. Shi, J. Zhang, M. K. Wang, X. Y. Jing, R. Humphry-Baker, P. Wang, S. M. Zakeeruddin, and M. Grätzel. Enhance the optical absorptivity of nanocrystalline TiO₂ film with high molar extinction coefficient ruthenium sensitizers for high performance dye-sensitized solar cells. *Journal of the American Chemical Society* **2008**, *130*, 10720–10728.
- [2] M. K. Nazeeruddin, F. De Angelis, S. Fantacci, A. Selloni, G. Viscardi, P. Liska, S. Ito, B. Takeru, and M. Grätzel. Combined Experimental and DFT-TDDFT Computational Study of Photoelectrochemical Cell Ruthenium Sensitizers. *Journal of the American Chemical Society* **2005**, *127*, 16835–16847.
- [3] Y. Chiba, A. Islam, Y. Watanabe, R. Komiya, N. Koide, and L. Han. Dye-sensitized solar cells with conversion efficiency of 11.1%. *Japanese Journal of Applied Physics* **2006**, *45*, L638–L640.
- [4] Y. Cao, Y. Bai, Q. Yu, Y. Cheng, S. Liu, D. Shi, F. Gao, and P. Wang. Dye-sensitized solar cells with a high absorptivity ruthenium sensitizer featuring a 2-(hexylthio)thiophene conjugated bipyridine. *The Journal of Physical Chemistry C* **2009**, *113*, 6290–6297.
- [5] C.-Y. Chen, M. Wang, J.-Y. Li, N. Pootrakulchote, L. Alibabaei, C.-h. Ngoc-le, J.-D. Decoppet, J.-H. Tsai, C. Grätzel, C.-G. Wu, S. M. Zakeeruddin, and M. Grätzel. Highly efficient light-harvesting ruthenium sensitizer for thin-film dye-sensitized solar cells. *ACS Nano* **2009**, *3*, 3103–3109.
- [6] H. Zollinger. *Color Chemistry: Syntheses, Properties, and Applications of Organic Dyes and Pigments*. Verlag Helvetica Chimica Acta and Wiley-VCH, Zürich and Weinheim, 3rd edition **2003**.
- [7] A. Mishra, M. K. R. Fischer, and P. Bäuerle. Metal-Free Organic Dyes for Dye-Sensitized Solar Cells: From Structure: Property Relationships to Design Rules. *Angewandte Chemie International Edition* **2009**, *48*, 2474–2499.
- [8] J. Roncali. Synthetic principles for bandgap control in linear π-conjugated systems. *Chemical Reviews* **1997**, *97*, 173–206.
- [9] G. Zhang, H. Bala, Y. Cheng, D. Shi, X. Lv, Q. Yu, and P. Wang. High efficiency and stable dye-sensitized solar cells with an organic chromophore featuring a binary π-conjugated spacer. *Chemical Communications* **2009**, 2198–2200.
- [10] S. Ito, H. Miura, S. Uchida, M. Takata, K. Sumioka, P. Liska, P. Comte, P. Pechy, and M. Grätzel. High-conversion-efficiency organic dye-sensitized solar cells with a novel indoline dye. *Chemical Communications* **2008**, 5194–5196.
- [11] Y. S. Chen, Z. H. Zeng, C. Li, W. B. Wang, X. S. Wang, and B. W. Zhang. Highly efficient co-sensitization of nanocrystalline TiO₂ electrodes with plural organic dyes. *New Journal of Chemistry* **2005**, *29*, 773–776.

- [12] J. H. Yum, S. R. Jang, P. Walter, T. Geiger, F. Nüesch, S. Kim, J. Ko, M. Grätzel, and M. K. Nazeeruddin. Efficient co-sensitization of nanocrystalline TiO₂ films by organic sensitizers. *Chemical Communications* **2007**, *1*, 4680–4682.
- [13] J. J. Cid, J. H. Yum, S. R. Jang, M. K. Nazeeruddin, E. Martínez-Ferrero, E. Palomares, J. Ko, M. Grätzel, and T. Torres. Molecular cosensitization for efficient panchromatic dye-sensitized solar cells. *Angewandte Chemie International Edition* **2007**, *46*, 8358–8362.
- [14] B. E. Hardin, E. T. Hoke, P. B. Armstrong, J.-H. Yum, P. Comte, T. Torres, J. M. J. Fréchet, M. K. Nazeeruddin, M. Grätzel, and M. D. McGehee. Increased light harvesting in dye-sensitized solar cells with energy relay dyes. *Nature Photonics* **2009**, *3*, 406–411.
- [15] J. Yum, B. E. Hardin, S.-J. Moon, E. Baranoff, F. Nüesch, M. D. McGehee, M. Grätzel, and M. K. Nazeeruddin. Panchromatic response in solid-state dye-sensitized solar cells containing phosphorescent energy relay dyes. *Angewandte Chemie International Edition* **2009**, *48*, 9277–9280.
- [16] L. Michaelis and S. Granick. Metachromasy of Basic Dyestuffs. *Journal of the American Chemical Society* **1945**, *67*, 1212–1219.
- [17] W. West and S. Pearce. The dimeric state of cyanine dyes. *The Journal of Physical Chemistry* **1965**, *69*, 1894–1903.
- [18] R. Katoh, A. Furube, A. V. Barzykin, H. Arakawa, and M. Tachiya. Kinetics and mechanism of electron injection and charge recombination in dye-sensitized nanocrystalline semiconductors. *Coordination Chemistry Reviews* **2004**, *248*, 1195–1213.
- [19] M. K. R. Fischer, S. Wenger, M. Wang, A. Mishra, S. M. Zakeeruddin, M. Grätzel, and P. Bäuerle. D-π-A sensitizers for dye-sensitized solar cells: Linear vs branched oligothiophenes. *Chemistry of Materials* **2010**, *22*, 1836–1845.
- [20] H. Qin, S. Wenger, M. Xu, F. Gao, X. Jing, P. Wang, S. M. Zakeeruddin, and M. Grätzel. An organic sensitizer with a fused dithienothiophene unit for efficient and stable dye-sensitized solar cells. *Journal of the American Chemical Society* **2008**, *130*, 9202–9203.
- [21] M. F. Xu, S. Wenger, H. Bala, D. Shi, R. Z. Li, Y. Z. Zhou, S. M. Zakeeruddin, M. Grätzel, and P. Wang. Tuning the energy level of organic sensitizers for high-performance dye-sensitized solar cells. *Journal of Physical Chemistry C* **2009**, *113*, 2966–2973.
- [22] S. Wenger, P.-A. Bouit, Q. Chen, J. Teuscher, D. D. Censo, R. Humphry-Baker, J.-E. Moser, J. L. Delgado, N. Martín, S. M. Zakeeruddin, and M. Grätzel. Efficient electron transfer and sensitizer regeneration in stable π-extended tetrathiafulvalene-sensitized solar cells. *Journal of the American Chemical Society* **2010**, *132*, 5164–5169.
- [23] Z. Ning and H. Tian. Triarylamine: A promising core unit for efficient photovoltaic materials. *Chemical Communications* **2009**, *1*, 5483–5495.

- [24] M. Thelakkat. Star-shaped, dendrimeric and polymeric triarylamines as photoconductors and hole transport materials for electro-optical applications. *Macromolecular Materials and Engineering* **2002**, *287*, 442–461.
- [25] K. R. Justin Thomas, Y.-C. Hsu, J. T. Lin, K.-M. Lee, K.-C. Ho, C.-H. Lai, Y.-M. Cheng, and P.-T. Chou. 2,3-Disubstituted Thiophene-Based Organic Dyes for Solar Cells. *Chemistry of Materials* **2008**, *20*, 1830–1840.
- [26] J. H. Yum, D. P. Hagberg, S. J. Moon, K. M. Karlsson, T. Marinado, L. C. Sun, A. Hagfeldt, M. K. Nazeeruddin, and M. Grätzel. A light-resistant organic sensitizer for solar-cell applications. *Angewandte Chemie International Edition* **2009**, *48*, 1576–1580.
- [27] D. P. Hagberg, J.-H. Yum, H. Lee, F. De Angelis, T. Marinado, K. M. Karlsson, R. Humphry-Baker, L. Sun, A. Hagfeldt, M. Grätzel, and M. K. Nazeeruddin. Molecular engineering of organic sensitizers for dye-sensitized solar cell applications. *Journal of the American Chemical Society* **2008**, *130*, 6259–6266.
- [28] G. Zhang, Y. Bai, R. Li, D. Shi, S. Wenger, S. M. Zakeeruddin, M. Grätzel, and P. Wang. Employ a bishtienothiophene linker to construct an organic chromophore for efficient and stable dye-sensitized solar cells. *Energy & Environmental Science* **2009**, *2*, 92–95.
- [29] D. Rohde, L. Dunsch, A. Tabet, H. Hartmann, and J. Fabian. Radical ions of α,α' -bis(diphenylamino)-capped oligothiophenes: A combined spectroelectrochemical and theoretical study. *The Journal of Physical Chemistry B* **2006**, *110*, 8223–8231.
- [30] R. Kawano and M. Watanabe. Equilibrium potentials and charge transport of an I^-/I_3^- redox couple in an ionic liquid. *Chemical Communications* **2003**, 330–331.
- [31] Y. Bai, Y. Cao, J. Zhang, M. Wang, R. Li, P. Wang, S. M. Zakeeruddin, and M. Grätzel. High-performance dye-sensitized solar cells based on solvent-free electrolytes produced from eutectic melts. *Nature Materials* **2008**, *7*, 626–630.
- [32] J. Bisquert and V. S. Vikhrenko. Interpretation of the time constants measured by kinetic techniques in nanostructured semiconductor electrodes and dye-sensitized solar cells. *Journal of Physical Chemistry B* **2004**, *108*, 2313–2322.
- [33] T. Marinado, K. Nonomura, J. Nissfolk, M. K. Karlsson, D. P. Hagberg, L. Sun, S. Mori, and A. Hagfeldt. How the nature of triphenylamine-polyene dyes in dye-sensitized solar cells affects the open-circuit voltage and electron lifetimes. *Langmuir* **2010**, *26*, 2592–2598.
- [34] D. P. Hagberg, T. Marinado, K. M. Karlsson, K. Nonomura, P. Qin, G. Boschloo, T. Brinck, A. Hagfeldt, and L. Sun. Tuning the HOMO and LUMO energy levels of organic chromophores for dye sensitized solar cells. *The Journal of Organic Chemistry* **2007**, *72*, 9550–9556.
- [35] S. Kim, J. K. Lee, S. O. Kang, J. Ko, J. H. Yum, S. Fantacci, F. De Angelis, D. Di Censo, M. K. Nazeeruddin, and M. Grätzel. Molecular engineering of organic sensitizers for solar cell applications. *Journal of the American Chemical Society* **2006**, *128*, 16701–16707.

- [36] H. Choi, C. Baik, S. O. Kang, J. Ko, M. S. Kang, M. K. Nazeeruddin, and M. Grätzel. Highly efficient and thermally stable organic sensitizers for solvent-free dye-sensitized solar cells. *Angewandte Chemie - International Edition* **2008**, *47*, 327–330.
- [37] M. Wang, M. Xu, D. Shi, R. Li, F. Gao, G. Zhang, Z. Yi, R. Humphry-Baker, P. Wang, S. Za-keeruddin, and M. Grätzel. High-performance liquid and solid dye-sensitized solar cells based on a novel metal-free organic sensitizer. *Advanced Materials* **2008**, *20*, 4460–4463.
- [38] J. L. Segura and N. Martín. New concepts in tetrathiafulvalene chemistry. *Angewandte Chemie International Edition* **2001**, *40*, 1372–1409.
- [39] N. Martín, L. Sánchez, M. Á. Herranz, B. Illescas, and D. M. Guldi. Electronic communication in tetrathiafulvalene (TTF)/C₆₀ systems: Toward molecular solar energy conversion materials? *Accounts of Chemical Research* **2007**, *40*, 1015–1024.
- [40] J. L. Segura, E. M. Priego, N. Martín, C. Luo, and D. M. Guldi. A new photoactive and highly soluble C₆₀TTF-C₆₀ dimer: Charge separation and recombination. *Organic Letters* **2000**, *2*, 4021–4024.
- [41] M. A. Herranz, N. Martín, J. Ramey, and D. M. Guldi. Thermally reversible C₆₀-based donor-acceptor ensembles. *Chemical Communications* **2002**, 2968–2969.
- [42] L. Sánchez, I. Pérez, N. Martín, and D. M. Guldi. Controlling short- and long-range electron transfer processes in molecular dyads and triads. *Chemistry - A European Journal* **2003**, *9*, 2457–2468.
- [43] M. A. Herranz, N. Martín, S. P. Campidelli, M. Prato, G. Brehm, and D. M. Guldi. Control over electron transfer in tetrathiafulvalene-modified single-walled carbon nanotubes. *Angewandte Chemie International Edition* **2006**, *45*, 4478–4482.
- [44] Y. Yamashita, Y. Kobayashi, and T. Miyashi. p-Quinodimethane Analogues of Tetrathiafulvalene. *Angewandte Chemie International Edition* **1989**, *28*, 1052–1053.
- [45] A. J. Moore and M. R. Bryce. Highly conjugated π-electron donors for organic metals: Synthesis and redox chemistry of new 1,3-dithiole and 1,3-selenathiole derivatives. *Journal of the Chemical Society, Perkin Transactions 1* **1991**, *1*, 157.
- [46] N. Martín, L. Sánchez, and C. Seoane. Synthesis, properties, and theoretical characterization of largely π-extended tetrathiafulvalene derivatives with quinonoid structures. *J. Org. Chem.* **1998**, *63*, 1268–1279.
- [47] M. C. Díaz, B. M. Illescas, N. Martín, I. F. Perepichka, M. R. Bryce, E. Levillain, R. Viruela, and E. Ortí. Electronic interactions in a new π-extended tetrathiafulvalene dimer. *Chemistry - A European Journal* **2006**, *12*, 2709–2721.
- [48] D. M. Guldi, L. Sánchez, and N. Martín. Formation and characterization of the π-radical cation and dication of π-extended tetrathiafulvalene materials. *Journal of Physical Chemistry B* **2001**, *105*, 7139–7144.

- [49] A. E. Jones, C. A. Christensen, D. F. Perepichka, A. S. Batsanov, A. Beeby, P. J. Low, M. R. Bryce, and A. W. Parker. Photochemistry of the π -extended 9,10-bis(1,3-dithiol-2-ylidene)-9,10-dihydroanthracene system: Generation and characterisation of the radical cation, dication, and derived products. *Chemistry - A European Journal* **2001**, *7*, 973–978.
- [50] P. Wang, S. M. Zakeeruddin, J.-E. Moser, and M. Grätzel. A new ionic liquid electrolyte enhances the conversion efficiency of dye-sensitized solar cells. *The Journal of Physical Chemistry B* **2003**, *107*, 13280–13285.
- [51] M. R. Bryce, A. J. Moore, M. Hasan, G. J. Ashwell, A. T. Fraser, W. Clegg, M. B. Hursthouse, and A. I. Karaulov. Electrical and magnetic properties and X-ray structure of a highly conductive 4:1 complex of tetracyanoquinodimethane and a tetrathiafulvalene derivative. *Angewandte Chemie International Edition* **1990**, *29*, 1450–1452.
- [52] B. C. O'Regan, I. López-Duarte, M. V. Martínez-Díaz, A. Forneli, J. Albero, A. Morandeira, E. Palomares, T. Torres, and J. R. Durrant. Catalysis of recombination and its limitation on open circuit voltage for dye sensitized photovoltaic cells using phthalocyanine dyes. *Journal of the American Chemical Society* **2008**, *130*, 2906–2907.
- [53] D. B. Kuang, S. Ito, B. Wenger, C. Klein, J. E. Moser, R. Humphry-Baker, S. M. Zakeeruddin, and M. Grätzel. High molar extinction coefficient heteroleptic ruthenium complexes for thin film dye-sensitized solar cells. *Journal of the American Chemical Society* **2006**, *128*, 4146–4154.

Chapter 4

Monolithic dye-sensitized $\text{TiO}_2/\text{Cu}(\text{In},\text{Ga})\text{Se}_2$ tandem solar cells

4.1 Introduction

The power conversion efficiency of solar cells can be extended beyond the Shockley-Queisser limit of about 30 % for a single-junction device [1] by using multiple subcells in a tandem device. Ideally, the subcells are connected optically and electrically in series and stacked in order of decreasing bandgap, where the cell with the largest bandgap is the top absorber (Figure 4.1). In this way, the absorption onset of the complete device is shifted to longer wavelengths. In addition, high energy photons are converted more efficiently since thermalization losses of the generated electron-hole pairs are reduced with the graded bandgap structure. In a series-connected double-junction device the ideal optical bandgaps are around 1.6–1.7 eV for the top cell and 1.0–1.1 eV for the bottom cell, which extends the efficiency limit to about 45 % [2]. Theoretically, the photovoltaic conversion efficiency of a tandem cell approaches the thermodynamic limit of about 85 % if an infinite number of subcells and maximum solar concentration is used [3, 4].

State-of-the-art tandem solar cells. A selection of record or notable tandem cell efficiencies is listed in Table 4.1. In practice, highest photovoltaic power efficiencies are reached with multi-junction concentrator solar cells based on III–V semiconductors. Stunning record conversion efficiencies of over 40 % at concentrated sunlight have been measured with epitaxially grown triple-junction GaInP/GaInAs/Ge devices [5, 6]. Though this expensive technology may be interesting for space and terrestrial concentrator applications, it plays a marginal role in the large-scale PV market.

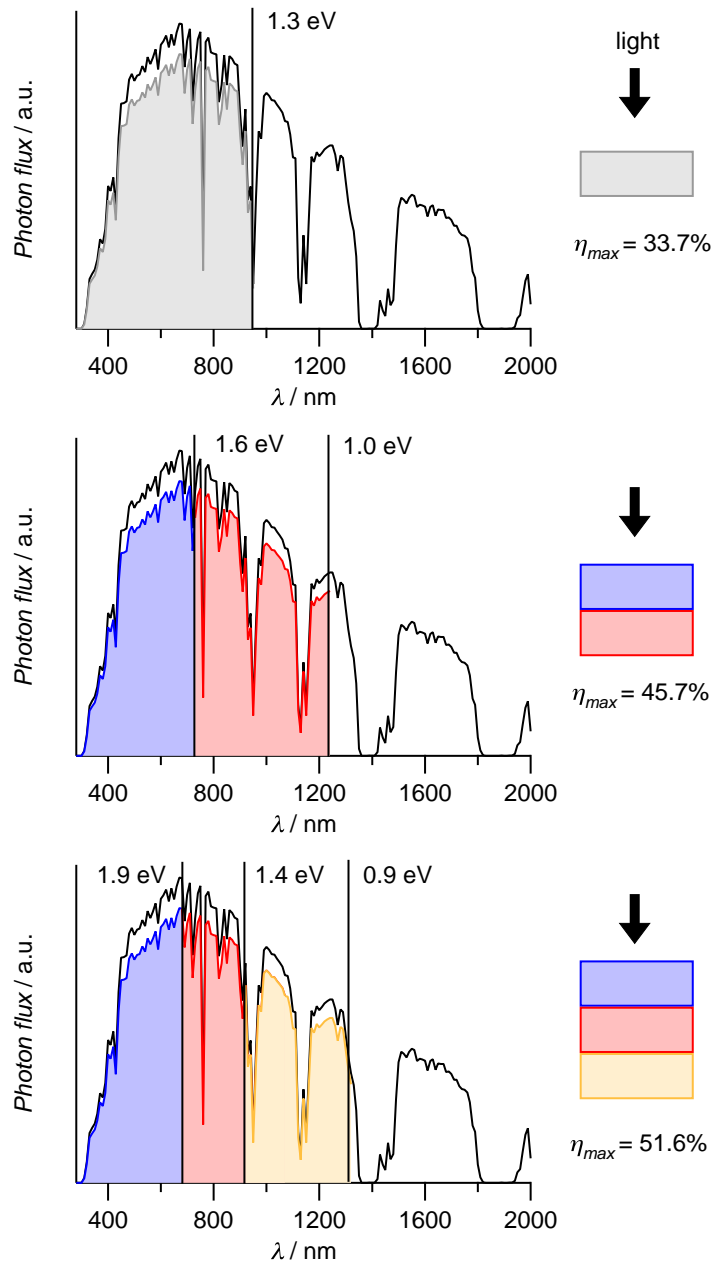


Figure 4.1: Calculated ideal bandgaps and maximum conversion efficiency for a single solar cell or a series-connected double- or triple-layer tandem cell under AM 1.5G [2]. Colored areas represent the number of photons converted to electrons by the individual subcells assuming a constant external quantum efficiency of 0.9. In a multi-layer tandem cell a larger fraction of the solar spectrum is absorbed, and thermalization losses are reduced.

The development of efficient tandem cells using *low-cost thin film technologies* is advancing well, though many challenges remain; double-junction cells based on amorphous and microcrystalline hydrogenated silicon (a-Si:H/ μ c-Si:h), which are deposited by plasma-enhanced chemical vapor deposition, have made good progress since their first report in 1994 by the Institut de Microtechnique (IMT) in Neuchâtel [14], reaching close to 12 % efficiency in a stabilized mini-module [8]. An interesting performance is also obtained with a-SiGe based tandem solar cells [9]. Single-junction devices using thin film chalcopyrite absorbers deposited by co-evaporation of elements reach high cell efficiencies of 19.9 % [15], but double-junction chalcopyrite devices are strongly limited by insufficient light transmittance to the bottom cell and processing issues in monolithic devices [10, 16, 17]. Progress in the development of organic polymers and small molecules for solar cells has been impressive in the past years. The most recent certified tandem efficiency record of 7.7 % was reached with evaporated small molecule absorbers on an over 1 cm^2 laboratory cell by the company Heliatek (press release April 2010 [11]), which so far exceeds the performance of organic single-junction devices with a similar surface area [18]. Some work has been done on two-level DSC tandems with a stan-

Table 4.1: Selection of state-of-the-art tandem solar cell technologies measured under the global AM1.5 spectrum (100 mW cm^{-2}). Bold efficiencies were measured by a recognized test center under standard testing conditions at 25°C on cells with an active area $\geq 1 \text{ cm}^2$. Efficiencies in brackets are certified measurements for cells with an area $< 1 \text{ cm}^2$.

Device	V_{oc} (V)	J_{sc} (mA cm^{-2})	FF —	η (%)	Reference
GaInP/GaInAs/Ge	2.62	-14.7	0.85	32.0 (41.6) ^a	Spectrolab [5, 6]
GaInP/GaAs	2.49	-14.2	0.86	30.3	Japan Energy [7]
a-Si/ μ c-Si (sub-module)	5.46	-3.0	0.71	11.7 ^b	Kaneka [8]
a-Si/a-SiGe/a-SiGe	2.01	-9.1	0.68	(12.5) ^c	United Solar [9]
CdTe/CIS (stacked)	—	—	—	(15.3) ^d	NREL [10]
Organic tandem	—	—	—	7.7	Heliatek [11]
DSC/CIGS (stacked)	1.45	-14.1	0.74	15.1	EPFL/ETHZ [12]
DSC/CIGS (monolithic)	1.22	-13.9	0.72	12.2	this work [13]

^ameasured at 364 suns, 0.32 cm^2 surface area

^bstabilized

^cstabilized, 0.27 cm^2 surface area

^d 0.41 cm^2 surface area

dard ruthenium dye in combination with an IR-enhanced “black” dye [19–21], but the spectral overlap of the two dyes proved too large to outperform current single-junction record cells. An innovative DSC tandem structure was proposed by He et. al., where the dye-sensitized TiO_2 photoanode is complemented by a photoactive cathode [22]. This system must be carefully fine-tuned from an energetics point of view, and recent discoveries in this field have been promising [23–25]. Co-sensitization of the mesoporous TiO_2 by different organic dyes has been investigated to increase the spectral response of the DSC [26, 27]. However, these devices tend to be visible absorbers to date, since the squarine dyes used for the harvest of low energy photons have an absorption maximum at about 650 nm.

$\text{TiO}_2/\text{Cu}(\text{In},\text{Ga})\text{Se}_2$ tandem solar cell. The absorption characteristics of the dye-sensitized solar cell (DSC) and the chalcopyrite $\text{Cu}(\text{In},\text{Ga})\text{Se}_2$ (CIGS) solar cell closely match the ideal optical gap requirements for a double-junction tandem device [2]. High-efficiency DSCs use ruthenium bipyridyl complexes with an estimated excitation transition energy of $E_{0-0} \approx 1.6\text{--}1.8$ eV to convert a large fraction of the visible spectrum [28–31]. CIGS is a polycrystalline material with a direct bandgap and hence a high absorption coefficient allowing for thin absorbing films ($\sim 1\text{--}2$ μm). The bandgap of the CIGS ($\text{CuIn}_{1-x}\text{Ga}_x\text{Se}_2$) absorber can be tuned between 1.0 eV and 1.7 eV by increasing the Ga content x ($x = 0$, CuInSe_2 or CIS; $x=1$, CuGaSe_2 or CGS). With increasing bandgap, the effective photovoltage in a device increases, and the photocurrent decreases. Highest efficiencies are obtained with an optimized Ga content of $x \approx 0.25$ and a bandgap of about 1.2 eV [32, 33]. A wide range of the solar spectrum can thus be harvested in a DSC/CIGS tandem device by efficiently converting high energy photons in a top DSC and transmitted low energy photons in an underlying CIGS cell. This principle was first demonstrated with a *mechanically stacked* DSC/CIGS tandem in 2006 [12].

One major objective of this thesis was to investigate the potential of *monolithic* DSC/CIGS tandem cells [13]. The work in this chapter was done in collaboration with the group of Prof. A. N. Tiwari at Empa, Dübendorf, Switzerland (formerly at ETH Zürich), which provided the CIGS cells. Monolithic test devices were assembled and characterized by the author at EPFL.

4.2 Tandem device structure

Electrical connection. Tandem subcells are most conveniently connected *in series*, since subcells with ideal bandgaps generate similar photocurrents but different pho-

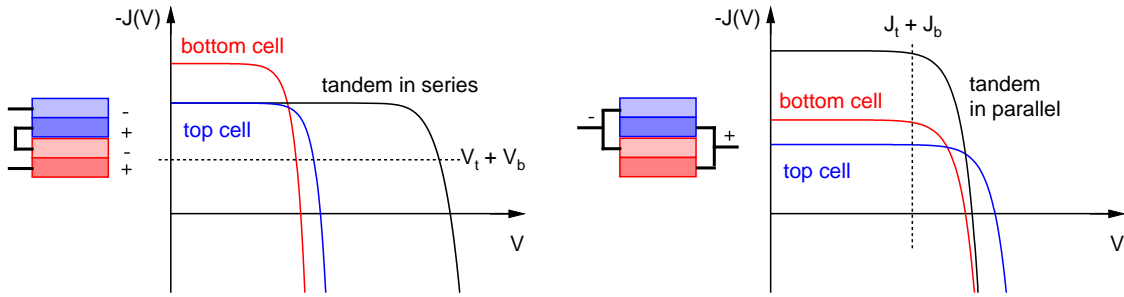


Figure 4.2: J - V curves of two subcells under illumination and of the tandem connected electrically in series (left) or in parallel (right). In a series connection, the photovoltage of the top (V_t) and bottom (V_b) cell add up at constant photocurrent. In a parallel connection, the photocurrent density of the top (J_t) and bottom (J_b) cell add up at constant photovoltage.

toppotentials. In a series-connected tandem, the total generated photocurrent J_{tandem} is constant throughout the device in steady-state. The photovoltages in the subcells add up to the total photovoltage V_{tandem} . In a double-junction tandem with a top and bottom cell, the following is valid for each point on the J - V curve:

$$J_{tandem} = J_{top} = J_{bottom} \quad \text{and} \quad V_{tandem} = V_{top} + V_{bottom}. \quad (4.1)$$

If the J - V curves of the subcells within a tandem setup are known, the total J - V curve of the series tandem device can be calculated by adding up the voltages at equal current (Figure 4.2, left).

In the (unideal) case where the subcells have similar photovoltages but differing currents, it might be more advantageous to connect the cells *in parallel*. In a parallel-connected double-junction tandem, the following relations are valid at each point of the J - V curve,

$$V_{tandem} = V_{top} = V_{bottom} \quad \text{and} \quad J_{tandem} = J_{top} + J_{bottom}. \quad (4.2)$$

Similarly, if the J - V curves of the subcells within a tandem setup are known, the total J - V curve of the parallel tandem device can be constructed by adding up the currents at equal voltage (Figure 4.2, right).

Device structure. In terms of assembly, the simplest tandem structure is obtained from *mechanically stacking* two individual cells on top of each other. The four electrodes are connected such that the stacked tandem is in series. In the *monolithic* approach, the top cell is directly grown or deposited on the bottom cell, leaving only two electrical

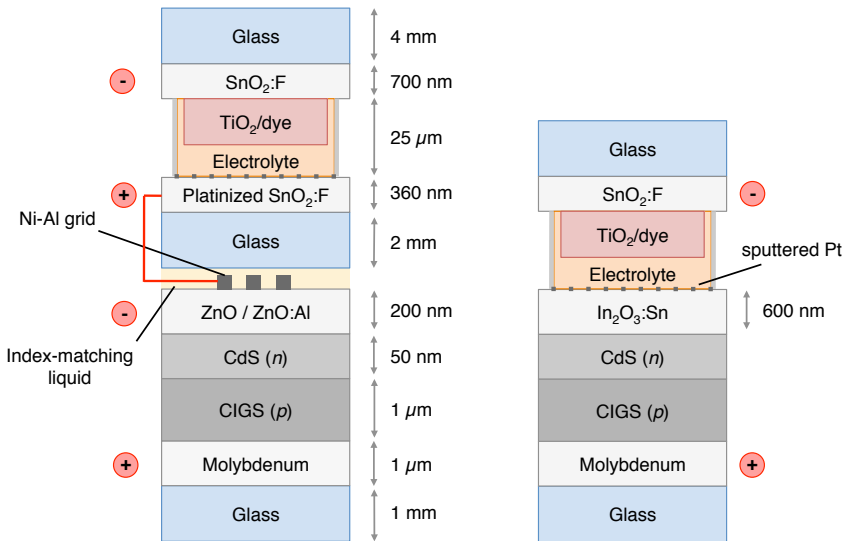


Figure 4.3: Schematic of the mechanically stacked (left) and monolithic (right) tandem device structure with a DSC top absorber and a CIGS bottom absorber. In the stacked tandem, the DSC is connected in series with the CIGS cell via a Ni-Al current collector grid. An index-matching liquid is used between the cells to reduce reflectance losses. In the monolithic device the DSC absorber (photoanode) is directly deposited on top of the CIGS cell.

contacts. In a monolithic tandem, needless layers and electrodes are omitted, which reduces material consumption and optical losses. All advanced tandem technologies — e.g. devices based on III–V semiconductors, a-Si/ μ c-Si, or organic semiconductors — use a monolithic assembly approach.

Our groups have reported in 2006 on a mechanically stacked DSC/CIGS device as shown in Figure 4.3, left, yielding a conversion efficiency of over 15 % [12]. A DSC was directly stacked on a CIGS cell covered with an evaporated Al/Ni current collector grid. An “index-matching” fluid with a refractive index of $n = 1.7$ (Cargille Labs) was used between the two cells to reduce reflection losses at the interface. This stack demonstrated the possibility of combining DSCs with CIGS thin film cells, but the obvious drawbacks of the stacked setup are reflection losses at the stack interface and absorption losses of low energy photons in the conducting glass of the top cell. In addition, the establishment of the electrical connection with the Al/Ni grid and handling of the index-matching liquid is cumbersome.

A monolithic DSC/CIGS tandem assembly as shown in Figure 4.3, right, is clearly more advantageous, since optical losses from the superfluous layers and interfaces and material and manufacturing costs are reduced.

4.3 Experimental

Device assembly. The monolithic device consisted of a mesoporous dye-sensitized TiO_2 film, which was directly sandwiched with a platinized CIGS solar cell using a Surlyn spacer, thus avoiding the back glass electrode commonly used in the DSC (Figure 4.4). The void was filled through a hole in the top electrode with an acetonitrile-based electrolyte containing the I^-/I_3^- redox couple. The *p*-type CIGS absorber ($\sim 1 \mu\text{m}$) was grown by sequential coevaporation of elements using a three-stage evaporation process [34] on a soda-lime glass substrate, coated with a $1 \mu\text{m}$ thick dc-sputtered layer of molybdenum, and covered with an *n*-type CdS window layer (50 nm). The detailed fabrication procedure of the complete CIGS solar cell is given elsewhere [33]. The front contact, a 600 nm thick layer of $\text{In}_2\text{O}_3:\text{Sn}$ (ITO), was covered with a transparent layer ($< 1 \text{ nm}$) of sputtered Pt particles. A 8 μm thick film of 20 nm sized TiO_2 particles was screen-printed on a $\text{SnO}_2:\text{F}$ (FTO) conducting glass electrode ($10 \Omega/\square$) and sensitized by immersing it overnight in a solution of 0.3 mM of C101 dye [35] and 0.3 mM $3\alpha, 7\alpha$ -dihydroxy- 5β -cholanic acid. The detailed fabrication procedure for the TiO_2 paste and film has been described elsewhere [36].

Photovoltaic characterization. The external quantum efficiency of test devices was measured with a monochromatic beam from a xenon lamp as described in Section 2.2.1. The current-voltage curve of devices was measured with irradiation from a 1000 W xenon lamp matched to AM 1.5G with filters in the range 350–1200 nm as described in

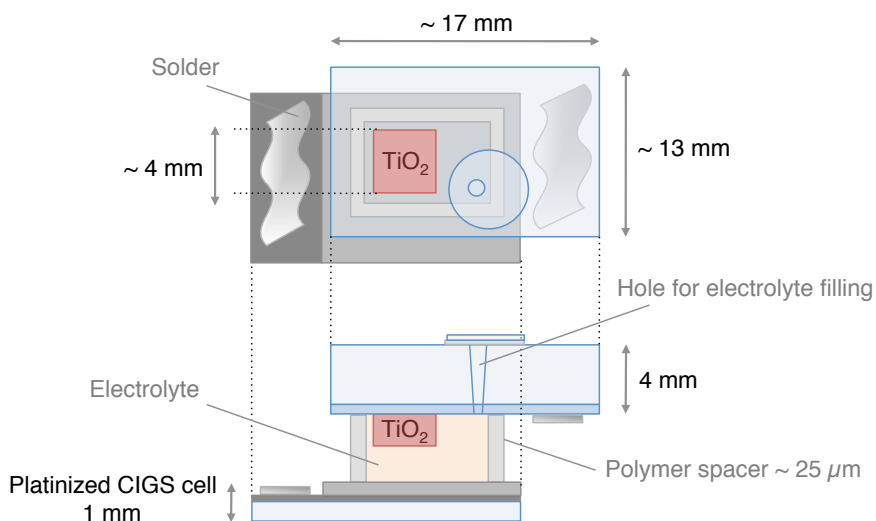


Figure 4.4: Cartoon of the sandwich-type DSC/CIGS monolithic tandem cell assembly.

Section 2.2.2. Measurements were performed with a metal mask with an aperture area of 0.125 cm^2 .

4.4 Results

4.4.1 Photovoltaic performance and stability

Initial performance. As shown by external quantum efficiency (EQE) measurements (Figure 4.5a), the DSC converts light in the visible region with an onset at 780 nm (optical gap of 1.6 eV) and the CIGS converts the remaining light up to 1160 nm (optical gap of 1.1 eV).

The subcells in the monolithic tandem are electrically connected in series. Intermediate charge recombination occurs at the catalytic Pt particles [37] on the electrolyte/ITO interface, that is, the “holes” from the top cell (oxidized I_3^- ions) react with electrons from the bottom cell via $\text{I}_3^- + 2e^- \rightarrow 3\text{I}^-$. It is thus crucial to match the current densities of the subcells to minimize electronic losses. The current density of the DSC can be tuned with the choice of sensitizer, by variation in the optical bandgap, and film thickness, by variation in the optical path length. Here we use a Ru-complex sensitizer with a suitable optical gap and a high molar extinction coefficient [29] to achieve large short-circuit currents at full sunlight on thin transparent TiO_2 films, ranging from 13.6 mA cm^{-2} ($5 \mu\text{m}$

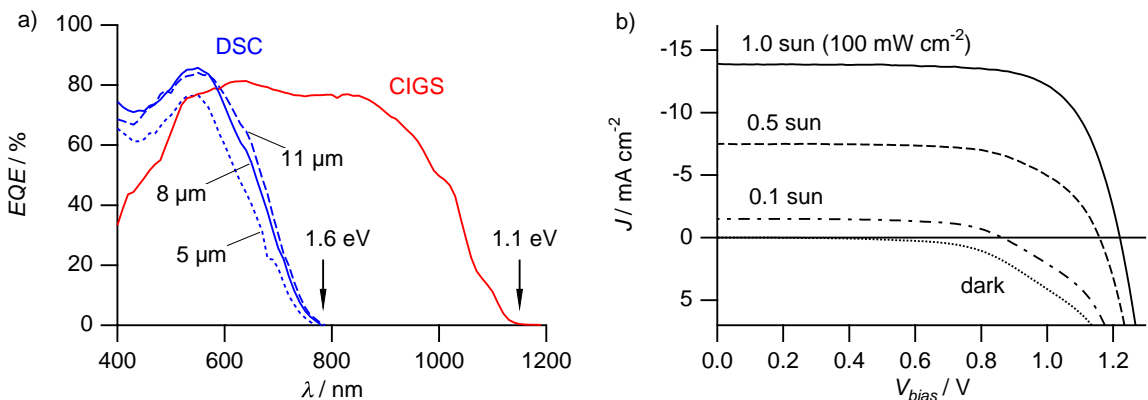


Figure 4.5: a) The EQE of the individual DSC and CIGS shows ideal onsets for use in a tandem device. The EQE of the DSC can be fine-tuned with variation of the TiO_2 film thickness. b) Current density-voltage curve of a monolithic DSC/CIGS tandem device at various light intensities. Notice the nonideal rectification in the dark curve. The device was tested under simulated standard testing conditions (AM 1.5G) using a metal mask with an aperture area of 0.125 cm^2 .

film) to 16.2 mA cm^{-2} ($11 \mu\text{m}$ film). The current density of the CIGS cell can be tuned with variation of the bandgap by changing the In/Ga ratio in the absorber [33].

The photovoltaic parameters of a monolithic DSC/CIGS device and its subcells are given in Table 4.2. The conversion efficiency of the monolithic device (12.2 %) slightly exceeded the performance of the individual CIGS cell (11.6 %), justifying the monolithic approach to enhance device efficiency. The open-circuit voltage (V_{oc}) of the tandem device was close to the sum of the V_{oc} 's of the DSC and CIGS cell, confirming the series connection of the subcells. The short-circuit current (J_{sc}) of the tandem device was lower than the J_{sc} of an individual DSC. A rough estimation of the J_{sc} of the filtered CIGS cell, using the transmittance spectrum of a DSC, suggests that the CIGS might be limiting the total photocurrent in the stack (see Section 4.4.2). The current density-voltage curves (Figure 4.5b) illustrate a drawback of the monolithic setup. The rectifying behavior in the dark and at a low light level is nonideal, suggesting internal electric shunt pathways. Indeed, the performance of the device degraded within hours; the V_{oc} and fill factor dropped substantially (see next paragraph). This is probably due to a corrosion of the CIGS cell by I_3^- ions in the electrolyte percolating through pinholes. The initial V_{oc} loss of 140 mV and the further degradation can be explained by a rapid corrosion of the p - n junction and shunting through the cracks.

Stability. The stability of the monolithic DSC/CIGS tandem cell is drastically impaired by the corroding effect of the iodine-based electrolyte, which is in direct contact with the front electrode of the CIGS cell. In a monolithic device using a standard CIGS cell (with a sputtered $\text{ZnO}/\text{ZnO:Al}$ front electrode of about 200 nm) the double junction degraded rapidly, which is seen in the V_{oc} loss from 1.30 V to 0.81 V in only 2 h after assembly (Figure 4.6a). The corroding effect of the electrolyte on the ZnO:Al electrode and the CIGS absorber material was confirmed with SEM images [38]. Thus, a suitable

Table 4.2: Photovoltaic performance of the DSC/CIGS monolithic device and the subcells (AM 1.5G, 100 mW cm^{-2}). A Ni/Al grid was evaporated on the CIGS cell to improve charge carrier collection.

Test device	V_{oc} / V	J_{sc} / mA cm^{-2}	FF	η / %
DSC (FTO back contact)	0.74	-15.3	0.74	8.4
CIGS (unfiltered)	0.62	-27.3	0.68	11.6
DSC/CIGS monolithic tandem	1.22	-13.9	0.72	12.2

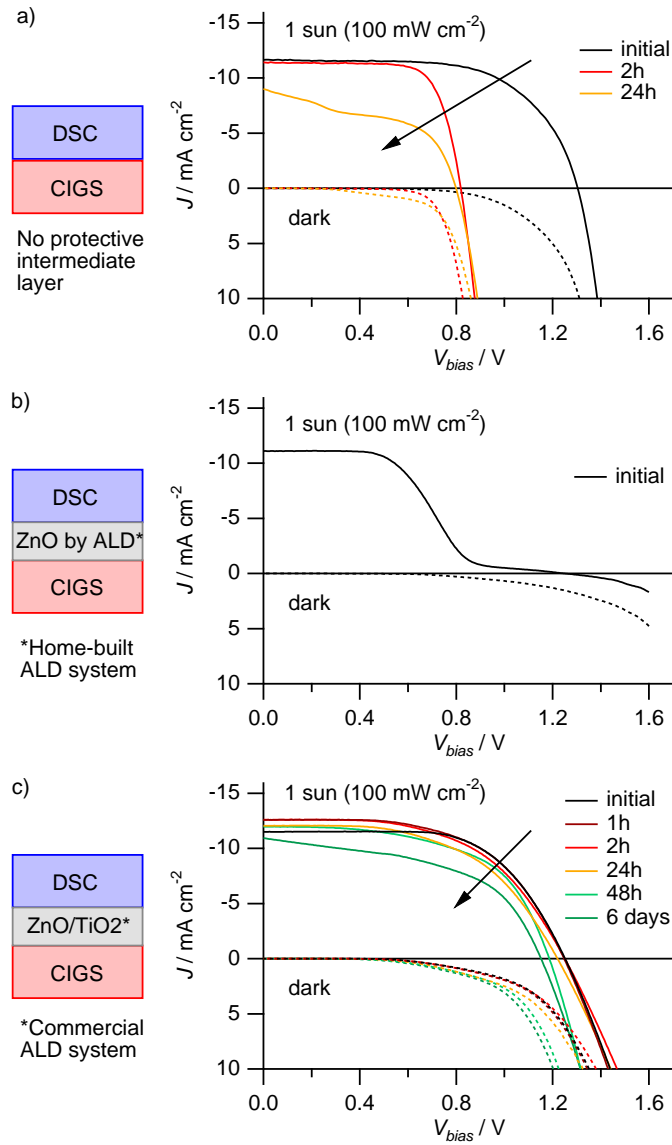


Figure 4.6: J - V curves under illumination and in the dark of monolithic DSC/CIGS tandem cells with different intermediate protective layers at the electrolyte/CIGS anode interface. a) CIGS with ZnO/ZnO:Al top electrode and no additional protective coating. The rapid loss in V_{oc} indicates a strong degradation of the double-junction, which is probably induced by corrosion of the ZnO and CIGS absorber by the electrolyte. b) CIGS cell (ITO top electrode) with an additional thin layer of ZnO ($\sim 10 \text{ nm}$) deposited with a home-built ALD system. The J - V curve suggests, that the ZnO layer is too insulating. c) CIGS cell (ITO top electrode) with an additional double-layer of ZnO (10 nm) and TiO₂ (2 nm) deposited with a state-of-the-art ALD system. With such a protective coating the device is stable for a few days.

protective layer between the CIGS front electrode and the electrolyte must be found, which is stable in the electrolyte environment, transparent in the wavelength range 600–1200 nm, electrically conductive, and which can be deposited at temperatures below 150 °C to prevent the interdiffusion of Cd into the CIGS absorber layer [39].

Since ZnO is known to be only fairly stable in the electrolyte environment, we first replaced the 200 nm thick ZnO:Al electrode by a 600 nm *sputtered ITO electrode*. ITO is frequently used as electrode material in DSCs and is stable in the electrolyte. The *J-V* curve of such devices had a higher fill factor, i.e. less shunt and series resistance losses at the junction between the two subcells and lead to a better initial performance (Table 4.2), but the performance of the device still degraded in a similar timeframe. Since the ITO itself is most probably not affected by the redox mediator, the CdS window layer and the CIGS absorber are likely attacked by the electrolyte percolating through pinholes in the ITO layer.

Thin films of *organic semiconductors* are alternative candidates for protective layers. In initial tests we spin-coated a dispersion of poly(3,4-ethylenedioxythiophene) poly(styrenesulfonate) (PEDOT:PSS) in water onto the electrode of the completed CIGS cell. Unfortunately, the electrode surface — both ZnO:Al and ITO — were not wetted well by the PEDOT, even after cleaning the surface with a UV/ozone treatment. The spin-coated PEDOT films were rather thick and uneven, and the monolithic device showed highly resistive behavior. Though the wetting behavior of the PEDOT might be improved with a different solvent, thin films of organic semiconductors are probably not ideal protective layers; they might swell or delaminate from the electrode in the electrolyte environment.

Ideally, the protective layer consists of an electrolyte-resistant, *conformal metal oxide layer*, which covers cracks and pinholes in the top CIGS electrode. Atomic Layer Deposition (ALD) is an established chemical vapor deposition technique to grow thin conformal films in a cyclic, self-limiting manner [40]. During one growth cycle, a first precursor is adsorbed to the surface of the substrate. The reaction chamber is purged, and a second precursor is fed in, which reacts with the surface-adsorbed first precursor layer to form about one monolayer of the material. The chamber is purged again, and the cycle is repeated to grow the desired film thickness. We first studied the effect of a ~ 10 nm thick ZnO layer deposited using a home-built ALD system with diethylzinc and water as precursors. Preliminary electrolyte corrosion tests on samples of ALD-ZnO on silver films, which were evaporated on microscope glass slides, showed a clear retardation of the dissolution of the underlying silver. Monolithic devices were assembled using a CIGS cell with an ITO front electrode, ~ 10 nm ZnO deposited by ALD at ambient

temperature, and a thin layer of sputtered Pt particles. The J - V curve of such a device (Figure 4.6b) showed a high series-resistance component indicative of a strongly insulating ZnO layer. The ZnO layer may be too insulating due to its amorphous structure and inhomogenous deposition.

We made a new attempt with a state-of-the-art ALD system (Savannah, Cambridge NanoTech) purchased by our laboratory in early 2010. A double-layer of 10 nm ZnO and 2 nm TiO_2 (using TiCl_4 and H_2O as precursors) was deposited on a CIGS cell with an ITO front electrode. TiO_2 , which is extremely stable in the electrolyte environment, was used to provide a compact protective layer. Pt particles were then sputtered on the TiO_2 surface, and the as-coated CIGS cell was assembled in a monolithic device. As seen in the J - V curve (Figure 4.6c), the performance of such a device was stable for a few days. In particular, the V_{oc} dropped from initially 1.25 V to only 1.16 V after six days, indicating that the double-junction was reasonably well preserved. This breakthrough is encouraging, as there is still much room to improving the conformal layer. The moderate initial fill factor ($FF = 0.63$) of the device may be raised by improving the crystal structure of the ZnO/ TiO_2 layer with a thermal post-treatment or by heating the CIGS cell during deposition ($T_{dep} < 150$ °C to maintain the CIGS elemental composition). Additionally, the ZnO layer could be doped by alternating ZnO and Al_2O_3 layers during the deposition process to obtain ZnO:Al [41].

4.4.2 Optical loss analysis

Preliminary estimation. The monolithic setup omits the transparent conductive oxide (TCO) back electrode of the DSC to avoid reflection and free charge carrier absorption losses [42]. We first estimated the enhancement in photocurrent with a monolithic setup compared to a mechanically stacked setup from the comparison of the transmission spectra of a DSC with a FTO back contact and a microscope glass back contact (Figure 4.7). Transmittance spectra were measured on a custom-built setup using a chopped white light probe and a monochromator to detect the transmitted light via a lock-in amplifier.

In the visible range, the transmittance of the two devices is attenuated by the dye absorption onset at 780 nm and the absorption of I_3^- ions around 400 nm. The transmittance losses above 780 nm are entirely due to absorption by free charge carriers in the FTO and reflection losses at interfaces. The replacement of the FTO back electrode with a microscope slide leads to an increase in transmittance of up to 20 % in the infrared region and to an overall integrated increase of 24 %. The short-circuit current (J_{sc}) of a “DSC-filtered” CIGS cell can be estimated from integration of the product of

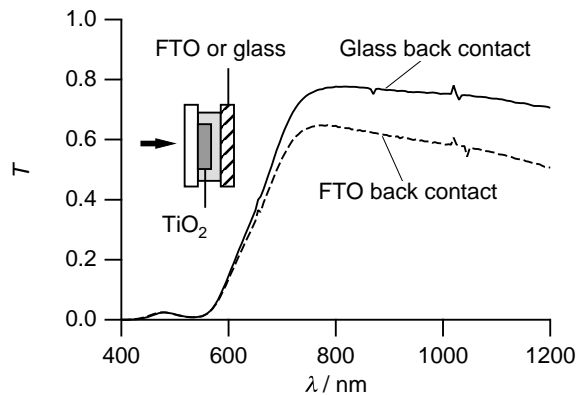


Figure 4.7: Transmission spectra of a DSC with a platinized FTO back contact ($15 \Omega/\square$) and a microscope glass slide back contact. Omitting the FTO back electrode leads to a substantial increase in transmittance in the near infrared region.

the EQE of the CIGS cell with the transmittance spectrum of the DSC and the AM 1.5G reference spectrum. The integrated current of the CIGS cell in Figure 4.5a, left, is $J_{sc} = 27.6 \text{ mA cm}^{-2}$ and reduces to $J_{sc} = 10.9 \text{ mA cm}^{-2}$ with the DSC/FTO filter and to $J_{sc} = 13.1 \text{ mA cm}^{-2}$ with a DSC/glass filter. The latter value is close to the photocurrent measured in the tandem device (Table 4.2). Even though this calculation underestimates the effective current of the CIGS cell in a monolithic device by at least 4 %, since reflection losses at the electrolyte/glass/air interfaces are not deducted, it gives a lower limit for the increase in photocurrent expected ($\sim 20 \%$), which can be exploited with a current-matching top DSC.

Optical modeling. The estimate of the photocurrent in the CIGS bottom cell based on the transmittance spectrum of the DSC top cell is only approximate. With the *transfer-matrix formalism*, the optical electric field (or the light intensity) and the total transmittance, reflectance, and absorptance in each layer of a multilayer stack can be computed accurately [43, 44]. This method gives a better understanding of the optical processes in the complete tandem device and a more accurate determination of the absorbed light in the CIGS absorber.

Within the transfer-matrix formalism the interfaces of the multilayer stack are assumed to be parallel. The stack is described by a product of matrices, the system transfer matrix. For coherent layers at normal incidence, the electric field $E(z) = E^+(z) + E^-(z)$, which is the sum of the forward and backward propagating field, is traced perpendicular to the stack. For a stack with m layers, the electric field just before the first interface, $E_0 = E_0^+ + E_0^-$, is linearly related to the field just after the last interface,

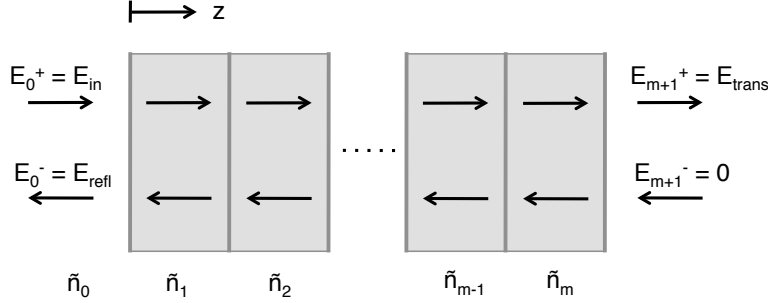


Figure 4.8: Schematic of a multilayer system with m layers and the forward and backward propagating electric field components. The field components $E_0 = E_0^+ + E_0^-$ and $E_{m+1} = E_{m+1}^+ + E_{m+1}^-$ are linearly related by a system transfer matrix, which is defined by the complex refractive indices, $\tilde{n}_i = n_i + ik_i$, and the thickness of the layers.

$E_{m+1} = E_{m+1}^+ + E_{m+1}^-$, via the system transfer matrix \mathbf{M} ,

$$\begin{pmatrix} E_0^+ \\ E_0^- \end{pmatrix} = \mathbf{M} \begin{pmatrix} E_{m+1}^+ \\ E_{m+1}^- \end{pmatrix}. \quad (4.3)$$

E_0^+ describes the incident field component, E_0^- the reflected field component, and E_{m+1}^+ the transmitted field component. E_{m+1}^- is zero if the illumination is incident from the front side only (Figure 4.8). The transfer matrix \mathbf{M} is a 2×2 matrix defined by the product of layer and interface matrices:

$$\mathbf{M} = \mathbf{I}_{01}\mathbf{L}_1\mathbf{I}_{12} \dots \mathbf{I}_{m-1,m}\mathbf{L}_m\mathbf{I}_{m,m+1}. \quad (4.4)$$

$\mathbf{I}_{i,i+1}$ describes the field propagation at the interface matrix between the layers i and $i+1$, and \mathbf{L}_i describes the field propagation through the layer i . The interface and layer matrices are completely defined by the complex refractive index of the layers and their thickness. For incoherent layers the electric field is substituted by the light intensity $U = |E|^2$ [45].

Optical simulations of the DSC/CIGS tandem stack were performed with the software package *SETFOS* [46]. The program accounts for both coherent and incoherent layers in a stack using a generalized transfer-matrix approach in which coherent layers are treated as equivalent incoherent interfaces [45]. The thickness and the complex index of refraction of each layer is given as input to calculate the total transmittance, reflectance, and the absorptance in each layer of the stack. From the product of the absorptance of the photoactive layer and the AM 1.5G solar spectrum one finds the maximum achievable short-circuit current. Simulations were carried out in the wavelength range $\lambda = 400-$

1400 nm with increments of $\Delta\lambda = 5$ nm. Layers with a thickness $d \leq 700$ nm were treated as coherent layers. The results for different simulations are shown in Table 4.3.

Simulations of transmittance and reflectance spectra were first calculated for the DSC alone. The complex refractive index of each layer was extracted from measured transmittance and reflectance spectra and from ellipsometry data. The simulations of the transmittance and reflectance spectra were in very good agreement with the measurements. The determination of the complex refractive indices and the experimental validation are discussed in detail in Chapter 5. For a standard DSC stack with an 8 μm thick TiO_2 layer and C101 dye we obtain a maximum photocurrent of 14.3 mA cm^{-2} , which is slightly lower than the measured value but in the same range (Table 4.3). The simulated DSC stack consisted of: 3.88 mm glass (NSG), 697 nm FTO (NSG), 8.0 μm TiO_2 , 17.0 μm bulk electrolyte, 360 nm FTO (TEC-15), 2.22 mm glass (TEC-15).

The optical simulations of the CIGS stack were carried out with refractive indices obtained from ellipsometry or literature, which are specified in Appendix A. These simulations could not be validated with experimental spectra, and the results must thus be considered as indicative. For the CIGS cell alone, we obtain a maximum photocurrent of 28.8 mA cm^{-2} . The CIGS stack is defined as: 600 nm ITO, 50 nm CdS, 1 μm CIGS, 1 μm molybdenum, thick substrate with $n = 1.5$.

For the simulation of a monolithic DSC/CIGS tandem device we use: 3.88 mm glass (NSG), 697 nm FTO (NSG), 8.0 μm TiO_2 , 17.0 μm bulk electrolyte, 600 nm ITO, 50 nm

Table 4.3: Comparison of measured photocurrents and calculated maximum photocurrents using the optical simulation of the DSC, CIGS cell, and the monolithic tandem. Simulations were performed for a stack similar to the experimental stack (8 μm TiO_2 , 600 nm ITO electrode on CIGS cell) and for an ideal stack with optimized layer thicknesses. The short-circuit current, J_{sc} , is given in mA cm^{-2} .

Test device	J_{sc} measured ^a	J_{sc} simulated ^b	J_{sc} optimum ^c
DSC (FTO back contact)	-15.3	-14.3	-16.1
CIGS (unfiltered)	-27.3	-28.8	-31.7
DSC/CIGS monolithic tandem	-13.9	—	—
<i>DSC subcell</i>		-14.2	-16.0
<i>CIGS subcell</i>		-15.6	-16.2

^aFrom Table 4.2.

^bDSC with 8 μm thick TiO_2 film, and CIGS cell with 600 nm thick ITO front electrode.

^cOptically optimized stack: DSC with 13 μm TiO_2 , and CIGS with 300 nm ITO.

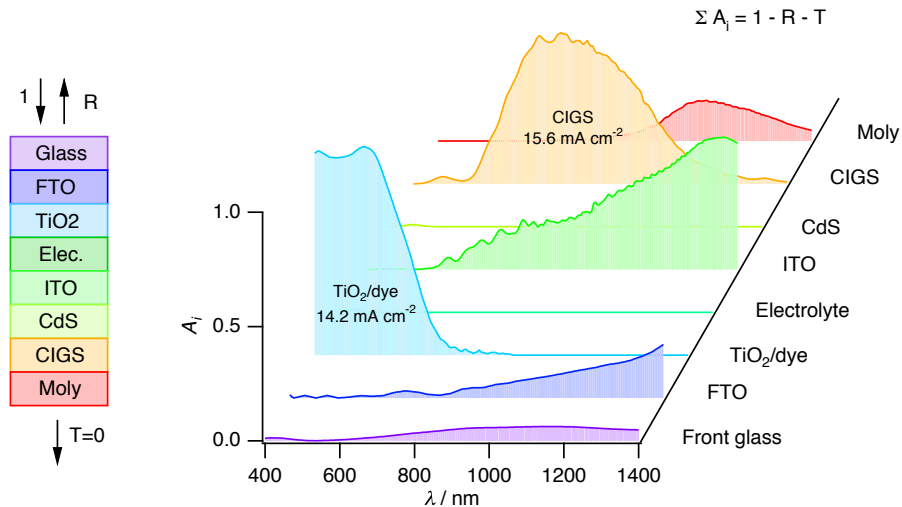


Figure 4.9: Calculated absorptance in each layer of a monolithic DSC/CIGS tandem cell. The sum of the absorptances and the total reflection add up to one. From the product of the AM 1.5G solar spectrum and the absorptance in the photoactive layer (dye-sensitized TiO_2 and CIGS, respectively) one finds the maximum achievable photocurrent. Modeled stack: 3.88 mm glass (NSG), 697 nm FTO (NSG), 8.0 μm TiO_2 , 17.0 μm bulk electrolyte, 600 nm ITO, 50 nm CdS, 1 μm CIGS, 1 μm molybdenum.

CdS , 1 μm CIGS, 1 μm molybdenum. The calculated absorptance in each layer is shown in Figure 4.9. In this configuration, the DSC subcell seems to be limiting the photocurrent of the complete device (see Table 4.3). The CIGS subcell delivers 10 % more current. We must note though, that the simulation underestimates the current of the DSC subcell, for which we experimentally measure a current of over 15 mA cm^{-2} . It is thus likely, that the photocurrents match closely in the real device, which is also supported by the “bump-free” J - V curve in Figure 4.5a. The strong absorptance of the 600 nm ITO layer in the red and near-infrared region is striking (Figure 4.9). At $\lambda = 1000 \text{ nm}$, 25 % of the incident light is absorbed by the ITO, compared to 7% by the FTO, and only 42% is absorbed by the CIGS layer. There is thus ample optical optimization potential for the intermediate ITO electrode.

The layer thicknesses in the tandem stack can be freely varied in the simulation to obtain an optimum stack with large matching photocurrents. For example, the calculation of a stack with a 13.0 μm TiO_2 layer and a 300 nm ITO intermediate electrode — the other layer thicknesses remain unchanged — yields matched photocurrents at about 16 mA cm^{-2} (Table 4.3). Here, the lower absorptance in the thinner ITO layer is beneficial for the CIGS photocurrent (at $\lambda = 1000 \text{ nm}$, 14 % is absorbed by the ITO, and 50 % is absorbed by the CIGS layer).

4.5 Conclusions

Research on CIGS-based tandem cells is still in a preliminary stage and the efficiency of the tandem cell presented does not yet exceed state-of-the-art CIGS cells (up to 19 %). However, the DSC/CIGS tandem cell concept remains promising: We have shown that a monolithic DSC/CIGS tandem device has the potential for increased efficiency over a mechanically stacked device due to increased light transmission to the bottom cell and demonstrated a monolithic DSC/CIGS device with an initial efficiency of 12.2 %.

The monolithic tandem suffers from rapid degradation due to the corrosive effect of the iodine-based electrolyte in contact with the top electrode of the CIGS cell. One should be able to make full use of the optical advantages of the monolithic setup — and to surpass the 15.1 % efficiency benchmark given by the stacked device [12] — with a suitable protective intermediate layer between the CIGS electrode and the electrolyte. Preliminary studies show, that enhanced stability for a few days can be achieved with an atomic layer deposited ZnO/TiO_2 double layer on top of the CIGS cell.

We can infer from optical calculations that the photocurrents in the subcells match closely, and that electrical losses due to a current mismatch are minimal. In the prototype tandem device, which has a thick intermediate ITO electrode to minimize degradation, absorption of low energy photons by the intermediate ITO electrode is quite strong. With an optimized, thinner, intermediate electrode and a thicker dye-sensitized TiO_2 film, however, the fabrication of tandem cells with a matched photocurrent of about 16.0 mA cm^{-2} seems feasible.

A deeper look into high mobility transparent conductive oxides with very high transparency, such as $\text{In}_2\text{O}_3:\text{Ti}$ (ITiO) [47, 48], might be interesting for high photocurrent tandem devices — provided the device is reasonably stable. In view of a potential large-scale production, inexpensive oxides, such as $\text{ZnO}:\text{Al}$ or $\text{SnO}_2:\text{F}$ should be more suitable.

From the obtained results, we can conservatively assess the potential of the monolithic DSC/CIGS tandem cell as follows; if a stable protective intermediate layer can be developed, which would improve the V_{oc} and fill factor of the tandem device, and if the J_{sc} can be matched at $\sim 16.0 \text{ mA cm}^{-2}$ with optimized layer thicknesses, conversion efficiencies of over 16 % seem reasonable (assuming $V_{oc} = 1.4 \text{ V}$, where $V_{DSC} = 0.75 \text{ V}$ and $V_{CIGS} = 0.65 \text{ V}$, $FF=0.72$).

In the long-run, DSC/CdTe/CI(G)S triple-junction devices might become interesting high efficiency tandem alternatives, since the optical gaps of this structure (1.7 eV, 1.5 eV, and 1.0 eV) closely match the ideal optical gaps of a triple-junction. So far,

this setup seems to be limited by transmittance losses to the bottom cell. Preliminary studies with a mechanically stacked triple-junction yield a photocurrent of only about 5 mA cm^{-2} [49]. For triple-junction tandem devices, substantial additional research efforts will be necessary, especially with regards to the monolithic integration of CdTe and CIGS solar cells.

Bibliography

- [1] W. Shockley and H. J. Queisser. Detailed balance limit of efficiency of *p-n* junction solar cells. *Journal of Applied Physics* **1961**, *32*, 510–519.
- [2] S. P. Bremner, M. Y. Levy, and C. B. Honsberg. Analysis of tandem solar cell efficiencies under AM1.5G spectrum using a rapid flux calculation method. *Progress in Photovoltaics: Research and Applications* **2008**, *16*, 225–233.
- [3] C. H. Henry. Limiting efficiencies of ideal single and multiple energy gap terrestrial solar cells. *Journal of Applied Physics* **1980**, *51*, 4494–4500.
- [4] A. Martí and G. L. Araújo. Limiting efficiencies for photovoltaic energy conversion in multigap systems. *Solar Energy Materials and Solar Cells* **1996**, *43*, 203–222.
- [5] R. R. King, D. C. Law, K. M. Edmondson, C. M. Fetzer, G. S. Kinsey, H. Yoon, R. A. Sherif, and N. H. Karam. 40% efficient metamorphic GaInP/GaInAs/Ge multijunction solar cells. *Applied Physics Letters* **2007**, *90*, 183516.
- [6] R. R. King, A. Boca, W. Hong, X.-Q. Liu, D. Bhusari, D. Larrabee, K. Edmondson, D. Law, C. Fetzer, S. Mesropian, and N. Karam. Band-gap-engineered architectures for high-efficiency multijunction concentrator solar cells. *Proceedings of the 24th European Photovoltaic Solar Energy Conference, Hamburg* **2009**, 55 – 61.
- [7] T. Takamoto, E. Ikeda, H. Kurita, and M. Ohmori. Over 30% efficient ingap/gaas tandem solar cells. *Applied Physics Letters* **1997**, *70*, 381–383.
- [8] K. Yamamoto, A. Nakajima, M. Yoshimi, T. Sawada, S. Fukuda, T. Suezaki, M. Ichikawa, Y. Koi, M. Goto, T. Meguro, T. Matsuda, M. Kondo, T. Sasaki, and Y. Tawada. A thin-film silicon solar cell and module. *Progress in Photovoltaics* **2005**, *13*, 489–494.
- [9] B. Yan, G. Yue, X. Xu, J. Yang, and S. Guha. High efficiency amorphous and nanocrystalline silicon solar cells. *Physica Status Solidi A* **2010**, *207*, 671–677.
- [10] X. Wu, J. Zhou, A. Duda, J. C. Keane, T. Gessert, Y. Yan, and R. Noufi. 13.9%-efficient CdTe polycrystalline thin-film solar cells with an infrared transmission of $\sim 50\%$. *Progress in Photovoltaics: Research and Applications* **2006**, *14*, 471–483.
- [11] <http://www.heliatek.com>.

- [12] P. Liska, K. R. Thampi, M. Grätzel, D. Brémaud, D. Rudmann, H. M. Upadhyaya, and A. N. Tiwari. Nanocrystalline dye-sensitized solar cell/copper indium gallium selenide thin-film tandem showing greater than 15% conversion efficiency. *Applied Physics Letters* **2006**, *88*, 203103.
- [13] S. Wenger, S. Seyrling, A. N. Tiwari, and M. Grätzel. Fabrication and performance of a monolithic dye-sensitized $\text{TiO}_2/\text{Cu}(\text{In},\text{Ga})\text{Se}_2$ thin film tandem solar cell. *Applied Physics Letters* **2009**, *94*, 173508.
- [14] J. Meier, S. Dubail, R. Flückiger, D. Fischer, H. Keppner, and A. Shah. Intrinsic microcrystalline silicon ($\mu\text{c-si:h}$) - a promising new thin film solar cell material. In *Proceedings of the 1st World Conference on Photovoltaic Energy Conversion*. Hawaii, pages 409–412.
- [15] I. Repins, M. A. Contreras, B. Egaas, C. DeHart, J. Scharf, C. L. Perkins, B. To, and R. Noufi. 19.9%-efficient $\text{ZnO}/\text{CdS}/\text{CuInGaSe}_2$ solar cell with 81.2% fill factor. *Progress in Photovoltaics: Research and Applications* **2008**, *16*, 235–239.
- [16] T. Nakada, S. Kijima, Y. Kuromiya, R. Arai, Y. Ishii, N. Kawamura, H. Ishizaki, and N. Yamada. Chalcopyrite thin-film tandem solar cells with 1.5 V open-circuit-voltage. *Proceedings of the IEEE 4th World Conference on Photovoltaic Energy Conversion, Hawaii* **2006**, 400–403.
- [17] W. Shafarman and P. Paulson. Losses in CuInSe_2 -based thin film monolithic tandem solar cells. In *Photovoltaic Specialists Conference, 2005. Conference Record of the Thirty-first IEEE*. pages 231–234.
- [18] M. A. Green, K. Emery, Y. Hishikawa, and W. Warta. Solar cell efficiency tables (version 35). *Progress in Photovoltaics: Research and Applications* **2010**, *18*, 144–150.
- [19] M. Dürr, A. Bamedi, A. Yasuda, and G. Nelles. Tandem dye-sensitized solar cell for improved power conversion efficiencies. *Applied Physics Letters* **2004**, *84*, 3397–3399.
- [20] W. Kubo, A. Sakamoto, T. Kitamura, Y. Wada, and S. Yanagida. Dye-sensitized solar cells: improvement of spectral response by tandem structure. *Journal of Photochemistry and Photobiology A: Chemistry* **2004**, *164*, 33–39.
- [21] M. Murayama and T. Mori. Novel tandem cell structure of dye-sensitized solar cell for improvement in photocurrent. *Thin Solid Films* **2008**, *516*, 2716–2722.
- [22] J. He, H. Lindstrom, A. Hagfeldt, and S.-E. Lindquist. Dye-sensitized nanostructured tandem cell-first demonstrated cell with a dye-sensitized photocathode. *Solar Energy Materials and Solar Cells* **2000**, *62*, 265–273.
- [23] E. A. Gibson, A. L. Smeigh, L. Le Pleux, J. Fortage, G. Boschloo, E. Blart, Y. Pellegrin, F. Odobel, A. Hagfeldt, and L. Hammarstrom. A *p*-Type NiO-Based Dye-Sensitized Solar Cell with an Open-Circuit Voltage of 0.35 V. *Angewandte Chemie International Edition* **2009**, *48*, 4402–4405.
- [24] L. Li, E. A. Gibson, P. Qin, G. Boschloo, M. Gorlov, A. Hagfeldt, and L. Sun. Double-layered NiO photocathodes for *p*-type DSSCs with record ipce. *Advanced Materials* **2010**, *22*, 1759–1762.

- [25] A. Nattestad, A. J. Mozer, M. K. R. Fischer, Y.-B. Cheng, A. Mishra, P. Bäuerle, and U. Bach. Highly efficient photocathodes for dye-sensitized tandem solar cells. *Nature Materials* **2010**, *9*, 31–35.
- [26] Y. S. Chen, Z. H. Zeng, C. Li, W. B. Wang, X. S. Wang, and B. W. Zhang. Highly efficient co-sensitization of nanocrystalline TiO₂ electrodes with plural organic dyes. *New Journal of Chemistry* **2005**, *29*, 773–776.
- [27] J. H. Yum, S. R. Jang, P. Walter, T. Geiger, F. Nüesch, S. Kim, J. Ko, M. Grätzel, and M. K. Nazeeruddin. Efficient co-sensitization of nanocrystalline TiO₂ films by organic sensitizers. *Chemical Communications* **2007**, *1*, 4680–4682.
- [28] M. K. Nazeeruddin, F. De Angelis, S. Fantacci, A. Selloni, G. Viscardi, P. Liska, S. Ito, B. Takeru, and M. Grätzel. Combined Experimental and DFT-TDDFT Computational Study of Photoelectrochemical Cell Ruthenium Sensitzers. *Journal of the American Chemical Society* **2005**, *127*, 16835–16847.
- [29] F. Gao, Y. Wang, D. Shi, J. Zhang, M. K. Wang, X. Y. Jing, R. Humphry-Baker, P. Wang, S. M. Zakeeruddin, and M. Grätzel. Enhance the optical absorptivity of nanocrystalline TiO₂ film with high molar extinction coefficient ruthenium sensitizers for high performance dye-sensitized solar cells. *Journal of the American Chemical Society* **2008**, *130*, 10720–10728.
- [30] Y. Cao, Y. Bai, Q. Yu, Y. Cheng, S. Liu, D. Shi, F. Gao, and P. Wang. Dye-sensitized solar cells with a high absorptivity ruthenium sensitizer featuring a 2-(hexylthio)thiophene conjugated bipyridine. *The Journal of Physical Chemistry C* **2009**, *113*, 6290–6297.
- [31] C.-Y. Chen, M. Wang, J.-Y. Li, N. Pootrakulchote, L. Alibabaei, C.-h. Ngoc-le, J.-D. Decoppet, J.-H. Tsai, C. Grätzel, C.-G. Wu, S. M. Zakeeruddin, and M. Grätzel. Highly efficient light-harvesting ruthenium sensitizer for thin-film dye-sensitized solar cells. *ACS Nano* **2009**, *3*, 3103–3109.
- [32] R. W. Birkmire and E. Eser. Polycrystalline thin film solar cells: Present status and future potential. *Annual Review of Materials Science* **1997**, *27*, 625–653.
- [33] S. Seyrling, S. Calnan, S. Bücheler, J. Hüpkes, S. Wenger, D. Brémaud, H. Zogg, and A. N. Tiwari. CuIn_{1-x}Ga_xSe₂ photovoltaic devices for tandem solar cell application. *Thin Solid Films* **2009**, *517*, 2411–2414.
- [34] A. M. Gabor, J. R. Tuttle, D. S. Albin, M. A. Contreras, R. Noufi, and A. M. Hermann. High-efficiency CuIn_xGa_{1-x}Se₂ solar cells made from (In_x,Ga_{1-x})₂Se₃ precursor films. *Applied Physics Letters* **1994**, *65*, 198–200.
- [35] F. Gao, Y. Wang, J. Zhang, D. Shi, M. K. Wang, R. Humphry-Baker, P. Wang, S. M. Zakeeruddin, and M. Grätzel. A new heteroleptic ruthenium sensitizer enhances the absorptivity of mesoporous titania film for a high efficiency dye-sensitized solar cell. *Chemical Communications* **2008**, 2635–2637.

- [36] S. Ito, T. N. Murakami, P. Comte, P. Liska, C. Grätzel, M. K. Nazeeruddin, and M. Grätzel. Fabrication of thin film dye sensitized solar cells with solar to electric power conversion efficiency over 10%. *Thin Solid Films* **2008**, *516*, 4613–4619.
- [37] N. Papageorgiou, W. F. Maier, and M. Grätzel. An iodine/triiodide reduction electrocatalyst for aqueous and organic media. *Journal of the Electrochemical Society* **1997**, *144*, 876–884.
- [38] S. Seyrling, S. Bucheler, A. Chirila, J. Perrenoud, S. Wenger, T. Nakada, M. Grätzel, and A. N. Tiwari. Development of multijunction thin film solar cells. *Proceedings of the 34th IEEE Photovoltaic Specialists Conference (PVSC), Philadelphia* **2009**, 622–625.
- [39] T. Nakada, N. Okano, Y. Tanaka, H. Fukuda, and A. Kunioka. Superstrate-type CuInSe₂ solar cells with chemically deposited CdS window layers. *Proceedings of the IEEE First World Conference on Photovoltaic Energy Conversion, Hawaii* **1994**, 95–98.
- [40] M. Leskelä and M. Ritala. Atomic Layer Deposition Chemistry: Recent Developments and Future Challenges. *Angewandte Chemie International Edition* **2003**, *42*, 5548–5554.
- [41] V. Lujala, J. Skarp, M. Tammenmaa, and T. Suntola. Atomic layer epitaxy growth of doped zinc oxide thin films from organometals. *Applied Surface Science* **1994**, *82-83*, 34–40.
- [42] T. J. Coutts, D. L. Young, and X. N. Li. Characterization of transparent conducting oxides. *MRS Bulletin* **2000**, *25*, 58–65.
- [43] M. Born and E. Wolf. *Principles of optics: electromagnetic theory of propagation, interference and diffraction of light*. Cambridge University Press, Cambridge, UK, 7th edition **1999**.
- [44] K. Ohta and H. Ishida. Matrix formalism for calculation of the light beam intensity in stratified multilayered films, and its use in the analysis of emission spectra. *Appl. Opt.* **1990**, *29*, 2466–2473.
- [45] E. Centurioni. Generalized matrix method for calculation of internal light energy flux in mixed coherent and incoherent multilayers. *Applied Optics* **2005**, *44*, 7532–7539.
- [46] <http://www.fluxim.com>.
- [47] J. W. Bowers, H. M. Upadhyaya, S. Calnan, R. Hashimoto, T. Nakada, and A. N. Tiwari. Development of nano-TiO₂ dye sensitised solar cells on high mobility transparent conducting oxide thin films. *Progress in Photovoltaics: Research and Applications* **2009**, *17*, 265–272.
- [48] M. F. A. M. van Hest, M. S. Dabney, J. D. Perkins, D. S. Ginley, and M. P. Taylor. Titanium-doped indium oxide: A high-mobility transparent conductor. *Applied Physics Letters* **2005**, *87*, 032111.
- [49] S. Seyrling, S. Buecheler, A. Chirila, J. Perrenoud, R. Verma, S. Wenger, M. Grätzel, and A. Tiwari. Towards the development of high efficiency multijunction thin film solar cells. *Proceedings of the 24th European Photovoltaic Solar Energy Conference, Hamburg* **2009**.

Chapter 5

Optical and electrical modeling of dye-sensitized solar cells

5.1 Introduction

In the past years, progress in dye-sensitized solar cell (DSC) research has been significant in mainly two areas: Metal-free and stable organic dyes have been designed, with which device efficiencies of up to 9.8 % have been measured (see references in Chapter 3). This development is key for the future industrial scale-up of inexpensive DSCs. Also, new ternary eutectic melts (ionic liquids) with low viscosity, high conductivity, and fast tri-iodide transport have become very promising redox mediators for solvent-free devices [1, 2]. In particular devices using flexible substrates, where negligible permeation rates through the plastic are required, could profit from advanced ionic liquids.

However, progress in efficiency enhancement has been slow. Since the first report of laboratory-scale device efficiencies over 11 % with ruthenium-complex dyes in 2005 [3], efficiencies have remained in the range of 11.1 % (certified) to 11.5 % [4–7]. The optimization of DSC performance by purely empirical means seems to be reaching limits. A comprehensive optoelectronic DSC simulator, which does not exist to date, could speed up materials and device architecture screening, quantify in detail optical and electric losses, and improve the understanding of DSC device physics.

Numerical simulators are used frequently in other photovoltaic research areas. Crystalline silicon solar cells are routinely optimized by programs like PC1D [8]. Simulators also exist for thin-film solar cells [9–11] and organic solar cells [12]. Good photovoltaic device models fulfill the following criteria:

- The light intensity in the stack is described accurately using coherent and incoherent optics.

- The charge density in the device, $n(x, y, z, t)$, is calculated using the basic semiconductor equations. In the most general case, these are the Poisson equations and the continuity equations for electrons and holes.
- Recombination terms in the continuity equations contain as little parameters as necessary, which are physically meaningful.
- Modeling results simulate different measurements of a test device (e.g. quantum efficiency, $J-V$ curves, current and voltage transients, impedance spectra ...) correctly with the same parameter set.
- Intrinsic optical and electrical parameters that are not directly accessible from measurements can be extracted by fitting to experimental data.
- The model quantifies optical and electric losses.

Modeling of the DSC is complicated by several factors. The photoactive layer constitutes a mixed mesoporous medium with three absorbing materials: anatase TiO_2 , dye molecules, and tri-iodide ions in the electrolyte. The molecular processes of dye excitation, injection into the TiO_2 network, and recombination of excited dye states can not be simulated using semiconductor physics. To obtain the absorption rate, often a simplified, Lambert-Beer-type, exponential absorption is used [13–15]. This approach, however, does not account for multiple reflections occurring at interfaces in the device and neglects coherence effects in thin films (e.g. FTO layers). Charge transport in the TiO_2 film can be described as purely diffusive, since the high concentration of mobile ions in the electrolyte effectively shields long-range electric fields in the mesoporous TiO_2 [16]. Hence, no coupling to the Poisson equations is necessary. The recombination routes from electrons in the TiO_2 film to oxidized species in the electrolyte, however, are still heavily debated. Experiments show, that the charge recombination rate in real devices is not first order, i.e. recombination does not occur only via the TiO_2 conduction band [17]. Charge could be additionally recombining via bandgap surface states [18, 19].

In this chapter, we present a coupled optical and electric DSC model, which was developed in collaboration with Dr. J. Schumacher and colleagues from the Institute of Computational Physics at the Zürcher Hochschule für Angewandte Wissenschaften (ZHAW). The mathematical description was developed jointly by EPFL and ZHAW, measurements and characterizations of the DSC were performed by the author at EPFL, and the source code was developed at ZHAW.

The key elements of the DSC model are shown in Figure 5.1. First, the light intensity perpendicular to the device stack is calculated accurately with a ray-tracing algorithm that accounts for both coherent and incoherent effects. As input, the complex index

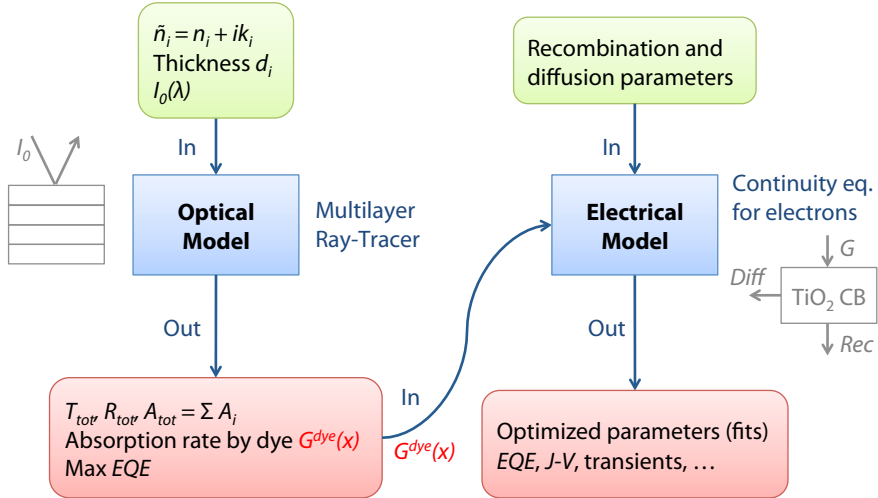


Figure 5.1: Flowchart of the coupled optical and electrical model of the DSC. The dye absorption rate as a function of film thickness, $G^{dye}(x)$ is computed with the optical model, a 1D multilayer ray-tracer. $G^{dye}(x)$ is then used as generation term in the electrical model, a 1D continuity equation for free electrons, to extract intrinsic parameters and simulate experiments.

of refraction and the thickness of each layer must be given. The calculated fraction of the incident light absorbed by the dye yields the spatially resolved dye absorption rate $G^{dye}(x)$ (Section 5.2.1). In the electrical model, the electron density in the TiO_2 film is described with a continuity equation for the electrons (Section 5.2.2). $G^{dye}(x)$ serves a generation rate term. Recombination and diffusion parameters must be given as input. The electrical model solves for the charge density, $n(x, t)$, as a function of film thickness and time. By varying the incident light intensity or an applied electric bias, we can simulate various measurements, including external quantum efficiency (*EQE*), *J-V* curves, current and voltage transients, and electrochemical impedance spectroscopy. In addition, intrinsic parameters, which are difficult to assess experimentally (e.g. injection efficiency, diffusion and trap parameters), can be extracted from fits to experimental data (Section 5.4.2 and Section 5.4.3). Finally, the different optical and electric losses in the as-specified device are separated and quantified (Section 5.4.4). The model is implemented with the software package *Mathematica* (Wolfram Research). Input can be given and output can be visualized with a graphical user interface using *Mathematica Player* (Section 5.4.5).

The DSC model has been experimentally validated for standard materials that have been used in our laboratory and other research groups for several years. The optical constants of the individual layers, in particular of the FTO layers and the mesoporous layer (including the absorption coefficient of the adsorbed dye in the electrolyte envi-

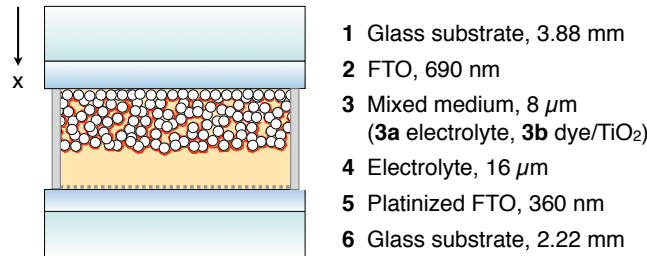


Figure 5.2: Device structure of the dye-sensitized solar cell depicting the six layers used to model the optics in the device.

ronment), were determined as accurately as possible. Well known ruthenium-based dyes were selected as reference systems: the standard **Z907** dye [20] and the bench-mark high absorptivity **C101** dye [4].

In the electrical model, the recombination rate was assumed to be of first order. This leads to a linear differential equation, which can be solved analytically (Section 5.2.2.1). Real devices, however, generally behave non-linearly, as seen from the dependence of photovoltage on illumination intensity [17]. Also, the quantum efficiency ratio for front and back side illumination depends on illumination intensity [14, 15, 21]. An adequate description of the device thus requires a non-linear recombination term in the continuity equation and a numerical solution (Section 5.2.2.2). To simulate time-dependent measurements, the non-stationary case must be solved. The experimentally observed variation of the time constants with illumination intensity [22] is modeled with a distribution of trap-states (Section 5.2.2.3). For small perturbations, however, the recombination term can be linearized around the steady-state solution, which leads to an exponential relaxation of the system (Section 5.2.2.4).

5.2 Theory

5.2.1 Optical model

The optical model calculates the light intensity along the x -axis of a six-layer stack as shown in Figure 5.2, i.e. the local photon flux density normalized to a given incident photon flux. A distinction is made between thick layers, whose optics is treated incoherently, and thin layers, where coherent optics applies. The x -axis is perpendicular to the interfaces. The model is based on a ray-tracing algorithm using geometrical, i.e. incoherent, optics [23]. The ray-tracer randomly generates light rays, which are geometrically traced through the stack, until the intensity of a ray is below a preset threshold

value. In this work, the rays are always perpendicular to the interfaces. The tracing procedure is repeated for different discrete wavelength values. At each interface between thick layers, the ray is split into a transmitted and a reflected beam. The reflectance and transmittance coefficients at the interfaces are calculated from the experimentally determined complex refractive indices of the layers ($\tilde{n}_i(\lambda) = n_i(\lambda) + i k_i(\lambda)$, $1 \leq i \leq 6$). In an absorbing medium of thickness d_i , the ray intensity is attenuated by the factor $\exp(-\alpha_i(\lambda) d_i)$, where $\alpha_i(\lambda) = 4\pi k_i/\lambda$ is the absorption coefficient. Thus, the incident ray is split into a “tree” of rays, which are all traced individually.

The two thin FTO films (layers **2** and **5**) must be treated using coherent optics, since their thickness is in the order of the sunlight coherence length (~ 600 nm) [24]. The transmittance and reflectance coefficients of the two thin FTO films are calculated with a transfer matrix approach [25, 26]. The mixed incoherent-coherent stack is then modeled as shown in Figure 5.3.

The absorption rate of photons per unit volume, $G_\lambda(x)$, for a given wavelength λ at position x is given by the derivative of the net photon flux $\phi_\lambda(x)$. Using the superposition principle, $\phi_\lambda(x)$ is calculated from the sum of the forward flux $\phi_\lambda^+(x)$, which includes all rays propagating in the forward direction, and the backward flux $\phi_\lambda^-(x)$, which includes all rays propagating in the backward direction. The photon absorption rate then is

$$G_\lambda(x) = -\frac{d\phi_\lambda^+(x)}{dx} + \frac{d\phi_\lambda^-(x)}{dx}. \quad (5.1)$$

It is convenient to normalize $G_\lambda(x)$ with respect to an arbitrary incident photon flux ϕ_λ^{inc} ,

$$g(\lambda, x) = \frac{G_\lambda(x)}{\phi_\lambda^{inc}}. \quad (5.2)$$

Light propagation and absorption in the mesoporous medium of layer **3** constitutes a special case. For this layer, the real part n_3 of the complex index of refraction ($\tilde{n}_3 = n_3 + ik_3$) is estimated using the Bruggeman effective medium approximation [27]. The porous medium is described as a mixture of medium **3a** (\tilde{n}_{3a}), the electrolyte, and medium **3b** (\tilde{n}_{3b}), a fictitious TiO_2/dye phase. The effective complex index of refraction, \tilde{n}_3 , then satisfies

$$P \frac{\tilde{n}_{3a}^2 - \tilde{n}_3^2}{\tilde{n}_{3a}^2 + 2\tilde{n}_3^2} + (1 - P) \frac{\tilde{n}_{3b}^2 - \tilde{n}_3^2}{\tilde{n}_{3b}^2 + 2\tilde{n}_3^2} = 0, \quad (5.3)$$

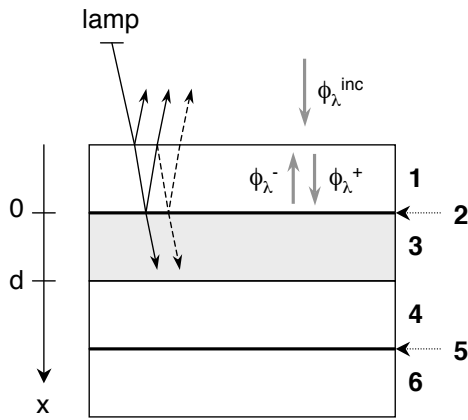


Figure 5.3: Schematic of the six layer stack used for the optical model. Bold numbers refer to the layers described in Figure 5.2. Incident rays are reflected and transmitted at interfaces and traced throughout the stack (thin dark arrows). Rays are perpendicular to the interfaces in the model and drawn at an angle for visualization only. For a given wavelength λ , ϕ_{λ}^{inc} is the photon flux incident on the stack, $\phi_{\lambda}^+(x)$ is the forward flux (the sum of all forward propagating rays), and $\phi_{\lambda}^-(x)$ is the backward flux (the sum of all backward propagating rays) at position x . The two thin FTO films **2** and **5** are represented by optically thin interfaces. Coherent optics are used to calculate the reflectance and transmittance coefficients of the FTO films. Layer **3** constitutes the mixed medium (mesoporous TiO₂, dye, electrolyte) with thickness *d*.

where P is the porosity of the mesoporous film. The parameters P , n_{3a} , n_{3b} , k_{3a} , and k_3 are known from experiments or literature (see Section 5.4.1). k_3 is experimentally determined using a four-flux model analysis [28] on transmittance and reflectance spectra of a simplified stack, where the two FTO electrodes (**1/2** and **5/6**) are replaced by microscope glass slides. Details on the four-flux analysis are given in the Appendix B.2. The unknown parameters n_3 and k_{3b} are back-calculated from Equation (5.3). k_{3b} , however, is needless for the remaining calculations, since it represents the extinction coefficient of a bulk dye/TiO₂ medium with $P \rightarrow 0$.

Using the effective refractive index \tilde{n}_3 , one obtains the normalized photon absorption rate in the photoactive layer **3**, which includes absorption by the dye and the tri-iodide ions in the electrolyte ($g(\lambda, x)$ for $0 \leq x \leq d$, where d is the TiO₂ film thickness). The absorption by the dye is separated from the total absorption using

$$g^{dye}(\lambda, x) = \frac{\alpha_{dye}(\lambda)}{\alpha_3(\lambda)} g(\lambda, x), \quad \text{where } 0 \leq x \leq d. \quad (5.4)$$

Here, $\alpha_3 = 4\pi k_3/\lambda$ is the effective absorption coefficient of all absorbers in layer **3**. α_3 and α_{dye} are determined from a four-flux model analysis (Appendix B.2).

By integrating $g^{dye}(\lambda, x)$ over the TiO_2 film thickness interval $[0, d]$, we find the total fraction of absorbed light by the dye in the film at wavelength λ (or the maximum achievable external quantum efficiency),

$$f_{abs}(d, \lambda) = \int_0^d g^{dye}(\lambda, x) dx. \quad (5.5)$$

The dye absorption rate for a given incident photon flux ϕ_λ^{inc} is

$$G_\lambda^{dye}(x) = \phi_\lambda^{inc} g^{dye}(\lambda, x). \quad (5.6)$$

We assume that the efficiency for electron injection from excited dye states into the TiO_2 conduction band is independent of wavelength ($\eta_{inj}(\lambda) = \eta_{inj}$). The spatially resolved electron generation rate is then

$$G_e(x) = \eta_{inj} G^{dye}(x), \quad \text{where} \quad G^{dye}(x) = \int_0^\infty G_\lambda^{dye}(x) d\lambda. \quad (5.7)$$

In addition, we obtain the maximum achievable short circuit current density using

$$j_{max} = e \int_0^d G_e(x) dx, \quad (5.8)$$

where e is the elementary charge.

Though we have only treated stationary incident illumination here, the model can also account for a time-dependent incident photon flux $\phi^{inc}(\lambda, t)$ yielding a time-dependent generation term $G_e(x, t)$.

The optical model does not account for scattering in its present form. It has been validated with TiO_2 films made from 20 nm sized particles, which scatter light only weakly. An extension of the ray-tracing algorithm to scattering layers should be possible in a successive project.

5.2.2 Electrical model

The output of the optical model, the charge generation function $G_e(x) = \eta_{inj} G^{dye}(x)$, is coupled to an electrical model for free charge carriers. The electrical model is based on a one-dimensional continuity equation for the electron number density in the conduction band of the TiO_2 layer, $n_{cb}(x, t)$, a continuity equation for the trapped electron density $n_t(x, t)$ in bandgap states, and on a purely diffusive transport equation for the electrical

current density j [22]:

$$\frac{\partial n_{cb}}{\partial t} = \frac{1}{e} \frac{\partial j}{\partial x} + G_e(x, t) - U_{cb}(x, t) - r_t + r_d, \quad (5.9)$$

$$\frac{\partial n_t}{\partial t} = r_t + r_d - U_t(x, t). \quad (5.10)$$

$$j = eD_0 \frac{\partial n_{cb}}{\partial x}. \quad (5.11)$$

U_{cb} and U_t are the recombination rates for conduction band and trapped electrons with oxidized species in the electrolyte, respectively. D_0 is the diffusion coefficient for conduction band electrons. r_t is the rate for trapping, and r_d is the rate for detrapping. These processes are illustrated in Figure 5.4.

Here, ionic transport in the electrolyte, the reduction of tri-iodide at the counter-electrode, and the series resistance in the device, are not included. These simplifications are acceptable since experimental devices contain a sufficiently high concentration of iodine in the electrolyte (no mass transport limitation at light intensities of ~ 1 sun), a Pt catalyst at the counter electrode (small overpotential at the counter electrode), a TiCl_4 treated FTO front contact with a “compact” TiO_2 underlayer (little back reaction at the FTO/electrolyte interface), and small overall dimensions (little series resistance).

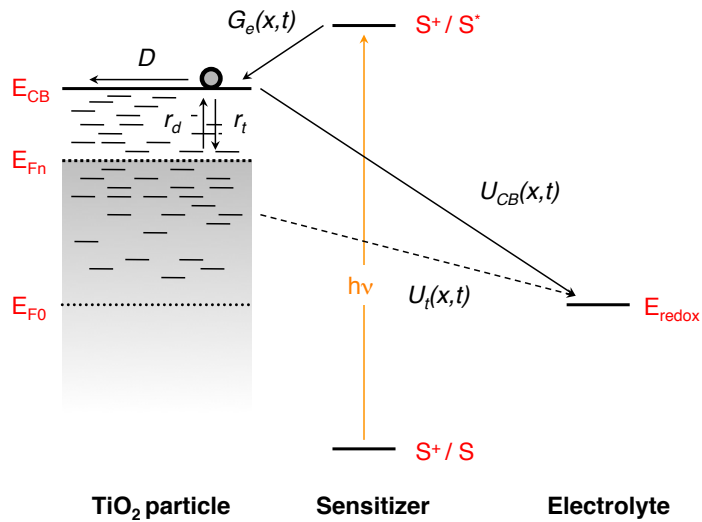


Figure 5.4: Processes described by the electrical model: Charge is generated in the TiO_2 conduction band (CB) with a rate $G_e(x, t)$, where x is the TiO_2 film thickness. Charge in the CB can be trapped or detrapped in localized bandgap states with rates r_t and r_d , respectively. Charge recombines with tri-iodide in the electrolyte via the CB with a rate U_{cb} or via traps close to the TiO_2 surface with a rate U_t . Diffusion in the CB is defined by a diffusion coefficient D .

However, ionic transport, resistances, and the overpotential are included in the model in a simplified manner as discussed in Section 5.2.2.5 and Section 5.2.2.6

In the simplest case — under steady-state conditions ($\partial n_{cb}/\partial t = 0$) and assuming a first-order recombination rate U_{cb} from the conduction band only — these equations can be solved analytically, as shown in the following Section. If a non-linear recombination term for trapped electrons U_t is included, the problem must be solved numerically (Section 5.2.2.2). The effects of trapping and detrapping are discussed in Section 5.2.2.3, and the time-dependent, non-stationary problem ($\partial n_{cb}/\partial t \neq 0$) is discussed in Section 5.2.2.4.

5.2.2.1 Linear recombination

Under steady-state conditions ($\partial n_{cb}/\partial t = 0$ and $G_e(x, t) \equiv G_e(x)$) the continuity equation (5.9) does not include terms due to trapping/detrapping if the quasi-equilibrium approximation is used (one single quasi-Fermi level for conduction band and trapped electrons, see Section 5.2.2.3) [22]. For convenience, we now denote $n_{cb}(x)$ by $n(x)$.

We only consider recombination of conduction band electrons with I_3^- in the electrolyte ($U_t = 0$). We assume a first-order recombination rate in $n(x) - \bar{n}$ [13, 29],

$$U_{cb}(x) = \frac{n(x) - \bar{n}}{\tau_0}. \quad (5.12)$$

Here, τ_0 is the lifetime of the conduction band electrons and \bar{n} is the electron number density at equilibrium in the dark. Evidence for a first-order reaction, rather than a second-order reaction as has been assumed for some time [30, 31], could be given with transient absorption studies of photoexcited TiO_2 in a I_2/I^- redox mediator. No $I_2^{•-}$ species were detected that would support a second-order reaction scheme. Instead, charge recombination from the TiO_2 probably involves weak dissociative chemisorption of I_2 on the oxide [32].

Combining equations (5.9), (5.11), and (5.12) leads to an inhomogeneous linear differential equation for $n(x)$,

$$L^2 \frac{d^2 n}{dx^2} - (n(x) - \bar{n}) + \tau_0 G_e(x) = 0, \quad (5.13)$$

where $L = \sqrt{D_0 \tau_0}$ is the constant electron diffusion length [22, 29].

The boundary conditions to equation (5.13) are

$$n(0) = N_c f(E_c, E_{F0} + eV) \quad \text{and} \quad \left. \frac{dn}{dx} \right|_{x=d} = 0, \quad (5.14)$$

where V is the photovoltage, N_c is the total density of conduction band states, f is the Fermi-Dirac distribution, E_c is the conduction band energy, and E_{F0} is the Fermi level in the dark. The photovoltage V corresponds to the internal cell voltage given by

$$V = \frac{1}{e} (E_{Fn}(0) - E_{F0}), \quad (5.15)$$

where $E_{Fn}(0)$ is the electron quasi-Fermi energy at $x = 0$. Setting $V = 0$, we obtain the short-circuit case.

The solution of the homogeneous part of equation (5.13) is given by

$$n_h(x) = a e^{-x/L} + b e^{x/L}, \quad (5.16)$$

where a and b are constants determined by the boundary conditions. Because the generation rate for excited dye states $G^{dye}(x)$ is known in numerical form, a particular solution of equation (5.13) is computed most conveniently using the Green's function defined by

$$L^2 \frac{d^2 \mathcal{G}}{dx^2} - \mathcal{G}(x) = \delta(x). \quad (5.17)$$

The particular solution then is the convolution of the Green's function¹ with the electron generation rate,

$$n_p(x) = \bar{n} - \tau_0 \int_0^d \mathcal{G}(x-y) G_e(y) dy. \quad (5.18)$$

From the complete solution

$$n(x) = n_h(x) + n_p(x), \quad (5.19)$$

¹The Green's function in equation (5.17) is calculated using the Fourier transform and is given by

$$\mathcal{G}(x) = -\frac{1}{2L} [H(-x) \exp(x/L) + H(x) \exp(-x/L)],$$

where $H(x)$ is the unit step function.

the current density at short-circuit can be calculated by

$$j_{sc} = e D_0 \frac{dn}{dx} \Big|_{x=0} \quad \text{for } V = 0. \quad (5.20)$$

Details of these calculations are found in Appendix B.3.

The external quantum efficiency (EQE) is simulated using monochromatic light of wavelength λ and incident photon flux density ϕ_λ to calculate the injected charge generation rate,

$$G_e^\delta(x) = \eta_{inj} G^{dye,\delta} = \eta_{inj} \phi_{\lambda_0} \int_0^\infty \delta(\lambda - \lambda_0) g^{dye}(\lambda, x) d\lambda \quad (5.21)$$

$$= \eta_{inj} \phi_{\lambda_0} g^{dye}(\lambda_0, x). \quad (5.22)$$

The EQE at wavelength λ_0 is then derived from the calculated j_{sc} by inserting $G_e^\delta(x)$ in equation (5.18),

$$EQE_{\lambda_0} = \frac{j_{sc}}{e \phi_{\lambda_0}}. \quad (5.23)$$

The short-circuit current density j_{sc} and $EQE(\lambda)$ will depend on the direction of illumination, i.e. illumination from the TiO_2 substrate electrode (SE) side or from the electrolyte electrode (EE) side. However, the ratio of the EQE with SE and EE illumination is independent of η_{inj} and only depends on L and the excited dye state generation functions $G_{SE}^{dye,\delta}$ and $G_{EE}^{dye,\delta}$ for SE and EE illumination (Appendix B.3). From the optical model, we find accurate and validated values for the respective charge generation profiles. L can thus be extracted from experimental EQE_{SE}/EQE_{EE} data using a single-parameter fit [14, 15, 29]. Alternatively, L can be obtained from the current density ratios.

The internal quantum efficiency (IQE), which specifies the number of electrons extracted against the number of photons absorbed by the dye in the TiO_2 film, is given by

$$IQE_{\lambda_0} = \frac{j_{sc}}{e \phi_{\lambda_0} f_{abs}(\lambda_0)} = \frac{EQE_{\lambda_0}}{f_{abs}(\lambda_0)}, \quad (5.24)$$

where f_{abs} is the fraction of light absorbed by the dye in the film (equation (5.5)).

The parameters of the electrical model are L , η_{inj} , τ , N_c , and the difference $E_c - E_{F0}$ between the conduction band edge and the Fermi level in the dark. The only relevant parameters in the expressions for j_{sc} and $EQE(\lambda)$ are η_{inj} and L . In the steady-state

linear model, j_{sc} and $EQE(\lambda)$ do not depend on N_c , τ and $E_c - E_{F0}$ at all (Appendix B.3). We can thus extract η_{inj} and L by comparing the simulations for j_{sc} and $EQE(\lambda)$ to experimental data.

5.2.2.2 Non-linear recombination

The linear recombination model predicts a logarithmic relationship between V_{oc} and incident light intensity (equation (B.14)),

$$V_{oc} \propto \frac{k_B T}{e} \ln I_0, \quad (5.25)$$

which corresponds to a slope of 59 mV/decade at 300 K for a plot of V_{oc} against the log of I_0 . This model does not describe accurately the behavior of real devices, which have slopes in the range of 60–120 mV/decade [17]. Also, the model does not describe the observed dependence of the quantum efficiency ratio on illumination intensity [14, 15, 21].

The non-linear behavior in real devices might be due to an additional recombination route via intraband surface states [19]. Recently, the continuity equation has been solved numerically for a non-linear term of the form [18, 21]

$$U(x) = k(n(x) - \bar{n})^\beta, \quad \text{where } \beta < 1. \quad (5.26)$$

Here, k is the rate constant for the back-reaction of injected electrons in the TiO_2 with tri-iodide or the oxidized sensitizer.

Non-linear recombination is not implemented in the electrical model at present, primarily because a recombination term as given in equation (5.26) does not provide physically meaningful information. Instead, recombination via a defined distribution of surface states could be envisaged. This was, however, beyond the scope of this work.

5.2.2.3 Trapping and detrapping

We know from various time-dependent measurements on DSCs — including small-perturbation photocurrent or voltage decays, intensity modulated photocurrent and voltage spectroscopy (IMPS and IMVS), and electrochemical impedance spectroscopy (EIS) — that the time constants of the system depend on the charge density in the TiO_2 film, which is varied with light intensity or applied electrical bias [30, 33–35]. These time constants are interpreted as “effective” diffusion coefficient D_n and electron lifetime τ_n . D_n increases exponentially with increasing charge density, whereas τ_n decreases expo-

nentially. These charge density dependencies are attributed to a distribution of traps in the TiO₂ bandgap.

To include trapping effects in the simulation, we must account for the large fraction of trapped charge density n_t in the TiO₂ film (equation (5.10)). The trapping and detrapping rates r_t and r_d can not be measured experimentally. However, there exists an elegant approach to solving the problem without knowing r_t and r_d explicitly. In the *quasi-static approximation*, r_t and r_d are expected to be so large that the electrons in the conduction band and in trap states remain in a common equilibrium, even when displaced from equilibrium by a small perturbation [22]. n_{cb} and n_t are then described by a Fermi-Dirac distribution around the same quasi-Fermi level E_{Fn} :

$$n_{cb}(x, t) = N_c f(E_c, E_{Fn}), \quad (5.27)$$

$$n_t(x, t) = \int_{E_{F0}}^{E_c} g_t(E) f(E, E_{Fn}) dE, \quad \text{where} \quad (5.28)$$

$$f(E, E_{Fn}) = \frac{1}{1 + \exp \frac{E - E_{Fn}}{k_B T}}. \quad (5.29)$$

N_c is the total density of conduction band states, E_c is the conduction band energy, and E_{F0} is the Fermi level in the dark. Since $n_t = n_t(n_{cb})$, one can use the relation

$$\frac{\partial n_t}{\partial t} = \frac{\partial n_t}{\partial n_{cb}} \frac{\partial n_{cb}}{\partial t} \quad (5.30)$$

and the equations (5.9), (5.10), and (5.11) to find a differential equation for the conduction band charge density n_{cb} ,

$$\frac{\partial}{\partial t} (n_{cb} + n_t) = \left(1 + \frac{\partial n_t}{\partial n_{cb}}\right) \frac{\partial n_{cb}}{\partial t} = D_0 \frac{\partial^2 n_{cb}}{\partial x^2} + G_e(x, t) - U_{cb}(x, t) - U_t(x, t), \quad (5.31)$$

for which r_t and r_d must not be known. The “effective”, trap-mediated, diffusion coefficient is then defined as

$$D_n = \left(1 + \frac{\partial n_t}{\partial n_{cb}}\right)^{-1} D_0. \quad (5.32)$$

With the quasi-static approximation, the factor $\partial n_t / \partial n_{cb}$ can be calculated for any distribution of trap states $g_t(E)$ using [22]

$$\frac{\partial n_t}{\partial n_{cb}} = \frac{\partial n_t}{\partial E_{Fn}} \frac{\partial E_{Fn}}{\partial n_{cb}} = g(E_{Fn}) \frac{k_B T}{N_c}. \quad (5.33)$$

Here, the zero temperature limit of the Fermi function is used for n_t , and the Boltzmann statistics instead of the Fermi function is used for n_{cb} . We note that $\partial n_t / \partial n_{cb}$ is independent of time. Due to the experimental observations, frequently an exponential distribution of trap states is assumed,

$$g_t(E) = \frac{N_t}{k_B T_0} \exp\left(-\frac{E_c - E}{k_B T_0}\right) \quad (5.34)$$

where T_0 is a tailing parameter.

If we assume recombination from the conduction band only ($U_t = 0$) and a *linear* recombination term as in equation (5.12), we can define an “effective” lifetime

$$\tau_n = \left(1 + \frac{\partial n_t}{\partial n_{cb}}\right) \tau_0. \quad (5.35)$$

The electron diffusion length

$$L_n = \sqrt{D_n \tau_n} = \sqrt{D_0 \tau_0} \quad (5.36)$$

is a constant and consistent with what was obtained in Section 5.2.2.1.

5.2.2.4 Time-dependent case

For *small* time-dependent perturbations of the form

$$G_e(x, t) = G_0(x) + \delta G(x, t), \quad \text{where } \delta G \ll G_0, \quad (5.37)$$

we can separate $n(x, t)$ into a stationary and a time-dependent part:

$$n(x, t) = n_0(x) + \delta n(x, t), \quad \text{where } \delta n \ll n_0. \quad (5.38)$$

The recombination rate $U(n(x, t))$ can then be linearized around the stationary solution $n_0(x)$,

$$U(n(x, t)) \approx U(n_0) + \frac{\partial U}{\partial n} \Big|_{n_0} (n - n_0) = U_0(x) + \delta U(x, t). \quad (5.39)$$

Inserting the ansatz (5.38) into the general continuity equation (5.9), we obtain

$$0 = D_0 \frac{d^2 n_0}{dx^2} + G_0(x) - U_0(x) \quad \text{and} \quad (5.40)$$

$$\frac{\partial \delta n}{\partial t} = D_0 \frac{\partial^2 \delta n}{\partial x^2} + \delta G(x, t) - \delta U(x, t) \quad (5.41)$$

for the stationary and the time-dependent part, respectively. Equation (5.41) is a second order linear partial differential equation that can be solved numerically by reducing the equation to one variable with dimensional analysis.

This is a universal approach, which can be used for any kind of recombination term $U(x, t)$ as long as the system reacts linearly to small time-dependent perturbations around a steady state.

For *linear* recombination from the conduction band only, under the quasi-static approximation we find (equation (5.31) and equation (5.12) in equation (5.41)):

$$\tau_n \frac{\partial \delta n_{cb}}{\partial t} = L^2 \frac{\partial^2 \delta n_{cb}}{\partial x^2} + \tau_0 \delta G(x, t) - \delta n_{cb}. \quad (5.42)$$

Here, τ_n (as defined in equation (5.35)), is the effective response time of the system, which depends on the distribution of trap states.

Single perturbations. Small perturbation current- and voltage decay transients can be simulated by calculating the perturbed response δG to a small square-wave light perturbation δI with the optical model and then solving equation (5.42) with the boundary conditions given in equation (5.14).

Periodic perturbations. Periodic sinusoidal perturbations, e.g. voltage perturbations in electrochemical impedance spectroscopy (EIS) or irradiation perturbations in intensity-modulated voltage or photocurrent spectroscopy (IMVS, IMPS), are conveniently treated by taking the Fourier transform of equation (5.42). One then directly finds the expressions for current and voltage in the frequency domain.

In the framework of the project, we have started to implement an impedance spectroscopy solver for conditions in the dark or under steady illumination ($\delta G = 0$). For this, a sinusoidal voltage bias

$$V(\omega) = V_0 + \Delta V \sin(\omega t), \quad \text{where} \quad \delta V \ll V_0, \quad (5.43)$$

is inserted into the boundary condition in equation (5.14). One then finds a solution for the electrical current $I(\omega)$ and can compute the impedance of the system according to $Z(\omega) = V(\omega)/I(\omega)$.

The experimental impedance spectra of standard DSCs exhibit three distinct semi-circles, which are attributed to the charge transfer resistance in the electrolyte (low frequency range), at the TiO_2 /electrolyte interface (middle frequency range), and at the electrolyte/Pt interface at the counter electrode (high frequency range), respectively [36]. Impedance spectra are generally modeled using an equivalent electric circuit based on a transmission line model [37]. To accurately simulate experimental impedance spectra using the continuity equation, the three charge transfer processes must be included, which adds a high degree of complexity. So far, this problem has been treated only in part [38, 39].

5.2.2.5 Ionic transport in the electrolyte

The transport of ions in the electrolyte — namely of I^- , I_3^- , and the cations (K) — is modeled under the assumption that no electric fields are present in the whole electrolyte, i.e. neither in the pores of the TiO_2 , nor in the bulk electrolyte layer.

For a solution of the continuity equation $n(x)$ (from which we find the current density $j_e(x)$ of electrons in the TiO_2 conduction band), we can set up the transport equations for the ionic species:

$$j_K(x) = -eD_K \frac{dn_k}{dx} = 0, \quad (5.44)$$

$$j_{\text{I}_3^-}(x) = -eD_{\text{I}_3^-} \frac{dn_{\text{I}_3^-}}{dx} = \frac{j_e(x)}{2} - \frac{j_t}{2}, \quad (5.45)$$

$$j_{\text{I}^-}(x) = -eD_{\text{I}^-} \frac{dn_{\text{I}^-}}{dx} = -\frac{3j_e(x)}{2} + \frac{3j_t}{2}, \quad \text{and} \quad (5.46)$$

$$j_t = j_e + j_{\text{I}_3^-} + j_{\text{I}^-} + j_K. \quad (5.47)$$

j_t is the total electric current density in the cell. Here, we consider that for two electrons moving through the external circuit one I_3^- ion moves to the cathode and three I^- ions move to the anode. The ionic charge concentrations n_k , $n_{\text{I}_3^-}$, and n_{I^-} are unambiguously determined by taking into account the continuity at the mesoporous TiO_2 /bulk electrolyte interface, the conservation of cations, iodine atoms (using $\text{I}_2 + \text{I}^- \rightarrow \text{I}_3^-$), and total charge (where the trapped electron charge density n_t must be included²).

² Only for the determination of ionic currents do trapped electrons influence the stationary state of the cell.

This approach has the disadvantage that local electroneutrality of charges is not fulfilled. For an accurate description one would have to include the effect of electric fields by coupling the transport equations to Poisson's equations with a drift term (see e.g. [40]) at the cost of computation speed.

In our model we do not incorporate ambipolar diffusion, i.e. spatially constrained diffusion of electrons and ions so that local electrical neutrality is maintained. Kopidakis et. al. have shown that the ambipolar diffusion coefficient D_{amb} essentially equals the diffusion coefficient of D of electrons in the TiO₂ since the concentration of ions largely exceeds the concentration of electrons [41].

5.2.2.6 Resistances and overpotential at the counter electrode

The series and parallel (or shunt) resistance R_s and R_p in a device and the overpotential U_{Pt} at the counter electrode are included following the approach of Ferber [40, 42].

The internal voltage at any point along the $J-V$ curve is given by

$$U_{int} = \frac{1}{e} (E_{Fn}(0) - E_{redox}) = \frac{1}{e} (E_{Fn}(0) - E_{redox}^{oc}) - U_{Pt}. \quad (5.48)$$

Here, E_{redox}^{oc} is the redox energy level under open-circuit conditions, and U_{Pt} is the overpotential at the platinized counter electrode. Under device operation, the redox energy level is given by

$$E_{redox} = E_{redox}^{oc} + U_{Pt}. \quad (5.49)$$

The overpotential U_{Pt} is related to the charge density $j_e(0)$ at the TCO/TiO₂ interface via the Butler-Volmer equation

$$j_e(0) = j_{Pt} \left(\exp \left[(1 - \beta) \frac{U_{Pt}}{k_B T} \right] - \exp \left[-\beta \frac{U_{Pt}}{k_B T} \right] \right), \quad (5.50)$$

where β is a symmetry parameter.

The internal voltage U_{int} is then related to the external voltage U_{ext} via

$$U_{int} = \frac{U_{ext} + R_s I_{int}}{1 + \frac{R_s}{R_p}} = \frac{U_{ext} + R_s A j_e(0)}{1 + \frac{R_s}{R_p}}, \quad (5.51)$$

where I_{int} is the internal current (the generated photocurrent), and A is the surface area of the device.

The equations (5.48), (5.50), and (5.51) are solved for U_{Pt} and $E_{Fn}(0)$. $E_{Fn}(0)$ is then used as a boundary condition in the continuity equation for free electrons.

5.3 Experimental

Device preparation. Complete test devices, as shown in Figure 5.2, were fabricated following the standard procedures described in Section 2.1.2. The FTO-coated top glass electrode (Nippon Sheet Glass, $10 \Omega/\square$), was first immersed in an aqueous $TiCl_4$ solution to produce a thin TiO_2 charge blocking layer. An $8\text{--}10 \mu m$ thick mesoporous layer of 20 nm sized TiO_2 particles was then screen-printed on the treated FTO electrode. The cell geometry was $0.4 \times 0.4 \text{ cm}^2$ for test devices and $2 \times 2 \text{ cm}^2$ for optical characterization. The TiO_2 film was sensitized with the ruthenium-based dye **Z907** [20] or **C101** [4] by overnight immersion in a 0.3 mM solution in a mixture of acetonitrile and *tert*-butanol (volume ratio 1:1). 0.03 mM chenodeoxycholic acid was added as coadsorbant to the **C101** dye solution to prevent aggregation [4]. The cell was sealed with a thermally platinized FTO counter electrode (TEC15, Pilkington, $15 \Omega/\square$) using a $25 \mu m$ thick polymer spacer (Surlyn, DuPont). The void was then filled with an acetonitrile-based iodide/tri-iodide electrolyte coded Z960 (see page 27). In some cases, 0.05 mM LiI was added to the electrolyte.

Optical characterization of layers. The thickness of the glass substrates (layers **1** and **6**) was measured with a digital micrometer. To determine the complex refractive index of the glass substrates ($\tilde{n}_1 = n_1 + ik_1$ and $\tilde{n}_6 = n_6 + ik_6$), the FTO films were removed with hydrochloric acid and zinc powder. The complex refractive indices were then extracted by fitting the Fresnel equations to measured transmittance and reflectance spectra (Appendix B.1). Transmittance and reflectance spectra were measured with a spectrophotometer (Varian Cary 5) equipped with an integrating sphere.

The thickness of the FTO films (layers **2** and **5**) was estimated from cross-sectional scanning electron micrographs. The real part of the refractive index of the top FTO layer **2** (n_2) was determined using a spectroscopic ellipsometer (SOPRA GES5E). Beforehand, the strongly textured surface of the FTO was polished using chemical mechanical planarization to minimize depolarization of the incident light beam [43]. n_2 was extracted by fitting the ellipsometric data to a Cauchy-model, yielding values in good agreement with reported data [43]. Extraction of k_2 requires an accurate fitting model taking into account high-energy photon bandgap absorption and low-energy photon absorption by free charge carriers. Our models were not accurate enough to extract reasonable values

for k_2 . Instead, k_2 was obtained by fitting measured transmittance and reflectance spectra using the optical model and the extracted n_2 . For the bottom FTO film (layer **5**), the refractive index was set to $n_5 = n_2$, and k_5 was determined with the same method as k_2 . The thin layer of platinum particles on the bottom electrode is virtually transparent and its optical effect was thus neglected in this study.

The layer **3**, consisting of the dye-sensitized mesoporous anatase TiO_2 and the electrolyte permeating the pores, was treated as a Bruggeman effective medium [27] (see Section 5.2.1). The TiO_2 film thickness was measured with a Alpha-Step 500 profilometer (KLA-Tencor), and its porosity was measured with a surface area analyzer (Micromeritics ASAP 2000) using the BET method ($P = 0.68$). For the bulk electrolyte medium **3a**, n_{3a} was taken from literature values for acetonitrile [44], and k_{3a} was derived from absorbance measurements of tri-iodide in acetonitrile, which is the only absorbing species in the electrolyte. For the fictitious TiO_2 /dye medium **3b**, n_{3b} was taken from literature values for anatase [45]. The effective imaginary index k_3 was obtained from a four-flux model analysis [28] on transmittance and reflectance spectra of a simplified stack, where the two FTO electrodes (**1/2** and **5/6**) were replaced by soda-lime microscope glasses (Menzel Gläser).

The complex index of refraction of the electrolyte layer **4** was set to $\tilde{n}_4 = \tilde{n}_{3a}$.

Photovoltaic characterization The external quantum efficiency of test devices was measured using chopped monochromatic light (4 Hz) and a white light bias (10 mW cm^{-2}) as described in Section 2.2.1. The current-voltage curve of devices was measured with irradiation from a 450 W xenon lamp matched to AM 1.5G with filters as described in Section 2.2.2. All measurements were performed with a metal mask with an aperture area of 0.25 cm^2 , which was slightly larger than the TiO_2 film area of 0.16 cm^2 , to optimally capture the direct and diffuse incident light and to minimize measurement artifacts [46].

5.4 Results and discussion

5.4.1 Optical simulations

Optical constants of individual layers. The extracted complex refractive indices of the six layers used as input for the optical model are shown in Figure 5.5.

The glass substrates (layers **1** and **6**) clearly have a higher refractive index than typical soda-lime microscope glass (n_M). This increases the reflection losses at the first

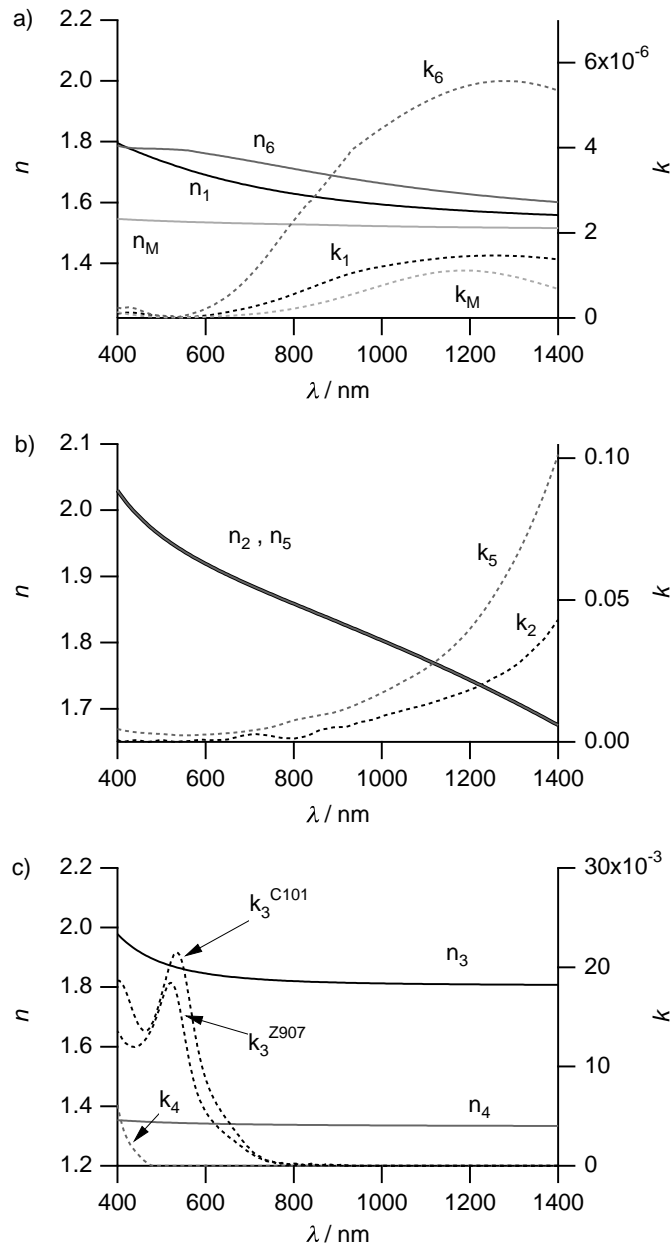


Figure 5.5: Extracted complex refractive indices of the layers **1–6** of a complete dye-sensitized solar cell used as input for the optical model (Figure 5.2). a) Values for the glass substrates (**1** and **2**) and the reference soda-lime microscope glass (n_M , k_M) were obtained from fits of the Fresnel equations to measured transmittance and reflectance spectra. b) The n of the FTO films (**2** and **6**) were derived from spectroscopic ellipsometry, and k from fits to transmittance and reflectance spectra with the determined n fixed. c) the $\text{TiO}_2/\text{dye}/\text{electrolyte}$ layer **3** was described with a Bruggemann effective medium approximation. $k_3^{\text{Z}907}$ and $k_3^{\text{C}101}$ were derived from a four-flux model analysis ($k_3^{\text{Z}907} = 1.84 \times 10^{-2}$ at 521 nm, $k_3^{\text{C}101} = 2.15 \times 10^{-2}$ at 534 nm). For the electrolyte layer **4**, the refractive index of acetonitrile and the extinction coefficient of tri-iodide were used.

air/glass interface. Also, the extinction coefficient is quite high in the infrared region. For layer **6**, k_6 is about six times larger than for soda lime glass (k_M).

The complex refractive indices of the FTO films (layers **2** and **5**) are in good agreement with previously published data [43]. Though k_2 is about half as large as k_5 , the absorptance of the two films is in the same range, since layer **2** is about twice as thick as layer **5**.

The refractive index n_3 of the mesoporous medium $\text{TiO}_2/\text{dye}/\text{electrolyte}$ (layer **3**) lies between the refractive index of anatase (~ 3.1 at 400 nm) [44] and acetonitrile (n_4), reflecting the volume ratios of the porous TiO_2 and the pore-filling electrolyte.

The imaginary parts of the refractive index of layer **3**, k_3^{Z907} and k_3^{C101} , include the absorption of the dye (**Z907** or **C101**) and tri-iodide in the pores (see Appendix B.1 for values of the absorption coefficients of the dye only). The magnitude and maxima agree well with reported values [4]. We note, that k_3^{Z907} and k_3^{C101} were extracted from a complete system ($\text{TiO}_2/\text{dye}/\text{solvent}$). Spectral shifts due to deprotonation of the dye after adsorption on the TiO_2 surface and due to polarization effects by the surrounding solvent are thus implicitly accounted for. The absorption in the electrolyte (k_4) is only due to tri-iodide. We confirmed with absorbance measurements that the other species in the electrolyte do not absorb in the range of interest.

The calculated total reflectance (R_{tot}) and transmittance (T_{tot}) spectra of individual layers using the complex refractive indices of Figure 5.5 are compared to measured spectra in air in Figure 5.6. The agreement is excellent for the glass substrates (Figure 5.6a and Figure 5.6b). The surface of the top FTO (layer **2**) is strongly textured, causing substantial diffuse transmittance and reflectance of the top electrode (layers **1/2**) below 800 nm (Figure 5.6c). In complete devices, however, only negligible diffusive components are visible in the measured T_{tot} and R_{tot} spectra since the optical contrast at the FTO/ TiO_2 interface is smaller than at the FTO/air interface. The spectra of the FTO electrode **1/2** cannot be well reproduced with a two-layer stack, since the optical model does not account for surface scattering. With the addition of a fictitious third Bruggemann effective mixed medium layer FTO/air of 55 nm ($P = 0.5$) the spectrum can be well simulated (Figure 5.6d). The polished sample shows no more scattering but clear interference fringes instead, and the spectra can be well simulated with a two-layer model. The surface of the bottom electrode (layers **5/6**) is smooth (negligible diffuse components), but interference fringes are not well pronounced (Figure 5.6e). In this case the simulation is less accurate. The simulation of the spectra of the microscope glass slide used for the determination of k_3 with the four-flux model (see Section 5.2.1 and Appendix B.2) is also shown.

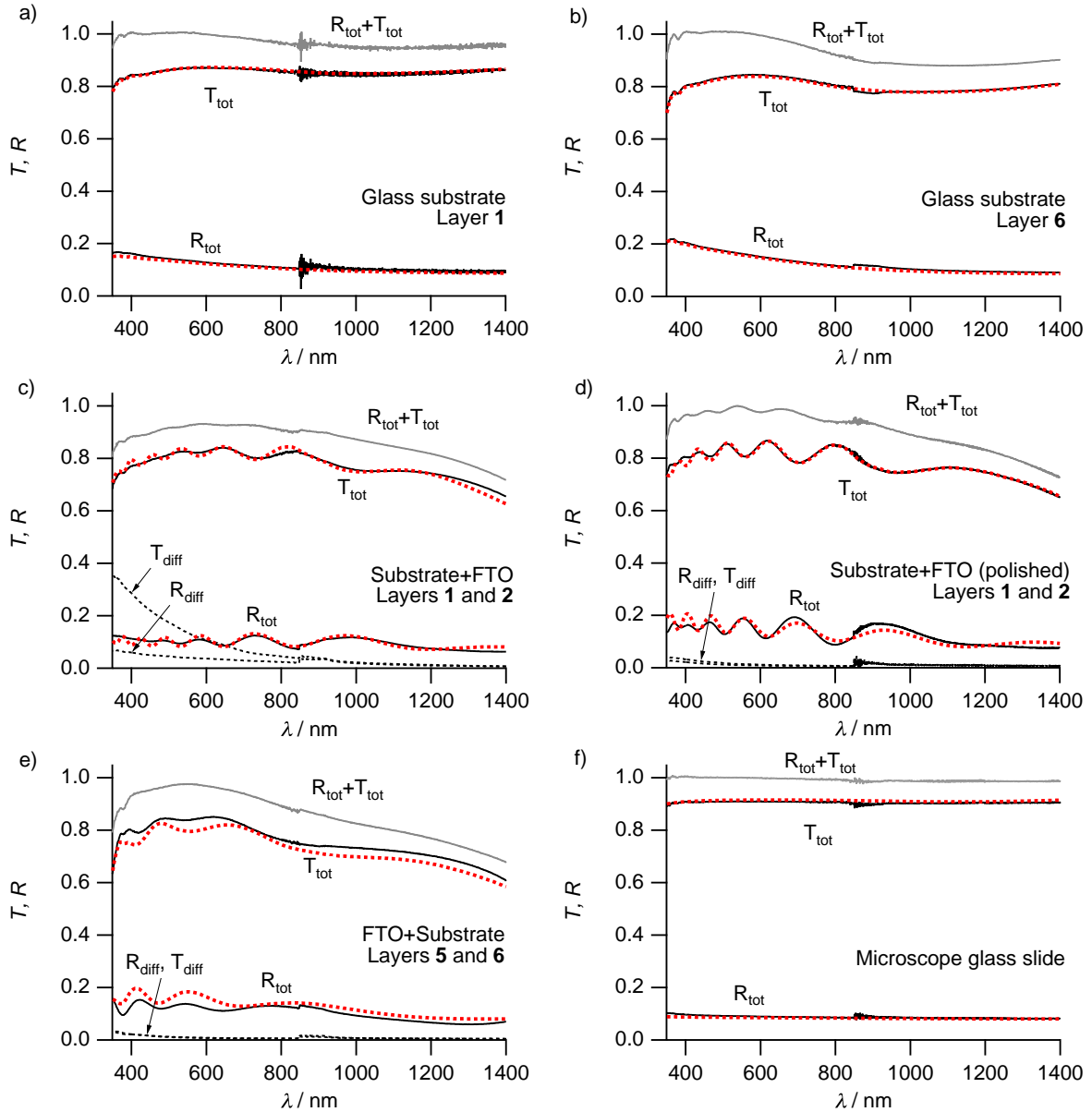


Figure 5.6: Measured and simulated T and R spectra of different layers. Measurements are represented by bold dark lines and simulations by red dashed lines. a,b) The spectra of the glass substrates (layers **1** and **6**) show no diffusive components ($T_{\text{diff}}, R_{\text{diff}} \sim 0$). c) The diffuse transmittance, T_{diff} , of the FTO electrode (stack **1/2**) is quite high for $\lambda < 800$ nm due to the structured surface of the FTO film. The stack is simulated with an additional Bruggemann effective mixed medium layer (55 nm) with porosity $P = 0.5$ between the FTO (642 nm) and the air. d) T_{diff} and R_{diff} almost vanish for the polished sample, and T_{tot} and R_{tot} are well simulated with a two-layer stack only (FTO 650 nm). e) The bottom electrode (stack **5/6**) can not be simulated perfectly. f) The spectra of the microscope glass slide are simulated accurately.

Optical simulations of complete devices. Now that the thickness and the complex refractive index of each layer in the DSC stack (Figure 5.2) is known, we can simulate the optics in the complete device. The optical model gives us the total reflectance and transmittance, the absorptance in each layer, and the dye absorption rate in the film, $G^{dye}(x)$, as a function of film thickness.

We first validate the optical model by comparing the calculated and measured total transmittance (T_{tot}) and reflectance (R_{tot}) spectra of different devices. In Figure 5.7a we compare the spectra of a complete device with an 8.3 μm thick **Z907**-sensitized TiO_2 film. The illumination is incident from the TiO_2 substrate electrode (*SE*) side. The measured and simulated spectra are in good agreement. We attribute the small differences mainly to the slightly inaccurate optical constants of the FTO films. For illumination from

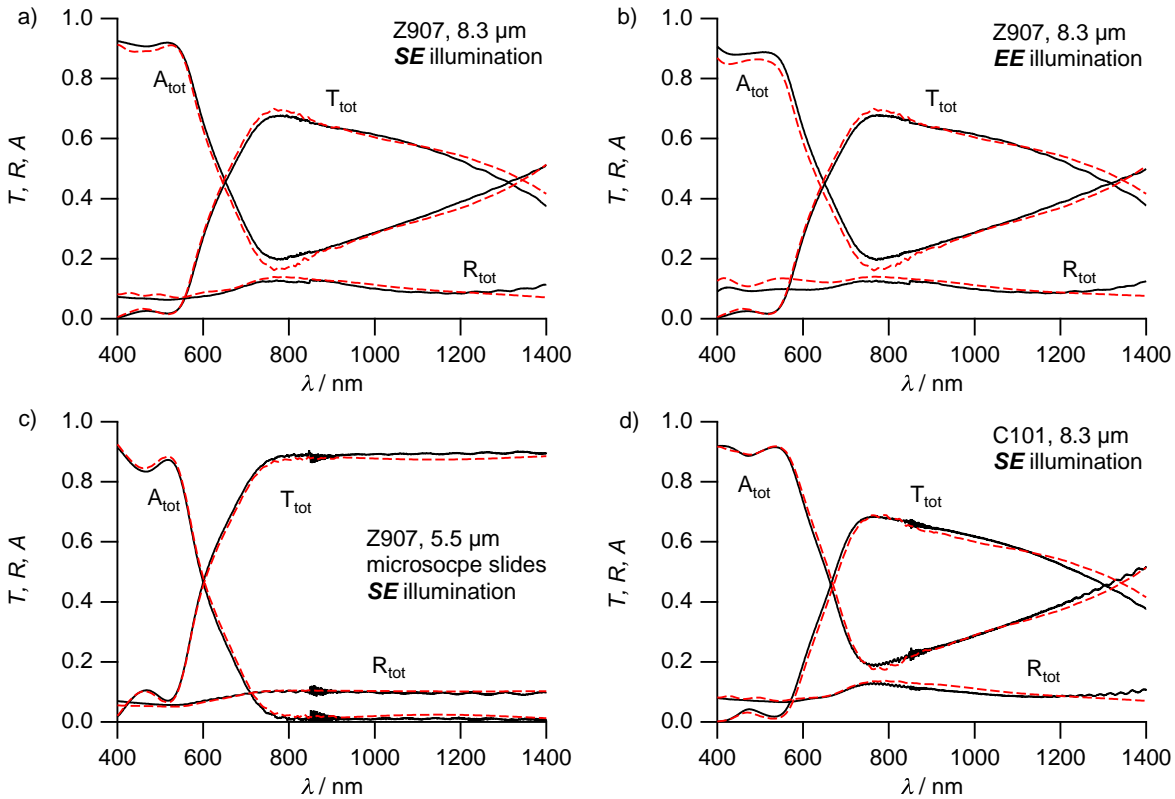


Figure 5.7: Measured and simulated total transmittance (T_{tot}), reflectance (R_{tot}), and absorptance ($A_{tot} = 1 - T_{tot} - R_{tot}$) spectra of different stacks. Measurements are represented by bold dark lines and simulations by red dashed lines. a,b) Complete device as shown in Figure 5.2 with **Z907** dye, illuminated from the substrate electrode (*SE*) or electrolyte electrode (*EE*) side (3.88 mm glass, 697 nm FTO, 8.3 μm TiO_2 with porosity $P = 0.68$, 16.7 μm bulk electrolyte, 360 nm FTO, 2.22 mm glass). c) Simplified stack using microscope glass slides instead of FTO electrodes and **Z907** dye (1.00 mm glass, 5.5 μm TiO_2 with porosity $P = 0.68$, 19.5 μm bulk electrolyte, 1.00 mm glass). d) Device as in a) with **C101** dye.

the electrolyte electrode side (*EE*), which is shown in Figure 5.7b, the model slightly overestimates the total reflectance of the complete device and underestimates the total absorptance for $\lambda < 700$ nm (e.g. at $\lambda = 520$ nm: $R_{meas} = 0.096$, $R_{sim} = 0.128$, $A_{meas} = 0.857$, and $A_{sim} = 0.887$, i.e. a misestimation of about 3 %). This is clearly due to the inaccurate refractive indices of the back electrode (layers **5** and **6**), as the simulation of a device with microscope glass slides instead of FTO electrodes shows excellent agreement with the measurements (Figure 5.7c). The optics in the mixed mesoporous medium can thus be well described by a Bruggemann effective medium approach. The optical model was also validated with spectra of a device with **C101** dye (Figure 5.7d).

Optical loss analysis. The optical model is very helpful to quantify the different optical loss channels. This is exemplified for a device with an 8.3 μm TiO_2 film and **Z907** dye in Figure 5.8. The calculated R_{tot} , the absorptance in each layer (A_i , where $1 \leq i \leq 6$), and T_{tot} are shown in a stack diagram for illumination incident from the substrate electrode (*SE*, Figure 5.8a) or the electrolyte electrode (*EE*, Figure 5.8b) side.

We find $R_{tot} + \sum A_i + T_{tot} = 1$ in accordance with energy conservation. T_{tot} is independent of illumination direction. R_{tot} and A_i , however, strongly depend on the illumination direction. We see for instance, that the reflection loss for *EE* illumination is larger than for *SE* illumination since the optical contrast is higher at the air/**6** interface ($n_6 > n_1$). The absorptance losses in the glass substrates and in the FTO films in the visible region are uncritical for *SE* illumination, but are not negligible for *EE* illumination, which is mainly due to the high values of k_5 and k_6 . In the infrared region the absorptance losses are substantial. The accurate, layer-resolved quantification of these losses could become useful for the optimization of tandem solar cells, where a DSC is used as top cell, and the transmitted near-infrared light is absorbed by a bottom cell (see Chapter 4 and references therein).

The absorptance in the photoactive layer **3** is separated into the absorptance by the dye, $A_{dye}(\lambda) = f_{abs}(\lambda)$, and the absorptance by the remaining components, A'_3 (mostly tri-iodide in the pores, but also some impurities in the TiO_2 , see Figure B.3). A_{dye} and A'_3 are labeled as **3_{dye}** and **3_{elec}** in the Figures, respectively. As can be seen in Figure 5.8a, light absorption by tri-iodide in the pores (**3_{elec}**) is not negligible for *SE* illumination. Only very little light is absorbed in the subsequent bulk electrolyte layer (**4**). For *EE* side illumination (Figure 5.8b), absorption by the bulk electrolyte layer is substantial and considerably attenuates the amount of light, which can be absorbed by the dye molecules. Absorption by tri-iodide in the pores is marginal. Bulk electrolyte

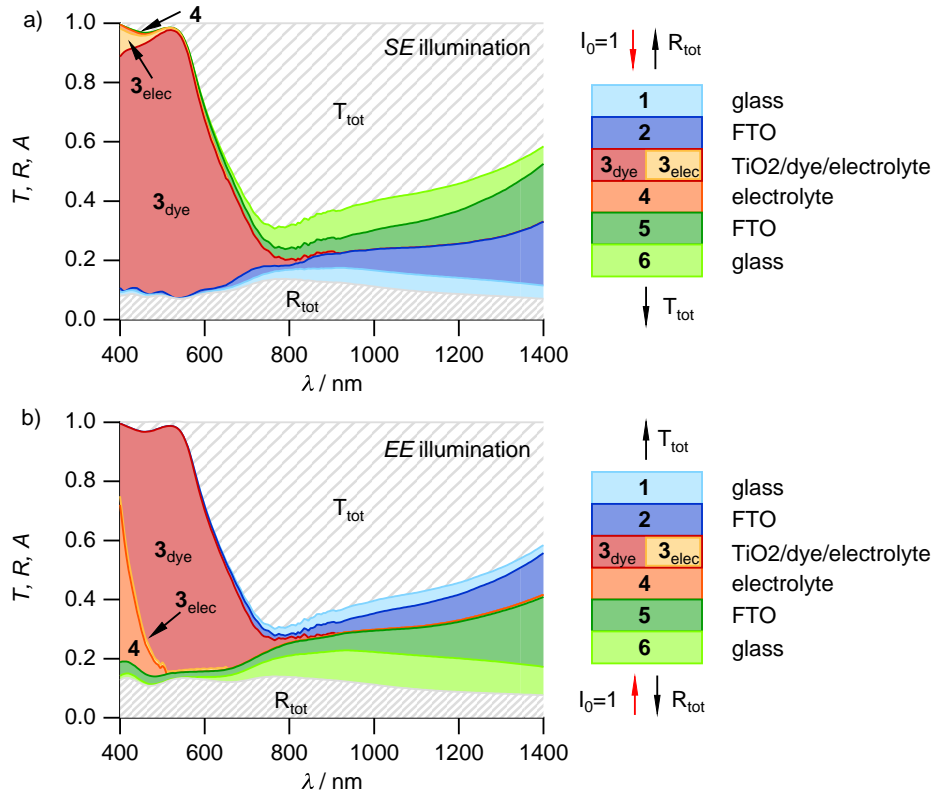


Figure 5.8: Detailed optical loss analysis of a DSC stack as in Figure 5.2 (8.3 μm TiO₂, **Z907** dye). The calculated total reflectance R_{tot} , the absorptance in each layer A_i ($1 \leq i \leq 6$), and the total transmittance (T_{tot}) are stacked in the graphs and add up to one. Simulated for substrate electrode (*SE*, a) or electrolyte electrode (*EE*, b) side illumination. The absorptance of the dye and the electrolyte in the mesoporous layer **3** is separated in the graphs (labeled 3_{dye} and 3_{elec} , respectively).

absorption is a real concern for DSCs that require *EE* side illumination, for instance if a metal foil substrate electrode is used. This loss can only be reduced by decreasing the effective volume of the electrolyte, for instance by replacing the bulk layer with a mesoporous SiO₂ layer infiltrated with the redox mediator [47].

Dye absorption rate $G^{dye}(x)$. With the optical model we can find accurate values for the rate of absorption of photons by the dye per volume element as a function of TiO₂ film thickness ($G^{dye}(x)$, see equations (5.6) and (5.7)). In Figure 5.9, $G^{dye}(x)$ is plotted for a device with **Z907** or **C101** dye (11.2 μm TiO₂) for AM 1.5G illumination (1000 W m⁻²) from the *SE* or *EE* side. For comparison, we show an exponential Lambert-Beer type absorption, as frequently used in other DSC models [14, 15, 21]. For

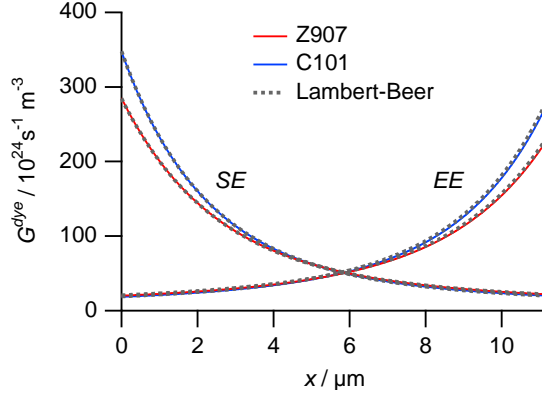


Figure 5.9: Comparison of the dye absorption rate $G^{dye}(x)$ for dyes **Z907** and **C101** for AM 1.5G irradiance from the *SE* or *EE* side. $G^{dye}(x)$ is calculated with the optical model (colored lines), and with the Lamber-Beer type approximation (grey dotted lines). TiO_2 film thickness $d = 11.2 \mu m$.

SE and *EE* illumination, the generation rate for excited dye states is approximated by

$$G_{SE} = (1 - R_{NSG}) \alpha_{dye} \phi_{inc} e^{-(\alpha_{dye} + \alpha_{redox})x} \quad \text{and} \quad (5.52)$$

$$G_{EE} = (1 - R_{TEC}) T_{Pt} T_{redox} \alpha_{dye} \phi_{inc} e^{-(\alpha_{dye} + \alpha_{redox})(d-x)}, \quad (5.53)$$

where R_{NSG} and R_{TEC} are the total reflectance of the front and back electrode measured in air (see Figure 5.6c and Figure 5.6e), α_{dye} and α_{redox} are the absorption coefficients of the dye and the tri-iodide in the pores, respectively, T_{Pt} is the transmittance of the Pt layer on the counterelectrode (for our thermal Pt depositions $T_{Pt} \sim 1$), and T_{redox} is the transmittance of the electrolyte bulk layer 4.

We find that G^{dye} is, surprisingly, quite similar for both calculation methods. For **Z907**, the maximum short-circuit current obtained with the ray-tracer is 14.72 mA cm^{-2} for *SE* illumination and 12.53 mA cm^{-2} for *EE* illumination. With the Lambert-Beer calculation one finds 14.46 mA cm^{-2} for *SE* illumination and 12.89 mA cm^{-2} for *EE* illumination. These differences are within experimental error.

We can thus conclude that the Lambert-Beer type generation function used by others [14, 15, 21] is approximately valid. However, the optical model based on the ray-tracing algorithm provides an unprecedented tool for the detailed analysis of optical losses, as has been demonstrated in the previous paragraph.

5.4.2 Steady-state electrical simulations

The dye absorption rate $G^{dye}(x)$, which is accurately calculated for *SE* and *EE* illumination with the optical model, is now inserted as a source term into the continuity equation (5.13) for free electrons to calculate the steady-state behavior of the device at short-circuit, i.e. the external quantum efficiency (*EQE*) and the short-circuit current density (j_{sc}). The free fitting parameters are the diffusion length L and the injection efficiency η_{inj} .

We analyzed three different cell systems with a TiO_2 film thickness of $d = 11.2 \mu m$: 1) **Z907** dye, 2) **C101** dye, and 3) **C101** dye and 0.05 M Li in the electrolyte. L was determined with a single-parameter fit from the ratio of the measured short-circuit current densities for *SE* and *EE* illumination. η_{inj} was subsequently determined with the fixed L by a single-parameter fit to the short-circuit current for *SE* illumination vs. incident illumination intensity (Figure 5.10).

In Figure 5.11 we plot the measured and calculated *EQEs* of these cell systems for illumination from the *SE* or *EE* side. We also show the fraction of absorbed light by the dye, $f_{abs} = EQE_{max}$. The extracted parameters L and η_{inj} for each system are given in Table 5.1. The maximum obtainable photocurrent for AM 1.5G irradiance ($j_{max}^{AM1.5G}$) calculated with the optical model, the measured current under Xe lamp illumination (j_{meas}^{Xe}), and the calculated current for AM 1.5G ($j_{calc}^{AM1.5G}$), from the electrical model and the respective L and η_{inj} , are also tabulated.

For the systems **Z907** and **C101** without Li ions in the electrolyte, there is a large difference between the maximum and the measured *EQE*. For the device with **Z907**, under *SE* side illumination, 91 % of the incident photons are absorbed by the dye at

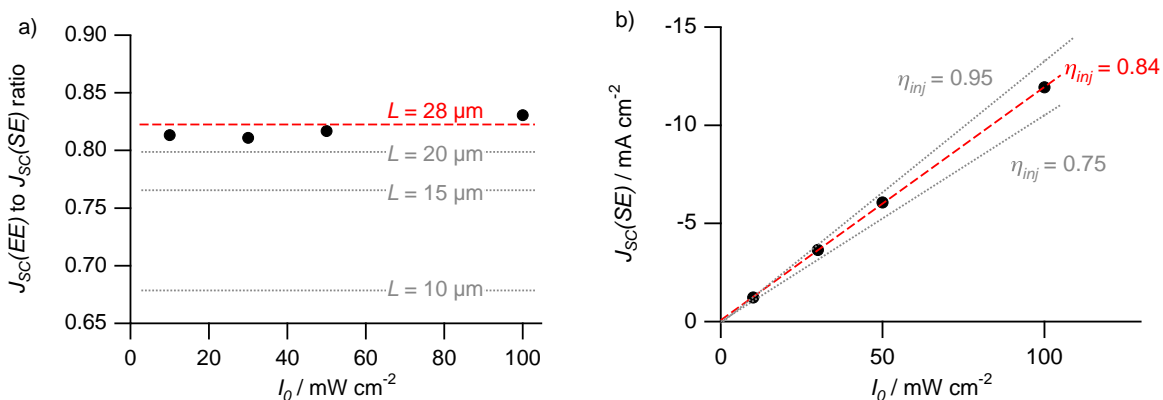


Figure 5.10: Illustration of the steady-state parameter extraction routine from measured data for the device with **Z907** dye. a) Extraction of L from the current density ratios for *SE* and *EE* illumination. b) Extraction of η_{inj} from the current vs. irradiance relationship.

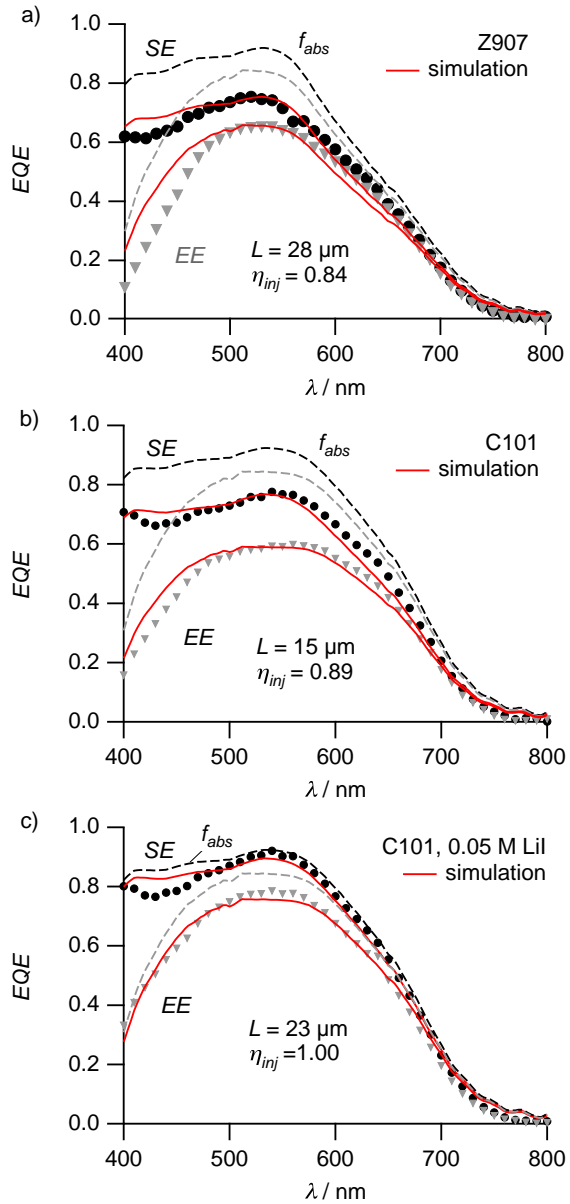


Figure 5.11: Measured EQE of different cells for illumination from the *SE* side (dark circles) or the *EE* side (grey triangles). TiO_2 film thickness $d = 11.2 \mu\text{m}$. a) **Z907** dye, b) **C101** dye, c) **C101** dye with 0.05 M LiI in the electrolyte. The calculated fraction of absorbed light f_{abs} (dashed lines) is shown for both illumination cases. Red bold lines are best fits to experimental data.

520 nm, but only 75 % of the photons are extracted as electrons in a real device. This corresponds to an *absorbed photon-to-current conversion efficiency* or *internal quantum efficiency* (*IQE*) of 82 %. In contrast, the device with the high absorptivity **C101** dye and additional lithium in the electrolyte has an *IQE* of 97 % at 520 nm under *SE* side illumination (see Table 5.1).

Absorbed photons may be lost by the following mechanisms:

1. Dye aggregates are present that absorb light but do not inject into the TiO_2 .
2. Excited dyes relax back to their ground state and do not inject ($\eta_{inj} < 1$).
3. Injected electrons in the TiO_2 conduction band recombine with oxidized dye species.
4. Injected electrons recombine with tri-iodide at the TiO_2 /electrolyte interface.

Dye aggregates are improbable since desorption studies suggest a TiO_2 surface coverage of $\leq 100 \%$.

The photoinduced injection of electrons from the excited dye into the TiO_2 conduction band seems to be restricted for both dye systems. A low injection yield for **Z907** ($\eta_{inj} \sim 0.9$) has also been observed with laser transient absorbance measurements in ionic liquid. However η_{inj} approached unity if Li ions were added to the electrolyte [48]. This “Li-effect” was also observed with other ruthenium bipyridine complexes [49] and with time-resolved single photon counting [50] and other *EQE* ratio studies [15]. The improved injection yield is attributed to a lowering of the TiO_2 conduction band subse-

Table 5.1: Comparison of maximum ($j_{max}^{\text{AM1.5G}}$), measured (j_{meas}^{Xe}), and calculated ($j_{calc}^{\text{AM1.5G}}$) short-circuit photocurrent densities for different cell systems under front (*SE*) or back (*EE*) side illumination. TiO_2 film thickness $d = 11.2 \mu\text{m}$. L and η_{inj} are best fits to experimental j_{sc} data. The internal quantum efficiency is defined as $\text{IQE} = \text{EQE}/f_{abs}$.

Dye	Irrad.	Li	$j_{max}^{\text{AM1.5G}}$	j_{meas}^{Xe}	$j_{calc}^{\text{AM1.5G}}$	L	η_{inj}	IQE
		(M)	(mA cm $^{-2}$)	(mA cm $^{-2}$)	(mA cm $^{-2}$)	(μm)		@520 nm
Z907	<i>SE</i>	–	14.7	11.9	11.9	28	0.84	0.82
	<i>EE</i>	–	12.5	10.0	9.9	28	0.84	0.78
C101	<i>SE</i>	–	15.9	12.6	12.8	15	0.89	0.83
	<i>EE</i>	–	13.6	10.1	9.8	15	0.89	0.70
C101	<i>SE</i>	0.05	15.9	15.1	15.1	23	1.00	0.97
	<i>EE</i>	0.05	13.6	12.1	12.3	23	1.00	0.90

quent to surface adsorption of Li^+ ions, which enhances the driving force for injection. In accordance, we observe that η_{inj} approaches unity when LiI is added to the **C101** system.

Following injection, electrons may recombine with the dye cation. This recombination mechanism is currently not implemented in the model. Nanosecond transient absorption studies on the **Z907** system indicate that a significant fraction of electrons (10–15 %) is recaptured by the dye cations [20]. If this recombination pathway were included, we would obtain a larger diffusion length, but the calculated IQE would remain unchanged. To date, there exist no dye recombination studies for **C101**, but a regeneration yield of 99 % (i.e. 1 % of the injected electrons recombine with the cation) has been reported for a similar system with extended conjugation in the hydrophobic system [51, 52].

The recombination of electrons in the TiO_2 with I_3^- is related to the magnitude of the diffusion length L . We found that recombination with I_3^- is larger in the **C101** system than in the **Z907** system. This was also observed with small perturbation photovoltage decay experiments (Figure 5.12a). Recombination might be enhanced by the formation of an iodine/dye complex at the thiophene units of the **C101** ligands, which would increase the concentration of electrolyte species close to the TiO_2 surface [53, 54]. We also observed that L increases in the **C101** system upon addition of Li ions. This is likely due to improved charge transport in the film because of electrostatic shielding by the positively charged Li ions. Small perturbation current decay measurements also show a

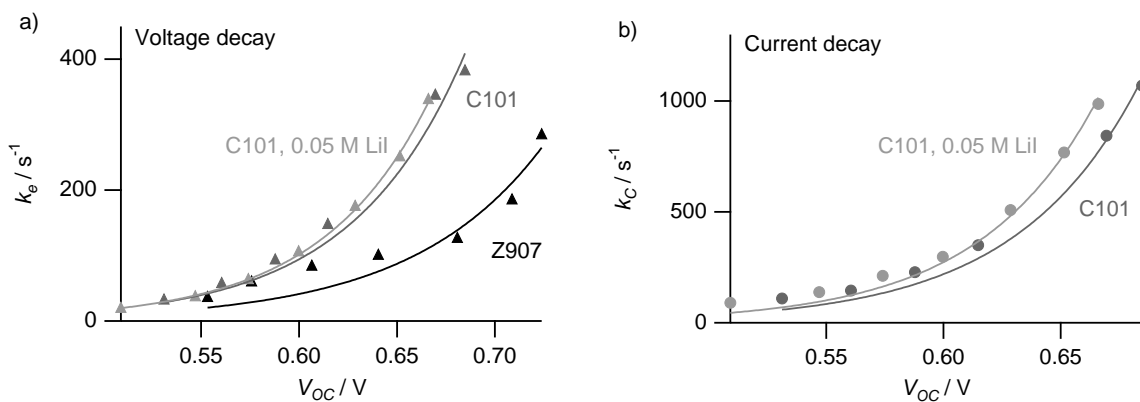


Figure 5.12: a) Charge recombination rate k_e with I_3^- obtained from small perturbation voltage decay transients (**Z907** or **C101** dye, acetonitrile-based electrolyte Z960 with possible addition of 0.05 M LiI, TiO_2 film thickness $d = 9.5 \mu\text{m}$). The **Z907** system with hydrophobic ligands has a markedly reduced recombination rate compared to the **C101** system with the thiophene units in the ligands. We note that k_e can be lower for **C101** in high-efficiency cells [4]. b) Current decay rate k_C obtained from small perturbation current decay transients showing the better transport properties of **C101** when Li ions are added to electrolyte.

more rapid current decay (i.e. charges are extracted more rapidly at the front electrode) when Li is added to the **C101** system (Figure 5.12b).

5.4.3 Time-dependent electrical simulations

Once the diffusion length L and the injection efficiency η_{inj} of a device have been extracted from fits to steady-state measurements (J_{sc} or EQE), the distribution of trap parameters and the electron lifetime can be obtained from the small perturbation photocurrent and voltage decays.

Specifically, the trap distribution N_t and the tailing parameter T_0 can be extracted from fits to current transients measured at various white bias light intensities. The lifetime τ_0 of electrons in the TiO_2 conduction band and the density of conduction band states N_c is extracted from voltage transients at various white bias light intensities.

In Figure 5.13, fits to the current and voltage transients of a device with **Z907** and a TiO_2 film thickness of $9.5 \mu\text{m}$ are shown for illustration purposes. We note, that this device was not particularly efficient ($\eta = 6.7\%$ for *SE* illumination at AM 1.5G). The extracted steady-state parameters were $L = 13 \mu\text{m}$ and $\eta_{inj} = 0.92$. From the current transients (Figure 5.13a) values of $N_t = 1 \times 10^{19} \text{ cm}^{-3}$ and $T_0 = 720 \text{ K}$ were found. The voltage transients (Figure 5.13b) additionally yielded $N_c = 6.4 \times 10^{20} \text{ cm}^{-3}$ and $\tau_0 = 3.2 \text{ ms}$.

The simulation of current and voltage transients, and the extraction of related parameters, clearly gives a more detailed picture of the system and potentially is a valuable tool

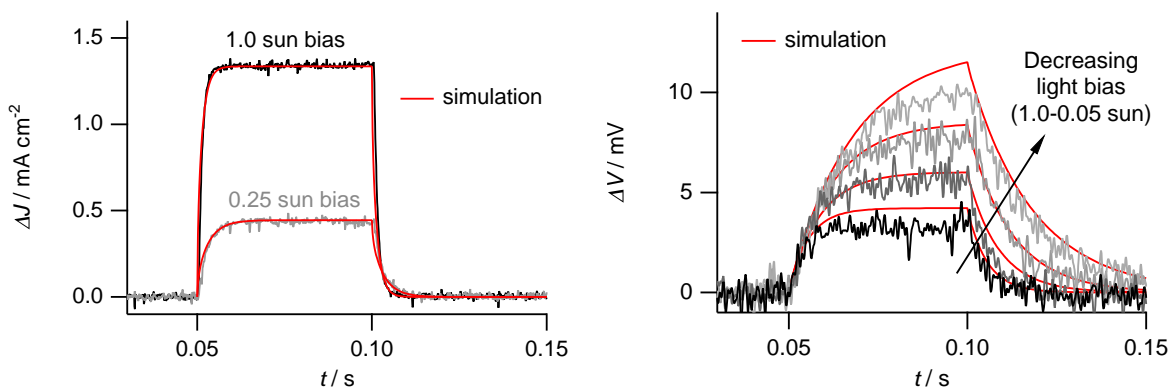


Figure 5.13: Small perturbation current (a) and voltage (b) transients at different bias light intensities of a device with **Z907** (TiO_2 thickness $d = 9.5 \mu\text{m}$). Measurements are depicted by dark and grey solid lines, and simulations are drawn with red lines. The values of the fit parameters are given in the text.

to study the effect of different materials or treatments (e.g. variation of nanostructure, addition of coadsorbants, core-shell coatings) on intrinsic parameters.

5.4.4 Loss analysis

A particularly instructive feature of the coupled optical and electrical DSC model is the quantification of optical and electric losses.

As illustrated in Figure 5.14, only a small fraction of the total incident solar spectrum is converted into electric power ($\sim 10\text{--}11\%$ in high-efficiency DSCs). A large share of the solar flux is lost due to reflection, absorption in materials other than the dye, and transmittance through the cell. Excited dye states might relax back to the ground state (injection loss). After injection, much of the energy of the photon is lost due to thermalization of the injected electron to the TiO_2 conduction band level, and due to the offset between the dye ground state and the redox energy level. Also the electron may recombine with I_3^- in the electrolyte or with dye cations.

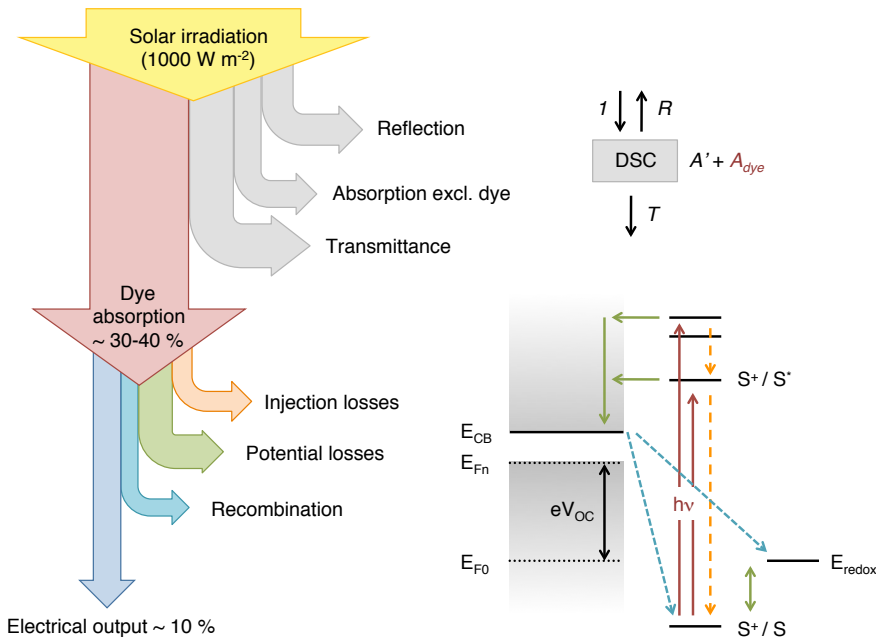


Figure 5.14: Schematic of the various optical and electrical losses in a DSC. A large fraction of the incident irradiation is lost due to reflection, absorption by materials other than the dye, and transmittance. Excited dye states either relax back to the ground state (injection loss) or inject an electron into the TiO_2 conduction band. The final potential difference at the electrodes is given by the quasi-Fermi level E_{Fn} and the redox energy level (potential and recombination losses). At the maximum operating point, a good DSC finally converts about 10 % of the incident irradiation into electrical power.

In the model, losses are quantified in terms of power per unit area. Optical losses are calculated by integrating the product of total reflectance (R_{tot}), transmittance (T_{tot}), and absorptance in materials other than the dye ($A' = 1 - R_{tot} - T_{tot} - f_{abs}$), respectively, with the incident spectral irradiance. The integration boundaries are $\lambda_{min} = 400$ nm and $\lambda_{max} = 800$ nm, since the studied dyes do not absorb above this wavelength³,

$$P_R = \int_{\lambda_{min}}^{\lambda_{max}} R_{tot}(\lambda) I_0(\lambda) d\lambda, \quad (5.54)$$

$$P_T = \int_{\lambda_{min}}^{\lambda_{max}} T_{tot}(\lambda) I_0(\lambda) d\lambda, \quad (5.55)$$

$$P_A = \int_{\lambda_{min}}^{\lambda_{max}} A'(\lambda) I_0(\lambda) d\lambda. \quad (5.56)$$

Injection losses are quantified using

$$P_{inj} = \int_{\lambda_{min}}^{\lambda_{max}} (1 - \eta_{inj}) f_{abs}(\lambda) I_0(\lambda) d\lambda. \quad (5.57)$$

Recombination and potential losses are evaluated at the maximum power point (MPP):

$$P_{rec} = \int_0^d U(x) [E_{Fn}^{mpp}(x = 0) - E_{F0}(x = 0)] dx, \quad (5.58)$$

$$P_{pot} = \int_{\lambda_{min}}^{\lambda_{max}} \eta_{inj} f_{abs}(\lambda) I_0(\lambda) \left(1 - \frac{\lambda}{h c} [E_{Fn}^{mpp}(x = 0) - E_{F0}(x = 0)] \right) d\lambda. \quad (5.59)$$

Here, $U(x)$ is the recombination term as defined in equation (5.12), and $E_{Fn}^{mpp}(x = 0)$ is the calculated quasi-Fermi level under MPP conditions, which is virtually constant across the film thickness. The potential losses P_{tot} are calculated from the energy difference between the harvested photons and the electrons extracted at the anode.

Instead of quantifying the losses in units of power P , they can alternatively be given in terms of current density J (in units of mA cm⁻²). This is obtained from integration over the incident photon flux, instead of the irradiance, and multiplication by the elementary charge.

We give a sample calculation for the two devices treated in Section 5.4.2 (TiO₂ film thickness $d = 11.2$ μm): **Z907** with $L = 28$ μm and $\eta_{inj} = 0.84$ and **C101** with Li in the electrolyte, $L = 23$ μm, and $\eta_{inj} = 1.00$. The electron lifetime for electrons in the TiO₂ conduction band is set to $\tau_0 = 0.5$ ms. We note that trap distribution parameters must

³ In practice, the integration is limited to $\lambda_{max} = 1400$ nm, since the materials are not characterized beyond this wavelength.

not be known for steady-state calculations (Appendix B.3). The incident irradiance is AM 1.5G from the TiO₂ side. The losses are quantified in Table 5.2.

Since the losses are integrated over the wavelength range 400–800 nm, they are compared relative to the AM 1.5G incident irradiance in this range, i.e. a total irradiance of 543 W m⁻². A large fraction of this incident flux is lost due to reflection, transmittance, absorptance by materials, and insufficient injection. These flux losses amount to about 50 % for the **Z907** system and 36 % for the **C101** system. For these particular systems, losses could be reduced with anti-reflecting layers and back reflectors (e.g. a layer of large scattering TiO₂ particles behind the “transparent” mesoporous layer, as used in high efficiency cells). Injection losses can constitute a significant loss channel (close to

Table 5.2: Quantification of different loss channels with the optoelectric DSC simulator. Calculations are for devices with a TiO₂ film thickness $d = 11.2 \mu\text{m}$ and dye **Z907** ($L = 28 \mu\text{m}$, $\eta_{inj} = 0.84$) or **C101** ($L = 23 \mu\text{m}$, $\eta_{inj} = 1.00$). The incident irradiance is AM 1.5G from the TiO₂ side. Losses are integrated from $\lambda = 400\text{--}800 \text{ nm}$. Recombination and potential losses are evaluated at the maximum power point.

Loss channel	Dye	$P / \text{W m}^{-2}$	$J / \text{mA cm}^{-2}$	rel. percent
Incident spectrum	—	543.0	25.9	100.0 %
Reflection	Z907	45.7	2.3	8.4 %
	C101	49.8	2.5	9.2 %
Transmittance	Z907	150.5	8.4	27.7 %
	C101	138.9	7.8	25.6 %
Absorptance	Z907	19.8	1.1	3.6 %
	C101	7.2	0.4	1.3 %
Injection	Z907	52.3	2.3	9.6 %
	C101	0.0	0.0	0.0 %
Recombination	Z907	2.6	0.4	0.5 %
	C101	4.5	0.7	0.8 %
Potential	Z907	196.8	—	36.2 %
	C101	246.7	—	45.4 %
<i>Output</i>	Z907	72.5	11.1	13.4 %
	C101	92.4	14.0	17.0 %

10 % with **Z907**). After injection, a major fraction of the photon energy is lost due to potential losses (about 35–45 %). Surprisingly, only a negligible fraction of energy is lost due to charge recombination with I_3^- in the electrolyte (< 1 %). However, the position of the quasi-Fermi level at the MPP, used for the calculation of losses in equation (5.58) and equation (5.59), also depends on the recombination rate, and it is somewhat difficult to unambiguously differentiate between recombination and potential losses. Nevertheless, these losses must be tackled with the investigation of new redox mediators (with a redox energy level closer to the dye ground state level), the development of tandem systems to reduce thermalization losses (see Chapter 4), and strategies to reducing recombination (e.g. coadsorbants and core-shell structures). Finally, we find a power output of about 72 W m^{-2} for the **Z907** system and 92 W m^{-2} for the **C101** system, which corresponds to a photovoltaic power conversion efficiency of 7.2 % and 9.5 %, respectively⁴.

In the authors opinion, such a comprehensive loss analysis, which is now possible with the optoelectric DSC model, is an invaluable tool to assess the potential for optimization of the DSC and to identify the most promising optimization strategies.

5.4.5 Graphical user interface

The coupled optical and electrical model has been implemented with a graphical user interface in *Mathematica Player*. A screen-shot of a “results” window is shown in Figure 5.16. The following parameters must be given as input:

Material parameters: Dye system (**Z907** or **C101**). Injection efficiency (η_{inj}). Diffusion length of the electrons in the TiO_2 (L). Lifetime of the conduction band electrons (τ_0). Density of conduction band electrons (N_c) and of trapped electrons (N_t). Band gap of the TiO_2 (E_g , for integration of the trap states). Tailing parameter for distribution of trap states (T_0). Diffusion coefficient of the iodide (D_{I^-}), and the tri-iodide ($D_{I_3^-}$) and initial concentrations of the iodide (c_{I^-}) and tri-iodide ($c_{I_3^-}$).

Device parameters: Thickness of the TiO_2 film (d_{TiO_2}) and the bulk electrolyte layer (d_{bulk}). Porosity of the TiO_2 (p_{TiO_2}). Series resistance (R_s) and parallel resistance (R_p). Active surface area of the device (A).

Measurement conditions: Illumination spectrum (AM 1.5G, xe lamp, white or red LEDs) and wavelength range ($\lambda_{min}, \lambda_{max}$). Illumination direction (TiO_2 substrate or electrolyte side). Applied voltage bias, i.e. the working point (V_{ext}). For transient

⁴With respect to a total incident irradiance of 1000 W m^{-2} .

decay data: duration of pulse and intensity (ΔI). For electrochemical impedance: Applied bias (V_{app}), voltage perturbation (ΔV) and frequency range (f_{min}, f_{max}).

The program then yields the following data and functions:

Steady-state calculations: Electron generation rate ($G_e(x)$), fraction of absorbed light ($f_{abs}(\lambda)$), and external quantum efficiency ($EQE(\lambda)$). Charge concentration in the TiO_2 conduction band ($n_e(x)$) and in trap states ($n_t(x)$). Quasi-Fermi level ($E_{Fn}(x)$). Current density of electrons in the TiO_2 ($j_e(x)$) and of iodide ($j_{I^-}(x)$) and tri-iodide ($j_{I_3^-}(x)$) (incl. the charge densities of the ionic species, $n_{I^-}(x)$ and $n_{I_3^-}(x)$). $J-V$ curve of the device.

Time-dependent calculations: Current and voltage transient ($J(t), V(t)$). Impedance spectrum: Nyquist plot ($Re(Z)$ vs. $Im(Z)$) and Bode plots ($\log |Z|$ or phase-shift ϕ vs. radial frequency ω .)

Loss analysis: Wavelength-resolved reflection, transmittance, absorptance, and injection losses. Losses integrated over the spectral range, incl. recombination and potential losses, in units of power ($W\ m^{-2}$) or current density ($mA\ cm^{-2}$).

Postprocessing: HTML documentation of data, ASCII or graphical export.

Several different parameter sets can be defined and calculated in one run to compare the effects of parameter variations on cell performance.

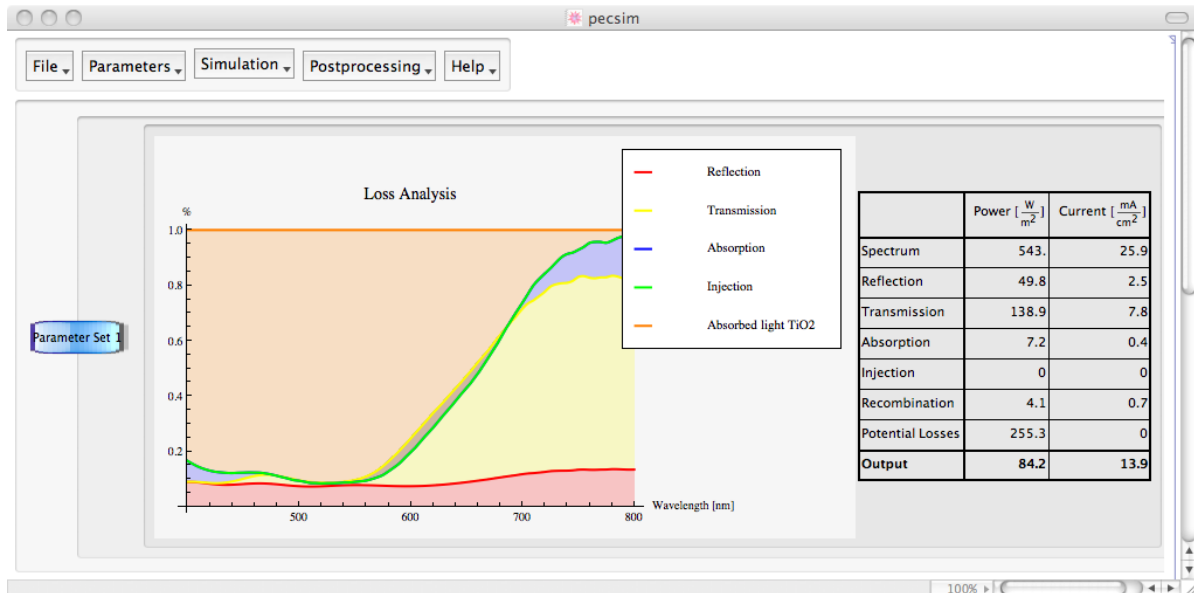


Figure 5.15: Screen-shot of the graphical user interface of the DSC model implemented in *Mathematica Player*. Here, the wavelength-resolved and integrated energy losses in a simulated device are shown in the graph and the table, respectively.

5.4.5.1 Simulation example

To demonstrate the capabilities of the simulator, we compare two parameter sets with different diffusion lengths $L_1 = 30 \mu\text{m}$ and $L_2 = 15 \mu\text{m}$ and otherwise equal parameters. The absorption is calculated for the dye **Z907**. The other simulation parameters are: $\eta_{inj} = 0.9$, $\tau_0 = 0.5 \text{ ms}$, $N_c = 2.5 \times 10^{25} \text{ m}^{-3}$, $N_t = 2.5 \times 10^{25} \text{ m}^{-3}$, $E_g = 3.2 \text{ eV}$, $T_0 = 1047 \text{ K}$, $D_{I^-} = D_{I_3^-} = 8.5 \times 10^{-10} \text{ m}^2 \text{ s}^{-1}$, $c_{I^-} = 0.97 \text{ M}$, $c_{I_3^-} = 0.97 \text{ M}$, $d_{TiO_2} = 8.3 \mu\text{m}$, $d_{bulk} = 16.7 \mu\text{m}$, $p_{TiO_2} = 0.68$, $R_{series} = 1 \Omega$, $R_{par} = 1 \times 10^4 \Omega$. The incident irradiance is AM 1.5G from the TiO_2 side. For transients: white LED bias light (100 mW cm^{-2}) and red LED perturbation light with $\Delta I = 0.1 \text{ sun}$ ($\sim 10 \text{ mW cm}^{-2}$). For impedance spectra: V_{app} = open-circuit voltage, $f_{min} = 10 \text{ Hz}$, $f_{max} = 10'000 \text{ Hz}$.

The output of the sample calculations is shown in Figure 5.16 (steady-state) and Figure 5.17 (time-dependent). With this simple simulation one can already identify a few properties that are characteristic for the device physics of DSCs:

- *EQE* (Figure 5.16a): For the simulation with $L_1 = 30 \mu\text{m}$, the *EQE* amounts to close to 90 % of the fraction of absorbed light at $\lambda = 520 \text{ nm}$, i.e. losses at short-circuit are restrained to injection losses. Recombination losses increase if the diffusion length is in the range of the film thickness ($EQE \approx 85 \%$ at $\lambda = 520 \text{ nm}$ for $L_2 = 15 \mu\text{m}$).
- *Quasi-Fermi level* (Figure 5.16b): The quasi-Fermi level E_{Fn} is flat throughout the film thickness at open-circuit conditions and bent at short-circuit conditions ($E_{Fn} = E_{F0}$ at $x = 0$ is a boundary condition). $E_{Fn}(x = d)$ is lower under short-circuit than under open-circuit conditions. This has also been observed experimentally [55].
- *Conduction band electron density* (Figure 5.16c): The electron density in the TiO_2 conduction band $n_e(x)$ has a similar profile as $E_{Fn}(x)$ under open- and short-circuit conditions, respectively. We note that the charge density at open-circuit is one order of magnitude larger than at short-circuit.
- *Trapped electron density* (Figure 5.16d): The quasi-static approximation (same E_{Fn} for electrons in the conduction band and in traps, see Section 5.2.2.3) implies that a very large fraction of electrons is trapped in intragap states (n_t in this example about 10^3 times higher than n_e).
- *Electronic and ionic currents* (Figure 5.16e): Under short-circuit conditions, the sum of the electronic and ionic current densities yields the short-circuit current J_{sc} of the device (see equation (5.47)).

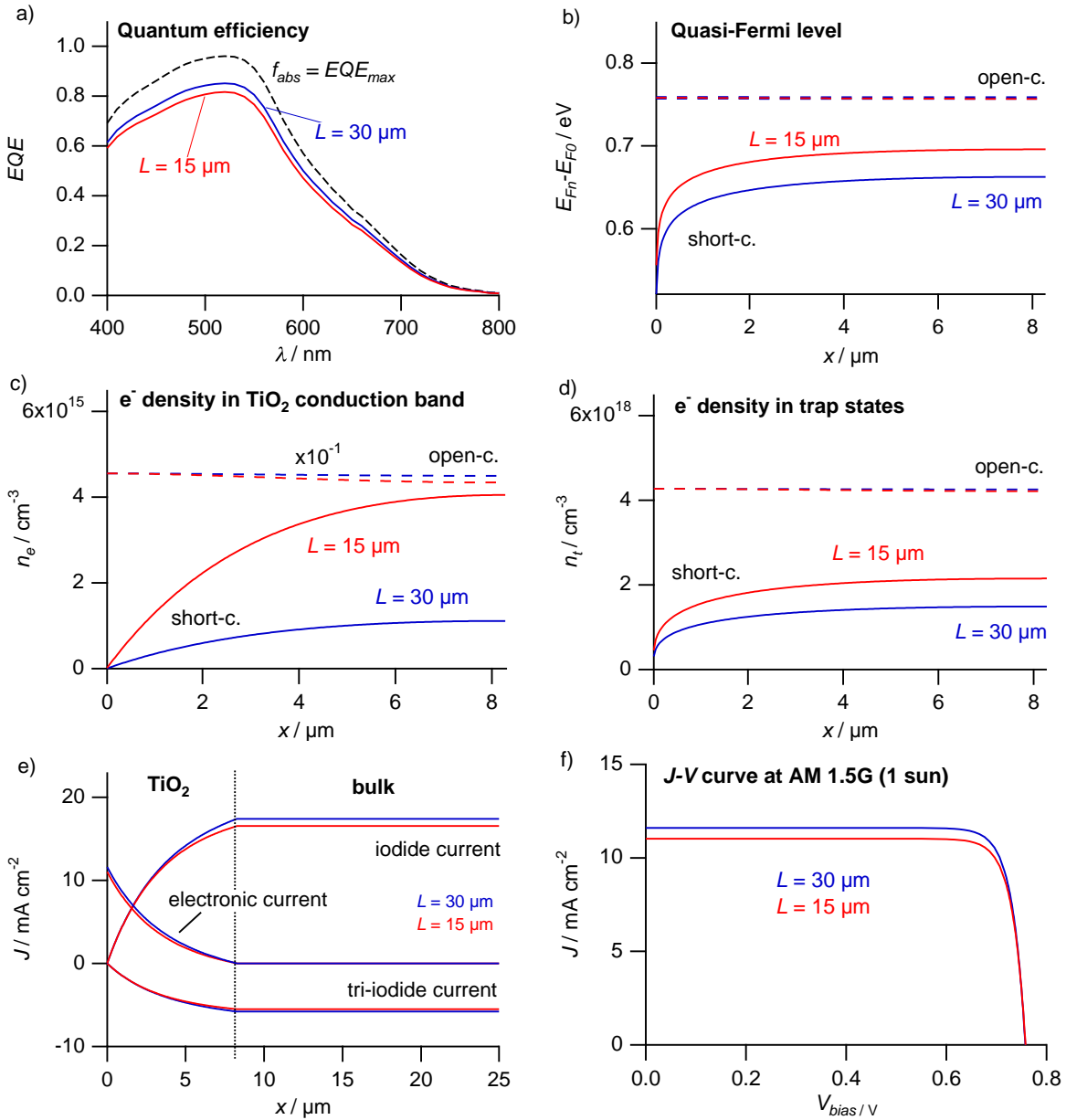


Figure 5.16: Comparison of steady-state calculations of two similar devices ($d_{TiO_2} = 8.3 \mu\text{m}$) with different diffusion lengths $L_1 = 30 \mu\text{m}$ (in blue) and $L_2 = 15 \mu\text{m}$ (in red). The values of the other simulation parameters are given in the text. The EQE (a) and the electronic and ionic current densities (e) are calculated under short-circuit conditions. The quasi-Fermi level (b) and the charge density in the TiO_2 conduction band (c) and trap states (d) are compared under open- and short-circuit conditions.

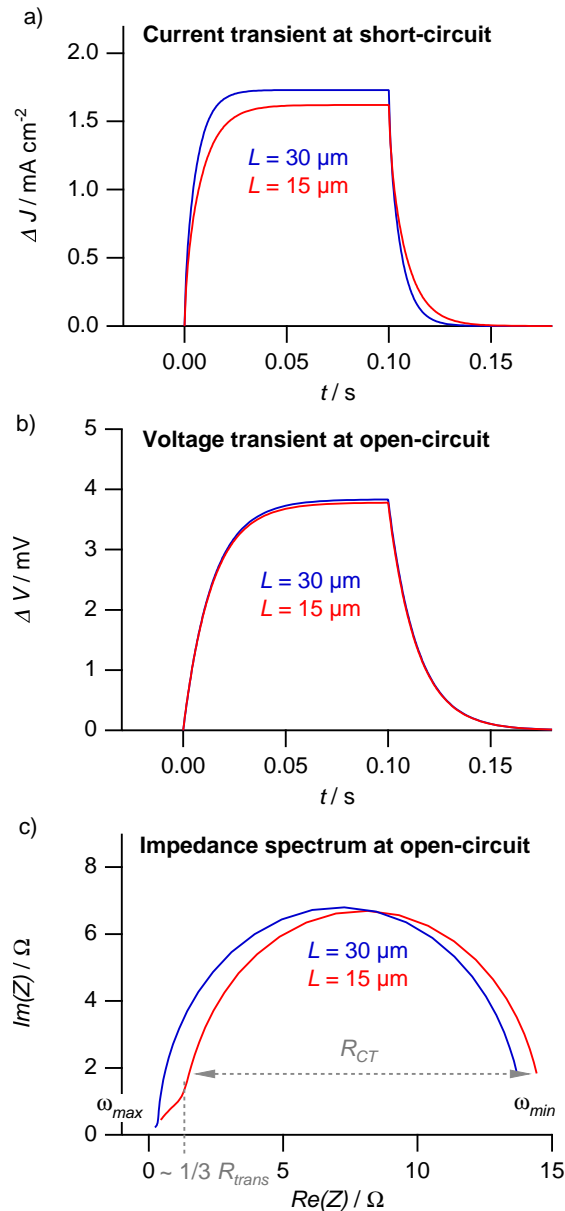


Figure 5.17: Comparison of time-dependent calculations of two similar devices ($d_{TiO_2} = 8.3 \mu\text{m}$) with different diffusion lengths $L_1 = 30 \mu\text{m}$ (in blue) and $L_2 = 15 \mu\text{m}$ (in red). The values of the other simulation parameters are given in the text. Small perturbation current transients at short-circuit (a), voltage transients at open-circuit (b), and impedance spectra in the dark at open-circuit (c) are shown.

- *J-V curve* (Figure 5.16f): We note that we find a similar V_{oc} for both parameter sets. If a non-linear model were used, the differences in V_{oc} would be larger.
- *Current transient* (Figure 5.17a): As expected, the small perturbation current ΔJ is smaller for the parameter set with the shorter diffusion length $L_2 = 15 \mu\text{m}$. Also the decay is longer, even though E_{Fn} is higher for $L_2 = 15 \mu\text{m}$ as shown in Figure 5.16b (one would intuitively assumes a shorter decay, see Section 2.3.2). In this case, the better transport for the first parameter set ($L_1 = 30 \mu\text{m}$) seems to dominate the current decay time constant. Here we see, that the interpretation of current transients is not straightforward and depends on the relation between several factors, like the position of E_{Fn} , the trapped charge density n_t , and the diffusion length L .
- *Voltage transient* (Figure 5.17b): For now, the simulated voltage transients provide only moderately interesting data since non-linear recombination is not implemented.
- *Impedance spectrum* (Figure 5.17c): The impedance spectrum is only simulated for the diffusion and recombination of electrons and does not take into account charge transfer at the counter electrode or ionic diffusion (see Section 5.2.2.4). This case was previously discussed by Bisquert [39]. For $L_1 = 30 \mu\text{m}$ we find the characteristic semicircle for charge transfer at the $\text{TiO}_2/\text{electrolyte}$ interface ($R_{CT} \approx 13 \Omega$, obtained from the diameter of the semicircle). For $L_2 = 15 \mu\text{m}$ we find a similar value for R_{CT} and additionally a small linear component at high frequencies, which describes the transport resistance R_{trans} in the TiO_2 . Here R_{trans} is about 3Ω (for L_1 , R_{trans} is negligible). R_{CT} and R_{trans} are related to the effective lifetime τ_n , the effective diffusion coefficient D_n , the film thickness d , and the chemical capacitance C_μ of the TiO_2 via [39, 56]

$$R_{CT} = \frac{\tau_n}{C_\mu}, \quad \text{and} \quad (5.60)$$

$$R_{trans} = \frac{d^2}{D_n C_\mu}. \quad (5.61)$$

The electron diffusion length then is

$$L_n = \sqrt{\tau_n D_n} = d \sqrt{\frac{R_{CT}}{R_{trans}}}. \quad (5.62)$$

The effective lifetime τ_n , as defined in equation (5.35), is equal for both parameter sets. Hence, we find the same charge transfer resistance R_{CT} . However, D_n ,

as defined in equation (5.32), is different since we use different diffusion lengths $L = \sqrt{\tau_0 D_0}$. As expected, the charge transport resistance R_{trans} increases with decreasing L .

- *Loss analysis* (not shown): The two systems only differ with respect to the recombination losses. For both systems, the relative losses are 8.4 % reflectance, 27.7 % transmittance, 8.2 % absorptance, 5.6 % injection, and 35.9 % potential loss. The recombination loss accounts for 0.3 % with $L_1 = 30 \mu\text{m}$ and 0.9 % with $L_2 = 15 \mu\text{m}$. The final power output is $P_1 = 73.0 \text{ W m}^{-2}$ ($\eta_1 = 7.3 \%$ overall conversion efficiency, $J_1 = 11.0 \text{ mA cm}^{-2}$ current density at the MPP) and $P_2 = 69.5 \text{ W m}^{-2}$ ($\eta_2 = 7.0 \%$, $J_2 = 10.5 \text{ mA cm}^{-2}$).

We see that only a small increase in performance is obtained with the doubling of the diffusion length. This is due to a saturation of the extractable current with increasing diffusion length. This is illustrated in the J_{sc} vs. L relationship in Figure 5.18. For a diffusion length larger than three times the TiO_2 film thickness there is virtually no increase in extractable current.

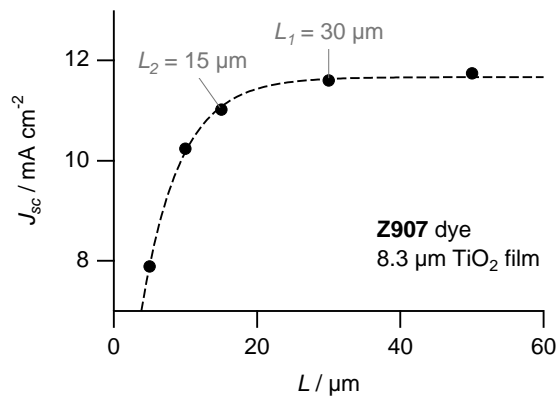


Figure 5.18: Calculated short-circuit current density as a function of the diffusion length L for a device with **Z907** dye and a TiO_2 film thickness of $d = 8.3 \mu\text{m}$ (AM 1.5G irradiance from the TiO_2 side). The values of other simulation parameters are given in the text. The dotted line is an exponential fit to the data points.

5.5 Conclusions

We have developed an experimentally validated optical and electrical model for DSCs. The optical model describes very accurately the optics in the device and allows to quantify the fraction of absorbed light by the dye and the shares lost due to reflection, absorption in the layers, and transmittance. With this information, we can now determine the internal quantum efficiency of devices with high precision.

Coupling of the optical model with an electrical model provides a tool to simulate various steady-state and time-dependent measurements and to extract intrinsic parameters. We have demonstrated parameter extraction with two different dye systems and “potential-determining” ions (Li^+) and found trends that agree with previously reported ones. Importantly, we can now conduct a comprehensive and quantitative optical and electric loss analysis, which is crucial for the development of specific optimization strategies. The implementation of a graphical user interface allows for straightforward usage.

However, this model must be regarded as a first step towards a truly powerful DSC simulator. Several aspects require additional algorithms and experimental validation:

- So far, we only have optical data for the ruthenium-complex systems **Z907** and **C101**. This database should be enlarged in the future by characterizing additional dyes as described in Appendix [B.2](#).
- The refractive indices of the layers in the complete “standard” DSC stack are sufficiently well characterized. Different materials (i.e. conducting oxide, semiconductor) require a new careful optical characterization.
- At some point, the optical model should be extended to account for scattering, as back scattering by large TiO_2 particles is an integral part of high-efficiency DSCs. Also, anti-reflecting layers and metal back reflectors should be included as simulation options.
- At present, the electrical model considers recombination of electrons with I_3^- from the TiO_2 conduction band only (linear recombination term). This model does not predict the non-linearity observed in experimental devices. In particular, conditions close to open-circuit — where recombination is dominant — are not described correctly. The implementation of a non-linear recombination term seems necessary, although it is not quite clear which type of expression is the most meaningful in terms of device physics. Also, it might be reasonable to include a recombination term for the back reaction with oxidized dye molecules.

- A fitting routine in the graphical user interface to directly extract parameters from experimental data would be desirable.
- The graphical user interface is not “stress-tested”. The development of a stable, reliable, and bug-free program with additional user-friendly features should be part of a future project.

Now that the basic model is validated comes the time to “play” with it. As demonstrated, the model is instrumental in understanding the effects of single-parameter variations on cell performance and assessing the magnitude of the different loss mechanisms. Ultimately, such a comprehensive, simulation-assisted, understanding of the DSC paves the way for a systematic analysis and reduction of losses, which was the decisive route to success for several established photovoltaic technologies.

Bibliography

- [1] Y. Bai, Y. Cao, J. Zhang, M. Wang, R. Li, P. Wang, S. M. Zakeeruddin, and M. Grätzel. High-performance dye-sensitized solar cells based on solvent-free electrolytes produced from eutectic melts. *Nature Materials* **2008**, *7*, 626–630.
- [2] D. Shi, N. Pootrakulchote, R. Li, J. Guo, Y. Wang, S. M. Zakeeruddin, M. Grätzel, and P. Wang. New efficiency records for stable dye-sensitized solar cells with low-volatility and ionic liquid electrolytes. *The Journal of Physical Chemistry C* **2008**, *112*, 17046–17050.
- [3] M. K. Nazeeruddin, F. De Angelis, S. Fantacci, A. Selloni, G. Viscardi, P. Liska, S. Ito, B. Takeru, and M. Grätzel. Combined Experimental and DFT-TDDFT Computational Study of Photoelectrochemical Cell Ruthenium Sensitizers. *Journal of the American Chemical Society* **2005**, *127*, 16835–16847.
- [4] F. Gao, Y. Wang, D. Shi, J. Zhang, M. K. Wang, X. Y. Jing, R. Humphry-Baker, P. Wang, S. M. Zakeeruddin, and M. Grätzel. Enhance the optical absorptivity of nanocrystalline TiO₂ film with high molar extinction coefficient ruthenium sensitizers for high performance dye-sensitized solar cells. *Journal of the American Chemical Society* **2008**, *130*, 10720–10728.
- [5] Y. Chiba, A. Islam, Y. Watanabe, R. Komiya, N. Koide, and L. Han. Dye-sensitized solar cells with conversion efficiency of 11.1%. *Japanese Journal of Applied Physics* **2006**, *45*, L638–L640.
- [6] Y. Cao, Y. Bai, Q. Yu, Y. Cheng, S. Liu, D. Shi, F. Gao, and P. Wang. Dye-sensitized solar cells with a high absorptivity ruthenium sensitizer featuring a 2-(hexylthio)thiophene conjugated bipyridine. *The Journal of Physical Chemistry C* **2009**, *113*, 6290–6297.
- [7] C.-Y. Chen, M. Wang, J.-Y. Li, N. Pootrakulchote, L. Alibabaei, C.-h. Ngoc-le, J.-D. Decoppet, J.-H. Tsai, C. Grätzel, C.-G. Wu, S. M. Zakeeruddin, and M. Grätzel. Highly efficient light-harvesting ruthenium sensitizer for thin-film dye-sensitized solar cells. *ACS Nano* **2009**, *3*, 3103–3109.

- [8] <http://www.pv.unsw.edu.au/links/products/pc1d.asp>.
- [9] M. Burgelman, J. Verschraegen, S. Degrave, and P. Nollet. Modeling Thin-film PV devices. *Progress in Photovoltaics: Research and Applications* **2004**, *12*, 143–153.
- [10] J. Krč, F. Smole, and M. Topič. Analysis of light scattering in amorphous Si:H solar cells by a one-dimensional semi-coherent optical model. *Progress in Photovoltaics: Research and Applications* **2003**, *11*, 15–26.
- [11] J. Springer, A. Poruba, and M. Vanecak. Improved three-dimensional optical model for thin-film silicon solar cells. *Journal of Applied Physics* **2004**, *96*, 5329–5337.
- [12] R. Häusermann, E. Knapp, M. Moos, N. A. Reinke, T. Flatz, and B. Ruhstaller. Coupled optoelectronic simulation of organic bulk-heterojunction solar cells: Parameter extraction and sensitivity analysis. *Journal of Applied Physics* **2009**, *106*, 104507.
- [13] L. M. Peter. Characterization and modeling of dye-sensitized solar cells. *Journal of Physical Chemistry C* **2007**, *111*, 6601–6612.
- [14] J. Halme, G. Boschloo, A. Hagfeldt, and P. Lund. Spectral characteristics of light harvesting, electron injection, and steady-state charge collection in pressed TiO₂ dye solar cells. *The Journal of Physical Chemistry C* **2008**, *112*, 5623–5637.
- [15] P. R. F. Barnes, A. Y. Anderson, S. E. Koops, J. R. Durrant, and B. C. O'Regan. Electron injection efficiency and diffusion length in dye-sensitized solar cells derived from incident photon conversion efficiency measurements. *Journal of Physical Chemistry C* **2009**, *113*, 1126–1136.
- [16] U. Würfel, M. Peters, and A. Hinsch. Detailed experimental and theoretical investigation of the electron transport in a dye solar cell by means of a three-electrode configuration. *Journal of Physical Chemistry C* **2008**, *112*, 1711–1720.
- [17] L. Peter. “Sticky Electrons” Transport and Interfacial Transfer of Electrons in the Dye-Sensitized Solar Cell. *Accounts of Chemical Research* **2009**, *42*, 1839–1847.
- [18] J. Bisquert and I. Mora-Seró. Simulation of steady-state characteristics of dye-sensitized solar cells and the interpretation of the diffusion length. *The Journal of Physical Chemistry Letters* **2009**, *450*–456.
- [19] J. Bisquert, F. Fabregat-Santiago, I. Mora-Seró, G. Garcia-Belmonte, and S. Giménez. Electron lifetime in dye-sensitized solar cells: Theory and interpretation of measurements. *The Journal of Physical Chemistry C* **2009**, *113*, 17278–17290.
- [20] P. Wang, S. M. Zakeeruddin, J. E. Moser, M. K. Nazeeruddin, T. Sekiguchi, and M. Grätzel. A stable quasi-solid-state dye-sensitized solar cell with an amphiphilic ruthenium sensitizer and polymer gel electrolyte. *Nature Materials* **2003**, *2*, 402–407.
- [21] J. Villanueva-Cab, H. Wang, G. Oskam, and L. M. Peter. Electron diffusion and back reaction in dye-sensitized solar cells: The effect of nonlinear recombination kinetics. *The Journal of Physical Chemistry Letters* **2010**, *748*–751.

- [22] J. Bisquert and V. S. Vikhrenko. Interpretation of the time constants measured by kinetic techniques in nanostructured semiconductor electrodes and dye-sensitized solar cells. *Journal of Physical Chemistry B* **2004**, *108*, 2313–2322.
- [23] J. O. Schumacher. *Numerical simulation of silicon solar cells with novel device structures*. PhD thesis, University of Konstanz **2000**.
- [24] A. Donges. The coherence length of black-body radiation. *European Journal of Physics* **1998**, *19*, 245–249.
- [25] E. Centurioni. Generalized matrix method for calculation of internal light energy flux in mixed coherent and incoherent multilayers. *Applied Optics* **2005**, *44*, 7532–7539.
- [26] M. Born and E. Wolf. *Principles of optics: electromagnetic theory of propagation, interference and diffraction of light*. Cambridge University Press, Cambridge, UK, 7th edition **1999**.
- [27] D. A. G. Bruggeman. Calculation of various physics constants in heterogenous substances: 1. Dielectricity constants and conductivity of mixed bodies from isotropic substances. *Annalen der Physik* **1935**, *24*, 636–664.
- [28] G. Rothenberger, P. Comte, and M. Grätzel. A contribution to the optical design of dye-sensitized nanocrystalline solar cells. *Solar Energy Materials and Solar Cells* **1999**, *58*, 321–336.
- [29] S. Soedergren, A. Hagfeldt, J. Olsson, and S.-E. Lindquist. Theoretical models for the action spectrum and the current-voltage characteristics of microporous semiconductor films in photoelectrochemical cells. *Journal of Physical Chemistry* **1994**, *98*, 5552–5556.
- [30] A. C. Fisher, L. M. Peter, E. A. Ponomarev, A. B. Walker, and K. G. U. Wijayantha. Intensity dependence of the back reaction and transport of electrons in dye-sensitized nanocrystalline TiO₂ solar cells. *Journal of Physical Chemistry B* **2000**, *104*, 949–958.
- [31] N. W. Duffy, L. M. Peter, R. M. G. Rajapakse, and K. G. U. Wijayantha. Investigation of the kinetics of the back reaction of electrons with tri-iodide in dye-sensitized nanocrystalline photovoltaic cells. *Journal of Physical Chemistry B* **2000**, *104*, 8916–8919.
- [32] A. N. M. Green, R. E. Chandler, S. A. Haque, J. Nelson, and J. R. Durrant. Transient absorption studies and numerical modeling of iodine photoreduction by nanocrystalline tio2 films. *The Journal of Physical Chemistry B* **2004**, *109*, 142–150.
- [33] N. W. Duffy, L. M. Peter, and K. G. U. Wijayantha. Characterisation of electron transport and back reaction in dye-sensitised nanocrystalline solar cells by small amplitude laser pulse excitation. *Electrochemistry Communications* **2000**, *2*, 262–266.
- [34] L. Dloczik, O. Ileperuma, I. Lauermann, L. M. Peter, E. A. Ponomarev, G. Redmond, N. J. Shaw, and I. Uhlendorf. Dynamic response of dye-sensitized nanocrystalline solar cells: Characterization by intensity-modulated photocurrent spectroscopy. *Journal of Physical Chemistry B* **1997**, *101*, 10281–10289.

- [35] Q. Wang, S. Ito, M. Grätzel, F. Fabregat-Santiago, I. Mora-Sero, J. Bisquert, T. Bessho, and H. Imai. Characteristics of high efficiency dye-sensitized solar cells. *Journal of Physical Chemistry B* **2006**, *110*, 25210–25221.
- [36] L. Han, N. Koide, Y. Chiba, and T. Mitate. Modeling of an equivalent circuit for dye-sensitized solar cells. *Applied Physics Letters* **2004**, *84*, 2433–2435.
- [37] F. Fabregat-Santiago, G. Garcia-Belmonte, J. Bisquert, A. Zaban, and P. Salvador. Decoupling of transport, charge storage, and interfacial charge transfer in the nanocrystalline TiO₂/electrolyte system by impedance methods. *The Journal of Physical Chemistry B* **2002**, *106*, 334–339.
- [38] R. Kern, R. Sastrawan, J. Ferber, R. Stangl, and J. Luther. Modeling and interpretation of electrical impedance spectra of dye solar cells operated under open-circuit conditions. *Electrochimica Acta* **2002**, *47*, 4213–4225.
- [39] J. Bisquert. Theory of the impedance of electron diffusion and recombination in a thin layer. *The Journal of Physical Chemistry B* **2002**, *106*, 325–333.
- [40] J. Ferber, R. Stangl, and J. Luther. An electrical model of the dye-sensitized solar cell. *Solar Energy Materials and Solar Cells* **1998**, *53*, 29–54.
- [41] N. Kopidakis, E. A. Schiff, N. G. Park, J. van de Lagemaat, and A. J. Frank. Ambipolar diffusion of photocarriers in electrolyte-filled, nanoporous tio2. *Journal of Physical Chemistry B* **2000**, *104*, 3930–3936.
- [42] J. Ferber. *Elektrische und optische Modellierung von Farbstoffsolarzellen*. Ph.D. thesis, Universität Freiburg **1991**.
- [43] P. D. Paulson and S. S. Hegedus. Accurate determination of optical constants of textured SnO₂ using low incidence angle spectroscopic ellipsometry. *Journal of Applied Physics* **2004**, *96*, 5469–5477.
- [44] I. Z. Kozma, P. Krok, and E. Riedle. Direct measurement of the group-velocity mismatch and derivation of the refractive-index dispersion for a variety of solvents in the ultraviolet. *Journal of the Optical Society of America B* **2005**, *22*, 1479–1485.
- [45] H. Tang, H. Berger, P. E. Schmid, and F. Lévy. Optical properties of anatase (TiO₂). *Solid State Communications* **1994/10**, *92*, 267–271.
- [46] S. Ito, M. K. Nazeeruddin, P. Liska, P. Comte, R. Charvet, P. Péchy, M. Jirousek, A. Kay, S. M. Zakeeruddin, and M. Grätzel. Photovoltaic characterization of dye-sensitized solar cells: Effect of device masking on conversion efficiency. *Progress in Photovoltaics* **2006**, *14*, 589–601.
- [47] S. Ito, S. M. Zakeeruddin, P. Comte, P. Liska, D. Kuang, and M. Grätzel. Bifacial dye-sensitized solar cells based on an ionic liquid electrolyte. *Nature Photonics* **2008**, *2*, 693–698.
- [48] P. Wang, S. M. Zakeeruddin, J.-E. Moser, and M. Grätzel. A new ionic liquid electrolyte enhances the conversion efficiency of dye-sensitized solar cells. *The Journal of Physical Chemistry B* **2003**, *107*, 13280–13285.

- [49] Y. Tachibana, S. A. Haque, I. P. Mercer, J. E. Moser, D. R. Klug, and J. R. Durrant. Modulation of the rate of electron injection in dye-sensitized nanocrystalline TiO₂ films by externally applied bias. *The Journal of Physical Chemistry B* **2001**, *105*, 7424–7431.
- [50] S. E. Koops, B. C. O'Regan, P. R. F. Barnes, and J. R. Durrant. Parameters influencing the efficiency of electron injection in dye-sensitized solar cells. *Journal of the American Chemical Society* **2009**, *131*, 4808–4818.
- [51] D. B. Kuang, S. Ito, B. Wenger, C. Klein, J. E. Moser, R. Humphry-Baker, S. M. Zakeeruddin, and M. Grätzel. High molar extinction coefficient heteroleptic ruthenium complexes for thin film dye-sensitized solar cells. *Journal of the American Chemical Society* **2006**, *128*, 4146–4154.
- [52] P. Wang, C. Klein, R. Humphry-Baker, S. M. Zakeeruddin, and M. Grätzel. A high molar extinction coefficient sensitizer for stable dye-sensitized solar cells. *Journal of the American Chemical Society* **2004**, *127*, 808–809.
- [53] T. Marinado, K. Nonomura, J. Nissfolk, M. K. Karlsson, D. P. Hagberg, L. Sun, S. Mori, and A. Hagfeldt. How the nature of triphenylamine-polyene dyes in dye-sensitized solar cells affects the open-circuit voltage and electron lifetimes. *Langmuir* **2010**, *26*, 2592–2598.
- [54] B. C. O'Regan, I. López-Duarte, M. V. Martínez-Díaz, A. Forneli, J. Albero, A. Morandeira, E. Palomares, T. Torres, and J. R. Durrant. Catalysis of recombination and its limitation on open circuit voltage for dye sensitized photovoltaic cells using phthalocyanine dyes. *Journal of the American Chemical Society* **2008**, *130*, 2906–2907.
- [55] K. Lobato, L. M. Peter, and U. Würfel. Direct measurement of the internal electron quasi-Fermi level in dye sensitized solar cells using a titanium secondary electrode. *Journal of Physical Chemistry B* **2006**, *110*, 16201–16204.
- [56] F. Fabregat-Santiago, J. Bisquert, G. Garcia-Belmonte, G. Boschloo, and A. Hagfeldt. Influence of electrolyte in transport and recombination in dye-sensitized solar cells studied by impedance spectroscopy. *Solar Energy Materials and Solar Cells* **2005**, *87*, 117–131.

Chapter 6

Final conclusions and outlook

The work conducted during this thesis aimed at optimizing the DSC using three different strategies: the use of versatile organic sensitizers for stable and efficient DSCs, the study of tandem device architectures in combination with other solar cells to harvest a larger fraction of the solar spectrum, and the development of a validated optoelectric model of the DSC. As discussed in the respective chapters, valuable contributions could be made to all three optimization fields, in brief:

Organic sensitizers — Of the tested stable organic sensitizers, one achieved a new conversion efficiency record of 7.6 % in a solvent-free DSC. With a novel class of organic sensitizers (π -extended tetrathiafulvalenes) we could demonstrate efficient photovoltaic conversion in a system that had a very low thermodynamic driving force for dye regeneration. We also found correlations between the dye structures and the recombination dynamics of electrons with I_3^- in the electrolyte.

DSC/Cu(In,Ga)Se₂ tandem cell — A prototype monolithic DSC/CIGS tandem structure was developed with a promising initial efficiency of 12.2 % and a photovoltage of 1.22 V. First optical calculations with experimentally extracted optical constants showed that the amount of light absorbed in each photoactive layer was well balanced — a crucial condition for current-matching in series-connected tandem cells — and that there is ample room for optical optimization of the stack to achieve efficiencies of up to 16 %.

DSC device modeling — An experimentally validated coupled optical and electrical model of the DSC was developed. Important parameters, like the internal quantum efficiency, injection efficiency, electron diffusion length, or distribution of trap states in the TiO₂, could be extracted from experimental data. Importantly, for the first time, a comprehensive and quantitative loss analysis of the different optical and electric loss channels in the DSC could be conducted. Furthermore, an easy-to-use

graphical user interface allows to understand the effect of different parameters on steady-state and time-dependent measurements. This tool also provides insights of high educational value into the device physics of DSCs .

For the future development and commercialization of inexpensive and high efficiency DSCs, I see a large potential in the synergy of these three fields. Organic sensitizers could profit from an added device model analysis to quantify accurately the internal quantum efficiency and recombination. Also, the time-consuming “fine-tuning”, e.g. the optimization of the TiO₂ film thickness, could be assisted by the model. As could be concluded from the numerical DSC loss analysis, a large fraction of the incident energy is lost due to thermalization. These losses can be reduced with a tandem device approach, as shown in this work. However, it seems likely that an “all-DSC” tandem cell is more advantageous with regard to future industrial in-line production. For example, a combination of different organic sensitizers in a single device seems promising. Like single DSCs, high-efficiency tandem cells would also benefit from numerically assisted optimization.

To conclude, I want to stress once more the immense profit one obtains from a comprehensive view of the DSC on one side, and a detailed understanding of its device physics on the other side. Still, many aspects of the DSC are not well understood. Nevertheless, the findings of this thesis, and the developed tools, pave the way for a systematic analysis and reduction of losses as well as a better fundamental understanding of the DSC.

Appendix A

Optical constants of materials in CIGS solar cell

The complex refractive indices, $\tilde{n}_i = n_i + ik_i$, of the different layers in the CIGS solar cell used for the optical simulation of the stack in Section 4.4.2 are shown in Figure A.1. The values for $\text{In}_2\text{O}_3:\text{Sn}$ (ITO) were taken from Synowicki [1], and the values for CdS from the PhD thesis of Malmström [2]. The $\text{Cu}(\text{In},\text{Ga})\text{Se}_2$ (CIGS) absorber layer was characterized by spectroscopic ellipsometry by IBM Research - Zurich ($\sim 2 \mu\text{m}$ co-evaporated CIGS on $1 \mu\text{m}$ molybdenum on glass)¹. The extracted n and k values are in good agreement with previously reported values for CIGS [2]. The values for molybdenum were taken from Palik [3].

¹We thank M. Sousa for the measurements.

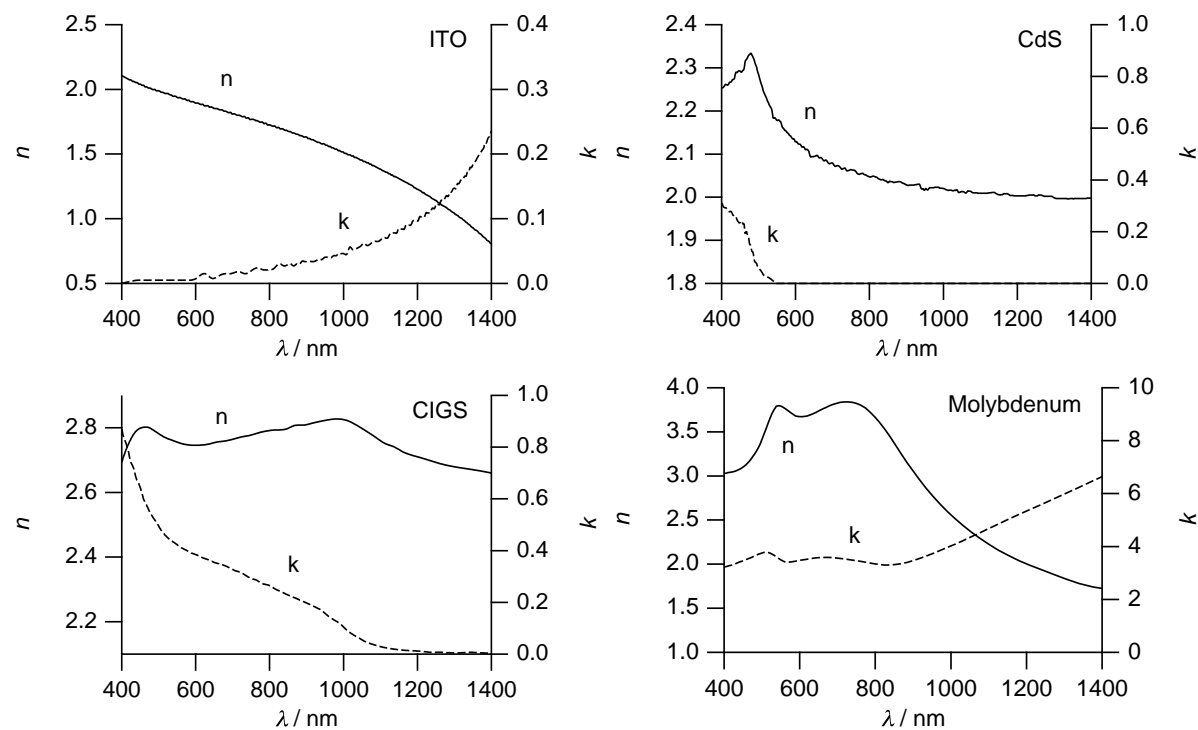


Figure A.1: Real and imaginary part of the the complex index of refraction, $\tilde{n} = n + ik$, of the different layers in the CIGS solar cell used for the optical simulations.

Appendix B

Modeling of dye-sensitized solar cells

B.1 Extracting the complex index of refraction of a thick film

To calculate the complex index of refraction $\tilde{n}(\lambda) = n(\lambda) + ik(\lambda)$ of a thick film (e.g glass substrates **1** and **6**, microscope glass slide) we assume incoherent light propagation in a film with thickness d (B.1). The absorption coefficient of the film is $\alpha(\lambda) = 4\pi k(\lambda)/\lambda$ in units of m^{-1} .

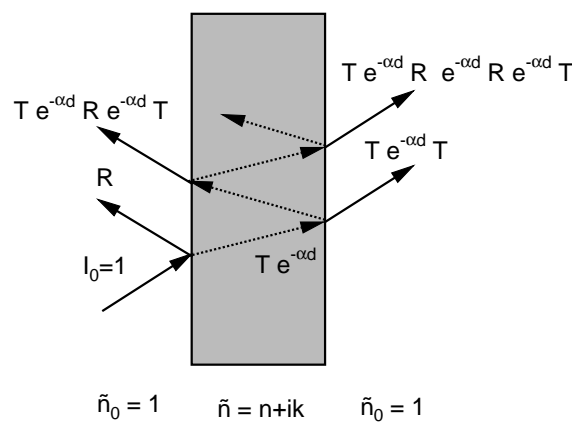


Figure B.1: Incoherent light propagation in a film with thickness d in air. R represents reflectance and T transmittance at the air/film interface, and $\alpha = 4\pi k/\lambda$ is the absorption coefficient of the film.

The reflectance from air ($\tilde{n}_0 = 1$) to a material with a refractive index \tilde{n} for normal incidence is given by the Fresnel equation [4],

$$R = \frac{(\tilde{n} - \tilde{n}_0)^2}{(\tilde{n} + \tilde{n}_0)^2} = \frac{(n - 1)^2 + k^2}{(n + 1)^2 + k^2}. \quad (\text{B.1})$$

Light traveling through the film is attenuated by a factor $e^{-\alpha d}$ due to absorption. The total reflectance is given by the sum of all intensities reflected at the air/film interface,

$$\begin{aligned} R_{tot} &= R + Te^{-\alpha d} \left(\sum_{i=0}^{\infty} (Re^{-\alpha d} Re^{-\alpha d})^i \right) Re^{-\alpha d} T \\ &= R + \frac{T^2 Re^{-2\alpha d}}{1 - R^2 e^{-2\alpha d}} = \frac{R (1 + (1 - 2R)e^{-2\alpha d})}{1 - R^2 e^{-2\alpha d}}, \end{aligned} \quad (\text{B.2})$$

where $R + T = 1$. Similarly, the total transmittance is

$$\begin{aligned} T_{tot} &= Te^{-\alpha d} \left(\sum_{i=0}^{\infty} (Re^{-\alpha d} Re^{-\alpha d})^i \right) T \\ &= \frac{T^2 e^{-\alpha d}}{1 - R^2 e^{-2\alpha d}} = \frac{(1 - R)^2 e^{-\alpha d}}{1 - R^2 e^{-2\alpha d}}. \end{aligned} \quad (\text{B.3})$$

The n and k values of the film are extracted from least-squares fits of equations (B.1), (B.2), and (B.3) to measured reflectance and transmittance spectra.

B.2 Four-flux analysis of sensitized mesoporous TiO₂ films between microscope glasses

The analysis of the absorption and scattering of mesoporous TiO₂ films between two microscope glass slides follows a previously described procedure [5]. In brief, the model separates the total light flux crossing the stack into four distinct fluxes: Two collinear fluxes (forward and backward), and two diffuse fluxes (forward and backward). A least-squares fit to experimental data (T_{coll} , T_{diff} , R_{coll} , and R_{diff}) yields an absorption coefficient $\alpha(\lambda) = \sigma_{abs}(\lambda) n_{abs} = 4\pi k/\lambda$ and a scattering coefficient $s(\lambda) = \sigma_{scatt}(\lambda) n_{scatt}$. Here, $\sigma_{abs}(\lambda)$ and $\sigma_{scatt}(\lambda)$ are the cross-sections for light absorption and scattering, respectively, and n_{abs} and n_{scatt} are the number density of absorbers and scatterers, respectively.

Two stacks as shown in Figure B.2 were analyzed: a) Plain TiO₂ in a mixture of acetonitrile and valeronitrile (volume ratio 85:15, ACN) as solvent to yield the absorp-

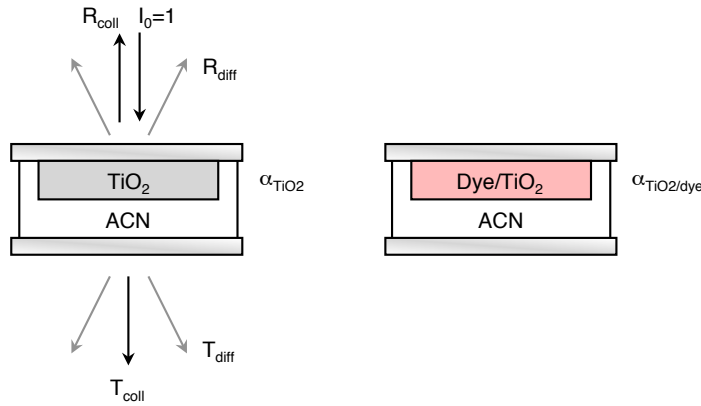


Figure B.2: Schematic of the two stacks used to obtain the absorption coefficient of mesoporous TiO₂ ($\alpha_{\text{TiO}2}$) only and the dye-sensitized TiO₂ ($\alpha_{\text{TiO}2/\text{dye}}$). Left: TiO₂ in a mixture of acetonitrile and valeronitrile (volume ratio 85:15, ACN). Right: Dye-sensitized TiO₂ in ACN. The absorption coefficients were obtained with a four-flux analysis of measured T and R spectra.

tion coefficient of the TiO₂ only ($\alpha_{\text{TiO}2}$), and b) dye-sensitized TiO₂ in ACN to yield the absorption coefficient of the sensitized TiO₂ ($\alpha_{\text{TiO}2/\text{dye}}$). The effective absorption coefficient α_3 of layer 3, including TiO₂, dye, and electrolyte absorption was calculated by adding the contribution of the electrolyte absorption in the pores,

$$\alpha_3 = \alpha_{\text{TiO}2/\text{dye}} + P \sigma_{I_3^-} n_{I_3^-}. \quad (\text{B.4})$$

$P = 0.68$ is the porosity in the film, $\sigma_{I_3^-}$ is the optical absorption cross-section of triiodide measured in solution, and $n_{I_3^-} = 1.8066 \times 10^{25} \text{ m}^{-3}$ is the number density of I_3^- ions in the electrolyte. The absorption coefficient of the dye alone was obtained by subtracting the TiO₂ absorption (and its impurity, as seen in Figure B.3),

$$\alpha_{\text{dye}} = \alpha_{\text{TiO}2/\text{dye}} - \alpha_{\text{TiO}2}. \quad (\text{B.5})$$

Measured T and R spectra are represented by bold dark lines, and calculated spectra using the extracted parameters are represented by dashed red lines.

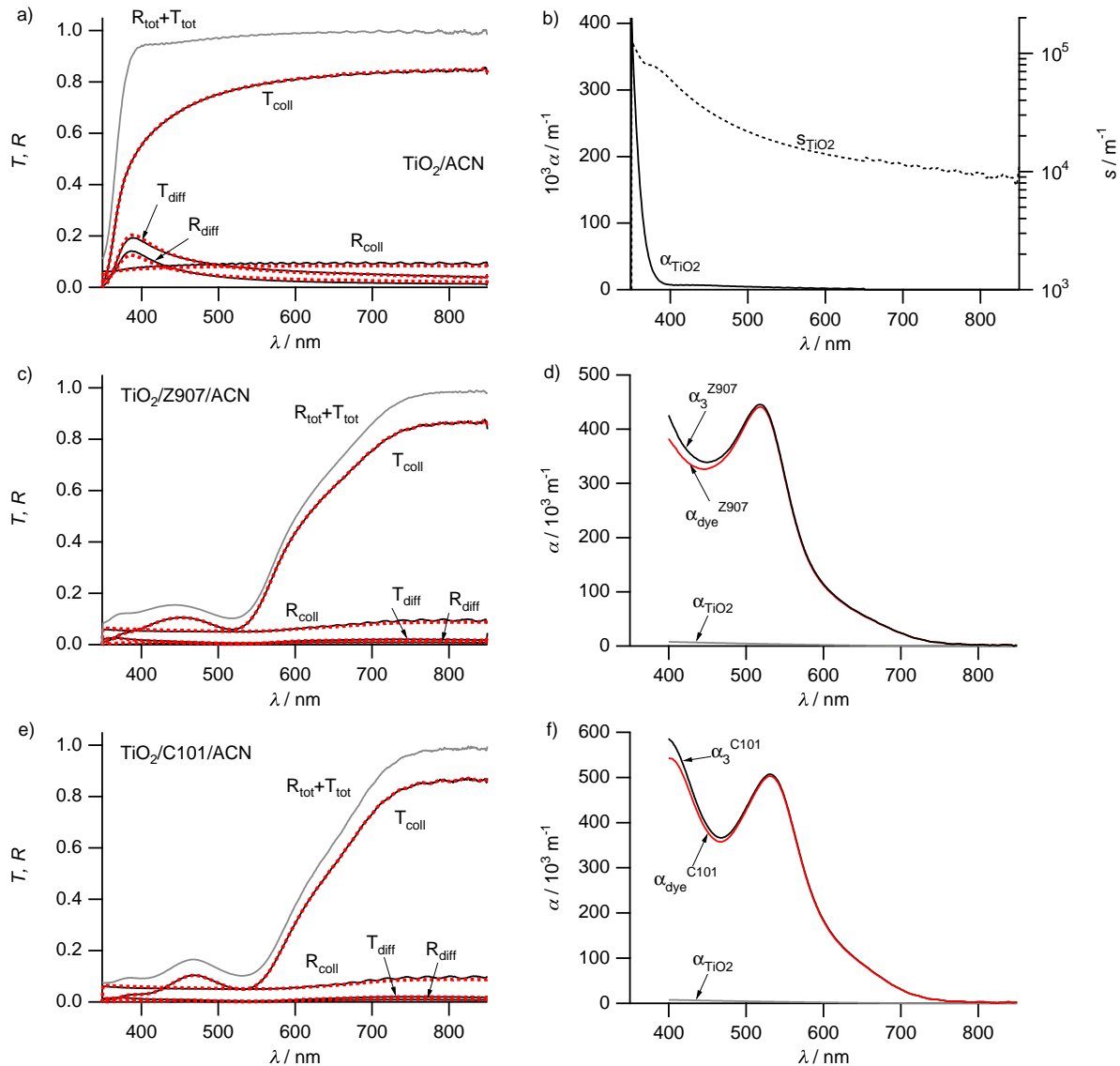


Figure B.3: a) Stack with 7.0 μm mesoporous TiO_2 and ACN. T_{diff} and R_{diff} , and consequently light scattering, become significant for $\lambda < 500$ nm. b) The strong onset below 400 nm due to bandgap excitation of TiO_2 is clearly seen in the absorption coefficient $\alpha_{\text{TiO}2}$. There is some weak absorption above 400 nm, whose origin is not clear but probably due to an impurity. The magnitude of the scattering coefficient $s_{\text{TiO}2}$ is characteristic for films made of colloidal particles smaller than about 20 nm in diameter. c) Stack with Z907-sensitized 5.5 μm mesoporous TiO_2 in ACN. T_{tot} is strongly attenuated for $\lambda < 800$ nm due to absorption by the dye. T_{diff} and R_{diff} are nearly zero below 500 nm. d) $\alpha_{\text{dye}}^{\text{Z907}}$ is the absorption coefficient of the dye only (absorption by impurities in the TiO_2 , $\alpha_{\text{TiO}2}$, is subtracted) and is characteristic for absorption by the dye Z907 in the range 400–800 nm. The absorption maximum is $\alpha_{\text{dye}}^{\text{Z907}} = 4.41 \times 10^5 \text{ m}^{-1}$ at 518 nm. The calculated absorption coefficient of the complete layer **3**, α_3^{Z907} , includes absorption by the electrolyte in the pores. e) Stack with C101-sensitized 5.5 μm mesoporous TiO_2 in ACN. f) The absorption maximum of the dye only is $\alpha_{\text{dye}}^{\text{C101}} = 5.03 \times 10^5 \text{ m}^{-1}$ at 530 nm. α_3^{C101} , includes absorption by the electrolyte in the pores.

B.3 General solution of the linear continuity equation for conduction band electrons

The inhomogeneous linear differential equation for the conduction band electron density $n(x)$ is

$$L^2 \frac{d^2 n}{dx^2} - (n(x) - \bar{n}) + \eta_{inj} G^{dye}(x) = 0, \quad (\text{B.6})$$

where L is the diffusion length, \bar{n} is the electron density in the dark, τ is the electron lifetime, and η_{inj} is the electron injection efficiency. The diffusion length is related to the diffusion coefficient and the lifetime of electrons in the TiO_2 conduction band by $L = \sqrt{D_0 \tau_0}$. $G^{dye}(x)$ is the excited dye state generation function for a given incident photon flux.

The complete solution for the conduction band electron density $n(x)$ is given by the sum of the homogeneous and the particular solution,

$$n(x) = n_h(x) + n_p(x) = a e^{-x/L} + b e^{x/L} - \eta_{inj} \tau_0 \Gamma_G(x), \quad (\text{B.7})$$

where a and b are integration constants. $\Gamma_G(x)$ is the convolution integral of G^{dye} with the Green's function,

$$\Gamma_G(x) := \int_0^d \mathcal{G}(x-y) G^{dye}(y) dy, \quad (\text{B.8})$$

The boundary conditions are

$$n(0) = N_c f(E_c, E_{F0} + eV) \quad \text{and} \quad \left. \frac{dn}{dx} \right|_{x=d} = 0. \quad (\text{B.9})$$

For an arbitrary photovoltage V , the general solution is

$$\begin{aligned} n(x) = & \bar{n} + \frac{\bar{n} \left[\exp\left(\frac{eV}{k_B T}\right) - 1 \right] \cosh\left(\frac{d-x}{L}\right)}{\cosh(d/L)} \\ & + \frac{\eta_{inj} \tau_0}{\cosh(d/L)} \left[\Gamma_G(x) \cosh(d/L) - \Gamma_G(0) \cosh\left(\frac{d-x}{L}\right) - L \Gamma'_G(d) \sinh(x/L) \right], \end{aligned} \quad (\text{B.10})$$

where

$$\Gamma'_G(x) := \int_0^d \mathcal{G}(x-y) \frac{dG^{dye}}{dy}(y) dy. \quad (\text{B.11})$$

To calculate the short-circuit current density j_{sc} , the photovoltage is set to $V = 0$. We obtain $n(0) = \bar{n}$ as expected, and

$$j_{sc} = e D_0 \left. \frac{dn}{dx} \right|_{x=0, V=0} = \frac{e \eta_{inj} L}{\cosh(d/L)} [\Gamma_G(0) \sinh(d/L) + L\Gamma'_G(0) \cosh(d/L) - L\Gamma'_G(d)]. \quad (\text{B.12})$$

The only free variables in the expression for j_{sc} are η_{inj} and L , which can be used as fitting parameters when comparing the calculation with experimental data.

The open-circuit voltage $V \equiv V_{oc}$ is obtained by imposing the condition

$$\left. \frac{dn}{dx} \right|_{x=0} = 0 \quad (\text{B.13})$$

on the general solution (B.10), which determines, that no electrons are extracted at the anode. This leads to an equation for V_{oc} ,

$$\exp \left(\frac{e V_{oc}}{k_B T} \right) = 1 + \frac{\eta_{inj} \tau}{\bar{n} \sinh(d/L)} [\Gamma_G(0) \sinh(d/L) + L\Gamma'_G(0) \cosh(d/L) - L\Gamma'_G(d)] \quad (\text{B.14})$$

To calculate the external quantum efficiency we use the excited dye state generation function for monochromatic illumination with photon flux density ϕ_{λ_0} at wavelength λ_0 ,

$$G^{dye,\delta}(x) = \phi_{\lambda_0} g^{dye}(\lambda_0, x) \quad (\text{B.15})$$

in equation (B.7). The convolution integral Γ_G is thus replaced by

$$\Gamma_G^\delta(x) := \int_0^d \mathcal{G}(x-y) G^{dye,\delta}(y) dy. \quad (\text{B.16})$$

The full expression for the external quantum efficiency (EQE) at wavelength λ_0 then is

$$\begin{aligned} EQE_{\lambda_0} &= \frac{j_{sc}}{e \phi_{\lambda_0}} \\ &= \frac{\eta_{inj} L}{\phi_{\lambda_0} \cosh(d/L)} [\Gamma_G^\delta(0) \sinh(d/L) + L\Gamma_G'^\delta(0) \cosh(d/L) - L\Gamma_G'^\delta(d)], \end{aligned} \quad (\text{B.17})$$

where

$$\Gamma'_G(x) := \int_0^d \mathcal{G}(x-y) \frac{dG^{dye,\delta}}{dy}(y) dy. \quad (\text{B.18})$$

The function $G^{dye,\delta}(x)$ will depend on the direction of illumination, i.e. illumination from the TiO₂ substrate electrode (*SE*) side or from the electrolyte electrode (*EE*) side. The ratio of the *EQE* with *SE* and *EE* illumination then only depends on the diffusion lenght,

$$\frac{EQE_{SE}(\lambda)}{EQE_{EE}(\lambda)} = \frac{[\Gamma_{G_{SE}}^\delta(0) \sinh(d/L) + L \Gamma_{G_{SE}}^\delta(0) \cosh(d/L) - L \Gamma_{G_{SE}}^\delta(d)]}{[\Gamma_{G_{EE}}^\delta(0) \sinh(d/L) + L \Gamma_{G_{EE}}^\delta(0) \cosh(d/L) - L \Gamma_{G_{EE}}^\delta(d)]}. \quad (\text{B.19})$$

Thus, L and η_{inj} can be extracted from experimental *EQE* data using single parameter fits.

Bibliography

- [1] R. A. Synowicki. Spectroscopic ellipsometry characterization of indium tin oxide film microstructure and optical constants. *Thin Solid Films* **1998**, *313-314*, 394–397.
- [2] J. Malmström. *On Generation and Recombination in Cu(In,Ga)Se₂ Thin-Film Solar Cells*. Ph.D. thesis, Uppsala University **2005**.
- [3] E. D. Palik. *Handbook of optical constants of solids*. Academic Press, Boston **1985**.
- [4] M. Born and E. Wolf. *Principles of optics: electromagnetic theory of propagation, interference and diffraction of light*. Cambridge University Press, Cambridge, UK, 7th edition **1999**.
- [5] G. Rothenberger, P. Comte, and M. Grätzel. A contribution to the optical design of dye-sensitized nanocrystalline solar cells. *Solar Energy Materials and Solar Cells* **1999**, *58*, 321–336.

Acknowledgements

Foremost, I thank Prof. Grätzel for giving me the opportunity to conduct a thesis in his prestigious and stimulating research group. I highly appreciated the great amount of freedom I was granted during my work and the dedicated support for new projects like the DSC simulator development.

I highly appreciated the fruitful collaborations with several external research groups; I thank the groups of Prof. Peng Wang (Chinese Academy of Sciences, China), Prof. Peter Bäuerle (University of Ulm, Germany), and Prof. Nazario Martín (Universidad de Complutense, Madrid, Spain) for the joint studies of organic dyes; Sieghard Seyrling and Prof. Ayodhya N. Tiwari (Empa, Switzerland) for the work on tandem cells; and Dr. Jürgen Schumacher, Dr. Matthias Schmid, and Adrian Gentsch (all ZHAW, Switzerland) for the joint development of the validated DSC model.

Dr. Frank Nüesch (Empa, Switzerland) has been an excellent coordinator of the Swiss ThinPV project under which the tandem solar cell project was running. I am grateful for the valuable experiences I could make as assistant to the ThinPV project in the field of project management. The active promotion of a common Swiss academic and industrial photovoltaics platform was a particularly rewarding task.

Financial support from the Swiss National Science Foundation (organic dyes), the Swiss Competence Center for Energy and Mobility (CCEM-CH, tandem cells), and the Gerbert Rüf Stiftung (DSC model) is gratefully acknowledged.

I am indebted to many colleagues at EPFL for the scientific and technical assistance and enlightening discussions. In particular, I want to thank Dr. Shaik M. Zakeeruddin for the preparation of countless dye solutions and electrolytes, Pascal Comte for the fabrication of TiO_2 films, Dr. Robin Humphry-Baker for very instructive scientific discussions, characterization expertise, and for proof-reading a large share of this thesis, and Dr. Guido Rothenberger for sharing his extensive knowledge on the device physics of DSCs and making vital contributions to the DSC modeling project. Several people have helped me with the art of DSC assembly and characterization. I especially want to mention Dr. Daibin Kuang (who taught me how to assemble my very first dye-sensitized

solar cell), Dr. Takeru Bessho, Dr. Paul Liska, Dr. Jun-Ho Yum, Dr. Joël Teuscher and Prof. Jaques-E. Moser (laser transient analysis), and Dr. Davide Di Censo (electrochemistry). I also thank Dr. Nicloas Tétreault for atomic layer deposition of metal oxides and Dr. Frédéric Sauvage for taking SEM images of the glass electrodes. A special word of thanks goes to Dr. Kevin Sivula for proof-reading several of my texts and for invaluable advice on the “social dimensions” of science (“it’s politics”).

I want to note the very professional service of the Center of MicroNanoTechnology (CMI) at EPFL; Dr. Philippe Langlet and Dr. Didier Bouvet are acknowledged for the introduction to the ellipsometer and for chemical mechanical polishing of glass electrodes, respectively.

My thesis at EPFL was accompanied by the reliable administrative support of Mme Gonthier, Mme Gourdou, and Anne-Lene Odegaard from the Doctoral School — thank you.

This experience was a very pleasant one, and it was largely due to the amicable, helpful, and enjoyable atmosphere within the group. Jérémie, Kevin, Nic, Takeru, Leo-Philipp, Florian, Adriana, David, Etienne, Francine, Jöel, Angela, Thomas ... and all the others — thank you so much for the good discussions and laughs around coffee, lunch, or beer.

Finally, there are no words to express my gratitude to my fiancé Wieland for his unconditional love, constant support, and the wonderful time we have spent together in Lausanne. I love you too.

Curriculum vitae

Sophie WENGER, Dipl. Phys. ETH
Born 23 December 1983 in Bern, Swiss

sophie.wenger@gmx.ch

Education

- 2007–2010 PhD Thesis, Ecole Polytechnique Fédérale de Lausanne (EPFL), Switzerland. Supervision by Prof. M. Grätzel
Thesis work: *Strategies to optimizing dye-sensitized solar cells: Organic sensitizers, tandem device structures, and numerical device modeling*
- 2001–2006 Diploma in Physics, Eidgnössische Technische Hochschule Zürich, Switzerland
Diploma work: *Synthesis and Properties of Thermoelectric Cobalt Oxides.*
- 1997–2001 Mathematisch-Naturwissenschaftliches Gymnasium Kirchenfeld, Bern, Switzerland.

List of publications

Organic sensitizers

S. Wenger, P.-A. Bouit, Q. Chen, J. Teuscher, D. Di Censo, R. Humphry-Baker, J.-E. Moser, J. L. Delgado, N. Martín, S. M. Zakeeruddin, and M. Grätzel. Efficient Electron Transfer and Sensitizer Regeneration in Stable π -Extended Tetrathiafulvalene-Sensitized Solar Cells. *Journal of the American Chemical Society* **2010**, *132*, 5164–5169.

M. K. R. Fischer, S. Wenger, M. Wang, A. Mishra, S. M. Zakeeruddin, M. Grätzel, and P. Bäuerle. Molecular Design of Metal-free D- π -A Substituted Oligothiophene Sensitizers for Dye-sensitized Solar Cells: Linear vs. Branched. *Chemistry of Materials* **2010**, *22*, 1836–1845.

M. F. Xu, S. Wenger, H. Bala, D. Shi, R. Z. Li, Y. Z. Zhou, S. M. Zakeeruddin, M. Grätzel, and P. Wang. Tuning the Energy Level of Organic Sensitizers for High-Performance Dye-Sensitized Solar Cells. *Journal of Physical Chemistry C* **2009**, *113*, 2966–2973.

G. Zhang, Y. Bai, R. Li, D. Shi, S. Wenger, S. M. Zakeeruddin, M. Grätzel, and P. Wang. Employ a bisthienothiophene linker to construct an organic chromophore for efficient and stable dye-sensitized solar cells. *Energy & Environmental Science* **2009**, *2*, 92–95.

J. M. Szeifert, D. Fattakhova-Rohlg, D. Georgiadou, V. Kalousek, J. Rathousky, D. Kuang, S. Wenger, S. M. Zakeeruddin, M. Grätzel, and T. Bein. “Brick and Mortar” Strategy for the Formation of Highly Crystalline Mesoporous Titania Films from Nanocrystalline Building Blocks. *Chemistry of Materials* **2009**, *21*, 1260–1265.

H. Qin, S. Wenger, M. Xu, F. Gao, X. Jing, P. Wang, S. M. Zakeeruddin, and M. Grätzel. An Organic Sensitizer with a Fused Dithienothiophene Unit for Efficient and Stable Dye-Sensitized Solar Cells. *Journal of the American Chemical Society* **2008**, *130*, 9202–9203.

Tandem solar cells

J.-H. Yum, E. Baranoff, S. Wenger, Md. N. Nazeeruddin, and M. Grätzel. Panchromatic Engineering of Dye-Sensitized Solar Cells. *Manuscript in preparation*.

S. Wenger, S. Seyrling, A. N. Tiwari, and M. Grätzel. Fabrication and performance of a monolithic dye-sensitized $\text{TiO}_2/\text{Cu}(\text{In},\text{Ga})\text{Se}_2$ thin film tandem solar cell. *Applied Physics Letters* **2009**, *94*, 173508.

S. Seyrling, S. Calnan, S. Bücheler, J. Hüpkes, S. Wenger, D. Brémaud, H. Zogg, and A. N. Tiwari. $\text{CuIn}_{1-x}\text{Ga}_x\text{Se}_2$ photovoltaic devices for tandem solar cell application. *Thin Solid Films* **2009**, *517*, 2411-2414.

S. Seyrling, S. Bücheler, A. Chirila, J. Perrenoud, R. Verma, S. Wenger, M. Grätzel, and A.N. Tiwari. Towards the Development of High Efficiency Multijunction Thin Film Solar Cells. *Proceedings of the 24th European Photovoltaic Solar Energy Conference and Exhibition*, Hamburg, Germany, 21–25 September **2009**, p. 2895–2897.

S. Seyrling, S. Bücheler, A. Chirila, J. Perrenoud, S. Wenger, T. Nakada, M. Grätzel, and A N. Tiwari. Development of multijunction thin film solar cells. *Proceedings of the 34th IEEE Photovoltaic Specialists Conference*, Philadelphia, USA, 7–12 June **2009**, p. 622–625.

S. Seyrling, S. Wenger, M. Grätzel, and A. N. Tiwari. Analysis of electronic and optical losses in CIGS/DSC tandem solar cells. *Proceedings of the E-MRS 2009 Spring Meeting*, Strasbourg, France, 8–12 June, **2009**.

Modeling of dye-sensitized solar cells

S. Wenger, M. Schmid, G. Rothenberger, M. Grätzel, and J. Schumacher. Coupled Optical and Electronic Modeling of Dye-Sensitized Solar Cells for Steady-State Parameter Extraction. *Manuscript in preparation*.

S. Wenger, M. Schmid, G. Rothenberger, M. Grätzel and J. Schumacher. Model-based optical and electrical characterization of dye-sensitized solar cells. *Proceedings of the 24th European Photovoltaic Solar Energy Conference and Exhibition*, Hamburg, Germany, 21–25 September **2009**, p. 675–680.

Presentations and Awards

- Materials Research Society (MRS) Spring Meeting, 5–9 April, 2010, San Francisco, USA. *Oral presentation.*
“Understanding Charge Transport and Recombination in Dye-Sensitized Solar Cells Using an Experimentally Validated Coupled Optical and Electrical Model”
- 24th European Photovoltaic Solar Energy Conference and Exhibition, September 21–25, 2009, Hamburg, Germany. *Poster presentation.*
“Model-based optical and electrical characterization of dye-sensitized solar cells”
- European Materials Research Society (E-MRS) Spring Meeting, June 8–12, 2009, Strasbourg, France. *Oral presentation.*
“Optimization of monolithic dye-sensitized $\text{TiO}_2/\text{Cu}(\text{In},\text{Ga})\text{Se}_2$ thin film tandem solar cells”
▷ *European Materials Research Society Young Scientist Award in recognition of an outstanding paper contributed to the E-MRS Spring Meeting 2009.*
- 3rd International Conference on the Industrialization of DSC, April 22-24, 2009, Nara, Japan. *Poster presentation.*
“Fabrication and performance of monolithic dye-sensitized $\text{TiO}_2/\text{Cu}(\text{In},\text{Ga})\text{Se}_2$ tandem solar cells”
- Empa Akademie: Workshop ”A look inside solar cells”, November 16–18, 2008, Ascona, Switzerland. *Oral presentation.*
“Loss mechanisms in monolithic dye-sensitized/Cu(In,Ga)Se₂ tandem solar cells”
- European Science Foundation Conference: Nanotechnology for Sustainable Energy, June 14–19, 2008, Obergurgl, Austria. *Poster presentation.*
“Loss mechanisms in stacked and monolithic dye-sensitized/thin-film tandem solar cells”
▷ *Poster award — 1st prize.*
- EPFL Research Day, Lausanne, Switzerland, 2008. *Poster presentation.*
“Tandem solar cells boost photovoltaic conversion efficiency: Application of dye-sensitized solar cells in tandem devices”
▷ *Best poster award in the category “Energy Related Technology”.*